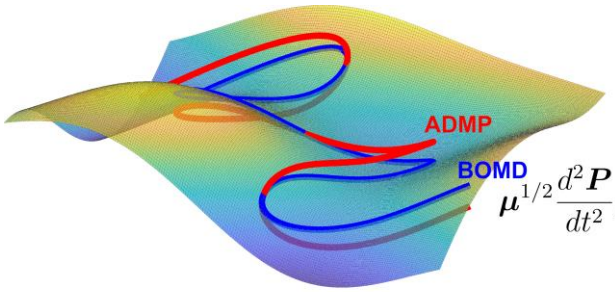
University of Naples Federico II
Polytechnic and Basic Sciences School

Department of Chemical Sciences

Ph.D. in Chemical Sciences

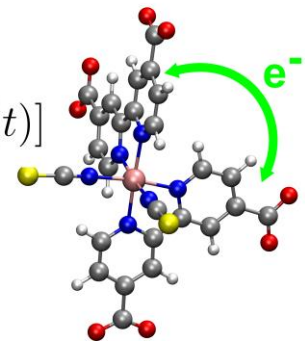
Development of an adaptive electronic approach for extended Lagrangian *ab initio* molecular dynamics



$$M\frac{d^2\boldsymbol{R}}{dt^2} = -\frac{\partial E(\boldsymbol{R},\boldsymbol{P})}{\partial \boldsymbol{R}}\Big|_{P}$$

$$\boldsymbol{\mu}^{1/2}\frac{d^2\boldsymbol{P}}{dt^2}\boldsymbol{\mu}^{1/2} = -\left[\frac{\partial E(\boldsymbol{R},\boldsymbol{P})}{\partial \boldsymbol{P}}\Big|_{R} + \boldsymbol{\Lambda}\boldsymbol{P} + \boldsymbol{P}\boldsymbol{\Lambda} - \boldsymbol{\Lambda}\right]$$

$$i\frac{d\boldsymbol{P}(t)}{dt} = [\boldsymbol{F}(t), \boldsymbol{P}(t)]$$



Fulvio Perrella

Advisor:
prof. Nadia Rega

Examiner:
prof. Andrea Correa

XXXIII Cycle 2018 – 2021
Coordinator: prof. Angela Lombardi

Contents

1 Introduction **1**

1.1 *Ab initio* Molecular Dynamics: theory and modern implementations 1

1.1.1 Born-Oppenheimer Molecular Dynamics 1

1.1.2 Car-Parrinello Molecular Dynamics 7

1.1.3 Atom-centered Density Matrix Propagation (ADMP) Molecular Dynamics 10

2 Rational mass-weighting schemes: theoretical details. **17**

2.1 Core subspace-based approaches. 18

2.1.1 Definition of the molecular core subspace. 18

2.1.2 Basis functions projection onto the molecular core subspace: AO weighting schemes. 20

2.1.3 Molecular orbitals projection onto the molecular core subspace: MO weighting schemes. 25

2.1.4 Implementation into Gaussian16. 28

2.2 Electronic Hessian-based approach. 29

2.2.1 Effects of $\tilde{\nu}$ frequency upon the dynamics. 36

2.2.2 Effects of $\boldsymbol{K}$ sparsity upon the dynamics. 37

2.2.3 Implementation into Gaussian16. 41

3 Evaluation of the developed weighting schemes: test simulations of model compounds. **44**

3.1 Introduction: how to measure the accuracy of an ADMP simulation? 44
3.2 Lithium Fluoride (LiF) 49
3.2.1 B3LYP/6-31G(d,p) level of theory. 49
3.2.2 LiF ADMP test simulations: summary 63
3.3 N-methylacetamide (NMA) 66
3.3.1 B3LYP/6-31G(d,p) level of theory. 66
3.3.2 B3LYP/6-311G(d,p) level of theory. 78
3.3.3 NMA ADMP test simulations: summary 93
3.4 Trans-dichloroethylene 99
3.4.1 B3LYP/6-31G(d,p) level of theory. 99
3.4.2 B3LYP/6-311G(d,p) level of theory. 114
3.4.3 Dichloroethylene ADMP test simulations: summary . 126
3.5 $[Ru(dcbpy)_2(NCS)_2]^{4-}$ ('$N3^{4-}$') Ru(II) complex. 132
3.5.1 B3LYP/SDD/def2-SVP level of theory. 132
3.5.2 Ru-$N3^{4-}$ ADMP test simulations: summary 142
3.6 Conclusions and future perspectives. 146

4 Ground state characterization of $N3^{4-}$ Ru(II) complex in water solution: solvation and vibrational analysis. 149
4.1 Introduction 149
4.2 Methods 150
4.2.1 Ground state Molecular Dynamics in explicit solvent solution. 150
4.2.2 Molecular Dynamics-based vibrational analysis. 153
4.3 Characterization of $N3^{4-}$ solvation through Molecular Dynamics. 154
4.4 $N3^{4-}$ vibrational analysis in water solution through Molecular Dynamics. 157

5 Exploring the ultra-fast excited state electronic dynamics of Ru(II) $N3^{4-}$ complex. 160
5.1 Methods 160

5.1.1 The Real-Time Time-Dependent Density Functional Theory approach. 160
5.1.2 Analysis of RT-TDDFT trajectories. 161
5.1.3 RT-TDDFT $N3^{4-}$ dynamics: initial conditions and computational details. 165
5.2 $N3^{4-}$ excited states. 169
5.3 $^1MLCT_A$ and $^1MLCT_B$ electronic dynamics: optimized gas-phase structure (M-G). 173
5.3.1 Charges and hole/electron distribution. 173
5.3.2 Electric dipole moment. 176
5.3.3 Molecular orbitals occupation numbers. 181
5.4 $^1MLCT_A$ and $^1MLCT_B$ electronic dynamics: solvent effects (D1-G and D1-W). 183
5.4.1 Charges and hole/electron distribution. 183
5.4.2 Electric dipole moment. 191
5.4.3 Molecular orbitals occupation numbers. 195
5.5 Inter-Ligand Electron Transfer in $N3^{4-}$: insights from theory. 200
5.6 $^1MLCT_A$ and $^1MLCT_B$ electronic dynamics: modelling first-shell solvent molecules (D1-C and D1-W). 203
5.7 Conclusions 212
5.8 Appendix: $N3^{4-}$ MOs. 214

Abstract

Ab initio Molecular Dynamics (AIMD) is nowadays a popular tool for the caracterization of equilibrium, ground state, properties of molecular systems. Beside the Born-Oppenheimer (BO) traditional approach to AIMD, extended Lagrangian methods such as Car-Parrinello Molecular Dynamics offer a good compromise between accuracy and computational cost, within the Density Functional Theory (DFT) framework. In order to explore photophysical and photochemical properties, the DFT Time-Dependent formalism is instead often chosen to perform excited states BOMD simulations. Extended Lagrangian ground state trajectories are nevertheless required to extensively sample the population being excited. The Atom-centered Density Matrix Propagation (ADMP) method is an extended Lagrangian (Car-Parrinello-like) *ab initio* Molecular Dynamics approach which relies upon the concurrent propagation of both the nuclear degrees of freedom and the density matrix in an orthonormal basis. The adiabaticity between the two sub-systems is crucial in order to keep only slight deviations from a true Born-Oppenheimer dynamics. In the first part of this work, novel fictitious electronic mass-weighting approaches have been developed, aimed at improving the separation between the nuclear and the electronic power spectra and so the adiabaticity. A first class of approaches is based upon the definition of a molecular core subspace, defined from the core atomic MOs. Then, the projection of the orthonormal atomic or molecular orbitals onto such subspace allows for a decomposition into a valence and several core components, which is exploited to evaluate the corresponding mass. ADMP test trajectories of several model compounds reveal that these weighting schemes allow one to use time steps greater than 0.1 fs, while still ensuring an acceptable accuracy. A second approach is instead derived from the definition of the electronic harmonic normal modes and the electronic Hessian. A mass-matrix is calculated imposing a common frequency to such modes. This method proves to be highly accurate at the lowest time steps, showing

little or no error in the calculated vibrational bands with respect to a BO dynamics. Beside smaller model systems, ADMP trajectories of the Ru(II) complex $[Ru(dcbpy)_2(NCS)_2]^{4-}$ ('N3', an efficient dye for light-harvesting applications) have been collected, again revealing an improved accuracy if a rational weighting scheme is implemented.

In the second part of this work, photophysical properties of N3 dye in solution have been explored, starting from a ground state characterization through ADMP simulations. In water solution, all the N3 solvation sites are highly solvated, as expected. Moreover, combined solvation and anharmonicity effects account for a $\sim 100\,\mathrm{cm}^{-1}$ red-shift in several N3 vibrational bands. The dynamics of two relevant MLCT excited states (called $^1\mathrm{MLCT}_A$ and $^1\mathrm{MLCT}_B$) after the photo-excitation has been then investigated through real-time TD-DFT. Simulations on N3 optimized gas-phase structure show that the hole oscillates between the NCS ligands and Ru (at $\sim 15\,000\,\mathrm{cm}^{-1}$), while the electron resides on the dcbpy ligands, although in $^1\mathrm{MLCT}_B$ a complete electron migration is observed after 15 fs. Moreover, the overall electron mobility appears reduced with respect to the hole in $^1\mathrm{MLCT}_A$. Water polarization counterbalances the distortion effects in the N3 solution structure excited state dynamics. In particular, the hole is more displaced towards the Ru center, while in $^1\mathrm{MLCT}_A$ the electron migration is still inhibited. On average, the charge carriers mobilities appear reduced in both states and the separation increased in $^1\mathrm{MLCT}_A$. An ultra-fast dcbpy/dcbpy inter-ligand electron transfer is instead observed in $^1\mathrm{MLCT}_B$ also in water solution.

As shown by this work, *ab initio* (adiabatic and non-adiabatic) Molecular and Electronic Dynamics prove to be powerful tools to gather insight into systems and processes of technological and biological interest.

Chapter 1

Introduction

1.1 *Ab initio* Molecular Dynamics: theory and modern implementations

1.1.1 Born-Oppenheimer Molecular Dynamics

One of the most challenging tasks given to modern theoretical chemistry is the accurate simulation of molecular phenomena occurring on a broad range of time scales, from ultra-fast electron transfer to molecular vibrations and slow collective motions. Nowadays, Molecular Dynamics (MD) has acquired a prominent role among the techniques available to the computational chemist, because of its proven investigation and prediction capabilities in chemistry, biology and materials science fields. [1–9]

A brief description of the *ab initio* Molecular Dynamics formalism will be given first. Moreover, the fundamental concepts of the Density Functional Theory (DFT) will be recalled. Due to its optimal balance between accuracy and computational cost, DFT is in fact the usually preferred level of theory for the calculation of electronic energy in most *ab initio* MD applications (and also in this work).

Most implementations of Molecular Dynamics rely upon the famous Born-Oppenheimer approximation, which allows to decouple electronic and nuclear motions, because of the high mass (and so velocity) difference. The

total molecular wavefunction can be decomposed in two distinct electronic and nuclear terms:

$$\Phi(\boldsymbol{r}, \boldsymbol{R}, t) = \Psi_k(\boldsymbol{r}; \boldsymbol{R})\chi_k(\boldsymbol{R}, t) \tag{1.1}$$

where $\boldsymbol{r}$ and $\boldsymbol{R}$ are the electronic and nuclear coordinates, respectively, t is the time and the index k refer to the *k-th* electronic state.

From the electrons viewpoint, the nuclei can be considered as "clamped", giving rise to a fixed external potential. An electronic (time-independent) Schrödinger equation for a given set $\boldsymbol{R} = \{\boldsymbol{R}_I\}$ of nuclear positions can provide stationary electronic states:

$$\hat{\mathcal{H}}_e \Psi_k(\boldsymbol{r}; \boldsymbol{R}) = E_{e,k}(\boldsymbol{R})\Psi_k(\boldsymbol{r}; \boldsymbol{R}) \tag{1.2}$$

$$\hat{\mathcal{H}}_e = \hat{T}_e + \hat{V}_{ee} + \hat{V}_{Ne} = -\frac{1}{2}\sum_i \nabla_i^2 + \sum_{i<j} \frac{1}{\|\boldsymbol{r}_i - \boldsymbol{r}_j\|} - \sum_{I,i} \frac{Z_I}{\|\boldsymbol{R}_I - \boldsymbol{r}_i\|} = \tag{1.3}$$

where $\hat{T}_e$, $\hat{V}_{ee}$ and $\hat{V}_{Ne}$ are the kinetic, electron-electron interaction and nuclear-electron interaction energy terms, respectively, i and I are electronic and nuclear indexes and Z_I is the *I-th* nucleus atomic number.

The electronic wavefunction has only a parametric dependence upon nuclear coordinates. Solving for the k-th electronic state for distinct nuclear configurations $\boldsymbol{R}$, the corresponding Potential Energy Surface (PES) $E_k^{\mathrm{BO}}(\boldsymbol{R}) = E_{e,k}(\boldsymbol{R}) + V_{NN}(\boldsymbol{R})$ can be obtained.

On the other hand, nuclei evolve on a single adiabatic PES associated with the electronic state k:

$$\begin{aligned}
&\big[\hat{T}_N + E_{e,k}(\boldsymbol{R}) + \hat{V}_{NN}\big]\chi_k(\boldsymbol{R}, t) = \\
&= \Big[-\sum_I \frac{1}{2M_I}\nabla_I^2 + E_{e,k}(\boldsymbol{R}) + \sum_{I<J} \frac{Z_I Z_J}{\|\boldsymbol{R}_I - \boldsymbol{R}_J\|}\Big]\chi_k(\boldsymbol{R}, t) = i\frac{\partial}{\partial t}\chi_k(\boldsymbol{R}, t)
\end{aligned} \tag{1.4}$$

This is equivalent to neglect all non-adiabatic Ψ_k/Ψ_l coupling operators $\hat{\mathcal{C}}_{kl}$, as well as the diagonal terms $\hat{\mathcal{C}}_{kk}$.

Switching to classical dynamics, a Newton equation of motion governs the nuclear degrees of freedom time evolution:

$$M_I \ddot{\boldsymbol{R}}_I(t) = -\boldsymbol{\nabla}_I E_k^{\mathrm{BO}}(\boldsymbol{R}(t)) \tag{1.5}$$

A so-called Born-Oppenheimer Molecular Dynamics (BOMD) thus requires the calculation of the electronic eigenstates from Eq. (1.2) (providing energies and energy gradients with respect to the nuclear coordinates) at each time t along the trajectory, employing the given nuclear positions $\boldsymbol{R}(t)$ at that instant. [10] For the ground state, this implies in practice that the mininum of the energy functional $\min_{\{\psi_i\}} \langle\Psi|\hat{\mathcal{H}}_e|\Psi\rangle + V_{NN} = E_0^{\mathrm{BO}}$ has to be obtained at each step through $\{\psi_i\}$ orbitals self-consistent optimization. A BOMD simulation therefore does not involve an explicit electronic dynamics. The time evolution of the electronic structure is dictated instead by the (classical) nuclear dynamics, through its parametric dependence upon $\boldsymbol{R}(t)$.

Traditionally, a popular way to avoid the (costly) electronic structure calculation along the dynamics is the approximation of the potential energy surface with an expansion of few-body contributions (i.e., a force field):

$$E_0^{\mathrm{BO}}(\boldsymbol{R}) \approx \sum_I v_1(\boldsymbol{R}_I) + \sum_{I<J} v_2(\boldsymbol{R}_I, \boldsymbol{R}_J) + \sum_{I<J<K} v_3(\boldsymbol{R}_I, \boldsymbol{R}_J, \boldsymbol{R}_K) + \dots \tag{1.6}$$

where v_1, v_2 and $v_3 \dots$ are single-, two-, three-$\dots$ bodies energy terms.

While the elimination of the electronic degrees of freedom allows higher simulation times, a force field must be specifically parametrized for a given class of systems. Moreover, the quite drastic approximations cannot model substantial electronic structure rearrangements (such as bond breaking and forming).

Common implementations of *ab initio* molecular dynamics employ single-determinant, one-particle effective Hamiltonians, electronic structure methods. In particular, the popular Density Functional Theory (DFT) is often the preferred choice, because of its usually high accuracy/cost ratio [11–15]. Theoretical foundations of DFT lie in the Hohenberg-Kohn theorem. [16]

Given the Hamiltonian $\hat{\mathcal{H}}$ for an interacting N-electrons system

$$\hat{\mathcal{H}} = \hat{T} + \hat{V} + \hat{W} \tag{1.7}$$

$$\hat{T} = -\frac{1}{2}\sum_j \nabla_j^2; \qquad \hat{V} = \sum_j v(\boldsymbol{r}_j); \qquad \hat{W} = \sum_{j<k} \frac{1}{\|\boldsymbol{r}_j - \boldsymbol{r}_k\|} \tag{1.8}$$

where $\hat{T}$, $\hat{V}$ and $\hat{W}$ are the kinetic, electron-external potential and electron-electron interaction energies (being $v(\boldsymbol{r}_1)$ usually the Coulomb potential by the (fixed) nuclei), there exists a one-to-one correspondence between $v(\boldsymbol{r}_1)$ and the ground-state single-particle probability density $n_0(\boldsymbol{r}_1)$,

$$n_0(\boldsymbol{r}_1) = N \int d\sigma_1 d\boldsymbol{x}_2 \dots d\boldsymbol{x}_N |\Psi_0(\boldsymbol{r}_1, \sigma_1, \boldsymbol{x}_2, \dots, \boldsymbol{x}_N)|^2 \tag{1.9}$$

where N is the number of the electrons, σ_i and $\boldsymbol{r}_i$ are the electronic spin and spatial coordinates and $\boldsymbol{x}_i = \sigma_i, \boldsymbol{r}_i$.

Therefore, the external potential (and so the Hamiltonian and all the electronic eigenstates Ψ_k) is a unique functional of the ground-state density: $v[n_0](\boldsymbol{r}_1)$. Moreover, considering the total-energy functional for a given external potential $v_0(\boldsymbol{r}_1)$

$$E_{v_0}[n] = \langle \Psi[n] | \hat{T} + \hat{W} + \hat{V}_0 | \Psi[n] \rangle \tag{1.10}$$

where $\Psi[n]$ is the unique ground-state wavefunction related to the density $n(\boldsymbol{r}_1)$, a variational "principle" can be formulated also with respect to the density:

$$E_{v_0}[n] = \begin{cases} > E_0 & n(\boldsymbol{r}_1) \neq n_0(\boldsymbol{r}_1) \\ = E_0 & n(\boldsymbol{r}_1) = n_0(\boldsymbol{r}_1) \end{cases} \tag{1.11}$$

being $n_0(\boldsymbol{r}_1)$ the ground-state density associated to $v_0(\boldsymbol{r}_1)$.

The energy functional Eq. (1.10) can be rewritten as:

$$E_{v_0}[n] = F[n] + \int d\,\boldsymbol{r}_1 n(\boldsymbol{r}_1) v_0(\boldsymbol{r}_1) \tag{1.12}$$

where $F[n] = \langle \Psi[n] | \hat{T} + \hat{W} | \Psi[n] \rangle = T[n] + W[n]$ is a "universal" (but un-

known) functional, independent of the specific external potential.

The variational principle Eq. (1.11) suggests that the ground-state density could be obtained, at least in principle, through a minimization of the $E_{v_0}[n]$ functional:

$$\frac{\delta}{\delta n(\boldsymbol{r}_1)}\Big[E_{v_0}[n]-\mu(\int d\boldsymbol{r}'_1 n(\boldsymbol{r}'_1)-N)\Big] = \frac{\delta E_{v_0}[n]}{\delta n(\boldsymbol{r}_1)}-\mu = \frac{\delta F[n]}{\delta n(\boldsymbol{r}_1)}+v_0(\boldsymbol{r}_1)-\mu = 0 \tag{1.13}$$

having imposed the correct total number of electrons N through a Lagrange multiplier μ.

A practical method to solve Eq. (1.13) was formulated by the introduction of the Kohn-Sham non-interacting N-electrons system. [17]. The Hamiltonian, $\hat{\mathcal{H}}_s$, of such system is, by definition, exactly decomposed into one-particle contributions:

$$\hat{\mathcal{H}}_s = \hat{T} + \hat{V}_s = \sum_j \Big(-\frac{\nabla_j^2}{2} + v_s(\boldsymbol{r}_j)\Big) \tag{1.14}$$

The many-body ground-state wavefunction is exactly a Slater determinant:

$$\Psi_s(\boldsymbol{x}_1, \boldsymbol{x}_2, \ldots, \boldsymbol{x}_N) = \frac{1}{\sqrt{N!}} \begin{vmatrix} \psi_1(\boldsymbol{x}_1) & \psi_2(\boldsymbol{x}_1) & \ldots & \psi_N(\boldsymbol{x}_1) \\ \psi_1(\boldsymbol{x}_2) & \psi_2(\boldsymbol{x}_2) & \ldots & \psi_N(\boldsymbol{x}_2) \\ \vdots & \vdots & & \vdots \\ \psi_1(\boldsymbol{x}_N) & \psi_2(\boldsymbol{x}_N) & \ldots & \psi_N(\boldsymbol{x}_N) \end{vmatrix} \tag{1.15}$$

$$\Big(-\frac{\nabla_1^2}{2} + v_s(\boldsymbol{r}_1)\Big)\psi_j(\boldsymbol{x}_1) = \hat{f}^{\mathrm{KS}}(\boldsymbol{r}_1)\psi_j(\boldsymbol{x}_1) = \varepsilon_j\psi_j(\boldsymbol{x}_1) \tag{1.16}$$

The ground-state density can be obtained from the N lowest orbitals:

$$n_0(\boldsymbol{r}_1) = \sum_{j=1}^{N} \int d\sigma_1 |\psi_j(\boldsymbol{x}_1)|^2 \tag{1.17}$$

Considering the non-interacting system total-energy functional

$$E_{v_s}[n] = T_s[n] + \int d\boldsymbol{r}_1 n(\boldsymbol{r}_1) v_s(\boldsymbol{r}_1) \tag{1.18}$$

the minimum condition Eq. (1.13) becomes:

$$\frac{\delta T_s[n]}{\delta n(\boldsymbol{r}_1)} + v_s(\boldsymbol{r}_1) - \mu = 0 \tag{1.19}$$

The non-interacting electronic kinetic energy $T_s[n]$ can be expressed through the occupied orbitals:

$$T_s[n] = \sum_{j=1}^{N} \int d\boldsymbol{r}_1 \psi_j^*(\boldsymbol{r}_1)\Big(-\frac{\nabla_1^2}{2}\Big)\psi_j(\boldsymbol{r}_1) \tag{1.20}$$

On the other hand, the interacting system energy functional (Eq. (1.12)) can be rewritten, taking advantage of such independent-particles auxiliary system:

$$\begin{aligned} E_{v_0}[n] &= T[n] + W[n] + \int d\boldsymbol{r}_1 n(\boldsymbol{r}_1) v_0(\boldsymbol{r}_1) = \\ &= T_s[n] + \frac{1}{2}\int d\boldsymbol{r}_1 d\boldsymbol{r}'_1 \frac{n(\boldsymbol{r}_1)n(\boldsymbol{r}'_1)}{\|\boldsymbol{r}_1 - \boldsymbol{r}'_1\|} + \int d\boldsymbol{r}_1 n(\boldsymbol{r}_1) v_0(\boldsymbol{r}_1) + E_{\mathrm{xc}}[n] \end{aligned} \tag{1.21}$$

The exchange-correlation functional $E_{\mathrm{xc}}[n]$ thus collects the non-classic electron-electron interaction effects, as well as the kinetic energy deviation from the corresponding non-interacting system. Good approximations of $E_{\mathrm{xc}}[n]$ are mandatory in order to obtain accurate results.

Insertion of Eq. (1.21) into the minimization condition Eq. (1.13) yields:

$$\frac{\delta T_s[n]}{\delta n(\boldsymbol{r}_1)} + \int d\boldsymbol{r}'_1 \frac{n(\boldsymbol{r}'_1)}{\|\boldsymbol{r}_1 - \boldsymbol{r}'_1\|} + v_0(\boldsymbol{r}_1) + v_{\mathrm{xc}}[n](\boldsymbol{r}_1) - \mu = 0 \tag{1.22}$$

$$v_{\mathrm{xc}}[n](\boldsymbol{r}_1) = \frac{\delta E_{\mathrm{xc}}[n]}{\delta n(\boldsymbol{r}_1)} \tag{1.23}$$

Comparing the two (interacting and non-interacting) systems and so imposing that Eqs. (1.19) and (1.22) be identical, then:

$$v_s[n](\boldsymbol{r}_1) = \int d\boldsymbol{r}'_1 \frac{n(\boldsymbol{r}'_1)}{\|\boldsymbol{r}_1 - \boldsymbol{r}'_1\|} + v_0(\boldsymbol{r}_1) + v_{\mathrm{xc}}[n](\boldsymbol{r}_1) \tag{1.24}$$

The ground-state density of the interacting system can be therefore

obtained solving the Kohn-Sham equations Eqs. (1.16) and (1.17).

1.1.2 Car-Parrinello Molecular Dynamics

The fundamental idea behind Car and Parrinello approach to *ab initio* Molecular Dynamics [18–21] is to exploit the quantum-mechanical adiabatic time-scale separation existing between the quantum, fast, electronic motion and the classical, slow, nuclear one. In particular, the two-component quantum/classical problem is mapped onto a two-component fully classical problem, characterized by two separated energy scales (but losing the physical time-scale of the quantum electronic subsystem).

An *extended* Lagrangian can be thus introduced:

$$\mathcal{L}_{\mathrm{CP}} = \frac{1}{2}\sum_I M_I \left\|\dot{\boldsymbol{R}}_I\right\|^2 + \sum_{i=1}^{N} \mu \left\langle \dot{\psi}_i | \dot{\psi}_i \right\rangle - E(\boldsymbol{R})[\{\psi_i\}] + \sum_{i,j} \Lambda_{ij}(\langle \psi_i | \psi_j \rangle - \delta_{ij}) \tag{1.25}$$

where M_I and $\boldsymbol{R}_I$ are the mass and coordinates of the *I-th* nucleus.

The Kohn-Sham orbitals $\{\psi_i\}$, constituting the $\Psi = N^{-1/2}\det\{\psi_i\}$ Slater determinant, are here considered as classical complex scalar fields. The dimensionality of the total phase space is thus increased by the introduction of "auxiliary" (or "fictitious") degrees of freedom, characterized by positions $\{\psi_i\}$, velocities $\{\dot{\psi}_i\}$ and a mass μ. $E(\boldsymbol{R})[\{\psi_i\}] = \langle\Psi|\hat{\mathcal{H}}_e|\Psi\rangle + V_{NN}$ (i.e., the potential energy for the nuclear motion) is not only a function of the nuclear positions $\boldsymbol{R}$, but also a functional of the electronic state Ψ and so of the $\{\psi_i\}$ orbitals. $\{\psi_i\}$ orthonormality is imposed through Lagrange multipliers Λ_{ij}.

Euler-Lagrange equations for the nuclear positions and the orbitals

$$\frac{d}{dt}\frac{\partial \mathcal{L}}{\partial \dot{\boldsymbol{R}}_I} = \frac{\partial \mathcal{L}}{\partial \boldsymbol{R}_I} \tag{1.26}$$

$$\frac{d}{dt}\frac{\delta \mathcal{L}}{\delta \dot{\psi}_i^*} = \frac{\delta \mathcal{L}}{\delta \psi_i^*} \tag{1.27}$$

give the corresponding Car-Parrinello (CP) equations of motion, which should sample a microcanonical ensemble rigorously in the extended phase

space, but approximately also in the "physical" one:

$$M_I \ddot{\boldsymbol{R}}_I(t) = -\boldsymbol{\nabla}_I E(\boldsymbol{R})[\{\psi_i\}] \tag{1.28}$$

$$\mu \ddot{\psi}_i(t) = -\frac{\delta}{\delta \psi_i^*} E(\boldsymbol{R})[\{\psi_i\}] + \sum_j \Lambda_{ij}\psi_j = -\hat{f}^{\mathrm{KS}}\psi_i + \sum_j \Lambda_{ij}\psi_j \tag{1.29}$$

Forces on the orbitals are given by functional derivatives of the energy with respect to them, also including "constraint forces".

The CP propagation scheme thus seeks to exploit the smooth time-evolution of the electronic structure, avoiding the Hamiltonian diagonalization at each step. Moreover, since the fictitious orbital time-scales are nevertheless higher than the real electronic ones, higher time steps can be employed than in explicit electronic dynamics approaches.

The conserved total energy (i.e., the Hamiltonian function associated to the CP extended Lagrangian Eq. (1.25)) must include also the kinetic energy $T_{\mathrm{fict}} = \sum_{i=1}^{N} \mu \langle \dot{\psi}_i | \dot{\psi}_i \rangle$ of the fictitious degrees of freedom:

$$E_{\mathrm{tot}} = \frac{1}{2}\sum_I M_I \left\| \dot{\boldsymbol{R}}_I \right\|^2 + \sum_{i=1}^{N} \mu \langle \dot{\psi}_i | \dot{\psi}_i \rangle + E(\boldsymbol{R})[\{\psi_i\}] \tag{1.30}$$

The total "physical" energy

$$E_{\mathrm{phys}} = \frac{1}{2}\sum_I M_I \left\| \dot{\boldsymbol{R}}_I \right\|^2 + E(\boldsymbol{R})[\{\psi_i\}] \tag{1.31}$$

is instead, in principle, not a constant of motion (although in practice being so, with a good approximation).

A large part of this thesis is focused on the control of the adiabaticity in extended Lagrangian simulations and on its relation with the Lagrangian fictitious terms. The fictitious electronic kinetic energy T_{fict} can offer useful hints about how close the electronic subsystem is to the BO surface. Tipically, T_{fict} shows small-amplitude, high-frequency oscillations, intrinsic to the $\{\psi_i\}$ dynamics, superimposed onto lower frequency ones, induced instead by the drag that the nuclei exert on the electronic structure during the vibrational motions. Nevertheless, for well-behaved CP simulations T_{fict} oscillation

is bound and around a constant value, demonstrating that the fictitious electronic degrees of freedom do not heat up. A small T_{fict} suggests that, if starting at $t = 0$ with an optimized wavefunction, the electronic subsystem remains close to the ground state also along the simulation.

It appears therefore crucial for the accuracy of CP dynamics to decouple the two nuclear and electronic subsystems and achieve a quasi-adiabatic time evolution, in order to keep the orbitals "cold". In particular, a wide gap between the two subsystems vibrational power spectra can induce a metastability condition which allows only a small energy flow during the simulation time scale. [22–25]

The inertia parameter μ has a direct role in the adiabaticity control. In fact, an harmonic analysis of CP orbitals motion [22] shows that the lowest orbital frequency can be estimated as:

$$\omega_e^{\min} = \Big(\frac{\varepsilon_{\text{LUMO}} - \varepsilon_{\text{HOMO}}}{\mu}\Big)^{1/2} \tag{1.32}$$

A decrease of μ therefore leads to an upwards shift of the vibrational fictitious electronic spectrum, thus increasing the frequency gap between the highest nuclear vibration and the lowest electronic one. On the other hand, the maximum allowed time step $\Delta t^{\max}$ is inversely proportional to the maximum electronic frequency $\omega_e^{\max}$ and therefore it increases with μ. CP simulations therefore always require to make a compromise between accuracy (smaller μ, higher adiabaticity) and computational cost (bigger μ, bigger Δt). A commonly employed (and often unavoidable) "trick" to employ bigger time steps is reducing the highest nuclear vibrational frequencies (the stretching modes involving H atoms, if present) through H/D isotopic substitutions. The drawback is of course an unwanted isotope effect, affecting, for example, the vibrational spectrum.

It has been shown that there always exists an upper limit to μ for a proper CP simulation. [26] Employing even bigger μ values, a loss of adiabatic decoupling and a progressive increase of T_{fict} (and the deviation from the BO surface) occur (i.e., T_{fict} and the deviation from the BO trajectory are not bound anymore). Nevertheless, a finite $\mu > 0$ fictitious mass also affects well-

behaved CP simulations. In particular, the difference between the CP forces on the nuclei and those from a converged electronic structure is always small, but non-zero, showing high/low frequencies bound oscillations, similarly to T_{fict}. It has been suggested that the small-amplitude, high-frequency oscillations (therefore occurring within only a few steps) contribute to an averaging effect on the (bigger) nuclear time scales, so that CP average forces are close to the correct BO ones. [22] A first-order perturbative treatment of ψ_i deviations from the BO converged orbitals leads to a CP-BO forces deviation (averaged over time scales intermediate between those of the orbitals and nuclei) linear in μ (and so vanishing for $\mu \to 0$). [24] Moreover, in such "intermediate" time scale, the acceleration of the orbitals is on average zero, $\overline{\ddot{\psi}_i(t)} \approx 0$ and so also the average energy gradient $\delta E/\delta\psi_i^*$ (i.e., the electronic structure is on average close to the BO surface). The dynamical effects due to such μ-dependent force error can be explained as a renormalization of nuclear masses as $M_I + \Delta_\mu M_I$, where $\Delta_\mu M_I > 0$ depends upon μ. The electrons, in fact, following (and being dragged by) the nuclei, add a further inertia, given by the orbitals fictitious mass. The finite μ fictitious mass effect is mostly observed in dynamical, mass-dependent, quantities like nuclear velocities and vibrational power spectra. [27]

1.1.3 Atom-centered Density Matrix Propagation (ADMP) Molecular Dynamics

The high flexibility of the *Extended Lagrangian* approach allows to include almost arbitrary additional degrees of freedom and constraints, thus offering the opportunity to go beyond the standard CP molecular dynamics implementation.

In particular, the Atom-centered Density Matrix Propagation (ADMP) method, while retaining the original spirit of the CP approach, employs the elements of the reduced, one-particle, density matrix $\boldsymbol{P}$ as the additional electronic degrees of freedom, instead of the orbitals $\{\psi_i\}$. [28–32]

An extended Lagrangian in an orthonormal basis can be defined:

$$\mathcal{L} = \frac{1}{2}\,\mathrm{Tr}(\boldsymbol{V}^T\boldsymbol{M}\boldsymbol{V}) + \frac{1}{2}\,\mathrm{Tr}\big[(\boldsymbol{\mu}^{1/4}\boldsymbol{W}\boldsymbol{\mu}^{1/4})^2\big] - E(\boldsymbol{R},\boldsymbol{P}) - \mathrm{Tr}\big[\boldsymbol{\Lambda}(\boldsymbol{P}^2-\boldsymbol{P})\big] \tag{1.33}$$

where $\boldsymbol{V} = d\boldsymbol{R}/dt$ is the nuclear velocities matrix, $\boldsymbol{M}$ is the diagonal nuclear masses matrix, $\boldsymbol{\mu}$ is the fictitious electronic mass matrix and $\boldsymbol{W} = d\boldsymbol{P}/dt$ is the density velocity. $\boldsymbol{\mu}^{1/4}\boldsymbol{W}\boldsymbol{\mu}^{1/4}$ can be therefore considered as the mass-weighted density velocity. The Lagrangian constraints matrix $\boldsymbol{\Lambda}$ ensures the conservation of particles number and $\boldsymbol{P}$ idempotency. The potential energy for the nuclear motion $E(\boldsymbol{R},\boldsymbol{P})$ has the usual expression

$$\begin{aligned} E(\boldsymbol{R},\boldsymbol{P}) = \mathrm{Tr}\big[\boldsymbol{h}'\tilde{\boldsymbol{P}}' + \frac{1}{2}\boldsymbol{G}'(\tilde{\boldsymbol{P}}')\tilde{\boldsymbol{P}}'\big] + E_{\mathrm{xc}} + V_{NN} = \\ = \mathrm{Tr}\big[\boldsymbol{h}\tilde{\boldsymbol{P}} + \frac{1}{2}\boldsymbol{G}(\tilde{\boldsymbol{P}})\tilde{\boldsymbol{P}}\big] + E_{\mathrm{xc}} + V_{NN} \end{aligned} \tag{1.34}$$

where $\boldsymbol{h}$ and $\boldsymbol{G}(\tilde{\boldsymbol{P}})$ are the one- and two-electron Coulomb matrix in the orthonormal basis, respectively, while the primed quantities are in the AO basis. The "purified" density $\tilde{\boldsymbol{P}} = 3\boldsymbol{P}^2 - 2\boldsymbol{P}^3$ [33] is employed.

The AO overlap matrix $\boldsymbol{S}'$ can be factorized as $\boldsymbol{S}' = \boldsymbol{U}^T\boldsymbol{U}$. The orthonormal transformation can be obtained as $\boldsymbol{X} = \boldsymbol{U}^{-1}$ (having to verify $\boldsymbol{X}^T\boldsymbol{S}'\boldsymbol{X} = \boldsymbol{I}$). Cholesky (upper-triangular matrix $\boldsymbol{U}$) or Löwdin ($\boldsymbol{U} = \boldsymbol{S}'^{1/2}$) orthonormal bases are common choices. Transformations between the two basis are therefore $\boldsymbol{h} = \boldsymbol{X}^T\boldsymbol{h}'\boldsymbol{X} = \boldsymbol{U}^{-T}\boldsymbol{h}'\boldsymbol{U}^{-1}$, $\boldsymbol{G} = \boldsymbol{X}^T\boldsymbol{G}'\boldsymbol{X} = \boldsymbol{U}^{-T}\boldsymbol{G}'\boldsymbol{U}^{-1}$ and $\boldsymbol{P} = \boldsymbol{X}^{-1}\boldsymbol{P}'\boldsymbol{X}^{-T} = \boldsymbol{U}\boldsymbol{P}'\boldsymbol{U}^T$.

Gaussian, atom-centered, basis sets are employed, in place of originless plane waves. This is the most common choice in quantum chemistry electronic structure calculations due to their localized and compact character and their ability to better describe the higher electron density regions around the nuclei. Fewer basis functions are therefore usually needed. [34] Moreover, the original CP implementation actually *requires* to replace core electrons with pseudopotentials [35], in order to reduce the size of the basis set and to avoid to use plane waves to describe the high density regions in proximity of the nuclei. In the ADMP method, instead, the explicit treatment of all the

electrons is not precluded.

CP codes are usually restricted to pure (GGA or meta-GGA, [36]) exchange-correlation functionals, since the inclusion of exact Hartree-Fock exchange leads to a substantial slowing down (an increase of computer time up to an order of magnitude is expected, [10]) and so it is still considered "experimental". [37] Unsatisfactory performances are often reported with pure functionals; a striking example is the simulation of liquid water. [38–43] Hybrid functionals, usually preferred because of their higher accuracy, can be easily handled by ADMP in energy and forces calculations (Eq. (1.34)).

Introducing the ADMP Lagrangian Eq. (1.33) into the Euler-Lagrange equations, the following equations of motion for the nuclei and the density can be derived:

$$\boldsymbol{M}\frac{d^2\boldsymbol{R}}{dt^2} = -\frac{\partial E(\boldsymbol{R},\boldsymbol{P})}{\partial \boldsymbol{R}}\Big|_{\boldsymbol{P}} \tag{1.35}$$

$$\boldsymbol{\mu}^{1/2}\frac{d^2\boldsymbol{P}}{dt^2}\boldsymbol{\mu}^{1/2} = -\Big[\frac{\partial E(\boldsymbol{R},\boldsymbol{P})}{\partial \boldsymbol{P}}\Big|_{\boldsymbol{R}} + \boldsymbol{\Lambda}\boldsymbol{P} + \boldsymbol{P}\boldsymbol{\Lambda} - \boldsymbol{\Lambda}\Big] \tag{1.36}$$

Eqs. (1.35) and (1.36) are integrated with a finite Δt time step by the velocity Verlet scheme. [21] In particular, the density and the density velocity at the next step are obtained as:

$$\begin{aligned}\boldsymbol{P}^{(i+1)} &= \boldsymbol{P}^{(i)} + \boldsymbol{W}^{(i)}\Delta t + \\ &- \frac{\Delta t^2}{2}\boldsymbol{\mu}^{-1/2}\Big[\frac{\partial E(\boldsymbol{R}^{(i)},\boldsymbol{P}^{(i)})}{\partial \boldsymbol{P}}\Big|_{\boldsymbol{R}} + \boldsymbol{\Lambda}^{(i)}\boldsymbol{P}^{(i)} + \boldsymbol{P}^{(i)}\boldsymbol{\Lambda}^{(i)} - \boldsymbol{\Lambda}^{(i)}\Big]\boldsymbol{\mu}^{-1/2}\end{aligned} \tag{1.37}$$

$$\begin{aligned}\boldsymbol{W}^{(i+1/2)} &= \frac{\boldsymbol{P}^{(i+1)} - \boldsymbol{P}^{(i)}}{\Delta t} = \boldsymbol{W}^{(i)} + \\ &- \frac{\Delta t}{2}\boldsymbol{\mu}^{-1/2}\Big[\frac{\partial E(\boldsymbol{R}^{(i)},\boldsymbol{P}^{(i)})}{\partial \boldsymbol{P}}\Big|_{\boldsymbol{R}} + \boldsymbol{\Lambda}^{(i)}\boldsymbol{P}^{(i)} + \boldsymbol{P}^{(i)}\boldsymbol{\Lambda}^{(i)} - \boldsymbol{\Lambda}^{(i)}\Big]\boldsymbol{\mu}^{-1/2}\end{aligned} \tag{1.38}$$

$$\begin{aligned}\boldsymbol{W}^{(i+1)} = \boldsymbol{W}^{(i+1/2)} &- \frac{\Delta t}{2}\boldsymbol{\mu}^{-1/2}\Big[\frac{\partial E(\boldsymbol{R}^{(i+1)},\boldsymbol{P}^{(i+1)})}{\partial \boldsymbol{P}}\Big|_{\boldsymbol{R}} + \\ &+ \boldsymbol{\Lambda}^{(i+1)}\boldsymbol{P}^{(i+1)} + \boldsymbol{P}^{(i+1)}\boldsymbol{\Lambda}^{(i+1)} - \boldsymbol{\Lambda}^{(i+1)}\Big]\boldsymbol{\mu}^{-1/2}\end{aligned} \tag{1.39}$$

An iterative procedure is employed to find $\boldsymbol{\Lambda}^{(i+1)}$ constraints matrix, so that $\boldsymbol{P}^{(i+1)}$ and $\boldsymbol{W}^{(i+1)}$ satisfy the idempotency condition $(\boldsymbol{P}^{(i+1)})^2 = \boldsymbol{P}^{(i+1)}$ and its time derivative $\boldsymbol{P}^{(i+1)}\boldsymbol{W}^{(i+1)} + \boldsymbol{W}^{(i+1)}\boldsymbol{P}^{(i+1)} = \boldsymbol{W}^{(i+1)}$.

Analytic expressions for both forces on the nuclei and the density [44–46] are available. The potential energy derivative with respect to nuclear positions has to take into account that the density is not converged (i.e., $[\boldsymbol{F}, \boldsymbol{P}] \neq 0$) and that the transformation to the orthonormal basis $\boldsymbol{U}$ depends upon $\boldsymbol{R}$ (and so also upon t), since the basis functions are atom-centered. [29] Both the Hellmann-Feynman (i.e., the Hamiltonian derivatives) and the Pulay forces (i.e., the wavefunction derivatives, not vanishing for finite, atom-centered basis sets [47]) are included in the ADMP nuclear forces calculation.

$$\frac{\partial E(\boldsymbol{R},\boldsymbol{P})}{\partial \boldsymbol{R}}\Big|_{\boldsymbol{P}} = \mathrm{Tr}\Big[\frac{d\boldsymbol{h}'}{d\boldsymbol{R}}\tilde{\boldsymbol{P}}' + \frac{1}{2}\frac{\partial \boldsymbol{G}'}{\partial \boldsymbol{R}}\Big|_{\boldsymbol{P}'}\tilde{\boldsymbol{P}}'\Big] + \\ - \mathrm{Tr}\Big[\boldsymbol{F}'\boldsymbol{U}^{-1}\frac{d\boldsymbol{U}}{d\boldsymbol{R}}\tilde{\boldsymbol{P}}' + \tilde{\boldsymbol{P}}'\frac{d\boldsymbol{U}^T}{d\boldsymbol{R}}\boldsymbol{U}^{-T}\boldsymbol{F}'\Big] + \frac{\partial E_{\mathrm{xc}}}{\partial \boldsymbol{R}}\Big|_{\boldsymbol{P}} + \frac{\partial V_{NN}}{\partial \boldsymbol{R}} \quad (1.40)$$

$$\frac{\partial E(\boldsymbol{R},\boldsymbol{P})}{\partial \boldsymbol{P}}\Big|_{\boldsymbol{R}} = 3(\boldsymbol{F}\boldsymbol{P} + \boldsymbol{P}\boldsymbol{F}) - 2(\boldsymbol{F}\boldsymbol{P}^2 + \boldsymbol{P}\boldsymbol{F}\boldsymbol{P} + \boldsymbol{P}^2\boldsymbol{F}) \quad (1.41)$$

where $\boldsymbol{F}' = \boldsymbol{h}' + \boldsymbol{G}'(\tilde{\boldsymbol{P}}') + \partial E_{\mathrm{xc}}/\partial \boldsymbol{P}'$ and $\boldsymbol{F} = \boldsymbol{U}^{-T}\boldsymbol{F}'\boldsymbol{U}^{-1}$ are the Fock matrices in the AO and orthonormal bases, respectively.

Like the CP method, the ADMP extended Lagrangian Eq. (1.33) is conservative. Again, the *total* energy (i.e., the Hamiltonian function $\mathcal{H}$ associated with the Lagrangian $\mathcal{L}$) is constant, $d\mathcal{H}/dt = 0$.

$$\mathcal{H}(\boldsymbol{R},\mathcal{V},\boldsymbol{P},\mathcal{W},t) = \mathrm{Tr}(\mathcal{V}^T\boldsymbol{V}) + \mathrm{Tr}(\mathcal{W}\boldsymbol{W}) - \mathcal{L}(\boldsymbol{R},\boldsymbol{V},\boldsymbol{P},\boldsymbol{W},t) = \\ = \frac{1}{2}\mathrm{Tr}(\boldsymbol{V}^T\boldsymbol{M}\boldsymbol{V}) + \frac{1}{2}\mathrm{Tr}\big[(\boldsymbol{\mu}^{1/4}\boldsymbol{W}\boldsymbol{\mu}^{1/4})^2\big] + E(\boldsymbol{R},\boldsymbol{P}) + \mathrm{Tr}\big[\boldsymbol{\Lambda}(\boldsymbol{P}^2 - \boldsymbol{P})\big] \quad (1.42)$$

where $\mathcal{V} = \partial\mathcal{L}/\partial\boldsymbol{V} = \boldsymbol{M}\boldsymbol{V}$ and $\mathcal{W} = \partial\mathcal{L}/\partial\boldsymbol{W} = \boldsymbol{\mu}^{1/2}\boldsymbol{W}\boldsymbol{\mu}^{1/2}$ are the conjugate momenta of $\boldsymbol{R}$ and $\boldsymbol{P}$, respectively.

The fictitious part of the total energy is the fictitious kinetic energy of the density matrix: $\mathcal{H}_{\mathrm{fict}} = \frac{1}{2}\mathrm{Tr}\big[(\boldsymbol{\mu}^{1/4}\boldsymbol{W}\boldsymbol{\mu}^{1/4})^2\big]$. The rate of its change

along the trajectory

$$\frac{d\mathcal{H}_{\text{fict}}}{dt} = \text{Tr}\Big(\boldsymbol{W}\boldsymbol{\mu}^{1/2}\frac{d^2\boldsymbol{P}}{dt^2}\boldsymbol{\mu}^{1/2}\Big) \tag{1.43}$$

can be taken as an "adiabaticity index", estimating the rate of deviation of the ADMP trajectory from the BO one. In fact,

$$\frac{d(\mathcal{H}_{\text{real}} - \mathcal{H}_{\text{BO}})}{dt} = \frac{d\mathcal{H}_{\text{real}}}{dt} \tag{1.44}$$

$$\frac{d\mathcal{H}_{\text{ADMP}}}{dt} = \frac{d(\mathcal{H}_{\text{real}} + \mathcal{H}_{\text{fict}})}{dt} = 0 \implies \frac{d\mathcal{H}_{\text{real}}}{dt} = -\frac{d\mathcal{H}_{\text{fict}}}{dt} \tag{1.45}$$

since $d\mathcal{H}_{\text{BO}}/dt = 0$ and $d\mathcal{H}_{\text{ADMP}}/dt = 0$.

From Eq. (1.43), the fictitious mass $\boldsymbol{\mu}$ clearly contributes to the extent of such deviation. Bound oscillations by $d\mathcal{H}_{\text{fict}}/dt$ suggest that the ADMP trajectory remains close to the BO surface and so that time-averaged quantities should not significantly differ from the BO values.

An extended Lagrangian trajectory can be compared to a not fully converged BO one, characterized by a non-zero $[\boldsymbol{F}, \boldsymbol{P}]$ commutator. [31] Its norm $\|[\boldsymbol{F}, \boldsymbol{P}]\|$ can be indeed considered as a measure of the distance of the electronic structure from the BO surface (being zero for a converged density). It can be shown that the deviation rate of an approximate-BO Hamiltonian from the exact-BO one depends upon $[\boldsymbol{F}, \boldsymbol{P}]$:

$$\frac{d(\mathcal{H}_{\text{appr.BO}} - \mathcal{H}_{\text{BO}})}{dt} = \text{Tr}([\boldsymbol{F}, \boldsymbol{P}][\boldsymbol{P}, \boldsymbol{W}]) \tag{1.46}$$

For an extended Lagrangian dynamics equally deviating from the BO trajectory, the deviations Eqs. (1.43) and (1.46) are equal. So, the fictitious mass $\boldsymbol{\mu}$ is related to the $[\boldsymbol{F}, \boldsymbol{P}]$ commutator, contributing therefore to the deviation from the BO trajectory:

$$\text{Tr}(\boldsymbol{W}\boldsymbol{\mu}^{1/2}\frac{d^2\boldsymbol{P}}{dt^2}\boldsymbol{\mu}^{1/2}) = \text{Tr}([\boldsymbol{F}, \boldsymbol{P}][\boldsymbol{P}, \boldsymbol{W}]) \tag{1.47}$$

In particular, according to Eq. (1.47), a fixed $\boldsymbol{\mu}$ for the extended Lagrangian trajectory corresponds to an approximate-BO dynamics with a

non-constant, time-dependent, $[\boldsymbol{F}, \boldsymbol{P}]$ commutator. Using a matrix norm (for example, the Frobenius one), the following inequality holds:

$$\|[\boldsymbol{F}, \boldsymbol{P}]\| \geq \frac{\left|\mathrm{Tr}(\boldsymbol{W}\boldsymbol{\mu}^{1/2}\frac{d^2\boldsymbol{P}}{dt^2}\boldsymbol{\mu}^{1/2})\right|}{\|[\boldsymbol{P}, \boldsymbol{W}]\|} \tag{1.48}$$

The fictitious mass $\boldsymbol{\mu}$ therefore determines the lower bound of the distance from the BO surface.

The extended Lagrangian "nature" of the ADMP approach imposes an accurate adjustment of the (fictitious) time-scale of the electronic structure with respect to that of the nuclear motion, in order to ensure an acceptable degree of electronic-nuclear adiabaticity and so a sufficient accuracy. In an electronic structure representation with Gaussian atom-centered functions (such as in the ADMP method) instead of plane waves, the changes in orbital coefficients do not include the density changes induced by nuclear motion (since the basis functions themselves follow the nuclei), but only the "adjustment" of the density around the nuclei. A reduced amplitude of the oscillation of the coefficients allows smaller fictitious masses than in the original CP scheme. A practical consequence is the possibility for the ADMP simulations to retain hydrogen atoms. Taking advantage of the general nature of the fictitious mass $\boldsymbol{\mu}$ included in the ADMP Lagrangian Eq. (1.33), effective strategies to optimize the vibrational density of states of the $\boldsymbol{P}$ electronic density through a rational mass-weighting procedure have been pursued. Early works [29] suggested that a non-scalar (i.e., a non-uniform) mass can lead to an higher separation in time-scales, giving the opportunity to safely employ bigger time steps while still keeping an acceptable adiabaticity. Nevertheless, no developments in this direction were actually made.

The ADMP molecular dynamics approach has been already successfully employed to study ground-state structural, reactive and spectroscopic properties of organic and biomolecular systems, [48–53] also in explicit solvent solution, through non-periodic boundary conditions. [54, 55] Nevertheless, several difficulties in all-electron simulations with elements beyond the first

and second rows and with some extended basis sets actually occur, often preventing a stable trajectory propagation.

This work, therefore, albeit having its roots in the physics underlying the extended Lagrangian dynamics, actually has a practical purpose, aiming at increasing both the efficiency and the scope of the ADMP method. The discussion is organized as follows: in Chapter 2 the theoretical aspects of the approaches developed to adjust the fictitious electronic time-scales and to calculate $\boldsymbol{\mu}$ are discussed in detail; in Chapter 3 a comprehensive and systematic analysis of model compounds test simulations is carried out, in order to assess the performances of the proposed weighting schemes. Results from the simulation of a "real-world" system (the $[Ru(dcbpy)_2(NCS)_2]^{4-}$ Ru(II) complex) are also shown. Due to its attractive light harvesting properties, its photophysics has been recently investigated by both experimental and theoretical means. In particular, in Chapter 4 the solvation properties and vibrational signatures in water solution are investigated, while in Chapter 5 some relevant excited charge-transfer states are characterized in the ultra-fast regime through explicit electronic dynamics techniques.

Chapter 2

Rational mass-weighting schemes: theoretical details.

In the following sections, several approaches aimed at readjusting the density matrix power spectrum through a rational evaluation of the fictitious mass matrix $\boldsymbol{\mu}$ are proposed. In particular, a compression of the vibrational distribution is sought. On the lower end, a sufficient separation from the nuclear motion ensures a good adiabaticity, while limiting the highest frequencies should instead allow bigger time steps and so an increased integration efficiency.

Two classes of mass-weighting methods have been devised. The first one (Section 2.1) employs a rigorous definition of a molecular core subspace and seeks to attribute a greater inertia to the core density, in order to make its oscillation frequencies closer to those of the valence one, while keeping a smaller valence mass for a better adiabaticity. In the second category instead (Section 2.2), starting from an harmonic analysis of the $\boldsymbol{P}$ normal modes, a mass $\boldsymbol{\mu}$ has been derived by imposing a common value for all the $\boldsymbol{P}$ frequencies.

2.1 Core subspace-based approaches.

Definitions of the quantities involved in the following derivations are here provided as reference:

$|\phi'_\lambda\rangle$: (non-orthonormal) AO basis functions,
$|\phi_\lambda\rangle$: orthonormalized basis functions,
$|\theta_c^{\mathrm{cr}}\rangle$: core "atomic MOs",
$|\theta_c^{\mathrm{cr,ort}}\rangle$: orthonormalized core atomic MOs,
$\boldsymbol{O'}$: representation of the $|\theta_c^{\mathrm{cr}}\rangle$ in the AO basis,
$\boldsymbol{O}$: representation of the $|\theta_c^{\mathrm{cr}}\rangle$ in the orthonormal basis,
$\boldsymbol{O}^{\mathrm{ort}}$: representation of the $|\theta_c^{\mathrm{cr,ort}}\rangle$ in the orthonormal basis,
$\boldsymbol{S'}$: AO basis overlap matrix,
$\boldsymbol{X}$: orthonormal transformation of the basis; $\boldsymbol{X} = \boldsymbol{S'}^{-1/2}$ (Löwdin orthogonalization) or $\boldsymbol{X} = \boldsymbol{U}^{-1}$, where $\boldsymbol{S'} = \boldsymbol{U}^T\boldsymbol{U}$ (Cholesky orthogonalization),
$\boldsymbol{S}^\theta$: core atomic MOs overlap matrix,
$\boldsymbol{X}^\theta$: orthonormal transformation of the core atomic MOs $|\theta_c^{\mathrm{cr}}\rangle$,
$\hat{\mathcal{P}}^{\mathrm{cr}}$: projection operator onto the molecular core subspace,
$\boldsymbol{P}^{\mathrm{cr}}$: representation of $\hat{\mathcal{P}}^{\mathrm{cr}}$ operator in the orthonormal basis,
N_b: number of basis functions,
N_{cr}: total number of the core atomic MOs.

2.1.1 Definition of the molecular core subspace.

Core atomic MOs $|\theta_c^{\mathrm{cr}}\rangle$ can be calculated for each atom composing the system under study, starting from the basis functions centered on that atom. Instead of a full SCF procedure, the approximated Harris functional (i.e., already knowing the atomic $n(r)$ density in the Kohn-Sham equations, [56]) can be used for a faster computation. The core atomic MOs can be represented both in the orthonormal and the AO basis:

$$|\theta_c^{\mathrm{cr}}\rangle = \sum_{\lambda}^{N_b} O_{\lambda c}\,|\phi_\lambda\rangle = \sum_{\lambda,\nu}^{N_b} O_{\lambda c}X_{\nu\lambda}\,|\phi'_\nu\rangle = \sum_{\nu}^{N_b} O'_{\nu c}\,|\phi'_\nu\rangle \implies \boldsymbol{O'} = \boldsymbol{XO} \tag{2.1}$$

The core atomic MOs are orthogonal only if centered on the same atom. An orthonormalized set of core atomic MOs, represented in the orthonormal basis, can be obtained from a transformation $\boldsymbol{X}^{\theta}$ of the $|\theta_c^{\mathrm{cr}}\rangle$:

$$\left|\theta_c^{\mathrm{cr,ort}}\right\rangle = \sum_{\lambda}^{N_b} O_{\lambda c}^{\mathrm{ort}} \left|\phi_\lambda\right\rangle = \sum_{d}^{N_{\mathrm{cr}}} X_{dc}^{\theta} \left|\theta_d^{\mathrm{cr}}\right\rangle = \sum_{d}^{N_{\mathrm{cr}}} \sum_{\lambda}^{N_b} X_{dc}^{\theta} O_{\lambda d} \left|\phi_\lambda\right\rangle$$

$$\Longrightarrow \boldsymbol{O}^{\mathrm{ort}} = \boldsymbol{O}\boldsymbol{X}^{\theta} \quad (2.2)$$

$$\left\langle \theta_c^{\mathrm{cr,ort}} \,\middle|\, \theta_d^{\mathrm{cr,ort}} \right\rangle = \sum_{k,l}^{N_{\mathrm{cr}}} X_{kc}^{\theta *} \left\langle \theta_k^{\mathrm{cr}} \,|\, \theta_l^{\mathrm{cr}} \right\rangle X_{ld}^{\theta} = \sum_{k,l}^{N_{\mathrm{cr}}} X_{ck}^{\theta \dagger} S_{kl}^{\theta} X_{ld}^{\theta} = \delta_{cd}$$

$$\Longrightarrow \boldsymbol{X}^{\theta\dagger}\boldsymbol{S}^{\theta}\boldsymbol{X}^{\theta} = \boldsymbol{I} \quad (2.3)$$

$$S_{cd}^{\theta} = \left\langle \theta_c^{\mathrm{cr}} \,|\, \theta_d^{\mathrm{cr}} \right\rangle = \sum_{\lambda,\nu}^{N_b} O_{\lambda c}^{\prime *} \left\langle \phi_\lambda' \,|\, \phi_\nu' \right\rangle O_{\nu d}' = \sum_{\lambda,\nu}^{N_b} O_{c\lambda}^{\prime \dagger} S_{\lambda\nu}' O_{\nu d}'$$

$$\Longrightarrow \boldsymbol{S}^{\theta} = \boldsymbol{O}'^{\dagger}\boldsymbol{S}'\boldsymbol{O}' \quad (2.4)$$

Löwdin orthonormalization of the core atomic MOs $|\theta_c^{\mathrm{cr}}\rangle$ is employed:

$$\boldsymbol{X}^{\theta} = (\boldsymbol{S}^{\theta})^{-1/2} = (\boldsymbol{O}'^{\dagger}\boldsymbol{S}'\boldsymbol{O}')^{-1/2} \quad (2.5)$$

The orthonormalized core atomic MOs $\{|\theta_c^{\mathrm{cr,ort}}\rangle\}$ constitute a basis for the molecular core subspace. A projection operator $\hat{\mathcal{P}}^{\mathrm{cr}}$ onto such subspace can be defined:

$$\hat{\mathcal{P}}^{\mathrm{cr}} = \sum_{c}^{N_{\mathrm{cr}}} \left|\theta_c^{\mathrm{cr,ort}}\right\rangle \left\langle\theta_c^{\mathrm{cr,ort}}\right| \quad (2.6)$$

From Eq. (2.2), the projection of $|\theta_c^{\mathrm{cr,ort}}\rangle$ along the $|\phi_\lambda\rangle$ basis function

can be expressed as $\langle \phi_\lambda \,|\, \theta_c^{\mathrm{cr,ort}} \rangle = O_{\lambda c}^{\mathrm{ort}}$. Therefore:

$$\begin{aligned} P_{\lambda\nu}^{\mathrm{cr}} = \left\langle \phi_\lambda \,\middle|\, \hat{\mathcal{P}}^{\mathrm{cr}} \,\middle|\, \phi_\nu \right\rangle = \sum_c^{N_{\mathrm{cr}}} \left\langle \phi_\lambda \,\middle|\, \theta_c^{\mathrm{cr,ort}} \right\rangle \left\langle \theta_c^{\mathrm{cr,ort}} \,\middle|\, \phi_\nu \right\rangle = \\ = \sum_c^{N_{\mathrm{cr}}} O_{\lambda c}^{\mathrm{ort}} O_{c\nu}^{\mathrm{ort}\dagger} \implies \boldsymbol{P}^{\mathrm{cr}} = \boldsymbol{O}^{\mathrm{ort}} \boldsymbol{O}^{\mathrm{ort}\dagger} \end{aligned} \tag{2.7}$$

Combining Eq. (2.2), Eq. (2.1) and Eq. (2.5):

$$\boldsymbol{O}^{\mathrm{ort}} = \boldsymbol{X}^{-1} \boldsymbol{O}' (\boldsymbol{O}'^{\dagger} \boldsymbol{S}' \boldsymbol{O}')^{-1/2} \tag{2.8}$$

$\hat{\mathcal{P}}^{\mathrm{cr}}$, like every projection operator, is Hermitean and idempotent:

$$\boldsymbol{P}^{\mathrm{cr}\dagger} = \boldsymbol{P}^{\mathrm{cr}}, \quad (\boldsymbol{P}^{\mathrm{cr}})^2 = \boldsymbol{P}^{\mathrm{cr}} \tag{2.9}$$

2.1.2 Basis functions projection onto the molecular core subspace: AO weighting schemes.

The schemes from now on named as *AO* employ a mass-matrix diagonal in the orthonormal basis $\{|\phi_\lambda\rangle\}$:

$$\mu_{\lambda\nu} = \delta_{\lambda\nu} \mu_\lambda \tag{2.10}$$

where the diagonal element μ_λ can be considered as the mass given to the $|\phi_\lambda\rangle$ orthonormal atomic basis function.

Every $|\phi_\lambda\rangle$ can be projected onto the core subspace. The projection $\mathrm{proj}_{\mathrm{cr}}$ onto the subspace spanned by the $\{|\theta_c^{\mathrm{cr,ort}}\rangle\}$ orbitals can be obtained through the application of the $\hat{\mathcal{P}}^{\mathrm{cr}}$ projector:

$$\mathrm{proj}_{\mathrm{cr}} |\phi_\lambda\rangle = \hat{\mathcal{P}}^{\mathrm{cr}} |\phi_\lambda\rangle \tag{2.11}$$

The norm p_λ of such projection can then be derived, exploiting the

properties of the $\hat{\mathcal{P}}^{\mathrm{cr}}$ operator (Eq. (2.9)):

$$\begin{aligned} p_\lambda^2 &= \|\mathrm{proj}_{\mathrm{cr}}\,|\phi_\lambda\rangle\|^2 = \left\langle \phi_\lambda \,\middle|\, \hat{\mathcal{P}}^{\mathrm{cr}\dagger}\hat{\mathcal{P}}^{\mathrm{cr}} \,\middle|\, \phi_\lambda \right\rangle = \left\langle \phi_\lambda \,\middle|\, \hat{\mathcal{P}}^{\mathrm{cr}} \,\middle|\, \phi_\lambda \right\rangle = P^{\mathrm{cr}}_{\lambda\lambda} = \\ &= \left(\boldsymbol{O}^{\mathrm{ort}}\boldsymbol{O}^{\mathrm{ort}\dagger}\right)_{\lambda\lambda} = \sum_c^{N_{\mathrm{cr}}} O^{\mathrm{ort}}_{\lambda c} O^{\mathrm{ort}\dagger}_{c\lambda} = \sum_c^{N_{\mathrm{cr}}} \left| O^{\mathrm{ort}}_{\lambda c} \right|^2 \end{aligned} \tag{2.12}$$

p_λ can assume values in the $[0,1]$ interval. In the two extreme situations, the basis function $|\phi_\lambda\rangle$ totally belongs to the valence or the core subspaces, respectively.

By application of the $\hat{\mathcal{P}}^{\mathrm{cr}}$ projector, every orthonormal basis function can be completely decomposed along orthogonal directions:

$$\begin{aligned} |\phi_\lambda\rangle = \left|\phi_\lambda^{\mathrm{val}}\right\rangle + \hat{\mathcal{P}}^{\mathrm{cr}}\,|\phi_\lambda\rangle &= \left|\phi_\lambda^{\mathrm{val}}\right\rangle + \sum_c^{N_{\mathrm{cr}}} \left|\theta_c^{\mathrm{cr,ort}}\right\rangle \left\langle \theta_c^{\mathrm{cr,ort}} \,\middle|\, \phi_\lambda \right\rangle = \\ &= \left|\phi_\lambda^{\mathrm{val}}\right\rangle + \sum_c^{N_{\mathrm{cr}}} \left|\theta_c^{\mathrm{cr,ort}}\right\rangle (O^{\mathrm{ort}}_{\lambda c})^* \end{aligned} \tag{2.13}$$

where the projection along each core atomic MO $\left|\theta_c^{\mathrm{cr,ort}}\right\rangle$ has been made explicit.

$\left|\phi_\lambda^{\mathrm{val}}\right\rangle = (1-\hat{\mathcal{P}}^{\mathrm{cr}})\,|\phi_\lambda\rangle$ lies in the orthogonal complement of the molecular core subspace and so it can be considered as the valence component of $|\phi_\lambda\rangle$; $\left\|\left|\phi_\lambda^{\mathrm{val}}\right\rangle\right\|^2 = 1 - p_\lambda^2$.

If a valence mass μ^{val} and a core mass μ_c^{cr} for every orthonormal core atomic MO $\left|\theta_c^{\mathrm{cr,ort}}\right\rangle$ are defined, the mass given to the basis function $|\phi_\lambda\rangle$ can be derived as a weighted root-mean-square, according to the above decomposition:

$$\begin{aligned} \mu_\lambda &= \left[\frac{(1-p_\lambda^2)(\mu^{\mathrm{val}})^2 + \sum_c^{N_{\mathrm{cr}}} |O^{\mathrm{ort}}_{\lambda c}|^2 (\mu_c^{\mathrm{cr}})^2}{(1-p_\lambda^2) + \sum_c^{N_{\mathrm{cr}}} |O^{\mathrm{ort}}_{\lambda c}|^2}\right]^{1/2} = \\ &= \left[(1-p_\lambda^2)(\mu^{\mathrm{val}})^2 + \sum_c^{N_{\mathrm{cr}}} |O^{\mathrm{ort}}_{\lambda c}|^2 (\mu_c^{\mathrm{cr}})^2\right]^{1/2} \end{aligned} \tag{2.14}$$

The sum of the masses coefficients in Eq. (2.14) is equal to unity, because

it is the squared norm of the $|\phi_\lambda\rangle$ basis function (see also Eq. (2.12)):

$$(1 - p_\lambda^2) + \sum_c^{N_{\mathrm{cr}}} |O_{\lambda c}^{\mathrm{ort}}|^2 = (1 - p_\lambda^2) + p_\lambda^2 = 1 \tag{2.15}$$

Eq. (2.14) fulfills several limit behaviours:

$$p_\lambda \to 0 \colon \mu_\lambda \to \mu^{\mathrm{val}}$$
$$\mu_c^{\mathrm{cr}} \to \mu^{\mathrm{val}} \text{ for every } \left|\theta_c^{\mathrm{cr,ort}}\right\rangle : \mu_\lambda \to \mu^{\mathrm{val}}$$
$$p_\lambda \to 1 \text{ and } \mu_c^{\mathrm{cr}} = \mu^{\mathrm{cr}} \text{ (i.e., if every } \left|\theta_c^{\mathrm{cr,ort}}\right\rangle \text{ has the same mass)} \colon \mu_\lambda \to \mu^{\mathrm{cr}}$$

Because of the core character of the $|\theta_c^{\mathrm{cr}}\rangle$ atomic MOs, the overlap between functions centered on different atoms is usually small, so $\boldsymbol{S}^\theta \approx \boldsymbol{I}$ and $\boldsymbol{X}^\theta \approx \boldsymbol{I}$. Every orthonormal $|\theta_c^{\mathrm{cr,ort}}\rangle$ core atomic MO is thus composed mainly of a single $|\theta_c^{\mathrm{cr}}\rangle$ atomic MO, so μ_c^{cr} can be actually related to the non-orthonormalized $|\theta_c^{\mathrm{cr}}\rangle$ orbital.

Projection-based AO scheme.

A substantial simplification of Eq. (2.14) can be derived imposing a common mass to each $|\theta_c^{\mathrm{cr}}\rangle$, i.e.: $\mu_c^{\mathrm{cr}} = \mu^{\mathrm{cr}} = f^{\mathrm{cr}}\mu^{\mathrm{val}}$ for every core atomic MO:

$$\mu_\lambda = \left[(1 - p_\lambda^2)(\mu^{\mathrm{val}})^2 + p_\lambda^2(\mu^{\mathrm{cr}})^2\right]^{1/2} = \mu^{\mathrm{val}}\left[1 + p_\lambda^2(f^{\mathrm{cr}\,2} - 1)\right]^{1/2} \tag{2.16}$$

μ_λ therefore can assume values between μ^{val} and μ^{cr}, according to p_λ. A bigger inertia is thus attributed to basis functions with a higher core character. Different fully core basis functions will have, however, the same mass μ^{cr}. $f^{\mathrm{cr}} > 1$ is a parameter; if $f^{\mathrm{cr}} = 1$, this scheme reduces to the *scalar AO* one (Section 2.1.2).

It is reasonable to expect more accurate results if the individual properties of the $|\theta_c^{\mathrm{cr}}\rangle$ core orbitals are also taken into account. In the following sections, two distinct approaches for the calculation of the μ_c^{cr} are proposed.

Projection/energy-based AO scheme.

The fictitious mass μ_c^{cr} of the *c-th* core atomic MO $|\theta_c^{\mathrm{cr}}\rangle$ can be assumed proportional to the absolute value of its energy eigenvalue ε_c:

$$\mu_c^{\mathrm{cr}} = k|\varepsilon_c| \tag{2.17}$$

Then, a threshold $f^{\mathrm{cr}}\mu^{\mathrm{val}}$, $f^{\mathrm{cr}} > 1$, mass value is attributed to the core atomic MO with the highest (that is, the less-negative) energy. f^{cr} therefore fixes the minimum μ_c^{cr}:

$$\mu_{\mathrm{min}}^{\mathrm{cr}} = f^{\mathrm{cr}}\mu^{\mathrm{val}} = k|\varepsilon_{\mathrm{max}}| \tag{2.18}$$

This allows to set a consistent, energy-based, mass-scale among the $|\theta_c^{\mathrm{cr}}\rangle$ of the molecular system under study. The costant k can be derived as:

$$k = \frac{f^{\mathrm{cr}}\mu^{\mathrm{val}}}{|\varepsilon_{\mathrm{max}}|} \tag{2.19}$$

After the μ_c^{cr}-s evaluation for every core atomic MO, Eq. (2.14) has to be used in order to calculate μ_λ for the orthonormal basis functions.

Projection/radius-based AO scheme.

The energy eigenvalue may not be the most accurate indicator of the orbital core character. [57] So, in constrast to the previous energy-based approach, the fictitious mass μ_c^{cr} attributed to the core atomic MO $|\theta_c^{\mathrm{cr}}\rangle$ could be estimated instead from its spatial extent $\langle r^2\rangle_c = \langle \theta_c^{\mathrm{cr}} \,|\, r^2 \,|\, \theta_c^{\mathrm{cr}}\rangle$, where r is the radial coordinate in a coordinate system centered on the atomic nucleus. An atomic MO $|\theta_c^{\mathrm{cr}}\rangle$ can be expressed as:

$$\theta_c^{\mathrm{cr}}(\vec{r}) = \sum_\lambda O'_{\lambda c}\,\phi'_\lambda(\vec{r}) = \sum_\lambda O'_{\lambda c} \sum_p d_{p\lambda}\, g_p(\alpha_{p\lambda}, \vec{r}) \tag{2.20}$$

where $g_p(\alpha_{p\lambda}, \vec{r})$ are Gaussian, atom-centered, primitive functions with exponents $\alpha_{p\lambda}$ and $d_{p\lambda}$ are the contraction coefficients.

Assuming non-normalized Gaussian $g_p(\alpha_{p\lambda}, \vec{r})$ functions, $\langle r^2\rangle_c$ can be

calculated as:

$$\langle r^2\rangle_c = 3\sum_{\lambda,\nu} O'_{\lambda c}O'_{\nu c}\sum_{p,q} d_{p\lambda}d_{q\nu}I_{p\lambda q\nu} \tag{2.21}$$

$$I_{p\lambda q\nu} = 2^{-1}\pi^{3/2}\big(\alpha_{p\lambda}+\alpha_{q\nu}\big)^{-5/2} \tag{2.22}$$

for s-type orbitals, where λ and ν are s-type basis functions, and:

$$\langle r^2\rangle_c = 5\sum_{t}\sum_{\lambda_t,\nu_t} O'_{\lambda c}O'_{\nu c}\sum_{p,q} d_{p\lambda}d_{q\nu}I_{p\lambda q\nu} \tag{2.23}$$

$$I_{p\lambda q\nu} = 2^{-2}\,\pi^{3/2}\big(\alpha_{p\lambda}+\alpha_{q\nu}\big)^{-7/2} \tag{2.24}$$

for p-type orbitals, where t: x, y, z and λ_t and ν_t are p_t-type basis functions (i.e., p_x, p_y or p_z).

Then, the fictitious mass of a core atomic MO $|\theta_c^{\rm cr}\rangle$ can be assumed inversely proportional to the square root of its spatial extension $\langle r^2\rangle_c$:

$$\mu_c^{\rm cr} = k\langle r^2\rangle_c^{-1/2} \tag{2.25}$$

The mass of the most diffuse core orbital of the system is defined as the limit value $f^{\rm cr}\mu^{\rm val}$. $f^{\rm cr} > 1$ again determines the minimum $\mu_c^{\rm cr}$:

$$\mu_{\rm min}^{\rm cr} = f^{\rm cr}\mu^{\rm val} = k\langle r^2\rangle_{\rm max}^{-1/2} \tag{2.26}$$

Now the mass-scale among the $|\theta_c^{\rm cr}\rangle$ core atomic MOs is therefore based upon a spatial measure of their extent. The constant k can be then obtained as:

$$k = f^{\rm cr}\mu^{\rm val}\langle r^2\rangle_{\rm max}^{1/2} \tag{2.27}$$

Current Gaussian©16 default scheme.

The non-uniform weighting scheme currently available in the Gaussian16 program (and actually the default one) defines an energy threshold (set at -2 hartree) between core and valence basis functions. If the Fock matrix diagonal element $F_{\lambda\lambda}$ (taken as the energy of $|\phi_\lambda\rangle$) is lower than -2 au, then

μ^{val} is scaled according to the following equation:[29]

$$\mu_\lambda = \begin{cases} \mu^{\text{val}} & \text{if } F_{\lambda\lambda} \geq -2\,\text{au} \\ \mu^{\text{val}}\left(2\sqrt{|F_{\lambda\lambda} - (-2)|} + 1\right)^2 & \text{if } F_{\lambda\lambda} < -2\,\text{au} \end{cases} \tag{2.28}$$

where $\boldsymbol{F}$ is the Fock matrix in the orthonormal basis $\{|\phi_\lambda\rangle\}$.

Scalar AO scheme.

A *scalar* weighting scheme corresponds to assign the same mass μ^{val} to each basis function:

$$\boldsymbol{\mu} = \mu^{\text{val}}\boldsymbol{I} \tag{2.29}$$

where $\boldsymbol{I}$ is the unit matrix.

2.1.3 Molecular orbitals projection onto the molecular core subspace: MO weighting schemes.

In contrast to the previous approaches, a definite fictitious mass can be assigned to each initially converged (i.e., at $t = 0$) molecular orbital $|\psi_i^\alpha(0)\rangle$, instead to the basis functions $|\phi_\lambda\rangle$. Therefore, in the following *MO* schemes, the mass-matrix is assumed diagonal in the MO basis:

$$\mu_{ij}^{\psi} = \mu_i \delta_{ij} \tag{2.30}$$

where $\boldsymbol{\mu}^\psi$ is the mass-matrix represented in the initial MO basis and μ_i is the mass of the $|\psi_i^\alpha(0)\rangle$ MO.

If $\boldsymbol{C}^\alpha(0)$ is the coefficient matrix of the $\{|\psi_i^\alpha(0)\rangle\}$ MOs expanded in the orthonormal $\{|\phi_\lambda\rangle\}$ basis, the fictitious mass representations in the MO ($\boldsymbol{\mu}^\psi$) and the orthonormalized-AO ($\boldsymbol{\mu}$) bases are related by unitary transformations:

$$\boldsymbol{\mu}^\psi = \boldsymbol{C}^\alpha(0)^\dagger \boldsymbol{\mu} \boldsymbol{C}^\alpha(0); \qquad \boldsymbol{\mu} = \boldsymbol{C}^\alpha(0)\boldsymbol{\mu}^\psi \boldsymbol{C}^\alpha(0)^\dagger \tag{2.31}$$

assuming of course that $\boldsymbol{C}^\alpha(0)$ is unitary (actually orthogonal, for real MOs),

due to the orthonormality of the $|\psi_i^\alpha(0)\rangle$ MOs : $\boldsymbol{C}^\alpha(0)^\dagger = \boldsymbol{C}^\alpha(0)^{-1}$.

Therefore, the mass-matrix $\boldsymbol{\mu}$ is now a non-diagonal, symmetric matrix.

The $\boldsymbol{C}^\alpha(0)$ MOs in the starting ($t = 0$) orthonormal basis can be obtained by application of the $\boldsymbol{X}(0)$ transformation:

$$\boldsymbol{C}^\alpha(0) = \boldsymbol{X}(0)^{-1}\boldsymbol{C}^{\alpha\prime}(0) \tag{2.32}$$

where $\boldsymbol{C}^{\alpha\prime}(0)$ represents the initial $|\psi_i^\alpha(0)\rangle$ MOs expressed in the atomic (non-orthonormal) $\{|\phi'_\lambda\rangle\}$ basis.

Each $|\psi_i^\alpha(0)\rangle$ can be projected onto the previously defined molecular core subspace (Eq. (2.6)):

$$\mathrm{proj}_{\mathrm{cr}}\,|\psi_i^\alpha(0)\rangle = \hat{\mathcal{P}}^{\mathrm{cr}}\,|\psi_i^\alpha(0)\rangle \tag{2.33}$$

The norm p_i of the projections $\mathrm{proj}_{\mathrm{cr}}\,|\psi_i^\alpha(0)\rangle$ can be derived:

$$\begin{aligned}
p_i^2 &= \left\|\hat{\mathcal{P}}^{\mathrm{cr}}\,|\psi_i^\alpha(0)\rangle\right\|^2 = \left\langle \psi_i^\alpha(0)\,\middle|\,\hat{\mathcal{P}}^{\mathrm{cr}\dagger}\hat{\mathcal{P}}^{\mathrm{cr}}\,\middle|\,\psi_i^\alpha(0)\right\rangle = \left\langle \psi_i^\alpha(0)\,\middle|\,\hat{\mathcal{P}}^{\mathrm{cr}}\,\middle|\,\psi_i^\alpha(0)\right\rangle = \\
&= \sum_{\lambda,\nu} C_{\lambda i}^\alpha(0)^* \left\langle \phi_\lambda\,\middle|\,\hat{\mathcal{P}}^{\mathrm{cr}}\,\middle|\,\phi_\nu\right\rangle C_{\nu i}^\alpha(0) = \\
&= \sum_{\lambda,\nu} C_{i\lambda}^\alpha(0)^\dagger P_{\lambda\nu}^{\mathrm{cr}} C_{\nu i}^\alpha(0) = \left(\boldsymbol{C}^\alpha(0)^\dagger \boldsymbol{P}^{\mathrm{cr}} \boldsymbol{C}^\alpha(0)\right)_{ii} = \\
&= \left(\boldsymbol{C}^\alpha(0)^\dagger \boldsymbol{O}^{\mathrm{ort}} \boldsymbol{O}^{\mathrm{ort}\dagger} \boldsymbol{C}^\alpha(0)\right)_{ii} = \left[\left(\boldsymbol{C}^\alpha(0)^\dagger \boldsymbol{O}^{\mathrm{ort}}\right)\left(\boldsymbol{C}^\alpha(0)^\dagger \boldsymbol{O}^{\mathrm{ort}}\right)^\dagger\right]_{ii} = \\
&= \sum_c^{N_{\mathrm{cr}}} \left(\boldsymbol{C}^\alpha(0)^\dagger \boldsymbol{O}^{\mathrm{ort}}\right)_{ic} \left(\boldsymbol{C}^\alpha(0)^\dagger \boldsymbol{O}^{\mathrm{ort}}\right)_{ci}^\dagger = \sum_c^{N_{\mathrm{cr}}} \left|\left(\boldsymbol{C}^\alpha(0)^\dagger \boldsymbol{O}^{\mathrm{ort}}\right)_{ic}\right|^2 = \\
&= \sum_c^{N_{\mathrm{cr}}} \left|\left(\boldsymbol{C}^\alpha(0)^\dagger \boldsymbol{O}^{\mathrm{ort}}\right)_{ic}^*\right|^2 = \sum_c^{N_{\mathrm{cr}}} \left|\left(\boldsymbol{O}^{\mathrm{ort}\dagger} \boldsymbol{C}^\alpha(0)\right)_{ci}\right|^2
\end{aligned} \tag{2.34}$$

having again exploited the properties of the $\hat{\mathcal{P}}^{\mathrm{cr}}$ projector (Eq. (2.9)).

$|\psi_i^\alpha(0)\rangle$ can be decomposed as:

$$
\begin{aligned}
|\psi_i^\alpha(0)\rangle &= \left|\psi_i^{\alpha\,\mathrm{val}}(0)\right\rangle + \hat{\mathcal{P}}^{\mathrm{cr}}\,|\psi_i^\alpha(0)\rangle = \left|\psi_i^{\alpha\,\mathrm{val}}(0)\right\rangle + \sum_c^{N_{\mathrm{cr}}} \left|\theta_c^{\mathrm{cr,ort}}\right\rangle \left\langle\theta_c^{\mathrm{cr,ort}}\,\middle|\,\psi_i^\alpha(0)\right\rangle = \\
&= \left|\psi_i^{\alpha\,\mathrm{val}}(0)\right\rangle + \sum_c^{N_{\mathrm{cr}}} \Big(\sum_\lambda^{N_b} \left\langle\theta_c^{\mathrm{cr,ort}}\,\middle|\,\phi_\lambda\right\rangle C_{\lambda i}^\alpha(0)\Big) \left|\theta_c^{\mathrm{cr,ort}}\right\rangle = \\
&= \left|\psi_i^{\alpha\,\mathrm{val}}(0)\right\rangle + \sum_c^{N_{\mathrm{cr}}} \Big(\sum_\lambda^{N_b} O_{\lambda c}^{\mathrm{ort}*} C_{\lambda i}^\alpha(0)\Big) \left|\theta_c^{\mathrm{cr,ort}}\right\rangle = \\
&= \left|\psi_i^{\alpha\,\mathrm{val}}(0)\right\rangle + \sum_c^{N_{\mathrm{cr}}} \big(\boldsymbol{O}^{\mathrm{ort}\dagger}\boldsymbol{C}^\alpha(0)\big)_{ci} \left|\theta_c^{\mathrm{cr,ort}}\right\rangle
\end{aligned}
\tag{2.35}
$$

where the length of the valence component $\left|\psi_i^{\alpha\,\mathrm{val}}(0)\right\rangle$ is equal to $(1-p_i^2)^{1/2}$ and the projection along each $\left|\theta_c^{\mathrm{cr,ort}}\right\rangle$ is $\langle\theta_c^{\mathrm{cr,ort}}\,|\,\psi_i^\alpha(0)\rangle = \big(\boldsymbol{O}^{\mathrm{ort}\dagger}\boldsymbol{C}^\alpha(0)\big)_{ci}$.

Eq. (2.35) suggests the following expression for the mass μ_i given to $|\psi_i^\alpha(0)\rangle$:

$$
\begin{aligned}
\mu_i &= \Big[\frac{(1-p_i^2)(\mu^{\mathrm{val}})^2 + \sum_c^{N_{\mathrm{cr}}} \Big|\big(\boldsymbol{O}^{\mathrm{ort}\dagger}\boldsymbol{C}^\alpha(0)\big)_{ci}\Big|^2 (\mu_c^{\mathrm{cr}})^2}{(1-p_i^2) + \sum_c^{N_{\mathrm{cr}}} \Big|\big(\boldsymbol{O}^{\mathrm{ort}\dagger}\boldsymbol{C}^\alpha(0)\big)_{ci}\Big|^2}\Big]^{1/2} = \\
&= \Big[(1-p_i^2)(\mu^{\mathrm{val}})^2 + \sum_c^{N_{\mathrm{cr}}} \Big|\big(\boldsymbol{O}^{\mathrm{ort}\dagger}\boldsymbol{C}^\alpha(0)\big)_{ci}\Big|^2 (\mu_c^{\mathrm{cr}})^2\Big]^{1/2}
\end{aligned}
\tag{2.36}
$$

The sum of the masses coefficients in the root-mean-square Eq. (2.36) is equal to one, because it coincides to the squared norm of $|\psi_i^\alpha(0)\rangle$:

$$
(1-p_i^2) + \sum_c^{N_{\mathrm{cr}}} \Big|\big(\boldsymbol{O}^{\mathrm{ort}\dagger}\boldsymbol{C}^\alpha(0)\big)_{ci}\Big|^2 = (1-p_i^2) + p_i^2 = 1 \tag{2.37}
$$

where the expression for p_i^2 in Eq. (2.34) has been employed.

After the μ_i-s evaluation, the mass-matrix $\boldsymbol{\mu}^\psi$ has to be transformed back to the orthonormal basis (according to Eq. (2.31)) in order to obtain $\boldsymbol{\mu}$.

Projection-based MO scheme.

If $\mu_c^{\rm cr} = \mu^{\rm cr} = f^{\rm cr}\mu^{\rm val}$ for every $|\theta_c^{\rm cr}\rangle$, Eq. (2.36) reduces to:

$$\mu_i = \left[(1-p_i^2)(\mu^{\rm val})^2 + p_i^2(\mu^{\rm cr})^2\right]^{1/2} = \mu^{\rm val}\left[1 + p_i^2(f^{\rm cr\,2}-1)\right]^{1/2} \qquad (2.38)$$

The similarity with the corresponding AO scheme (Section 2.1.2) is apparent, but now the MOs are weighted instead, according to the norm p_i of their core projection. A $f^{\rm cr} > 1$ parameter has again to be chosen in order to fix $\mu^{\rm cr}$.

Scalar MO scheme.

If the same mass $\mu^{\rm val}$ is given to each $|\psi_i^\alpha(0)\rangle$, $\boldsymbol{\mu}^\psi = \mu^{\rm val}\boldsymbol{I}$ and, from Eq. (2.31):

$$\boldsymbol{\mu} = \mu^{\rm val}\boldsymbol{C}^\alpha(0)\boldsymbol{C}^\alpha(0)^\dagger = \mu^{\rm val}\boldsymbol{I} \qquad (2.39)$$

The same previously shown scalar AO weighting scheme (Section 2.1.2) therefore results.

2.1.4 Implementation into Gaussian16.

All the previous core subspace-based approaches have been coded into the ADMP routine (Link121) of a Gaussian16 development version. The *pseudocode* is here provided.

AO weighting schemes.

`Calculate` $|\theta_c^{\rm cr}\rangle$`:` $\boldsymbol{O}'$, ε_c
`Read` $\boldsymbol{S}'$ `overlap matrix,` $\boldsymbol{X}$ `orthonormal transformation from disk`
`Calculate` $|\theta_c^{\rm cr,ort}\rangle$`:` $\boldsymbol{O}^{\rm ort} = \boldsymbol{X}^{-1}\boldsymbol{O}'(\boldsymbol{O}'^\dagger\boldsymbol{S}'\boldsymbol{O}')^{-1/2}$
`Calculate` $\boldsymbol{P}^{\rm cr} = \boldsymbol{O}^{\rm ort}\boldsymbol{O}^{\rm ort\dagger}$
`Calculate` $p_\lambda^2 = P_{\lambda\lambda}^{\rm cr}$
`Read Scheme,` $f^{\rm cr}$, $\mu^{\rm val}$ `from input file`
`If Scheme = proj AO`
    `Calculate` $\mu_\lambda = \mu^{\rm val}\left[1 + p_\lambda^2(f^{\rm cr\,2}-1)\right]^{1/2} \implies \boldsymbol{\mu}$

Elseif Scheme = proj/energy AO
  Find $\varepsilon_{\mathtt{max}}$ among ε_c
  Calculate $k = (f^{\mathtt{cr}}\mu^{\mathtt{val}})/|\varepsilon_{\mathtt{max}}|$
  Calculate $\mu_c^{\mathtt{cr}} = k|\varepsilon_c|$
  Calculate $\mu_\lambda = \left[(1-p_\lambda^2)(\mu^{\mathtt{val}})^2 + \sum_c^{N_{\mathtt{cr}}} |O_{\lambda c}^{\mathtt{ort}}|^2 (\mu_c^{\mathtt{cr}})^2\right]^{1/2} \implies \boldsymbol{\mu}$
Elseif Scheme = proj/radius AO
  Calculate $\langle r^2\rangle_c = \langle \theta_c^{\mathtt{cr}} \,|\, r^2 \,|\, \theta_c^{\mathtt{cr}}\rangle$ for each $|\theta_c^{\mathtt{cr}}\rangle$
  Find $\langle r^2\rangle_{\mathtt{max}}$ among $\langle r^2\rangle_c$
  Calculate $k = f^{\mathtt{cr}}\mu^{\mathtt{val}}\langle r^2\rangle_{\mathtt{max}}^{1/2}$
  Calculate $\mu_c^{\mathtt{cr}} = k\langle r^2\rangle_c^{-1/2}$
  Calculate $\mu_\lambda = \left[(1-p_\lambda^2)(\mu^{\mathtt{val}})^2 + \sum_c^{N_{\mathtt{cr}}} |O_{\lambda c}^{\mathtt{ort}}|^2 (\mu_c^{\mathtt{cr}})^2\right]^{1/2} \implies \boldsymbol{\mu}$

MO weighting scheme.

Calculate $|\theta_c^{\mathtt{cr}}\rangle$: $\boldsymbol{O}'$, ε_c
Read $\boldsymbol{S}'$ overlap matrix, $\boldsymbol{X}$ orthonormal transformation from disk
Calculate $|\theta_c^{\mathtt{cr,ort}}\rangle$: $\boldsymbol{O}^{\mathtt{ort}} = \boldsymbol{X}^{-1}\boldsymbol{O}'(\boldsymbol{O}'^{\dagger}\boldsymbol{S}'\boldsymbol{O}')^{-1/2}$
Calculate $\boldsymbol{P}^{\mathtt{cr}} = \boldsymbol{O}^{\mathtt{ort}}\boldsymbol{O}^{\mathtt{ort}\dagger}$
Read $f^{\mathtt{cr}}$, $\mu^{\mathtt{val}}$ from input file
Read $\boldsymbol{C}^{\alpha\prime}(0)$ MOs from disk
Calculate $\boldsymbol{C}^{\alpha}(0) = \boldsymbol{X}^{-1}\boldsymbol{C}^{\alpha\prime}(0)$
Calculate $p_i^2 = (\boldsymbol{C}^{\alpha}(0)^{\dagger}\boldsymbol{P}^{\mathtt{cr}}\boldsymbol{C}^{\alpha}(0))_{ii}$
Calculate $\mu_i = \mu^{\mathtt{val}}\left[1 + p_i^2(f^{\mathtt{cr}\,2} - 1)\right]^{1/2} \implies \boldsymbol{\mu}^{\psi}$
Calculate $\boldsymbol{\mu} = \boldsymbol{C}^{\alpha}(0)\boldsymbol{\mu}^{\psi}\boldsymbol{C}^{\alpha}(0)^{\dagger}$

2.2 Electronic Hessian-based approach.

Definitions of the quantities involved in the following derivations are here provided as reference:

$\boldsymbol{P}^{\alpha}$: alpha density matrix,

$\boldsymbol{P}_0^\alpha$: converged SCF alpha density matrix,
$\bar{\boldsymbol{P}}^\alpha$: mass-weighted alpha density matrix,
$\boldsymbol{K}$: matrix of energy second derivatives w.r.t. density matrix elements (electronic Hessian),
$\boldsymbol{U}$: mass-weighted electronic Hessian,
$\boldsymbol{\Lambda}$: diagonal matrix of $\boldsymbol{U}$ eigenvalues,
$\tilde{\nu}$: target electronic frequency.

Let $\bar{\boldsymbol{P}}^\alpha$ be a "mass-weighted" alpha density matrix in the orthonormal basis:

$$\bar{\boldsymbol{P}}^\alpha = \boldsymbol{\mu}^{1/4}(\boldsymbol{P}^\alpha - \boldsymbol{P}_0^\alpha)\boldsymbol{\mu}^{1/4} \tag{2.40}$$

where $\boldsymbol{P}_0^\alpha$ is the converged SCF density.

For small $\boldsymbol{P}^\alpha$ perturbations, the energy $E(\boldsymbol{R}, \bar{\boldsymbol{P}}^\alpha)$ can be expressed as a second order expansion around $\boldsymbol{P}_0^\alpha$ (i.e., $\bar{\boldsymbol{P}}^\alpha = \boldsymbol{0}$):

$$E(\boldsymbol{R}, \bar{\boldsymbol{P}}^\alpha) \approx E(\boldsymbol{R}, \boldsymbol{0}) + \sum_{\lambda,\nu} \Big(\frac{\partial E}{\partial \bar{P}^\alpha_{\lambda\nu}}\Big)_{\boldsymbol{0}} \bar{P}^\alpha_{\lambda\nu} + \frac{1}{2} \sum_{\lambda,\nu} \sum_{\sigma,\tau} \Big(\frac{\partial^2 E}{\partial \bar{P}^\alpha_{\lambda\nu}\, \partial \bar{P}^\alpha_{\sigma\tau}}\Big)_{\boldsymbol{0}} \bar{P}^\alpha_{\lambda\nu} \bar{P}^\alpha_{\sigma\tau} =$$
$$= \frac{1}{2} \sum_{\lambda,\nu} \sum_{\sigma,\tau} \Big(\frac{\partial^2 E}{\partial \bar{P}^\alpha_{\lambda\nu}\, \partial \bar{P}^\alpha_{\sigma\tau}}\Big)_{\boldsymbol{0}} \bar{P}^\alpha_{\lambda\nu} \bar{P}^\alpha_{\sigma\tau} \tag{2.41}$$

since the converged density $\boldsymbol{P}_0^\alpha$ is a minimum for the energy.

The first derivatives with respect to the elements of $\bar{\boldsymbol{P}}^\alpha$ can be then obtained in the harmonic approximation:

$$\frac{\partial E}{\partial \bar{P}^\alpha_{\lambda\nu}} = \sum_{\sigma,\tau} \Big(\frac{\partial^2 E}{\partial \bar{P}^\alpha_{\lambda\nu}\, \partial \bar{P}^\alpha_{\sigma\tau}}\Big)_{\boldsymbol{0}} \bar{P}^\alpha_{\sigma\tau} \tag{2.42}$$

It is useful to apply the vectorization operator (i.e., stacking the columns) to the $\bar{\boldsymbol{P}}^\alpha$ matrix: $\mathrm{vec}(\bar{P}^\alpha)_\delta = \bar{P}^\alpha_{\lambda\nu}$, where $(\lambda, \nu) \leftrightarrow \delta = N_b(\nu - 1) + \lambda$.

Eq. (2.42) can be therefore rewritten as:

$$\frac{\partial E}{\partial \operatorname{vec}(\bar{P}^{\alpha})_{\delta}} = \sum_{\varepsilon} \Big(\frac{\partial^2 E}{\partial \operatorname{vec}(\bar{P}^{\alpha})_{\delta} \, \partial \operatorname{vec}(\bar{P}^{\alpha})_{\varepsilon}} \Big)_{\mathbf{0}} \operatorname{vec}(\bar{P}^{\alpha})_{\varepsilon} = \\ = \sum_{\varepsilon} U_{\delta\varepsilon} \operatorname{vec}(\bar{P}^{\alpha})_{\varepsilon} \Longrightarrow \tag{2.43}$$

$$\frac{\partial E}{\partial \operatorname{vec}(\bar{\boldsymbol{P}}^{\alpha})} = \boldsymbol{U} \operatorname{vec}(\bar{\boldsymbol{P}}^{\alpha}) \tag{2.44}$$

$\boldsymbol{U}$ collects the second partial derivatives w.r.t. the elements of $\bar{\boldsymbol{P}}^{\alpha}$ and so it can be considered as the mass-weighted electronic Hessian of the energy E.

Vectorization of $\bar{\boldsymbol{P}}^{\alpha}$ definition (Eq. (2.40)) and its second derivative w.r.t. time yields, respectively:

$$\operatorname{vec}(\bar{\boldsymbol{P}}^{\alpha}) = \big((\boldsymbol{\mu}^{1/4})^T \otimes \boldsymbol{\mu}^{1/4}\big) \operatorname{vec}(\boldsymbol{P}^{\alpha} - \boldsymbol{P}_0^{\alpha}) = (\boldsymbol{\mu}^{1/4} \otimes \boldsymbol{\mu}^{1/4}) \operatorname{vec}(\boldsymbol{P}^{\alpha} - \boldsymbol{P}_0^{\alpha}) \tag{2.45}$$

$$\operatorname{vec}\Big(\frac{d^2 \bar{\boldsymbol{P}}^{\alpha}}{dt^2}\Big) = (\boldsymbol{\mu}^{1/4} \otimes \boldsymbol{\mu}^{1/4}) \operatorname{vec}\Big(\frac{d^2 \boldsymbol{P}^{\alpha}}{dt^2}\Big) \tag{2.46}$$

where $\otimes$ is the Kronecker product [58] between two matrices.[1]

The derivatives w.r.t. $\bar{\boldsymbol{P}}^{\alpha}$ and $\boldsymbol{P}^{\alpha}$ are related by:[2]

$$\frac{\partial E}{\partial \operatorname{vec}(\boldsymbol{P}^{\alpha})} = (\boldsymbol{\mu}^{1/4} \otimes \boldsymbol{\mu}^{1/4}) \frac{\partial E}{\partial \operatorname{vec}(\bar{\boldsymbol{P}}^{\alpha})} \tag{2.47}$$

The equation of motion for the density matrix

$$\boldsymbol{\mu}^{1/2} \frac{d^2 \boldsymbol{P}^{\alpha}}{dt^2} \boldsymbol{\mu}^{1/2} + \frac{\partial E}{\partial \boldsymbol{P}^{\alpha}} = \mathbf{0} \tag{2.48}$$

---

[1] $\boldsymbol{Y} = \boldsymbol{C}\boldsymbol{X}\boldsymbol{B} \Rightarrow \operatorname{vec}(\boldsymbol{Y}) = (\boldsymbol{B}^T \otimes \boldsymbol{C}) \operatorname{vec}(\boldsymbol{X})$

[2] If $\boldsymbol{x}' = \boldsymbol{A}(\boldsymbol{x} - \boldsymbol{x}_0)$,

$$\frac{\partial f}{\partial \boldsymbol{x}} = \boldsymbol{A}^{\dagger} \frac{\partial f}{\partial \boldsymbol{x}'}; \quad \frac{\partial^2 f}{\partial \boldsymbol{x}^2} = \boldsymbol{A}^{\dagger} \frac{\partial^2 f}{\partial \boldsymbol{x}'^2} \boldsymbol{A} \qquad \text{where: } \Big(\frac{\partial f}{\partial \boldsymbol{x}}\Big)_i = \frac{\partial f}{\partial x_i}; \quad \Big(\frac{\partial^2 f}{\partial \boldsymbol{x}^2}\Big)_{ij} = \frac{\partial^2 f}{\partial x_i \partial x_j}$$

can be vectorized as:[3]

$$(\boldsymbol{\mu}^{1/2} \otimes \boldsymbol{\mu}^{1/2}) \operatorname{vec}\Big(\frac{d^2\boldsymbol{P}^\alpha}{dt^2}\Big) + \operatorname{vec}\Big(\frac{\partial E}{\partial \boldsymbol{P}^\alpha}\Big) = \\ = (\boldsymbol{\mu}^{1/2} \otimes \boldsymbol{\mu}^{1/2}) \operatorname{vec}\Big(\frac{d^2\boldsymbol{P}^\alpha}{dt^2}\Big) + \frac{\partial E}{\partial \operatorname{vec}(\boldsymbol{P}^\alpha)} = \mathbf{0} \quad (2.49)$$

Switching to mass-weighted electronic degrees of freedom by substitution of Eq. (2.46) and Eq. (2.47) into Eq. (2.49),[4]

$$(\boldsymbol{\mu}^{1/2} \otimes \boldsymbol{\mu}^{1/2})(\boldsymbol{\mu}^{-1/4} \otimes \boldsymbol{\mu}^{-1/4}) \operatorname{vec}\Big(\frac{d^2\bar{\boldsymbol{P}}^\alpha}{dt^2}\Big) + (\boldsymbol{\mu}^{1/4} \otimes \boldsymbol{\mu}^{1/4}) \frac{\partial E}{\partial \operatorname{vec}(\bar{\boldsymbol{P}}^\alpha)} = \\ = \cancel{(\boldsymbol{\mu}^{1/4} \otimes \boldsymbol{\mu}^{1/4})} \operatorname{vec}\Big(\frac{d^2\bar{\boldsymbol{P}}^\alpha}{dt^2}\Big) + \cancel{(\boldsymbol{\mu}^{1/4} \otimes \boldsymbol{\mu}^{1/4})} \frac{\partial E}{\partial \operatorname{vec}(\bar{\boldsymbol{P}}^\alpha)} = \mathbf{0} \quad (2.50)$$

Introducing Eq. (2.44),[5]

$$\operatorname{vec}\Big(\frac{d^2\bar{\boldsymbol{P}}^\alpha}{dt^2}\Big) + \boldsymbol{U} \operatorname{vec}(\bar{\boldsymbol{P}}^\alpha) = \frac{d^2}{dt^2} \operatorname{vec}(\bar{\boldsymbol{P}}^\alpha) + \boldsymbol{U} \operatorname{vec}(\bar{\boldsymbol{P}}^\alpha) = \mathbf{0} \quad (2.51)$$

which represents a set of harmonic-type second-order differential equations in the dynamic variables $\operatorname{vec}(\bar{P}^\alpha)_\delta$.

Second derivatives w.r.t. plain density matrix (that is, the Hessian, or force constants, matrix $\boldsymbol{K} = \big(\frac{\partial^2 E}{\partial \operatorname{vec}(\boldsymbol{P}^\alpha)^2}\big)_{\boldsymbol{P}_0^\alpha}$) and those w.r.t. mass-weighted density matrix (the mass-weighted Hessian $\boldsymbol{U} = \big(\frac{\partial^2 E}{\partial \operatorname{vec}(\bar{\boldsymbol{P}}^\alpha)^2}\big)_{\mathbf{0}}$) can be related

---

[3] $$\operatorname{vec}\Big(\frac{\partial f}{\partial \boldsymbol{B}}\Big) = \frac{\partial f}{\partial \operatorname{vec}(\boldsymbol{B})}$$

[4] $$(\boldsymbol{B} \otimes \boldsymbol{C})^{-1} = \boldsymbol{B}^{-1} \otimes \boldsymbol{C}^{-1}; \qquad (\boldsymbol{B} \otimes \boldsymbol{C})(\boldsymbol{D} \otimes \boldsymbol{F}) = \boldsymbol{B}\boldsymbol{D} \otimes \boldsymbol{C}\boldsymbol{F}$$

[5] $$\operatorname{vec}\Big(\frac{d^2\boldsymbol{B}}{dt^2}\Big) = \frac{d^2}{dt^2} \operatorname{vec}(\boldsymbol{B})$$

as:[6]

$$\boldsymbol{U} = \Big(\frac{\partial^2 E}{\partial\,\mathrm{vec}(\bar{\boldsymbol{P}}^{\alpha})^2}\Big)_{\boldsymbol{0}} = (\boldsymbol{\mu}^{1/4}\otimes\boldsymbol{\mu}^{1/4})^{-1}\Big(\frac{\partial^2 E}{\partial\,\mathrm{vec}(\boldsymbol{P}^{\alpha})^2}\Big)_{\boldsymbol{P}_0^{\alpha}}(\boldsymbol{\mu}^{1/4}\otimes\boldsymbol{\mu}^{1/4})^{-1} = \\ = (\boldsymbol{\mu}^{1/4}\otimes\boldsymbol{\mu}^{1/4})^{-1}\boldsymbol{K}(\boldsymbol{\mu}^{1/4}\otimes\boldsymbol{\mu}^{1/4})^{-1} \quad (2.52)$$

Given the mass-weighted Hessian $\boldsymbol{U}$ eigen-decomposition,

$$\boldsymbol{L}^T\boldsymbol{U}\boldsymbol{L} = \boldsymbol{L}^T(\boldsymbol{\mu}^{1/4}\otimes\boldsymbol{\mu}^{1/4})^{-1}\boldsymbol{K}(\boldsymbol{\mu}^{1/4}\otimes\boldsymbol{\mu}^{1/4})^{-1}\boldsymbol{L} = \boldsymbol{\Lambda} = \mathrm{diag}(\lambda_k) \quad (2.53)$$

a common $\lambda_k = \lambda = 4\pi^2c^2\tilde{\nu}^2$ eigenvalue (and so the same wavenumber $\tilde{\nu}$) can be imposed to all the electronic normal modes. Therefore,

$$\boldsymbol{\Lambda} = \lambda\boldsymbol{I} \\ (\boldsymbol{\mu}^{1/4}\otimes\boldsymbol{\mu}^{1/4})^{-1}\boldsymbol{K}(\boldsymbol{\mu}^{1/4}\otimes\boldsymbol{\mu}^{1/4})^{-1} = \lambda\boldsymbol{L}\boldsymbol{I}\boldsymbol{L}^T = \lambda\boldsymbol{L}\boldsymbol{L}^T = \lambda\boldsymbol{I} \Longrightarrow \\ \boldsymbol{K} = \lambda(\boldsymbol{\mu}^{1/4}\otimes\boldsymbol{\mu}^{1/4})\boldsymbol{I}(\boldsymbol{\mu}^{1/4}\otimes\boldsymbol{\mu}^{1/4}) = \lambda(\boldsymbol{\mu}^{1/2}\otimes\boldsymbol{\mu}^{1/2}) \Longrightarrow \\ (\boldsymbol{\mu}^{1/2}\otimes\boldsymbol{\mu}^{1/2}) = \lambda^{-1}\boldsymbol{K} = (4\pi^2c^2\tilde{\nu}^2)^{-1}\boldsymbol{K} \quad (2.54)$$

having exploited the orthogonality of the eigenvector matrix: $\boldsymbol{L}^{-1} = \boldsymbol{L}^T$.

Here the vibrational problem is reversed: given a target frequency $\tilde{\nu}$ of the electronic normal modes and the force constants matrix $\boldsymbol{K}$, a mass-matrix $\boldsymbol{\mu}$ has to be found. Eq. (2.54) implies that a symmetric, non-diagonal, mass-matrix is required. [59] The chosen frequency should ensure a sufficient gap between the nuclear and the electronic time-scales and so a good adiabaticity.

The second derivatives are numerically evaluated as:

$$K_{\delta\varepsilon} = \frac{\partial^2 E}{\partial\,\mathrm{vec}(P^{\alpha})_{\delta}\,\partial\,\mathrm{vec}(P^{\alpha})_{\varepsilon}}\Big|_{\mathrm{vec}(\boldsymbol{P}_0^{\alpha})} = \frac{\partial^2 E}{\partial P^{\alpha}_{\lambda\nu}\,\partial P^{\alpha}_{\sigma\tau}}\Big|_{\boldsymbol{P}_0^{\alpha}} = \frac{\partial}{\partial P^{\alpha}_{\lambda\nu}}\Big(\frac{\partial E}{\partial P^{\alpha}_{\sigma\tau}}\Big)\Big|_{\boldsymbol{P}_0^{\alpha}} \approx \\ \approx \frac{\frac{\partial E}{\partial P^{\alpha}_{\sigma\tau}}\Big|_{(P_0^{\alpha})_{\lambda\nu}+\Delta} - \frac{\partial E}{\partial P^{\alpha}_{\sigma\tau}}\Big|_{(P_0^{\alpha})_{\lambda\nu}-\Delta}}{2\Delta} \quad (2.55)$$

[6] See Footnote 2

An analytic expression for the first derivative is available: [44–46]

$$\frac{\partial E}{\partial \boldsymbol{P}^{\alpha}} = 3(\boldsymbol{F}^{\alpha}\boldsymbol{P}^{\alpha} + \boldsymbol{P}^{\alpha}\boldsymbol{F}^{\alpha}) - 2(\boldsymbol{F}^{\alpha}\boldsymbol{P}^{\alpha\,2} + \boldsymbol{P}^{\alpha}\boldsymbol{F}^{\alpha}\boldsymbol{P}^{\alpha} + \boldsymbol{P}^{\alpha\,2}\boldsymbol{F}^{\alpha}) \tag{2.56}$$

In order to solve matrix equation Eq. (2.54) for $\boldsymbol{\mu}^{1/2}$, the approach from Refs. [60, 58] is followed. The Kronecker product decomposition or "nearest Kronecker product" of a matrix $\boldsymbol{A}$: $\boldsymbol{A} = \boldsymbol{B} \otimes \boldsymbol{C}$ ($\boldsymbol{A} \in \mathbb{R}^{m_1 m_2 \times n_1 n_2}$, $\boldsymbol{B} \in \mathbb{R}^{m_1 \times n_1}$, $\boldsymbol{C} \in \mathbb{R}^{m_2 \times n_2}$) is found by minimizing the function

$$\phi(\boldsymbol{B}, \boldsymbol{C}) = \|\boldsymbol{A} - \boldsymbol{B} \otimes \boldsymbol{C}\|_F \Longrightarrow \tag{2.57}$$

$$\phi(\boldsymbol{B}_{\text{opt}}, \boldsymbol{C}_{\text{opt}}) = \min\{\phi(\boldsymbol{B}, \boldsymbol{C})\} \tag{2.58}$$

It can be shown that the $\phi(\boldsymbol{B}, \boldsymbol{C})$ function can be rewritten as:

$$\phi(\boldsymbol{B}, \boldsymbol{C}) = \left\| \mathcal{R}(\boldsymbol{A}) - \text{vec}(\boldsymbol{B})\,\text{vec}(\boldsymbol{C})^T \right\|_F \tag{2.59}$$

$\mathcal{R}(\boldsymbol{A})$ is a specific rearrangement of $\boldsymbol{A}$:

$$\mathcal{R}(\boldsymbol{A}) = \begin{bmatrix} \text{vec}(\boldsymbol{A}^{(1,1)})^T \\ \vdots \\ \text{vec}(\boldsymbol{A}^{(i,j)})^T \\ \vdots \\ \text{vec}(\boldsymbol{A}^{(m_1,n_1)})^T \end{bmatrix} \tag{2.60}$$

where $\boldsymbol{A}^{(i,j)} \in \mathbb{R}^{m_2 \times n_2}$ is the (i,j) block of $\boldsymbol{A}$. $1 \le i \le m_1$, $1 \le j \le n_1$, with i running fast.

Each element $\mathcal{R}(A)_{\alpha\beta}$ of $\mathcal{R}(\boldsymbol{A})$ corresponds of course to an element $A_{\delta\varepsilon}$ of $\boldsymbol{A}$:

$$\mathcal{R}(A)_{\alpha\beta} = \left[\text{vec}(\boldsymbol{A}^{(i,j)})^T\right]_{\beta} = A^{(i,j)}_{\delta'\varepsilon'} = A_{\delta\varepsilon} \tag{2.61}$$

where:

$$\begin{cases} i = m_1, \quad j = \alpha // m_1 & \text{if } \alpha \,\%\, m_1 = 0 \\ i = \alpha \,\%\, m_1, \quad j = (\alpha // m_1) + 1 & \text{if } \alpha \,\%\, m_1 \neq 0 \end{cases}$$

$$\begin{cases} \delta' = m_2, \quad \varepsilon' = \beta // m_2 & \text{if } \beta \,\%\, m_2 = 0 \\ \delta' = \beta \,\%\, m_2, \quad \varepsilon' = (\beta // m_2) + 1 & \text{if } \beta \,\%\, m_2 \neq 0 \end{cases}$$

$$\delta = (i-1)m_2 + \delta'$$
$$\varepsilon = (j-1)n_2 + \varepsilon'$$

where // and % are the integer division (i.e., quotient without remainder) and the division remainder operators, respectively.

Since $\mathrm{vec}(\boldsymbol{B})\,\mathrm{vec}(\boldsymbol{C})^T$ (i.e., a column times a row) is a rank-1 matrix, the minimization of the $\phi(\boldsymbol{B}, \boldsymbol{C})$ function is equivalent to find the best (i.e., the nearest) rank-1 matrix approximating $\mathcal{R}(\boldsymbol{A})$. This can be obtained starting from the Singular Value Decomposition (SVD) of $\mathcal{R}(\boldsymbol{A})$: [61]

$$\mathcal{R}(\boldsymbol{A}) = \boldsymbol{U}\boldsymbol{\Sigma}\boldsymbol{V}^T \tag{2.62}$$

where $\boldsymbol{U} = [\boldsymbol{u}_i]$ and $\boldsymbol{V} = [\boldsymbol{v}_i]$ are the orthogonal matrices of left and right singular vectors, respectively, and $\boldsymbol{\Sigma}$ is a diagonal matrix containing the $\sigma_i > 0$, $1 \leq i \leq r$ singular values, with r being the rank of $\mathcal{R}(\boldsymbol{A})$. The rank-1 approximation is equal to:

$$\mathcal{R}(\boldsymbol{A}) \approx \sigma_1 \boldsymbol{u}_1 \boldsymbol{v}_1^T \tag{2.63}$$

having arranged the σ_i in decreasing order and so being σ_1 the highest singular value. So,

$$\mathrm{vec}(\boldsymbol{B}_{\mathrm{opt}})\,\mathrm{vec}(\boldsymbol{C}_{\mathrm{opt}})^T = \sigma_1 \boldsymbol{u}_1 \boldsymbol{v}_1^T \Longrightarrow \tag{2.64}$$

$$\mathrm{vec}(\boldsymbol{B}_{\mathrm{opt}}) = \pm(\sigma_1)^{1/2}\boldsymbol{u}_1; \qquad \mathrm{vec}(\boldsymbol{C}_{\mathrm{opt}}) = \pm(\sigma_1)^{1/2}\boldsymbol{v}_1 \tag{2.65}$$

choosing the same sign for $\mathrm{vec}(\boldsymbol{B}_{\mathrm{opt}})$ and $\mathrm{vec}(\boldsymbol{C}_{\mathrm{opt}})$.

If $\mathcal{R}(\boldsymbol{A})$ is symmetric, $\sigma_i = |\omega_i|$, given the eigen-decomposition $\mathcal{R}(\boldsymbol{A}) = \boldsymbol{Q}\boldsymbol{\Omega}\boldsymbol{Q}^T$, $\boldsymbol{Q} = [\boldsymbol{q}_i]$, $\boldsymbol{\Omega} = \mathrm{diag}(\omega_i)$. Therefore, $\sigma_1 = \max\{|\omega_i|\} = |\omega_1|$. If

$\omega_1 > 0$, $\sigma_1 = \omega_1$ and comparing $\sigma_1 \boldsymbol{u}_1 \boldsymbol{v}_1^T$ to $\omega_1 \boldsymbol{q}_1 \boldsymbol{q}_1^T$,

$$\begin{gathered} \sigma_1 \boldsymbol{u}_1 \boldsymbol{v}_1^T = \omega_1 \boldsymbol{q}_1 \boldsymbol{q}_1^T \Longrightarrow \\ \boldsymbol{u}_1 = \pm \boldsymbol{q}_1; \qquad \boldsymbol{v}_1 = \pm \boldsymbol{q}_1 \\ \mathrm{vec}(\boldsymbol{B}_{\mathrm{opt}}) = \pm (\omega_1)^{1/2} \boldsymbol{q}_1; \qquad \mathrm{vec}(\boldsymbol{C}_{\mathrm{opt}}) = \pm (\omega_1)^{1/2} \boldsymbol{q}_1 \end{gathered} \tag{2.66}$$

which implies $\boldsymbol{B}_{\mathrm{opt}} = \boldsymbol{C}_{\mathrm{opt}}$, having to choose the same $\pm$ sign.

Eq. (2.54) can be solved for $\boldsymbol{\mu}^{1/2}$, assuming $(4\pi^2 c^2 \tilde{\nu}^2)^{-1} \boldsymbol{K} = \boldsymbol{A}$ and $\boldsymbol{\mu}^{1/2} = \boldsymbol{B}_{\mathrm{opt}}$. Therefore, $\mathcal{R}(\boldsymbol{A}) = (4\pi^2 c^2 \tilde{\nu}^2)^{-1} \mathcal{R}(\boldsymbol{K})$. The equivalences between second derivatives due to the symmetry of the $\boldsymbol{P}$ matrix and the non-depencence from the order of derivation

$$\begin{aligned} \left. \frac{\partial^2 E}{\partial P^\alpha_{\lambda\nu} \, \partial P^\alpha_{\sigma\tau}} \right|_{\boldsymbol{P}^\alpha_0} = \left. \frac{\partial^2 E}{\partial P^\alpha_{\nu\lambda} \, \partial P^\alpha_{\sigma\tau}} \right|_{\boldsymbol{P}^\alpha_0} = \left. \frac{\partial^2 E}{\partial P^\alpha_{\lambda\nu} \, \partial P^\alpha_{\tau\sigma}} \right|_{\boldsymbol{P}^\alpha_0} = \left. \frac{\partial^2 E}{\partial P^\alpha_{\nu\lambda} \, \partial P^\alpha_{\tau\sigma}} \right|_{\boldsymbol{P}^\alpha_0} = \\ = \left. \frac{\partial^2 E}{\partial P^\alpha_{\sigma\tau} \, \partial P^\alpha_{\lambda\nu}} \right|_{\boldsymbol{P}^\alpha_0} = \dots \end{aligned} \tag{2.67}$$

give the Hessian matrix $\boldsymbol{K}$ a highly symmetric structure, so that the permuted matrix $\mathcal{R}(\boldsymbol{K})$ is itself symmetric. For instance, with $N_b = 2$:

$$\boldsymbol{K} = \begin{bmatrix} K_{11} & K_{21} & K_{21} & K_{41} \\ K_{21} & K_{22} & K_{22} & K_{42} \\ K_{21} & K_{22} & K_{22} & K_{42} \\ K_{41} & K_{42} & K_{42} & K_{44} \end{bmatrix} \quad \Longrightarrow \quad \mathcal{R}(\boldsymbol{K}) = \begin{bmatrix} K_{11} & K_{21} & K_{21} & K_{22} \\ K_{21} & K_{41} & K_{22} & K_{42} \\ K_{21} & K_{22} & K_{41} & K_{42} \\ K_{22} & K_{42} & K_{42} & K_{44} \end{bmatrix} \tag{2.68}$$

2.2.1 Effects of $\tilde{\nu}$ frequency upon the dynamics.

The effect of the choice of $\tilde{\nu}$ target frequency (Eq. (2.54)) upon the fictitious electronic dynamics and the (real) nuclear one was investigated in NMA B3LYP/6-31G(d,p) ADMP simulations, employing the previously shown Hessian-based mass-weighting scheme. Although the fictitious electronic frequencies distribution is always centered below the imposed $\tilde{\nu}$, a shift towards higher values as well as an increase of the bandwidth are observed for

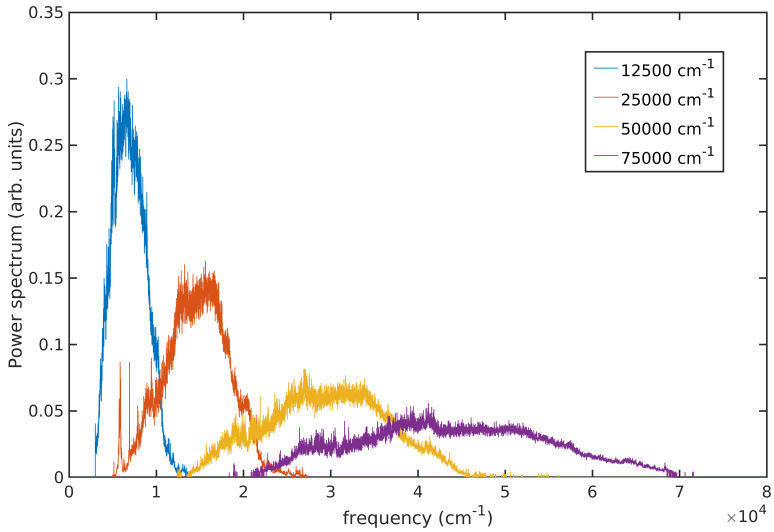


Figure 2.1: Distribution of the fictitious electronic frequencies from NMA B3LYP/6-31G(d,p) ADMP simulations with an Hessian-based mass-weighting scheme. Distinct target frequencies were employed. The spectrum from $\tilde{\nu} = 12\,500\,\mathrm{cm}^{-1}$ has been rescaled towards lower values for clarity.

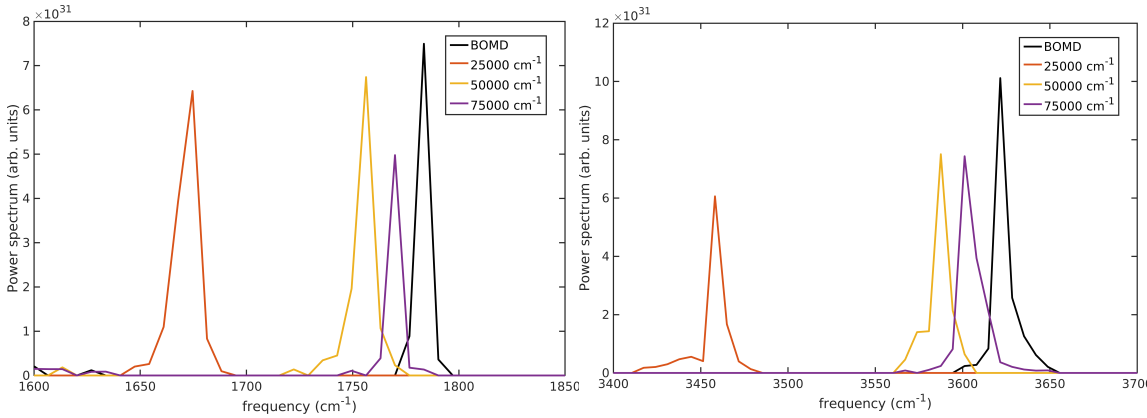
higher $\tilde{\nu}$. (Fig. 2.1 and Table 2.1). The resulting higher frequency separation between nuclear and electronic degrees of freedom leads to decreasing errors in Amide I and Amide A vibrational frequencies with respect to a reference BOMD trajectory. In particular, accurate results are obtained with $\tilde{\nu} \geq 50\,000\,\mathrm{cm}^{-1}$ (Fig. 2.2 and Table 2.2).

2.2.2 Effects of $\boldsymbol{K}$ sparsity upon the dynamics.

Some difficulties in storing in memory the electronic Hessian $N_b^2 \times N_b^2$ matrix $\boldsymbol{K}$ can occur, because of its considerable size for big systems and extended basis sets. Therefore, a "sparse" and more manageable $\boldsymbol{K}$ form has been introduced, retaining only the $\approx N_b^2$ highest (in absolute value) elements and thus approximating to zero all the others (Section 2.2.3). A "diagonal" form of the electronic Hessian, keeping only the N_b^2 $K_{\delta\delta} = \partial^2 E/(\partial P^\alpha_{\lambda\nu}\, \partial P^\alpha_{\lambda\nu})|_{\boldsymbol{P}^\alpha_0}$ diagonal elements, has been also tested, since it provides both reduced memory usage and computational cost. In fact, an analytic expression for

Table 2.1: $\boldsymbol{\mu}$ mass-matrix and fictitious electronic frequencies distribution from NMA B3LYP/6-31G(d,p) ADMP simulations with an Hessian-based mass-weighting scheme. Several target frequencies were tested.

Target frequency, cm^{-1}	$\|\boldsymbol{\mu}\|$ $(s_{\boldsymbol{\mu}})$ $[s_{\boldsymbol{\mu}}/\|\boldsymbol{\mu}\|]$, amu bohr^2	$\langle\nu_{\mathrm{el}}\rangle$ $(s_{\nu_{\mathrm{el}}})$, cm^{-1}
12500	26.37 (0.2389) $[9.060 \times 10^{-3}]$	6994 (1923)
25000	6.591 (5.973×10^{-2}) $[9.062 \times 10^{-3}]$	14557 (3930)
50000	1.648 (1.493×10^{-2}) $[9.059 \times 10^{-3}]$	28910 (8143)
75000	0.7324 (6.637×10^{-3}) $[9.062 \times 10^{-3}]$	42942 (13425)



Amide I Amide A

Figure 2.2: Calculated Amide I and Amide A vibrational bands from NMA B3LYP/6-31G(d,p) BOMD reference trajectory and ADMP simulations with an Hessian-based mass-weighting scheme. Several target frequencies were tested; the spectrum from $\tilde{\nu} = 12\,500\,\mathrm{cm}^{-1}$ target frequency showed no resolved Amide I and Amide A bands.

Table 2.2: Differences (in cm^{-1}) of calculated NMA B3LYP/6-31G(d,p) Amide I and Amide A vibrational frequencies between ADMP simulations with an Hessian-based mass-weighting scheme and a reference BOMD trajectory. Several target frequencies were tested.

	$\Delta\nu$, cm^{-1}	
	Amide I	Amide A
$25\,000\,cm^{-1}$	-109	-163
$50\,000\,cm^{-1}$	-27	-34
$75\,000\,cm^{-1}$	-14	-20

the diagonal elements of the electronic Hessian is available: [45]

$$\frac{\partial^2 E}{\partial P^{\alpha}_{\lambda\nu}\,\partial P^{\alpha}_{\lambda\nu}} = (3 - 2P^{\alpha}_{\lambda\lambda})F^{\alpha}_{\nu\nu} + (3 - 2P^{\alpha}_{\nu\nu})F^{\alpha}_{\lambda\lambda} - 4\big[(P^{\alpha}F^{\alpha})_{\lambda\lambda} + (P^{\alpha}F^{\alpha})_{\nu\nu}\big] \tag{2.69}$$

In order to evaluate the effect of a non-full electronic Hessian on the accuracy, NMA B3LYP/6-31G(d,p) (ts = 0.1 fs) ADMP simulations have been performed with a full, a sparse and a diagonal $\boldsymbol{K}$ Hessian matrix, employing for each calculation the highest allowed $\tilde{\nu}$ frequency. The full and the diagonal matrix trajectories can rely on a higher input $\tilde{\nu}$ frequency ($95\,000\,cm^{-1}$) than the sparse matrix one ($80\,000\,cm^{-1}$). The fictitious electronic frequencies distribution is therefore on average displaced towards lower values for the latter approach, due to slightly bigger masses (Table 2.3). However, the diagonal approach shows a slightly wider distribution than the sparse one.

Nevertheless, all the approaches ensure a high adiabaticity and accurate estimates of Amide vibrational frequencies ($-7\,cm^{-1}$ deviations from BOMD, except for the Amide A from the diagonal Hessian, $-21\,cm^{-1}$, Table 2.4). Non-full computations of the electronic Hessian appear therefore an advantageous option to estimate the optimal fictitious mass in ADMP simulations.

Table 2.3: $\boldsymbol{\mu}$ mass-matrix and fictitious electronic frequencies distribution from NMA B3LYP/6-31G(d,p) ADMP simulations with an Hessian-based mass-weighting scheme. A full, a sparse and a diagonal form of the electronic Hessian $\boldsymbol{K}$ have been employed.

Type	Max target freq., cm^{-1}	$\|\boldsymbol{\mu}\|$, amu bohr^2	$\langle\nu_{\mathrm{el}}\rangle$ ($s_{\nu_{\mathrm{el}}}$), cm^{-1}
full	95000	0.4565	54757 (18102)
sparse	80000	0.6354	44695 (15581)
diagonal	95000	0.4479	49158 (17476)

Table 2.4: Differences (in cm^{-1}) of calculated NMA B3LYP/6-31G(d,p) Amide I and Amide A vibrational frequencies between ADMP simulations with an Hessian-based mass-weighting scheme and a reference BOMD trajectory. A full, a sparse and a diagonal form of the electronic Hessian $\boldsymbol{K}$ have been employed.

	$\Delta\nu$, cm^{-1}	
	Amide I	Amide A
full	-7	-7
sparse	-7	-7
diagonal	-7	-21

2.2.3 Implementation into Gaussian16.

The previously shown Hessian-based mass-weighting scheme has been coded into a Gaussian16 development version. The user can choose between a full, a sparse or a diagonal electronic Hessian $\boldsymbol{K}$ computation (`TypHs`). In Sparse and Diagonal modes, $\mathcal{R}(\boldsymbol{K})$ is saved in a sparse matrix format. For the Sparse option, only the $\boldsymbol{K}$ elements greater than a `Threshold` are saved. The total number of such elements must not exceed N_b^2. In order to calculate the dominant ω_1 and $\boldsymbol{q}_1$ $\mathcal{R}(\boldsymbol{A})$ eigenvalue and eigenvector, a full diagonalization or the power iteration method can be chosen with a full Hessian, but only the power method is available with a sparse or diagonal Hessian. The power method allows to find the dominant eigenvector $\boldsymbol{x}_1$ of a matrix $\boldsymbol{M}$ through the following iteration (until convergence):

$$\boldsymbol{x}^{(k+1)} = \frac{\boldsymbol{M}\boldsymbol{x}^{(k)}}{\left\|\boldsymbol{M}\boldsymbol{x}^{(k)}\right\|} = \frac{\boldsymbol{M}^k\boldsymbol{x}^{(0)}}{\left\|\boldsymbol{M}^k\boldsymbol{x}^{(0)}\right\|} \qquad (2.70)$$

$$\lambda_1 = \boldsymbol{x}_1^T\boldsymbol{M}\boldsymbol{x}$$

```
Read TypHs from input file
If TypHs = Sparse
   Read Threshold
ElseIf TypHs = Full
   Read EigMethod
Read ν̃ from input file
Read F^α Fock matrix, P_0^α density matrix from disk
If TypHs = Full
   For α = 1 : N_b^2
     Calculate α → (i, j)
     For β = 1 : α
       Calculate β, (i, j) → (δ, ε)
       If Gradients not calculated for index δ
         Calculate δ → (λ, ν)
         Calculate Gradients (∂E/∂P^α)|_{(P_0^α)_λν+Δ}, (∂E/∂P^α)|_{(P_0^α)_λν−Δ}
```

$\dfrac{\partial E}{\partial \boldsymbol{P}^\alpha} = 3(\boldsymbol{F}^\alpha \boldsymbol{P}^\alpha + \boldsymbol{P}^\alpha \boldsymbol{F}^\alpha) - 2(\boldsymbol{F}^\alpha \boldsymbol{P}^{\alpha\,2} + \boldsymbol{P}^\alpha \boldsymbol{F}^\alpha \boldsymbol{P}^\alpha + \boldsymbol{P}^{\alpha\,2} \boldsymbol{F}^\alpha)$
Write Gradients on disk
ElseIf Gradients already calculated for index δ
Read Gradients from disk
Calculate $\varepsilon \to (\sigma, \tau)$
Calculate $\mathcal{R}(K)_{\alpha\beta} = \partial^2 E / (\partial P^\alpha_{\lambda\nu}\, \partial P^\alpha_{\sigma\tau})|_{\boldsymbol{P}^\alpha_0} =$
$= \big((\partial E/\partial P^\alpha_{\sigma\tau})|_{(P^\alpha_0)_{\lambda\nu}+\Delta} - (\partial E/\partial P^\alpha_{\sigma\tau})|_{(P^\alpha_0)_{\lambda\nu}-\Delta}\big)/(2\Delta)$
Write $\mathcal{R}(K)_{\alpha\beta}$, $\mathcal{R}(K)_{\beta\alpha} = \mathcal{R}(K)_{\alpha\beta}$ into $\mathcal{R}(\boldsymbol{K})$ matrix
ElseIf TypHs = Sparse or Diagonal
For $\alpha = 1 : N_b^2$
Calculate $\alpha \to (i, j)$
For $\beta = 1 : N_b^2$
Calculate $\beta, (i, j) \to (\delta, \varepsilon)$
If TypHs = Sparse
If Gradients not calculated for index δ
Calculate $\delta \to (\lambda, \nu)$
Calculate Gradients $(\partial E/\partial \boldsymbol{P}^\alpha)|_{(P^\alpha_0)_{\lambda\nu}+\Delta}$, $(\partial E/\partial \boldsymbol{P}^\alpha)|_{(P^\alpha_0)_{\lambda\nu}-\Delta}$
$\dfrac{\partial E}{\partial \boldsymbol{P}^\alpha} = 3(\boldsymbol{F}^\alpha \boldsymbol{P}^\alpha + \boldsymbol{P}^\alpha \boldsymbol{F}^\alpha) - 2(\boldsymbol{F}^\alpha \boldsymbol{P}^{\alpha\,2} + \boldsymbol{P}^\alpha \boldsymbol{F}^\alpha \boldsymbol{P}^\alpha + \boldsymbol{P}^{\alpha\,2} \boldsymbol{F}^\alpha)$
Write Gradients on disk
ElseIf Gradients already calculated for index δ
Read Gradients from disk
Calculate $\varepsilon \to (\sigma, \tau)$
Calculate $\mathcal{R}(K)_{\alpha\beta} = \partial^2 E / (\partial P^\alpha_{\lambda\nu}\, \partial P^\alpha_{\sigma\tau})|_{\boldsymbol{P}^\alpha_0} =$
$= \big((\partial E/\partial P^\alpha_{\sigma\tau})|_{(P^\alpha_0)_{\lambda\nu}+\Delta} - (\partial E/\partial P^\alpha_{\sigma\tau})|_{(P^\alpha_0)_{\lambda\nu}-\Delta}\big)/(2\Delta)$
ElseIf TypHs = Diagonal and $\varepsilon = \delta$
Calculate $\delta \to (\lambda, \nu)$
Calculate $\mathcal{R}(K)_{\alpha\beta} = \partial^2 E / (\partial P^\alpha_{\lambda\nu}\, \partial P^\alpha_{\lambda\nu})|_{\boldsymbol{P}^\alpha_0}$,
$\dfrac{\partial^2 E}{\partial P^\alpha_{\lambda\nu}\, \partial P^\alpha_{\lambda\nu}} =$
$= (3 - 2P^\alpha_{\lambda\lambda})F^\alpha_{\nu\nu} + (3 - 2P^\alpha_{\nu\nu})F^\alpha_{\lambda\lambda} - 4\big[(P^\alpha F^\alpha)_{\lambda\lambda} + (P^\alpha F^\alpha)_{\nu\nu}\big]$
If (TypHs = Sparse and $|\mathcal{R}(K)_{\alpha\beta}|$ > Thresh)
or (TypHs = Diag and $\varepsilon = \delta$)
Write $\mathcal{R}(K)_{\alpha\beta}$ into $\mathcal{R}(\boldsymbol{K})$ sparse matrix

Calculate $\mathcal{R}(\boldsymbol{A}) = (4\pi^2 c^2 \tilde{\nu}^2)^{-1} \mathcal{R}(\boldsymbol{K})$
If TypHs = Full
  If EigMethod = diag
    $\mathcal{R}(\boldsymbol{A})$ diagonalization $\rightarrow \omega_1, \boldsymbol{q}_1$
  ElseIf EigMethod = power_iter
    Power iteration method on $\mathcal{R}(\boldsymbol{A})$ $\rightarrow \omega_1, \boldsymbol{q}_1$
ElseIf TypHs = Sparse or Diagonal
  Power iteration method on sparse $\mathcal{R}(\boldsymbol{A})$ $\rightarrow \omega_1, \boldsymbol{q}_1$
Calculate $\mathrm{vec}(\boldsymbol{\mu}^{1/2}) = (\omega_1)^{1/2} \boldsymbol{q}_1 \implies \boldsymbol{\mu}$

Chapter 3

Evaluation of the developed weighting schemes: test simulations of model compounds.

3.1 Introduction: how to measure the accuracy of an ADMP simulation?

The performances of the new mass-weighting schemes were evaluated through simulations of model compounds, whose elements belong to the first three rows: LiF diatomic, trans-N-methylacetamide (NMA) and trans-dichloroethylene. Full-electrons simulations were performed, without employing pseudopotentials. The stability of ADMP simulations was thus tested with different core/valence atomic structures. A double (6-31G(d,p)) and a triple-zeta (6-311G(d,p)) basis sets were chosen, in association with the B3LYP functional. Time steps from 0.1 up to 0.4 fs and 0.1-0.2 fs were tested at the B3LYP/6-31G(d,p) and B3LYP/6-311G(d,p) levels, respectively.

Moreover, test trajectories of the Ru(II) complex $[Ru(dcbpy)_2(NCS)_2]^{4-}$ were collected as an example of calculation on a 'real word' system. A

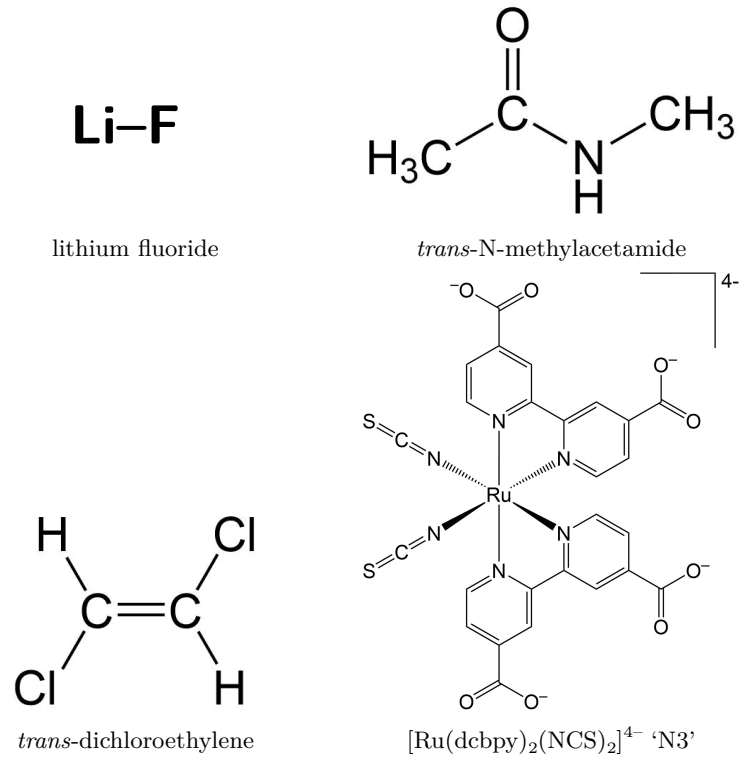


Figure 3.1: Molecular systems employed in ADMP test simulations.

B3LYP/SDD/def2-SVP level of theory was employed, in association with a 0.1 fs time step.

The molecular systems and the computational details employed for ADMP test calculations are summarized in Fig. 3.1 and Table 3.1.

The following strategy was adopted for the projection-based approaches (which rely on two parameters) in order to find the smallest values of fictitious masses able to give a stable propagation of the trajectories. An automated procedure found the optimal core-mass factor f^{cr} and valence mass μ^{val}, increasing the former in the $[2, 100)$ interval in an inner loop and the latter in the $[0.1, 0.4]$ amu bohr^2 interval in an outer loop, according to the following pseudocode:

Table 3.1: Levels of theory, time steps and trajectory lengths employed in ADMP test simulations.

system	level of theory	time steps (fs)	traj length (ps)
$LiF_{(g)}$	B3LYP/6-31G(d,p)	0.1, 0.2, 0.3, 0.4	5
NMA	B3LYP/6-31G(d,p)	0.1, 0.2, 0.3, 0.4	5
	B3LYP/6-311G(d,p)	0.1, 0.2	5
dichloroethylene	B3LYP/6-31G(d,p)	0.1, 0.2, 0.3, 0.4	5
	B3LYP/6-311G(d,p)	0.1, 0.2	5
N3 Ru(II) complex	B3LYP/SDD/def2-SVP	0.1	1

For $\mu^{\mathtt{val}} = 0.1 : 0.4$
  For $f^{\mathtt{cr}} = 2 : 99$
    `Try to propagate the trajectory...`

Several parameters were monitored in order to compare the different schemes. First, the total electronic mass can be measured as the Frobenius norm of the $\boldsymbol{\mu}$ mass-matrix:

$$\|\boldsymbol{\mu}\|_F = \left[\mathrm{Tr}(\boldsymbol{\mu}^\dagger \boldsymbol{\mu})\right]^{1/2} = \left[\mathrm{Tr}(\boldsymbol{\mu}^2)\right]^{1/2} \tag{3.1}$$

For the projection-based MO scheme, the equivalence

$$\|\boldsymbol{\mu}\|_F = \left\|\boldsymbol{\mu}^\psi\right\|_F = \left[\mathrm{Tr}(\boldsymbol{\mu}^{\psi\dagger} \boldsymbol{\mu}^\psi)\right]^{1/2} = \left[\mathrm{Tr}(\boldsymbol{\mu}^{\psi\,2})\right]^{1/2} \tag{3.2}$$

holds because of the unitary transformation relating $\boldsymbol{\mu}$ and $\boldsymbol{\mu}^\psi$ (Eq. (2.31)).

In the time domain, several time-averaged indicators are useful to evaluate the accuracy of an ADMP simulation: [30]

- The ratio between nuclear and fictitious electronic kinetic energies $E_{k,R}/E_{k,P}$ is an adiabaticity measure. A high (ideally, > 10) value suggests a low temperature of the electronic degrees of freedom and thus a more correct nuclear kinetic energy.

- The Frobenius norm of the $[\boldsymbol{F}, \boldsymbol{P}]$ commutator is practically zero (i.e., $\sim 10^{-13}$ hartree) for a converged electronic structure and can be considered as a measure of deviation of the electronic density from the converged, BO, one.

- The rate of variation $d\mathcal{H}_{\text{fict}}/dt$ of the fictitious part $\mathcal{H}_{\text{fict}}$ of the total ADMP Hamiltonian (i.e., the electronic kinetic energy $E_{k,P}$) can be monitored to check *on the fly* the rate of the deviation of the ADMP trajectory from an *exact* BOMD one. This quantity is therefore defined as an *adiabaticity index* of ADMP simulations (Section 1.1.3).

- The ADMP Lagrangian implies that the related Hamiltonian $\mathcal{H} = E_{\text{tot}}$ is a constant of motion, i.e., $d\mathcal{H}/dt = 0$. The standard deviation $s(E_{\text{tot}})$ of the ADMP total energy can be employed as a measure of energy conservation.

- If a BOMD trajectory starting from the same phase-space point and carried out with the same time step is also available, the ADMP-BOMD deviation of the potential and the real total energies and the root-mean-square deviation of nuclear coordinates and velocities can be followed.

Looking instead at the frequency domain, the nuclear vibrational dynamics exhibited by an ADMP simulation can be compared to the vibrational spectrum extracted from a reference BOMD one. [30] Therefore, the (red)shift $\Delta\nu$ of the ADMP-estimated vibrational frequencies relative to the BOMD values were used to assess the accuracy of the ADMP simulations.

The nuclear vibrational power spectrum can be obtained as the Fourier-transform of the autocorrelation function of the sampled mass-weighted

velocities $\dot{q}_{k,A}(t)$: [62]

$$\begin{aligned} S_N(\omega) &= \frac{1}{N_{\text{at}}} \sum_{A}^{N_{\text{at}}} \int_{-\infty}^{\infty} \langle \vec{v}_A(\tau) \cdot \vec{v}_A(t+\tau) \rangle_\tau \, e^{-i\omega t} dt = \\ &= \frac{1}{N_{\text{at}}} \sum_{A}^{N_{\text{at}}} \sum_{k=1}^{3} \int_{-\infty}^{\infty} \langle \dot{q}_{k,A}(\tau) \dot{q}_{k,A}(t+\tau) \rangle_\tau \, e^{-i\omega t} dt = \\ &= \frac{1}{N_{\text{at}}} \sum_{A}^{N_{\text{at}}} \sum_{k=1}^{3} \left| \int_{-\infty}^{\infty} \dot{q}_{k,A}(t) \, e^{-i\omega t} dt \right|^2 = \frac{1}{N_{\text{at}}} \sum_{A}^{N_{\text{at}}} \sum_{k=1}^{3} S_{k,A}(\omega) \end{aligned} \tag{3.3}$$

where the Wiener-Khinchin theorem [63] has been applied.

The frequencies distribution of the $\boldsymbol{P}$ density matrix can be informative about the degree of adiabaticity maintained between the nuclear and electronic subsystems in an ADMP simulation.

A "spectrum" of the density matrix fictitious motion can be derived:

$$\begin{aligned} S_{el}(\omega) &= \sum_{\lambda,\nu}^{N_b} \int_{-\infty}^{\infty} \langle W_{\lambda\nu}(\tau) W_{\lambda\nu}(t+\tau) \rangle_\tau \, e^{-i\omega t} dt = \\ &= \sum_{\lambda,\nu}^{N_b} \left| \int_{-\infty}^{\infty} W_{\lambda\nu}(t) \, e^{-i\omega t} dt \right|^2 = \sum_{\lambda,\nu}^{N_b} S_{\lambda\nu}(\omega) \end{aligned} \tag{3.4}$$

where $\boldsymbol{W}(t) = d\boldsymbol{P}(t)/dt$ is the velocity of the density matrix.

The spectrum of $\boldsymbol{P}(t)$ motion is always composed by low- and a high-frequency regions. The lowest peaks correspond to the nuclear vibrational bands and are generated by the "drag" exerted by the nuclear motion on the electronic density. The signals in the high-frequency region are instead related to the instrinsic dynamics of the density matrix generated by the ADMP Lagrangian $\mathcal{L}$. In particular, the distance $\nu_{el} - \nu_N$ between the highest nuclear fundamental frequency and the lowest intrinsic electronic one dictate the degree of adiabaticity between the two subsystems.[64, 65] The ratio τ_N/τ_{el} between the lowest fundamental nuclear time-scale and the highest electronic one is therefore expected to be > 1.

3.2 Lithium Fluoride (LiF)

LiF biatomic molecule was chosen as a simple model compound to test the developed ADMP weighting schemes. Li and F both belong to the second row; their 1s core orbitals are nevertheless quite different.

Initial velocities were randomly chosen in accordance with a $T = 300\,\mathrm{K}$ temperature. BOMD and ADMP simulations were carried out for 5ps.

3.2.1 B3LYP/6-31G(d,p) level of theory.

With the smallest (0.1 fs) time step, all the schemes employ, as expected, low mass parameters (Table 3.2). The high $\|\boldsymbol{\mu}\|_F$ shown by the default scheme is due to the high inertia imposed to the F 1s orbital. At ts = 0.2 fs, the scalar scheme already requires an increased ($0.3\,\mathrm{amu\,bohr}^2$) valence mass. This scheme proves moreover unable to run a trajectory for ts $\geq$ 0.3 fs. The projection-based approaches still employ a $0.1\,\mathrm{amu\,bohr}^2$ valence mass with a 0.3 fs time step, while the default one has to use a $0.2\,\mathrm{amu\,bohr}^2$ value. A ts = 0.4 fs time step necessarily requires $\mu^{\mathrm{val}} > 0.1\,\mathrm{amu\,bohr}^2$, but, again, the proj-based schemes can employ a lower value ($0.2\,\mathrm{amu\,bohr}^2$) than the default one ($0.3\,\mathrm{amu\,bohr}^2$). A high target frequency ($90\,000\,\mathrm{cm}^{-1}$) can be employed with the Hessian-based approach in association with the smallest (0.1 fs) time step. Then, an inverse proportionality seems to relate the chosen time step and the allowed frequency, up to ts = 0.4 fs.

Time-domain analysis.

$E_{k,R}/E_{k,P}$ oscillations in LiF B3LYP/6-31G(d,p) ts = 0.1 fs ADMP simulations are roughly confined between 0 and 80 for the default, scalar and the projection-based approaches, but between 0 and 500 for the Hessian-based one, occasionally exploring values up to $\sim$ 700. All the schemes ensure therefore a good accuracy at such time step, showing high ($\sim$ 90 by the Hessian method, $\sim$ 20 by the other ones) mean $E_{k,R}/E_{k,P}$ ratios, albeit with big oscillations. (Fig. 3.2 and Table 3.3). The $\|[\boldsymbol{F}, \boldsymbol{P}]\|$ commutator norm is distinctly displaced towards bigger values (~ 0.009 hartree) with the

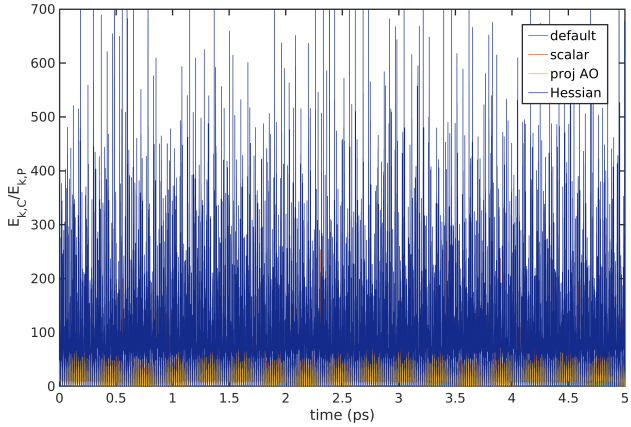
Table 3.2: Mass parameters and norm of $\boldsymbol{\mu}$ matrix employed for LiF B3LYP/6-31G(d,p) ADMP simulations.

LiF B3LYP/6-31G(d,p) (N_b: 30): ADMP mass parameters					
	Time Step (fs)				
	0.1	0.2	0.3	0.4	
default	–, 0.1 10.9	–, 0.1 10.9	–, 0.2 21.8	–, 0.3 32.7	f^{cr}, μ^{val} (amu bohr^2) / $\tilde{\nu}$ (cm^{-1}) $\|\boldsymbol{\mu}\|_F$ (amu bohr^2)
scalar	–, 0.1 0.548	–, 0.3 1.64			
proj AO	2, 0.1 0.600	8, 0.1 1.25	46, 0.1 6.53	36, 0.2 10.2	
proj/energy AO	2, 0.1 2.61	2, 0.1 2.61	4, 0.1 5.14	3, 0.2 7.74	
proj/radius AO	2, 0.1 0.881	3, 0.1 1.18	14, 0.1 4.96	11, 0.2 7.82	
proj MO	2, 0.1 0.600	8, 0.1 1.25	49, 0.1 6.95	30, 0.2 8.55	
Hessian	90000 0.58	45000 2.32	30000 5.22	20000 11.74	

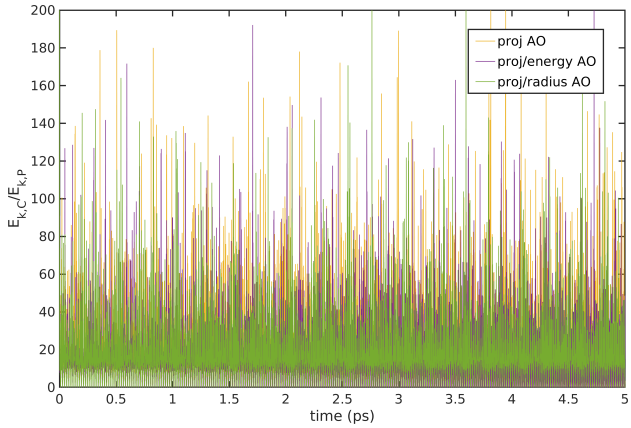
default method, while it is lowest (~ 0.004 hartree) with the Hessian-based one (Fig. 3.3). Among the new projection-based approaches, $\|[\boldsymbol{F}, \boldsymbol{P}]\|$ by the proj/energy AO scheme is slightly higher (~ 0.007 hartree) with respect to the other ones (about 0.005 hartree).

The performances of the scalar scheme rapidly decay for ts > 0.1 fs, due to the requirement of a tripled valence mass parameter at ts $= 0.2$ fs (Table 3.2). The default and the projection-based approaches seem instead largely unaffected by the time step increase from 0.1 to 0.2 fs, showing only small increases in the $\|[\boldsymbol{F}, \boldsymbol{P}]\|$ norm. Due to an halved input frequency, adiabaticity indicators from the Hessian-based method notably worsen at ts $= 0.2$ fs, aligning instead with those from the other approaches. Further increasing (0.3 fs) the time step, the kinetic energies ratio is still equal or greater than 10 (about 20 in particular for proj MO scheme) for the projection and Hessian-based approaches, but only around 8 for the default one. The $\|[\boldsymbol{F}, \boldsymbol{P}]\|$ norms are quite comparable (~ 0.01 hartree), except that from the proj AO scheme (0.05 hartree). Ts $= 0.4$ fs proves quite a limit time step value, even for a biatomic molecule. All the approaches, in fact, produce similar, but less than 10, $E_{k,R}/E_{k,P}$ ratios. The $\|[\boldsymbol{F}, \boldsymbol{P}]\|$ norm is instead still acceptable (~ 0.015 hartree).

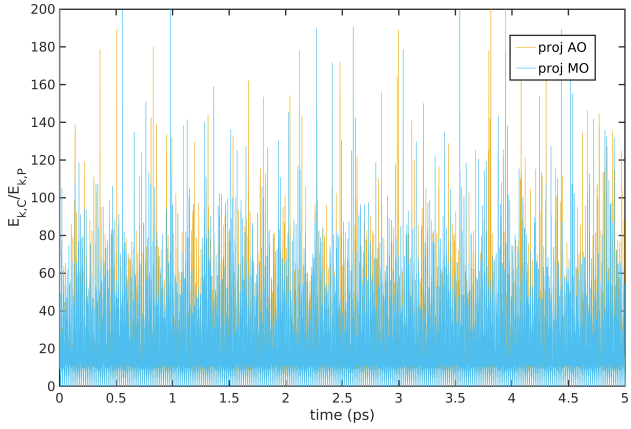
LiF ADMP (ts $= 0.1$ fs) test trajectories at the B3LYP/6-31G(d,p) level show a double-frequency oscillation (around zero) of E_{pot} deviation from the BOMD trajectory (Fig. 3.4 and Table 3.4). In particular, the slower frequency component is substantially lower in the Hessian-based approach, while slightly higher in the default and the proj/energy AO methods. The deviations amplitude (~ 0.0015 hartree) is instead similar for all the schemes. Due to a higher adiabaticity, the Hessian-based weighting scheme ensures a lower ADMP $E_{\text{real}} = E_{k,R} + E_{\text{pot}}$ deviation from BOMD E_{tot} (between 0 and -2×10^{-5} hartree, on average -8×10^{-6} hartree), if compared with the other approaches (Fig. 3.5). The current and the new projection-based one are in fact confined instead in the ~ -0.01, -0.1 mhartree range, around a -4×10^{-5} hartree average value. The RMS deviations of the coordinates (Fig. 3.6) and the mass-weighted velocities (Fig. 3.7) from the BOMD trajectory show trends similar to the ΔE_{pot}: a fast and a slow frequency



Default *vs.* scalar *vs.* proj AO *vs.* Hessian.

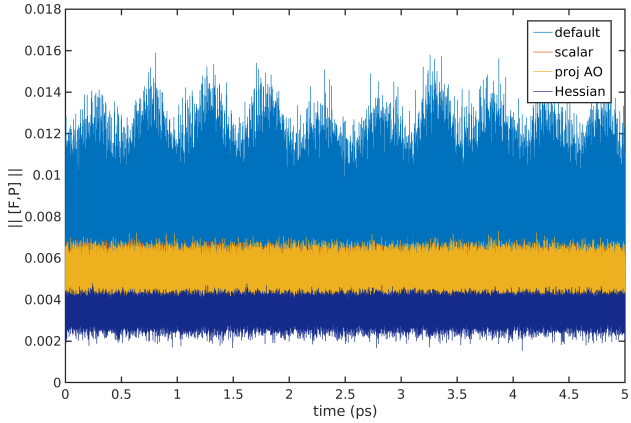


Proj *vs.* proj/energy *vs.* proj/radius AO.

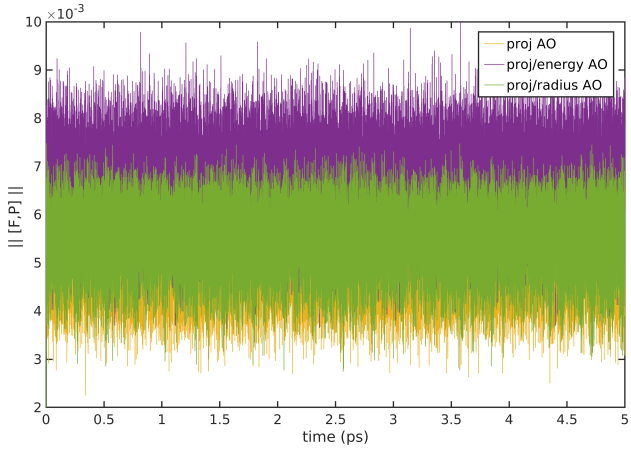


Proj AO *vs.* proj MO.

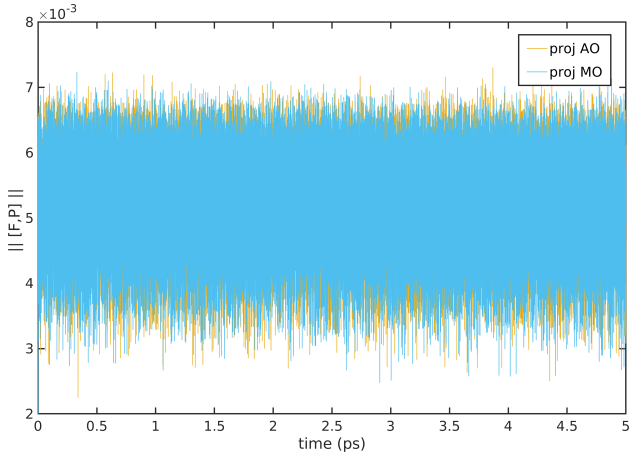
Figure 3.2: LiF B3LYP/6-31G(d,p) ADMP (ts = 0.1 fs) simulations: $E_{k,R}/E_{k,P}$ ratio.



Default *vs.* scalar *vs.* proj AO *vs.* Hessian.



Proj *vs.* proj/energy *vs.* proj/radius AO.



Proj AO *vs.* proj MO.

Figure 3.3: LiF B3LYP/6-31G(d,p) ADMP (ts = 0.1 fs) simulations: $\|[\boldsymbol{F}, \boldsymbol{P}]\|$ commutator norm.

Table 3.3: LiF B3LYP/6-31G(d,p) ADMP simulations; adiabaticity indicators. $E_{k,R}/E_{k,P}$, $\|[\boldsymbol{F},\boldsymbol{P}]\|$ and $|d\mathcal{H}_{\text{fict}}/dt|$ parameters are reported as: average (st.dev.).

LiF B3LYP/6-31G(d,p): ADMP adiabaticity					
	Time Step (fs)				
	0.1	0.2	0.3	0.4	
default	20 (10)	20 (10)	8 (7)	6 (5)	$E_{k,R}/E_{k,P}$
	0.9 (0.2)	0.9 (0.2)	1.3 (0.2)	1.7 (0.3)	$\|[\boldsymbol{F},\boldsymbol{P}]\|$ ($\cdot 10^{-2}$ Ha)
	1.0 (0.8)	3 (2)	3 (2)	3 (3)	$\|d\mathcal{H}_{\text{fict}}/dt\|$ ($\cdot 10^{-5}$ Ha fs^{-1})
	(0.02)	(0.06)	(0.2)	(0.3)	$s(E_{\text{tot}})$ ($\cdot 10^{-5}$ Ha)
scalar	20 (20)	6 (5)			
	0.51 (0.07)	1.0 (0.1)			
	1 (1)	1 (1)			
	(0.2)	(1)			
proj AO	20 (20)	20 (10)	10 (10)	7 (7)	
	0.52 (0.07)	0.8 (0.1)	5 (3)	1.6 (0.2)	
	1 (1)	3 (2)	40 (50)	4 (3)	
	(0.02)	(0.08)	(20)	(0.3)	
proj/energy AO	20 (10)	20 (10)	10 (10)	7 (6)	
	0.68 (0.08)	0.76 (0.09)	1.1 (0.1)	1.5 (0.2)	
	1.1 (0.9)	3 (2)	4 (3)	4 (3)	
	(0.02)	(0.07)	(0.2)	(0.4)	
proj/radius AO	20 (10)	20 (10)	10 (10)	7 (6)	
	0.55 (0.07)	0.75 (0.09)	1.1 (0.1)	1.6 (0.2)	
	1.1 (0.9)	3 (2)	4 (3)	3 (3)	
	(0.02)	(0.07)	(0.2)	(0.3)	
proj MO	20 (20)	20 (20)	20 (10)	8 (7)	
	0.52 (0.07)	0.8 (0.1)	1.5 (0.4)	1.5 (0.3)	
	1 (1)	3 (2)	20 (10)	5 (3)	
	(0.02)	(0.09)	(2)	(0.4)	
Hessian	90 (80)	20 (20)	10 (9)	4 (4)	
	0.35 (0.05)	0.70 (0.09)	1.1 (0.1)	1.4 (0.2)	
	4 (3)	3 (3)	3 (3)	3 (2)	
	(0.02)	(0.08)	(0.2)	(0.3)	

Table 3.4: ΔE_{pot}, ΔE_{tot}, RMSD Coor and RMSD m.w. Vel between LiF B3LYP/6-31G(d,p) ADMP test simulations and a BOMD reference trajectory (ts = 0.1 fs). Data are reported as mean (st.dev.).

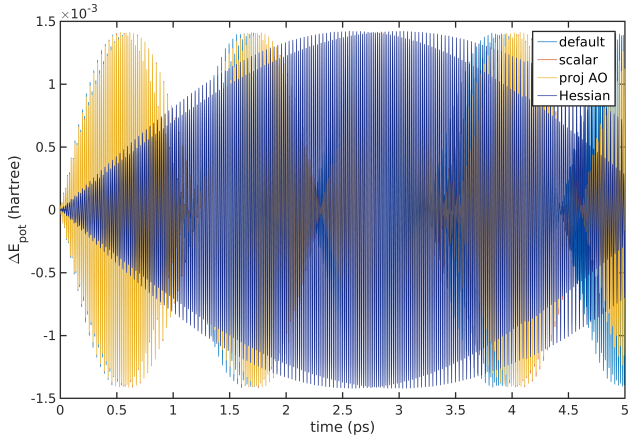
LiF B3LYP/6-31G(d,p): ADMP - BOMD deviations				
	ΔE_{pot} (10^{-4} hartree)	ΔE_{tot} (10^{-5} hartree)	RMSD Coor (10^{-2} bohr)	RMSD m.w. Vel (10^{13} amu$^{1/2}$ bohr s^{-1})
default	0 (7)	-4 (2)	5 (4)	3 (2)
scalar	0 (7)	-4 (3)	5 (4)	3 (2)
proj AO	0 (7)	-4 (3)	5 (4)	3 (2)
proj/energy AO	0 (7)	-5 (3)	5 (4)	3 (2)
proj/radius AO	0 (7)	-4 (2)	5 (4)	3 (2)
proj MO	0 (7)	-4 (3)	5 (4)	3 (2)
Hessian	0 (8)	-0.8 (0.5)	5 (4)	3 (2)

component, the latter being higher for the default and the proj/energy AO schemes, but much lower for the Hessian one. The tested approaches show analogous RMS coordinates and velocities deviations time-averages (0.05 bohr and 3×10^{13} amu$^{1/2}$ bohr s^{-1}, respectively).

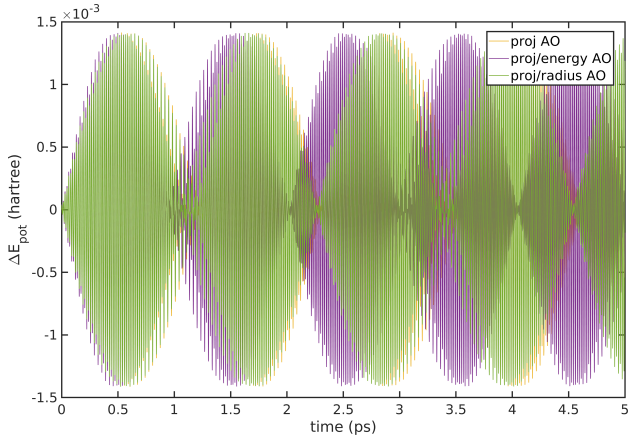
Frequency-domain analysis.

Li–F stretching band is located at 906 cm^{-1} in $LiF_{(g)}$ monomer experimental IR spectrum. [66] The B3LYP/6-31G(d,p) BOMD simulation overestimates the band position by $\sim$ 100 cm^{-1}. Since the introduction of a fictitious electronic mass in extended Lagrangian simulations induces a vibrational redshift with respect to the BOMD, [27] the greater accuracy here shown by the ADMP simulations is actually an errors compensation effect.

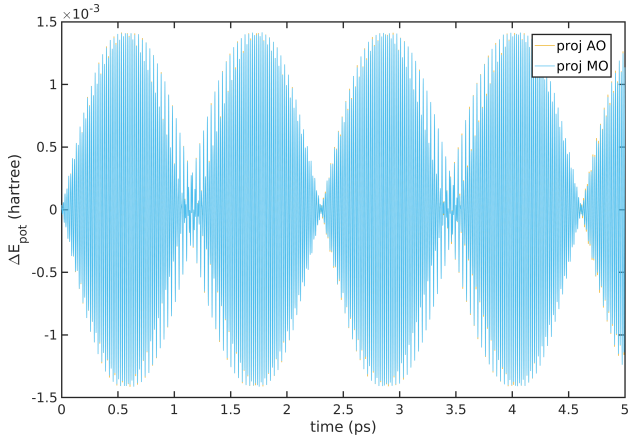
At the smallest (0.1 fs) time step, the Li–F stretching frequency estimated by ADMP at the B3LYP/6-31G(d,p) level is close to the calculated BOMD



Default *vs.* scalar *vs.* proj AO *vs.* Hessian.

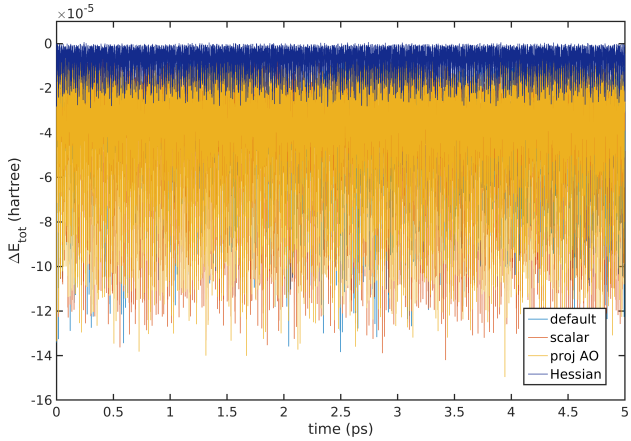


Proj *vs.* proj/energy *vs.* proj/radius AO.

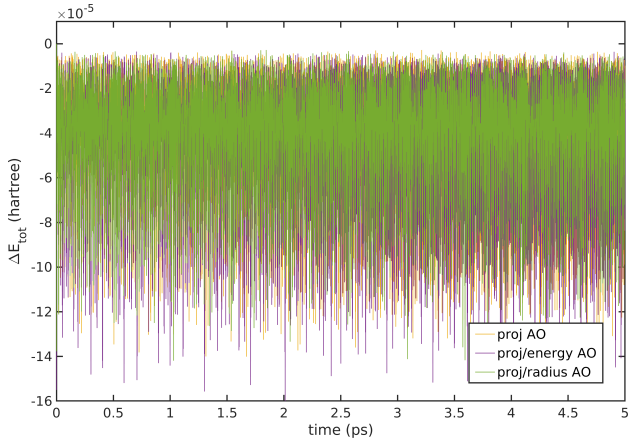


Proj AO *vs.* proj MO.

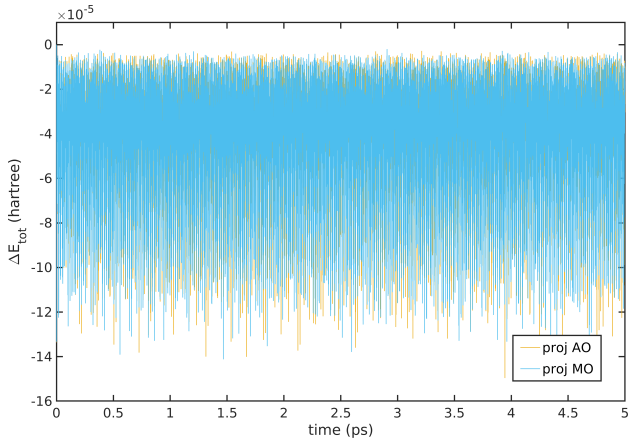
Figure 3.4: LiF B3LYP/6-31G(d,p) ADMP – BOMD (ts = 0.1 fs) E_{pot} deviations.



Default *vs.* scalar *vs.* proj AO *vs.* Hessian.

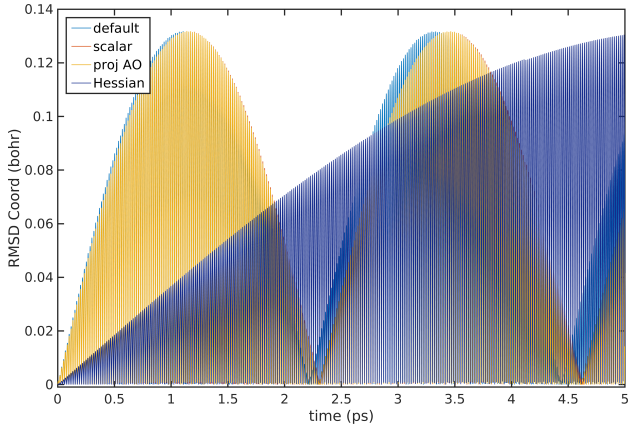


Proj *vs.* proj/energy *vs.* proj/radius AO.

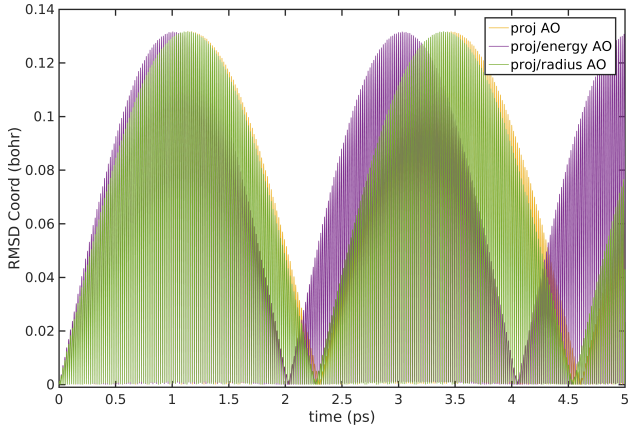


Proj AO *vs.* proj MO.

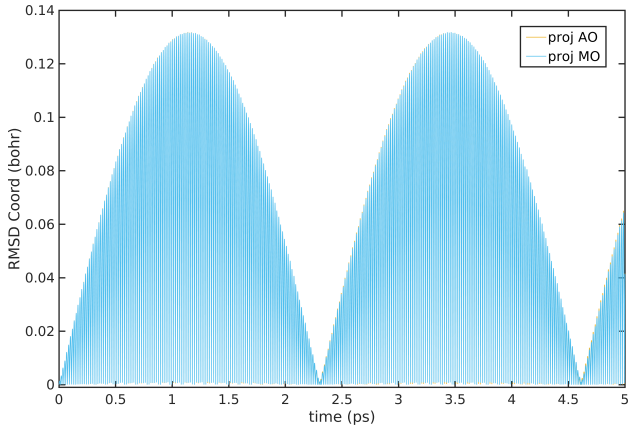
Figure 3.5: LiF B3LYP/6-31G(d,p) ADMP – BOMD (ts = 0.1 fs) $E_{\mathrm{tot,real}}$ deviations.



Default *vs.* scalar *vs.* proj AO *vs.* Hessian.

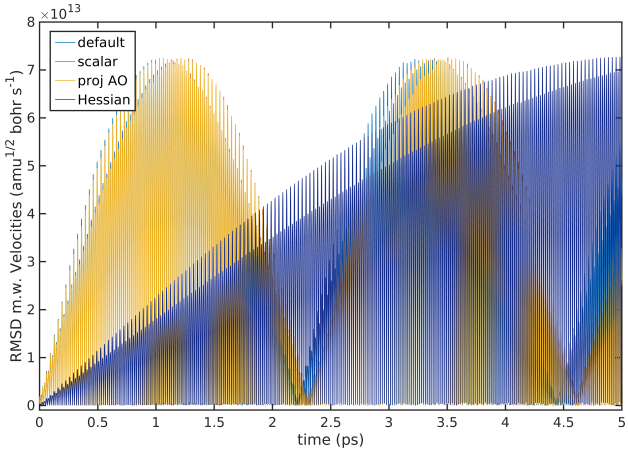


Proj *vs.* proj/energy *vs.* proj/radius AO.

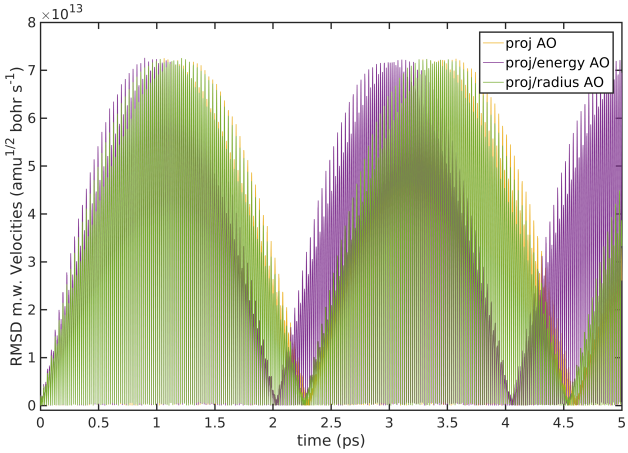


Proj AO *vs.* proj MO.

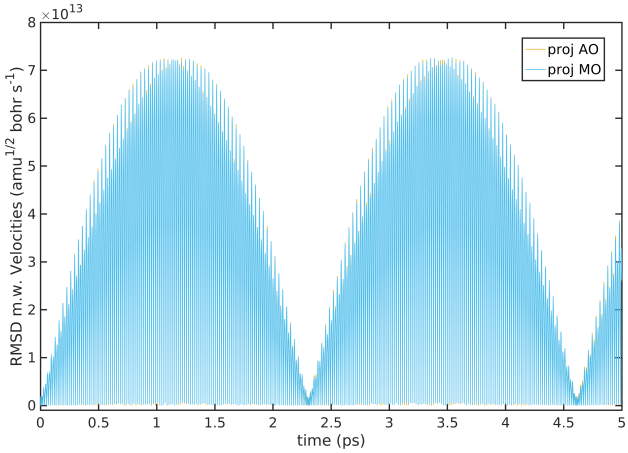
Figure 3.6: LiF B3LYP/6-31G(d,p) ADMP – BOMD (ts = 0.1 fs) RMSD of nuclear coordinates.



Default *vs.* scalar *vs.* proj AO *vs.* Hessian.



Proj *vs.* proj/energy *vs.* proj/radius AO.



Proj AO *vs.* proj MO.

Figure 3.7: LiF B3LYP/6-31G(d,p) ADMP – BOMD (ts = 0.1 fs) RMSD of mass-weighted nuclear velocities.

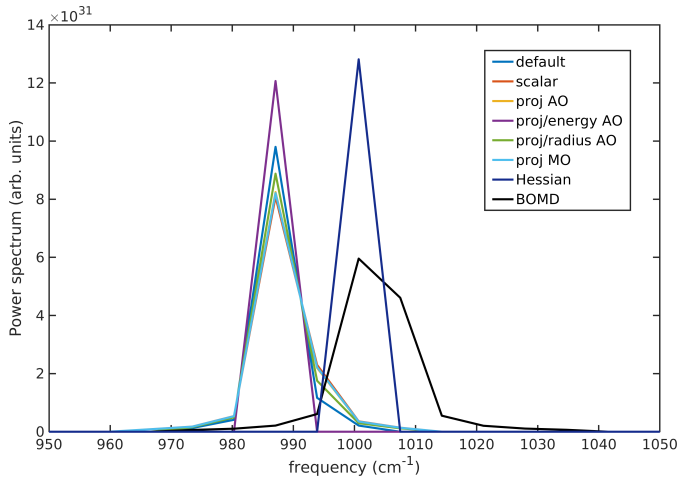


Figure 3.8: Li–F stretching band from LiF B3LYP/6-31G(d,p) BOMD and ADMP simulations (ts = 0.1 fs).

value, regardless of the weighting scheme (Fig. 3.8 and Table 3.5). While a $-14\,\mathrm{cm}^{-1}$ error is produced by the current and the projection-based approaches, the Hessian-based method predicts instead the same stretching frequency (within the frequency domain resolution) of the BOMD simulation. The relative nuclear kinetic energy deviation achieved by such scheme is in fact only about 1%, as a result of a very high ADMP adiabaticity (Table 3.6). The proj-based and the default schemes keep the ts = 0.1 fs deviations also with ts = 0.2 fs. The Hessian method still ensures the lowest ($-7\,\mathrm{cm}^{-1}$) deviation, despite being now not zero anymore. Remarkably, the proj schemes still show a $-14\,\mathrm{cm}^{-1}$ $\Delta\nu$ further increasing the time step to 0.3 fs, proving more accurate than the Hessian-based approach ($-20\,\mathrm{cm}^{-1}$). The default one leads instead to a higher error ($-28\,\mathrm{cm}^{-1}$). With the biggest (0.4 fs) time step, increased deviations from the BOMD frequency are instead obtained for all the schemes, demonstrating a significant ($> 10\%$) nuclear kinetic energy decrease.

The distribution of ADMP LiF B3LYP/6-31G(d,p) (ts = 0.1 fs) fictitious electronic frequencies is quite similar among the current and the proj-based weighting schemes (located in the 7500 – $20\,000\,\mathrm{cm}^{-1}$ range, around $\sim 16\,000\,\mathrm{cm}^{-1}$), but clearly displaced towards higher frequencies

Table 3.5: Deviations $\Delta\nu$ (in cm^{-1}) of ADMP B3LYP/6-31G(d,p) Li–F stretching frequency from the BOMD reference value. The experimental $LiF_{(g)}$ band position [66] and the results from harmonic and anharmonic static vibrational calculations are also reported.

LiF B3LYP/6-31G(d,p): vibrational spectrum				
experimental	harmonic	anharmonic	BOMD	
906	1010	990	1001	ν(Li–F) (cm^{-1})

LiF B3LYP/6-31G(d,p): ADMP - BOMD $\Delta\nu$ deviations					
	Time Step (fs)				
	0.1	0.2	0.3	0.4	
default	-14	-14	-28	-41	ν(Li–F) (cm^{-1})
scalar	-14	-41			
proj AO	-14	-14	-14	-34	
proj/energy AO	-14	-14	-14	-34	
proj/radius AO	-14	-14	-14	-34	
proj MO	-14	-14	-14	-28	
Hessian	0	-7	-20	-54	

Table 3.6: Relative deviations of LiF B3LYP/6-31G(d,p) ADMP average nuclear kinetic energy from the BOMD (ts = 0.1 fs) value at the same level of theory.

LiF B3LYP/6-31G(d,p): ADMP - BOMD $\Delta\langle E_{k,R}\rangle$				
	Time Step (fs)			
	0.1	0.2	0.3	0.4
default	-5.9%	-5.9%	-11.3%	-16.6%
scalar	-5.9%	-16.7%		
proj AO	-5.7%	-5.8%	-7.3%	-13.3%
proj/energy AO	-6.5%	-6.4%	-7.6%	-13.5%
proj/radius AO	-5.8%	-5.8%	-7.4%	-13.4%
proj MO	-5.7%	-5.7%	-6.1%	-11.4%
Hessian	-1.1%	-4.6%	-10.1%	-21.0%

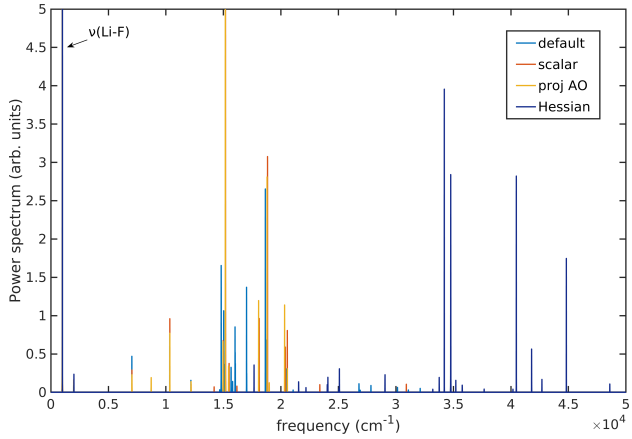
Table 3.7: Fictitious electronic frequencies distribution in LiF B3LYP/6-31G(d,p) ADMP simulations (ts = 0.1 fs). ν_{el} is reported as: wght. average (bandwidth).

LiF B3LYP/6-31G(d,p): fictitious electronic frequencies			
	$\nu_{\mathrm{el}}\,(\mathrm{cm}^{-1})$	$\nu_{el} - \nu_N\,(\mathrm{cm}^{-1})$	τ_N/τ_{el}
default	16335 (7517)	6052	7.13
scalar	16527 (6867)	6059	7.14
proj AO	16328 (5694)	6059	7.14
proj/energy AO	15307 (6291)	5500	6.57
proj/radius AO	16069 (6390)	6004	7.08
proj MO	16002 (6921)	6059	7.14
Hessian	36371 (9470)	16665	17.65

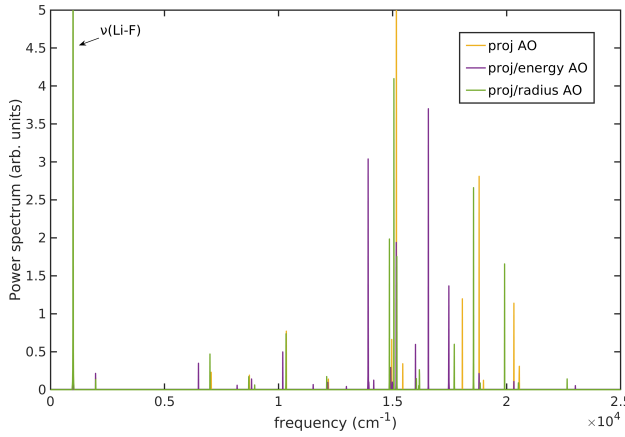
(from 18 000 to 50 000 cm^{-1}, around 36 000 cm^{-1}) for the Hessian-based approach (Fig. 3.9 and Table 3.7). Consequently, a good separation between nuclear and electronic time-scales is obtained, finding in particular for the latter method the lowest electronic frequencies $\sim$ 17 000 cm^{-1} above Li–F stretching frequency. The spectral distribution by the proj/energy AO scheme appears slightly red-shifted with respect to the other projection-based approaches, also resulting in a lower electronic/nuclear spectral distance (5500 cm^{-1}). Nevertheless, the observed adiabaticity does not seem to be affected (Table 3.3).

3.2.2 LiF ADMP test simulations: summary

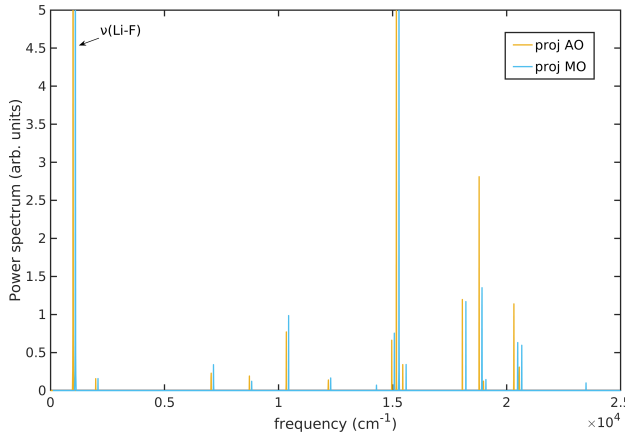
Test simulations carried out on $\mathrm{LiF}_{(g)}$ diatomic at the B3LYP/6-31G(d,p) level reveal that the Hessian-based scheme allows a reduced error with respect to the BO reference trajectory at the 0.1 and 0.2 fs time steps. A bigger (0.3 fs) time step appears moreover now feasible, if combined with projection-based mass-weighting schemes, which limit the deviation better



Default *vs.* scalar *vs.* proj AO *vs.* Hessian.



Proj *vs.* proj/energy *vs.* proj/radius AO.



Proj AO *vs.* proj MO.

Figure 3.9: Fictitious electronic dynamics from LiF B3LYP/6-31G(d,p) ADMP simulations (ts = 0.1 fs). The label indicates the Li–F stretching band.

than the currently available and the Hessian ones.

3.3 N-methylacetamide (NMA)

Trans-N-methylacetamide (NMA) is a popular model compound of the peptide bond found in proteins and polypeptides.

A preliminary NVT ($T = 300\,\mathrm{K}$) equilibration step was carried out for 10 ps. Velocity rescaling was applied every 100 fs to keep the temperature constant. Then 5 ps production trajectories were collected employing both the ADMP and BOMD methods.

3.3.1 B3LYP/6-31G(d,p) level of theory.

μ^{val} and f^{cr} optimal values for NMA B3LYP/6-31G(d,p) ADMP simulations are reported in Table 3.8. The high values of $\|\boldsymbol{\mu}\|_F$ shown by the default scheme reflect the high inertia given to the 1s core orbitals. Low mass parameters (μ^{val} and, for the projection-based schemes, f^{cr}) can be used along with the smallest time steps. Only the scalar scheme requires a $0.2\,\mathrm{amu\,bohr}^2$ mass for ts = 0.2 fs. Morever, such scheme appears unable to run a stable trajectory for ts $\geq$ 0.3 fs. With ts = 0.3 fs, the proj AO schemes can still employ a low ($0.1\,\mathrm{amu\,bohr}^2$) valence mass, but with higher f^{cr}. The proj MO one, instead, relies on a doubled ($0.2\,\mathrm{amu\,bohr}^2$, like the default scheme) μ^{val}, but a lower f^{cr}, achieving a smaller $\|\boldsymbol{\mu}\|_F$. The highest (0.4 fs) time step requires an increased mass for all the tested approaches. The imposed frequency in the Hessian-based method is high ($95\,000\,\mathrm{cm}^{-1}$) with a 0.1 fs time step, but swiftly decaying with the time step increase.

Time-domain analysis.

At ts = 0.1 fs, the Hessian-based scheme ensures the highest adiabaticity, standing out on the other methods. The $E_{k,R}/E_{k,P}$ kinetic energy ratio acquires a mean value of about 140 (Table 3.9), oscillating between 120 and 160 (Fig. 3.10). At the same time, the $\|[\boldsymbol{F}, \boldsymbol{P}]\|$ norm appears to be smaller (~ 0.016 hartree) and more constant along the simulation (Fig. 3.11). No clear differences can be observed among the other tested approaches, which all ensure a sufficiently high adiabaticity. An $E_{k,R}/E_{k,P}$ ratio roughly

Table 3.8: Mass parameters and norm of $\boldsymbol{\mu}$ matrix employed for NMA B3LYP/6-31G(d,p) ADMP simulations.

NMA B3LYP/6-31G(d,p) (N_b: 110): ADMP mass parameters					
	Time Step (fs)				
	0.1	0.2	0.3	0.4	
default	–, 0.1 13.06	–, 0.1 13.06	–, 0.2 26.12	–, 0.3 39.18	f^{cr}, μ^{val} (amu bohr^2) / $\tilde{\nu}$ (cm^{-1}) $\|\boldsymbol{\mu}\|_F$ (amu bohr^2)
scalar	–, 0.1 1.05	–, 0.2 2.10			
proj AO	2, 0.1 1.12	6, 0.1 1.69	44, 0.1 9.89	32, 0.2 14.46	
proj/energy AO	2, 0.1 1.18	3, 0.1 1.35	28, 0.1 8.23	17, 0.2 10.12	
proj/radius AO	2, 0.1 1.14	4, 0.1 1.44	30, 0.1 7.62	22, 0.2 11.26	
proj MO	2, 0.1 1.12	6, 0.1 1.69	8, 0.2 4.12	10, 0.3 7.38	
Hessian	95000 0.46	45000 2.03	25000 6.59	20000 10.30	

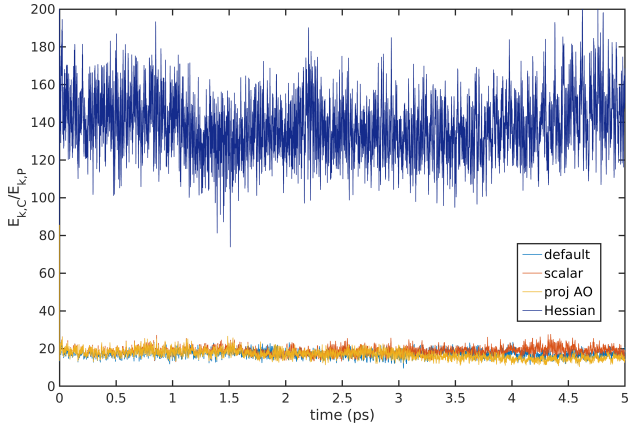
between 15 and 20 (on average, 17-18 for the default and the projection-based methods and 19 for the scalar one) is found. Moreover, a similar $\|[\boldsymbol{F}, \boldsymbol{P}]\|$ norm (~ 0.025 hartree) is obtained, except for the default scheme, displaced at higher (~ 0.035 hartree) values and also characterized by a clearer drift.

A time step increase from 0.1 to 0.2 fs does not affect the default and proj-schemes $E_{k,R}/E_{k,P}$ ratio, only inducing a 0.01 hartree increase in the $\|[\boldsymbol{F}, \boldsymbol{P}]\|$ norm. Despite a relevant $E_{k,R}/E_{k,P}$ decrease, the Hessian scheme is still offering the highest adiabaticity ($E_{k,R}/E_{k,P} = 31$). Distinct behaviors between the original default scheme and the proj AO ones are instead observed at ts = 0.3 fs. In particular, the latter show $E_{k,R}/E_{k,P} > 10$ ratios, even for this high time step, due to the capability to still employ a small (0.1 amu bohr^2, Table 3.8) valence mass. The differences among the mass-weighting approaches are instead greatly reduced with the highest (0.4 fs) time step. No scheme appears in fact able to give completely satisfactory adiabaticity performances.

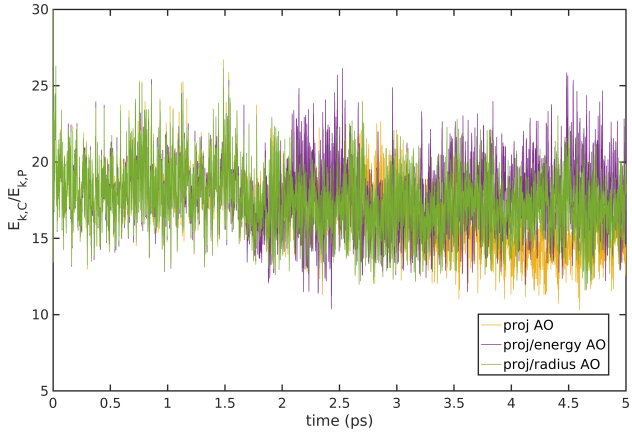
Comparing the NMA B3LYP/6-31G(d,p) ADMP test trajectories (ts = 0.1 fs) with the reference BOMD one, all of them are, on average, close to the BO PES, regardless the chosen mass-weighting scheme (Fig. 3.12 and Table 3.10). E_{pot} from the scalar scheme simulation is slightly displaced by ~ -0.001 hartree. ADMP E_{real} deviation by the Hessian approach (on average -8×10^{-5} hartree) is clearly lower by an order of magnitude (and also with reduced oscillations) than the other schemes, due to the higher abiabaticity and so an $E_{k,R}$ closer to the BOMD one. A slightly lower deviation is given by the proj/energy AO scheme among the new proj-based approaches (Fig. 3.13). Coordinates deviations are quite comparable, ranging from 1.2 (Hessian) to 2 bohr (scalar and proj MO) (Fig. 3.14). Mass-weighted velocities deviations are even more similar among all the tested approaches (Fig. 3.15).

Frequency-domain analysis.

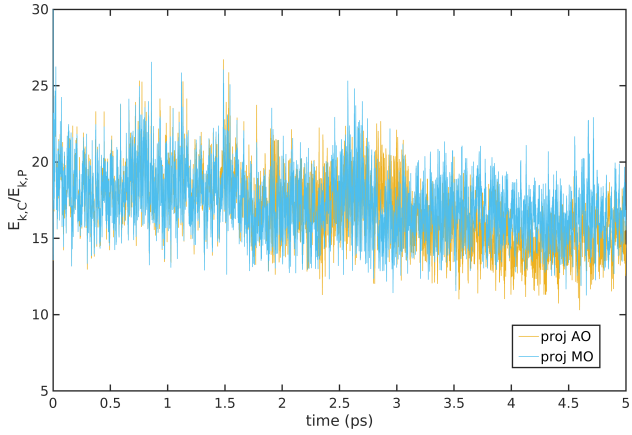
NMA vibrational dynamics produced by the ADMP test simulations at the B3LYP/6-31G(d,p) level has been compared with that from the reference



Default *vs.* scalar *vs.* proj AO *vs.* Hessian.

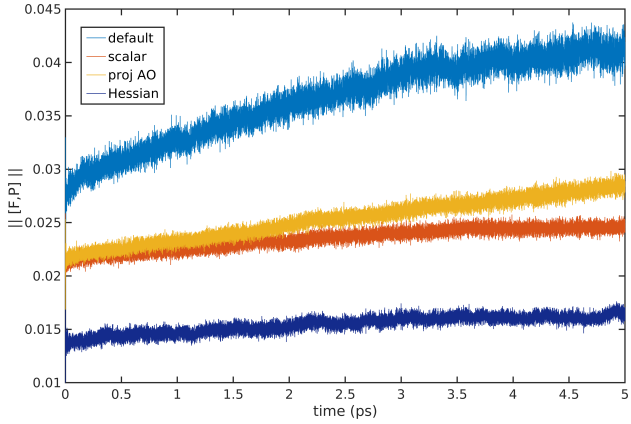


Proj *vs.* proj/energy *vs.* proj/radius AO.

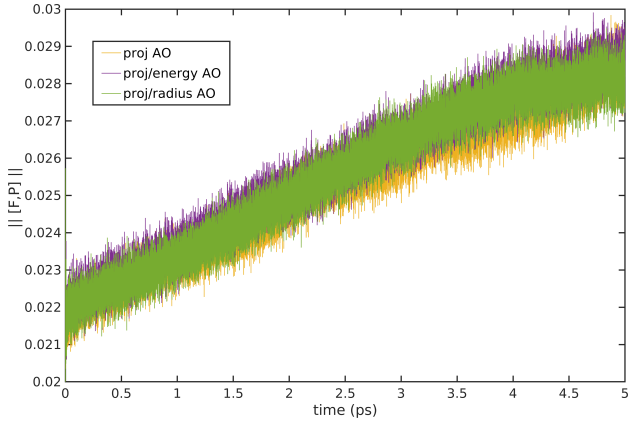


Proj AO *vs.* proj MO.

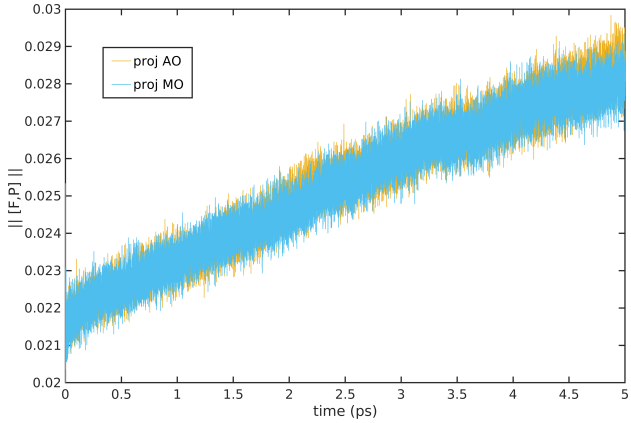
Figure 3.10: NMA B3LYP/6-31G(d,p) ADMP (ts = 0.1 fs) simulations: $E_{k,R}/E_{k,P}$ ratio.



Default *vs.* scalar *vs.* proj AO *vs.* Hessian.



Proj *vs.* proj/energy *vs.* proj/radius AO.

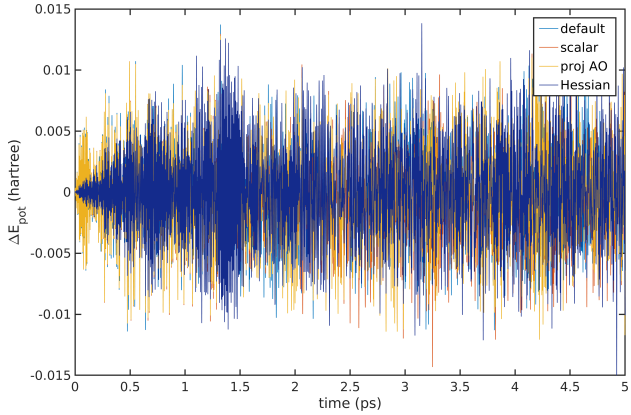


Proj AO *vs.* proj MO.

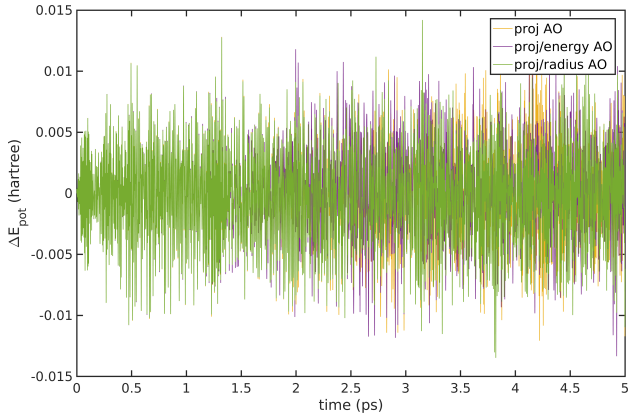
Figure 3.11: NMA B3LYP/6-31G(d,p) ADMP (ts = 0.1 fs) simulations: $\|[\boldsymbol{F}, \boldsymbol{P}]\|$ commutator norm.

Table 3.9: NMA B3LYP/6-31G(d,p) ADMP simulations; adiabaticity indicators. $E_{k,R}/E_{k,P}$, $\|[\boldsymbol{F},\boldsymbol{P}]\|$ and $|d\mathcal{H}_{\text{fict}}/dt|$ parameters are reported as: average (st.dev.).

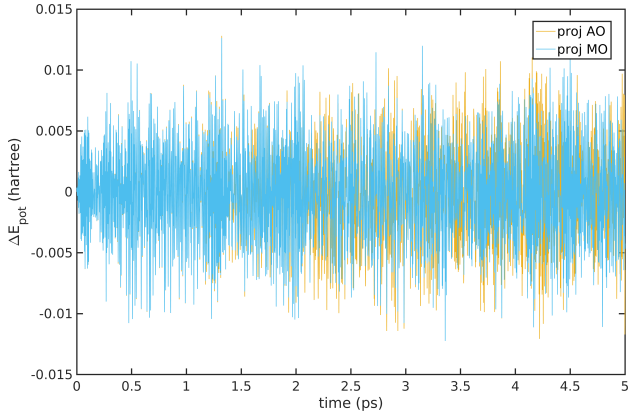
NMA B3LYP/6-31G(d,p): ADMP adiabaticity					
	Time Step (fs)				
	0.1	0.2	0.3	0.4	
default	17 (2)	18 (2)	7 (1)	3.9 (0.9)	$E_{k,R}/E_{k,P}$
	3.7 (0.4)	3.9 (0.4)	6.3 (0.9)	9 (2)	$\|[\boldsymbol{F},\boldsymbol{P}]\|$ ($\cdot 10^{-2}$ Ha)
	9 (3)	40 (8)	50 (10)	80 (30)	$\|d\mathcal{H}_{\text{fict}}/dt\|$ ($\cdot 10^{-5}$ Ha fs^{-1})
	(7)	(9)	(20)	(20)	$s(E_{\text{tot}})$ ($\cdot 10^{-5}$ Ha)
scalar	19 (2)	1.6 (0.6)			
	2.4 (0.1)	459 (2)			
	11 (3)	2523 (5)10^2			
	(30)	(6000)			
proj AO	17 (2)	17 (2)	12 (1)	5 (1)	
	2.5 (0.2)	3.5 (0.2)	5.5 (0.5)	8 (1)	
	12 (4)	49 (9)	80 (10)	90 (30)	
	(10)	(8)	(20)	(50)	
proj/energy AO	18 (2)	17 (2)	13 (2)	6.3 (0.9)	
	2.6 (0.2)	3.6 (0.2)	5.5 (0.6)	7.7 (0.9)	
	12 (4)	50 (10)	110 (30)	100 (20)	
	(10)	(9)	(10)	(30)	
proj/radius AO	17 (2)	17 (2)	13 (2)	5.6 (0.9)	
	2.6 (0.2)	3.7 (0.2)	5.8 (0.6)	8 (1)	
	12 (4)	60 (10)	140 (30)	100 (30)	
	(20)	(9)	(9)	(20)	
proj MO	17 (2)	17 (2)	7.7 (0.9)	4.1 (0.9)	
	2.5 (0.2)	3.4 (0.2)	5.4 (0.5)	8 (1)	
	12 (4)	50 (10)	60 (10)	90 (30)	
	(9)	(20)	(20)	(40)	
Hessian	140 (10)	31 (3)	9 (1)	5.2 (0.7)	
	1.55 (0.08)	3.2 (0.2)	5.6 (0.3)	7.9 (0.7)	
	69 (7)	54 (7)	32 (7)	40 (10)	
	(1)	(6)	(10)	(20)	



Default *vs.* scalar *vs.* proj AO *vs.* Hessian.

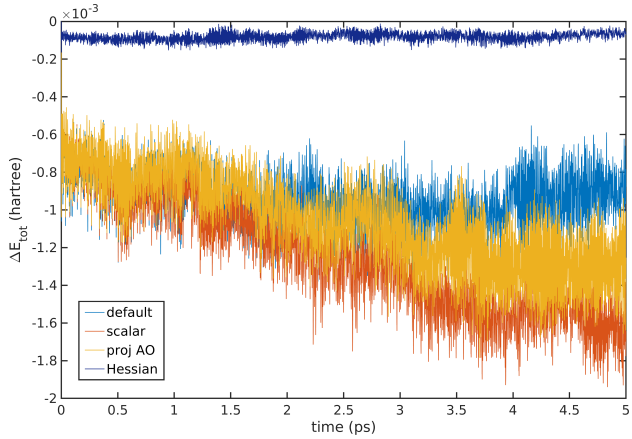


Proj *vs.* proj/energy *vs.* proj/radius AO.

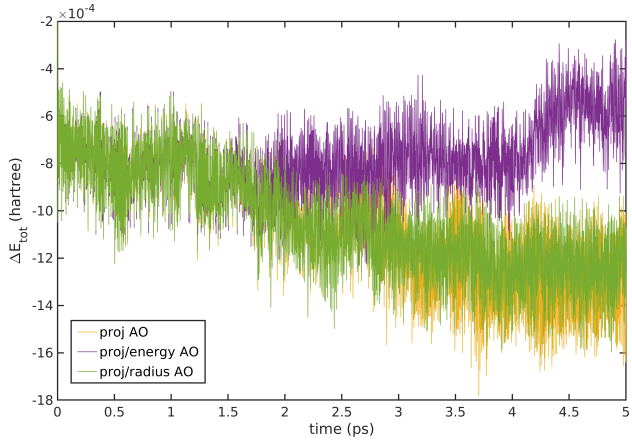


Proj AO *vs.* proj MO.

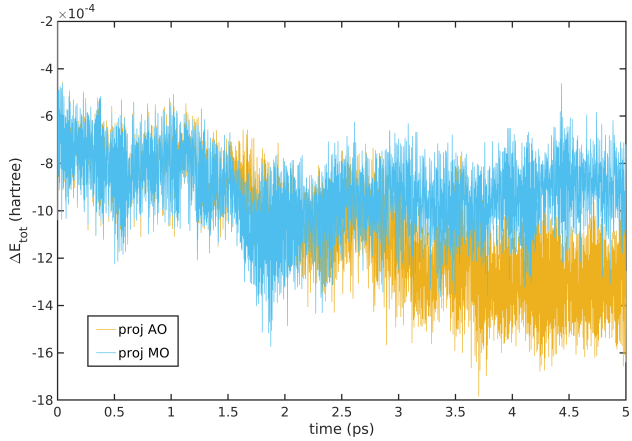
Figure 3.12: NMA B3LYP/6-31G(d,p) ADMP – BOMD (ts = 0.1 fs) E_{pot} deviations.



Default *vs.* scalar *vs.* proj AO *vs.* Hessian.

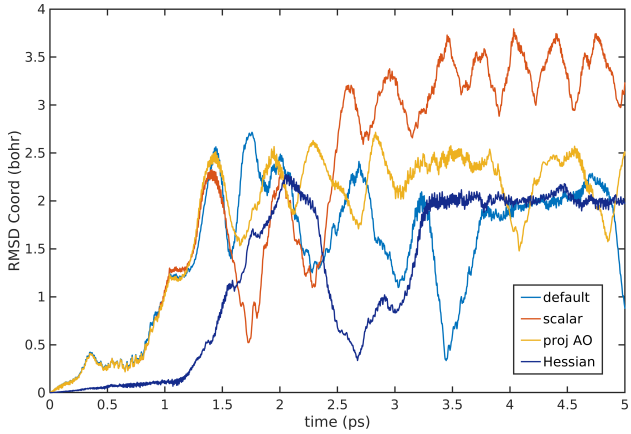


Proj *vs.* proj/energy *vs.* proj/radius AO.

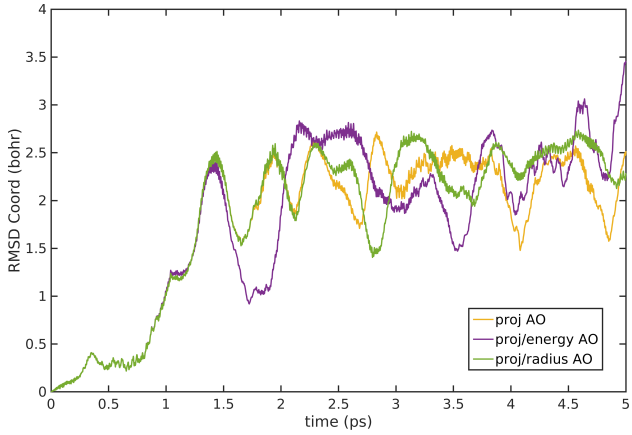


Proj AO *vs.* proj MO.

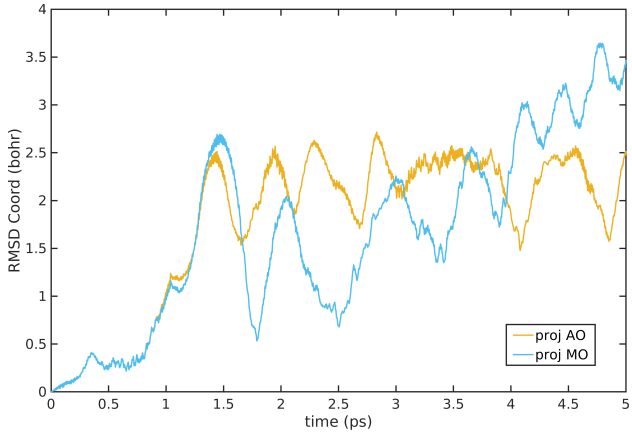
Figure 3.13: NMA B3LYP/6-31G(d,p) ADMP – BOMD (ts = 0.1 fs) $E_{\mathrm{tot,real}}$ deviations.



Default *vs.* scalar *vs.* proj AO *vs.* Hessian.

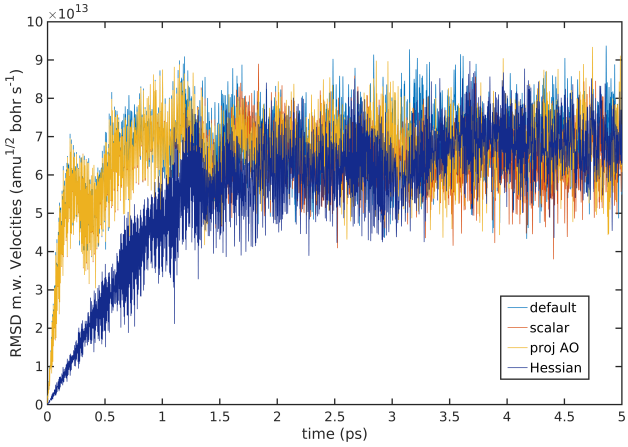


Proj *vs.* proj/energy *vs.* proj/radius AO.

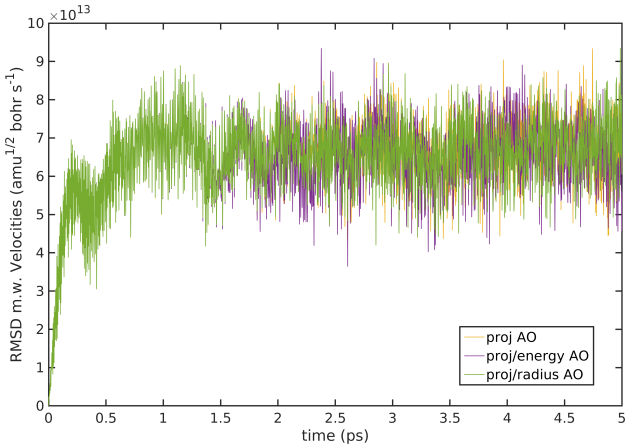


Proj AO *vs.* proj MO.

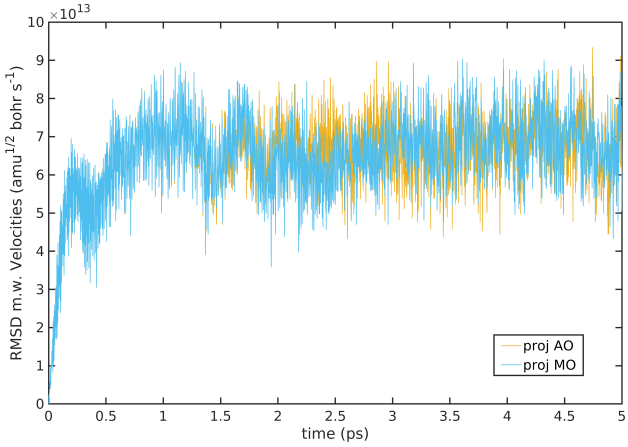
Figure 3.14: NMA B3LYP/6-31G(d,p) ADMP – BOMD (ts = 0.1 fs) RMSD of nuclear coordinates.



Default *vs.* scalar *vs.* proj AO *vs.* Hessian.



Proj *vs.* proj/energy *vs.* proj/radius AO.



Proj AO *vs.* proj MO.

Figure 3.15: NMA B3LYP/6-31G(d,p) ADMP – BOMD (ts = 0.1 fs) RMSD of mass-weighted nuclear velocities.

Table 3.10: ΔE_{pot}, ΔE_{tot}, RMSD Coor and RMSD m.w. Vel between NMA B3LYP/6-31G(d,p) ADMP test simulations and a BOMD reference trajectory (ts = 0.1 fs). Data are reported as mean (st.dev.).

NMA B3LYP/6-31G(d,p): ADMP - BOMD deviations				
	ΔE_{pot} (10^{-4} hartree)	ΔE_{tot} (10^{-5} hartree)	RMSD Coor (10^{-2} bohr)	RMSD m.w. Vel (10^{13} amu$^{1/2}$ bohr s^{-1})
default	0 (40)	-90 (10)	150 (70)	6.8 (0.9)
scalar	-10 (30)	-130 (30)	200 (100)	6.4 (0.8)
proj AO	0 (40)	-110 (20)	180 (80)	6.6 (0.8)
proj/energy AO	0 (40)	-80 (20)	180 (90)	6.5 (0.9)
proj/radius AO	0 (40)	-110 (20)	190 (80)	6.6 (0.8)
proj MO	0 (40)	-90 (20)	200 (100)	6.6 (0.9)
Hessian	0 (40)	-8 (2)	120 (80)	6 (2)

BOMD trajectory at the same level of theory. In particular, the vibrational analysis has been focused on NMA Amide I (a C=O and C-N stretching) and Amide A (N-H stretching) bands (which, together with Amide II, are well-known protein spectroscopic features [67]).

At the smallest (ts = 0.1 fs) time step (Fig. 3.16 and Table 3.11), the clear higher accuracy given by the Hessian-based approach (a $-7\,\mathrm{cm}^{-1}$ deviation for both bands) is the direct effect of the high adiabaticity achieved (Table 3.9), implying a small $E_{k,R}$ deviation (-1%, Table 3.12) from the BOMD trajectory. The other schemes are clustered instead at lower frequencies, showing errors not lower than $-48\,\mathrm{cm}^{-1}$ for Amide I (by the proj AO, proj/radius AO and proj MO schemes) and $-82\,\mathrm{cm}^{-1}$ for Amide A. The slightly bigger Amide I red-shift by the the default scheme is probably due to the higher deviation (higher $\|[\boldsymbol{F},\boldsymbol{P}]\|$) from the BO PES (Table 3.9). Amide A deviations are higher (except with the Hessian scheme) than Amide I, probably because the Amide A vibration, involving a light H atom, is more affected by the ADMP non-complete nuclear/electronic adiabaticity than lower-frequency motions. As suggested by the adiabaticity parameters (Table 3.9), a time step increase from 0.1 to 0.2 fs does not significantly alter calculated Amide I and Amide A band positions for the default and the proj-based schemes. The Hessian approach still ensures the greatest accuracy, albeit lower than the ts = 0.1 fs simulation. Of course, the poor perfomances of the scalar scheme with such time step lead to large red-shifts with respect to the BO dynamics. At ts = 0.3 fs, Amide I deviations are just below $100\,\mathrm{cm}^{-1}$ only for the proj AO-type approaches, which show the highest kinetic energy $E_{k,R}/E_{k,P}$ ratios. The lowest Amide A red-shifts ($-144\,\mathrm{cm}^{-1}$), obtained with two of such schemes (the proj/energy and proj/radius AO), are themselves quite high. Significantly lower $E_{k,R}/E_{k,P}$ values (as those from the default and proj MO schemes) induce instead bigger errors in both the Amide I and Amide A bands. At ts = 0.4 fs, due to the low adiabaticity (Table 3.9) no ADMP mass-weighting approach can accurately reproduce the Amide bands. The lowest red-shifts (obtained with the proj/energy AO scheme, which has the highest adiabaticity) are in fact $\sim -140\,\mathrm{cm}^{-1}$ and $-240\,\mathrm{cm}^{-1}$ for Amide I and Amide A, respectively. Again, Amide A seems

more sensitive to the adiabaticity degree than Amide I.

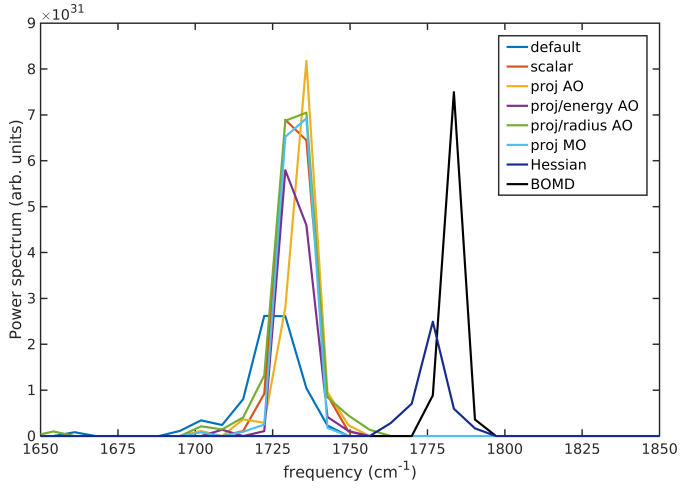
A continuous band describes the spectrum of NMA ADMP B3LYP/6-31G(d,p) fictitious electronic dynamics (ts = 0.1 fs) (Fig. 3.17). The distributions from the current and the new projection-based approaches appear largely comparable, roughly confined in the 10 000 – 40 000 cm^{-1} range and centered around 21 000 cm^{-1} (Table 3.13). The fictitious electronic dynamics from the Hessian-based approach spans instead the wider 30 000 – 90 000 cm^{-1} interval, being therefore located at much higher frequencies ($\sim$ 55 000 cm^{-1} on average). The significantly higher distance ($\sim$ 23 000 cm^{-1}) between the lowest electronic frequencies and the highest nuclear fundamental vibration (i.e., the Amide A) justifies the high $E_{k,R}/E_{k,P}$ ratio found for the Hessian approach (Table 3.9). The other schemes show instead a smaller ($\sim$ 5000 cm^{-1}) distance, which nevertheless seems to ensure a sufficient adiabaticity.

3.3.2 B3LYP/6-311G(d,p) level of theory.

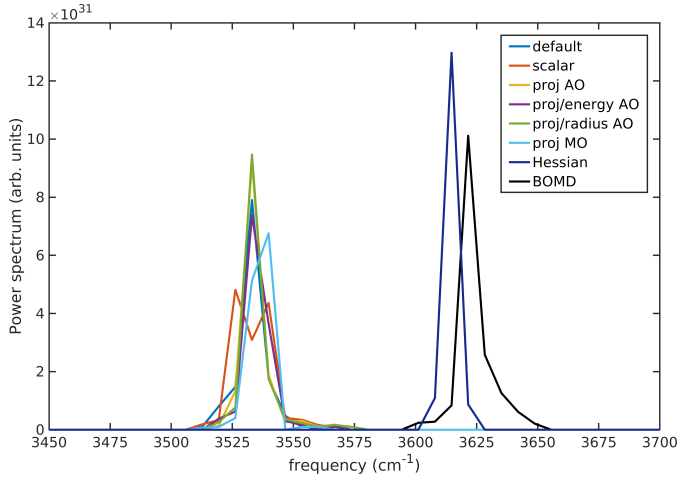
If the triple-zeta 6-311G(d,p) basis set is employed, the default method appears unable to run NMA ADMP simulations with any ts $\geq$ 0.1 fs (Table 3.14). Moreover, the scalar approach requires a 0.2 amu $bohr^2$ valence mass to get a stable propagation with ts = 0.1 fs. The projection-based AO methods can use instead small values of both μ^{val} (0.1 amu $bohr^2$) and f^{cr}. The proj MO approach, nevertheless, also requires a doubled valence mass. The highest frequency allowed by the Hessian-based method (65 000 cm^{-1}) is lower than the corresponding one with the double-zeta basis. The higher (ts = 0.2 fs) time step can be employed with only the proj AO-type schemes, which however require both an increased μ^{val} valence mass and quite high f^{cr} values, and the Hessian one, with a rather low target frequency.

Time-domain analysis.

With the smaller (0.1 fs) time step, the adiabaticity performances by the Hessian scheme are noticeably high ($E_{k,R}/E_{k,P} = 42$, $\|[\boldsymbol{F}, \boldsymbol{P}]\| \approx 0.02$ hartree, Figs. 3.18 and 3.19 and Table 3.15), suggesting accurate results also for a



Amide I



Amide A

Figure 3.16: Amide I and Amide A vibrational bands from NMA B3LYP/6-31G(d,p) BOMD and ADMP simulations (ts = 0.1 fs).

Table 3.11: Deviations $\Delta\nu$ (in cm^{-1}) of ADMP B3LYP/6-31G(d,p) NMA Amide I and Amide A stretching frequencies from the BOMD reference values. Results from harmonic and anharmonic static vibrational calculations, as well as the experimental gas-phase band positions [68], are also reported.

NMA B3LYP/6-31G(d,p): vibrational spectrum				
experimental	harmonic	anharmonic	BOMD	
1713, 1731	1789	1759	1784	Amide I (cm^{-1})
3490	3658	3484	3622	Amide A (cm^{-1})

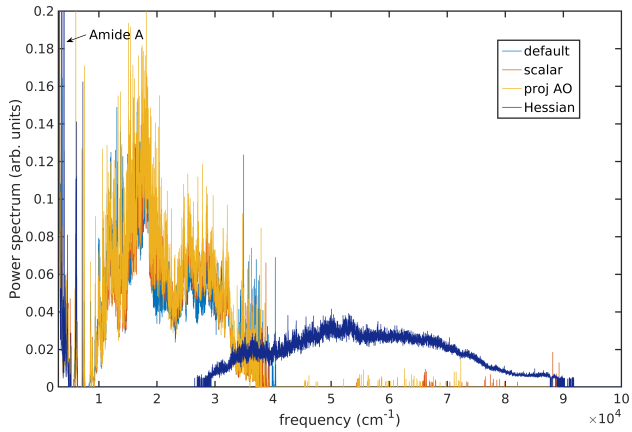
NMA B3LYP/6-31G(d,p): ADMP - BOMD $\Delta\nu$ deviations					
	Time Step (fs)				
	0.1	0.2	0.3	0.4	
default	-62	-62	-109	-164	Amide I (cm^{-1})
	-89	-82	-184	-273	Amide A (cm^{-1})
scalar	-55	-191			
	-96, -82	-457			
proj AO	-48	-55	-96	-145	
	-89	-89	-178	-302	
proj/energy AO	-55	-55	-96	-137	
	-89	-89	-144	-239	
proj/radius AO	-48	-48	-89	-143	
	-89	-82	-144	-259	
proj MO	-48	-48	-103	-143	
	-82	-82	-178	-266	
Hessian	-7	-34	-109	-163	
	-7	-41	-164	-252	

Table 3.12: Relative deviations of NMA B3LYP/6-31G(d,p) ADMP average nuclear kinetic energy from the BOMD (ts = 0.1 fs) value at the same level of theory.

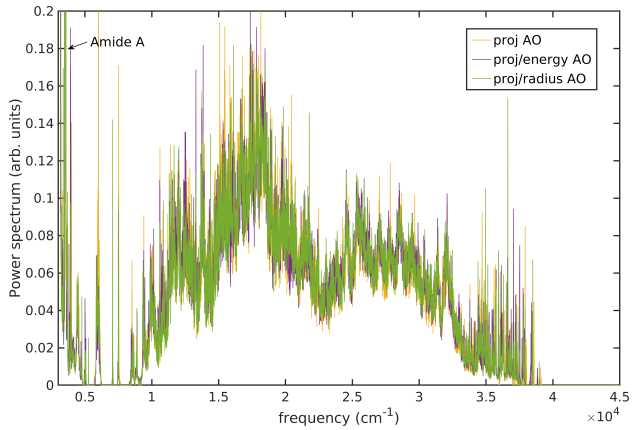
NMA B3LYP/6-31G(d,p): ADMP - BOMD $\Delta\langle E_{k,R}\rangle$				
	Time Step (fs)			
	0.1	0.2	0.3	0.4
default	-4.3%	-2.7%	-12.9%	-19.5%
scalar	-4.6%	228.0%		
proj AO	-5.9%	-6.3%	-6.7%	-19.7%
proj/energy AO	-5.6%	-6.5%	-4.8%	-13.5%
proj/radius AO	-5.7%	-6.3%	-7.7%	-16.1%
proj MO	-5.6%	-6.6%	-10.3%	-16.9%
Hessian	-1.0%	-2.8%	-9.2%	-14.5%

Table 3.13: Fictitious electronic frequencies distribution in NMA B3LYP/6-31G(d,p) ADMP simulations (ts = 0.1 fs). ν_{el} is reported as: wght. average (bandwidth).

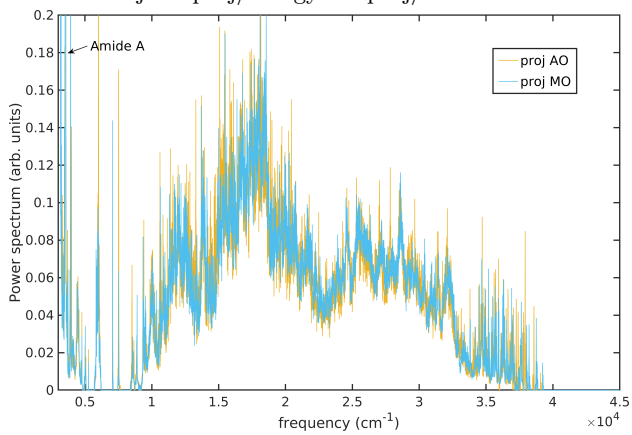
NMA B3LYP/6-31G(d,p): fictitious electronic frequencies			
	$\nu_{\mathrm{el}}\,(\mathrm{cm}^{-1})$	$\nu_{el}-\nu_N\,(\mathrm{cm}^{-1})$	τ_N/τ_{el}
default	20765 (9631)	5051	2.43
scalar	21662 (12555)	5044	2.43
proj AO	21065 (12136)	4990	2.41
proj/energy AO	21200 (13109)	4922	2.39
proj/radius AO	21463 (13912)	5004	2.42
proj MO	21086 (9867)	5004	2.41
Hessian	54757 (18102)	22887	7.33



Default *vs.* scalar *vs.* proj AO *vs.* Hessian.



Proj *vs.* proj/energy *vs.* proj/radius AO.



Proj AO *vs.* proj MO.

Figure 3.17: Fictitious electronic dynamics from NMA B3LYP/6-31G(d,p) ADMP simulations (ts = 0.1 fs). The label indicates the highest nuclear fundamental vibration.

Table 3.14: Mass parameters and norm of $\boldsymbol{\mu}$ matrix employed for NMA B3LYP/6-311G(d,p) ADMP simulations.

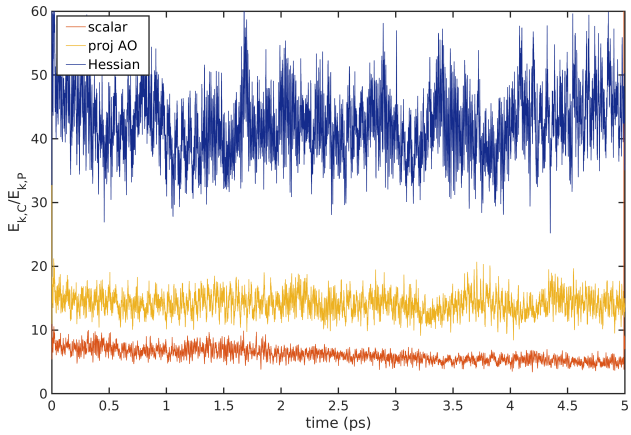
NMA B3LYP/6-311G(d,p) (N_b: 132): ADMP mass parameters			
	Time Step (fs)		
	0.1	0.2	
default			f^{cr}, μ^{val} (amu bohr^2) / $\tilde{\nu}$ (cm^{-1}) $\|\boldsymbol{\mu}\|_F$ (amu bohr^2)
scalar	–, 0.2 2.30		
proj AO	5, 0.1 1.59	26, 0.2 11.84	
proj/energy AO	3, 0.1 1.43	14, 0.2 8.47	
proj/radius AO	4, 0.1 1.51	19, 0.2 9.75	
proj MO	2, 0.2 2.42		
Hessian	65000 5.40	30000 25.36	

triple-zeta basis. Nevertheless, also the results from the proj, proj/energy and proj/radius AO approaches appear still satisfactory ($E_{k,R}/E_{k,P} = 14$, $\|[\boldsymbol{F}, \boldsymbol{P}]\| \approx 0.03$ hartree) and not so different from those obtained with the smaller basis set (Table 3.9). The $E_{k,R}/E_{k,P}$ kinetic energy ratio is instead only around 5-6 for the scalar and proj MO ones, due to the requirement of bigger fictitious mass parameters (Table 3.14). Likewise, the $\|[\boldsymbol{F}, \boldsymbol{P}]\|$ commutator norm is higher (~ 0.05 hartree) and more rapidly increasing.

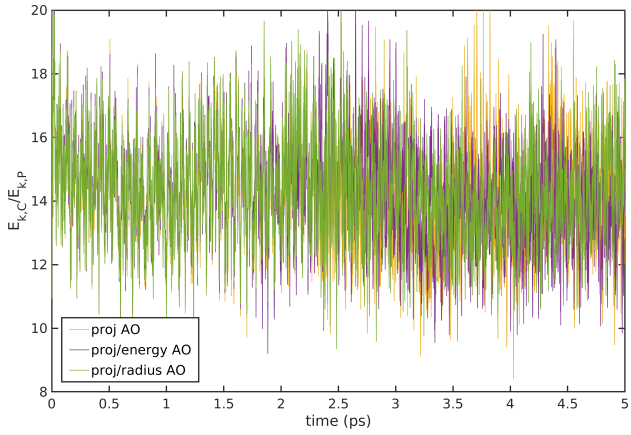
The most effective schemes at ts = 0.1 fs are moreover the only ones able to run stable trajectories with the bigger (0.2 fs) time step, but with a lower nuclear/electronic adiabaticity ($E_{k,R}/E_{k,P} = 9$ for the Hessian scheme and 4-5 for the projection-based ones).

Comparing the NMA ADMP B3LYP/6-311G(d,p) trajectories (ts = 0.1 fs) with the reference BOMD one at the same level of theory, only the sampled potential energy deviation by the Hessian approach actually oscillates around zero, while it is similar for all the other tested schemes (on average ~ -0.063 hartree, Fig. 3.20 and Table 3.16), indicating a small systematic deviation from the BOMD potential energy. Similarly, the total energy deviation obtained by the Hessian scheme is two orders of magnitude lower than the other ones. Bigger deviations (with a noticeable drift) of the total real energy can be seen in particular for the scalar and proj MO approaches, due to the lower adiabaticity perturbing the nuclear kinetic energy (Fig. 3.21). Average RMS coordinates deviations are similar and roughly between 2 and 3 bohr (Fig. 3.22). Analogously, no differences are found for RMS mass-weighted velocities deviations (about 6×10^{13} amu$^{1/2}$ bohr s^{-1}, Fig. 3.23).

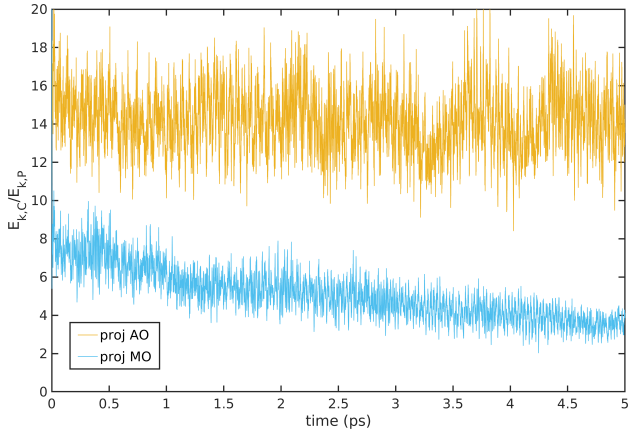
The use of a bigger 6-311G(d,p) basis determines a hundred- and a tenfold increase in ΔE_{pot} (with the notable exception of the Hessian method) and ΔE_{tot}, respectively, with respect to the double-zeta 6-31G(d,p) basis (Table 3.10).



Scalar *vs.* proj AO *vs.* Hessian.

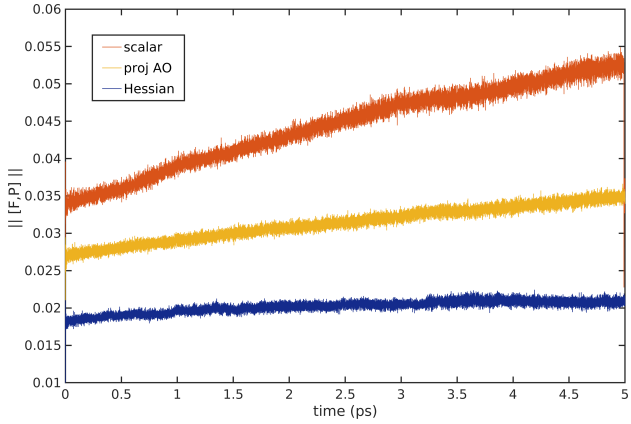


Proj *vs.* proj/energy *vs.* proj/radius AO.

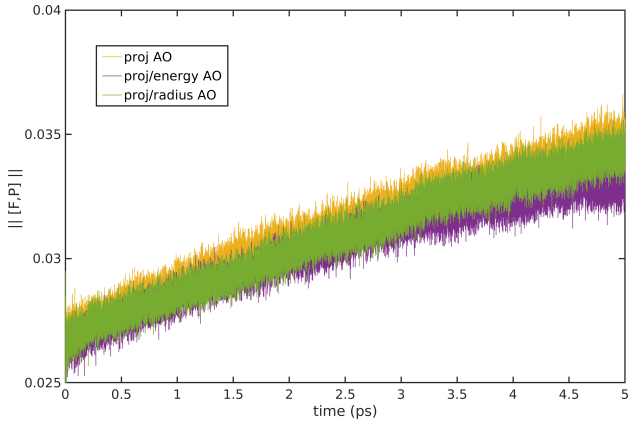


Proj AO *vs.* proj MO.

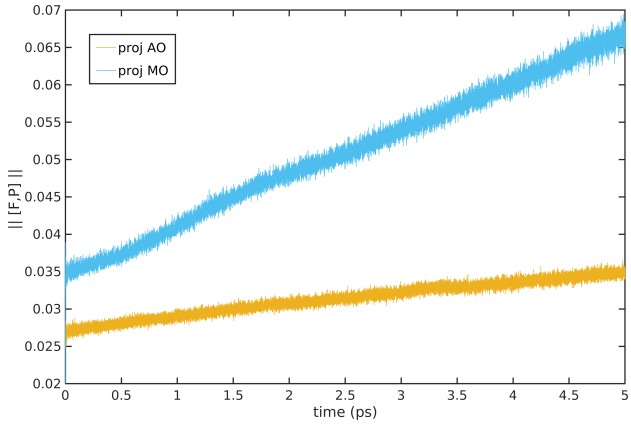
Figure 3.18: NMA B3LYP/6-311G(d,p) ADMP (ts = 0.1 fs) simulations: $E_{k,R}/E_{k,P}$ ratio.



Scalar *vs.* proj AO *vs.* Hessian.



Proj *vs.* proj/energy *vs.* proj/radius AO.

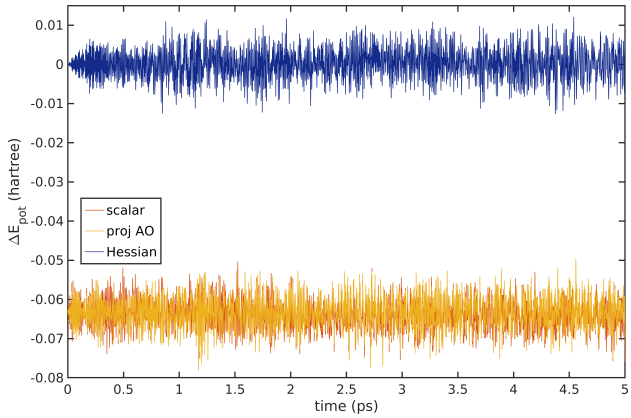


Proj AO *vs.* proj MO.

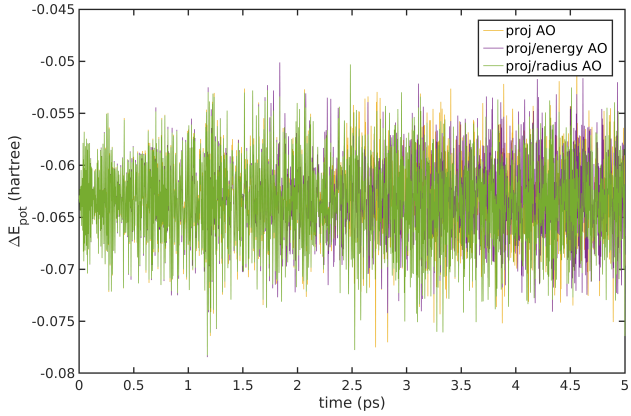
Figure 3.19: NMA B3LYP/6-311G(d,p) ADMP (ts = 0.1 fs) simulations: $\|[\boldsymbol{F}, \boldsymbol{P}]\|$ commutator norm.

Table 3.15: NMA B3LYP/6-311G(d,p) ADMP simulations; adiabaticity indicators. $E_{k,R}/E_{k,P}$, $\|[\boldsymbol{F},\boldsymbol{P}]\|$ and $|d\mathcal{H}_{\text{fict}}/dt|$ parameters are reported as: average (st.dev.).

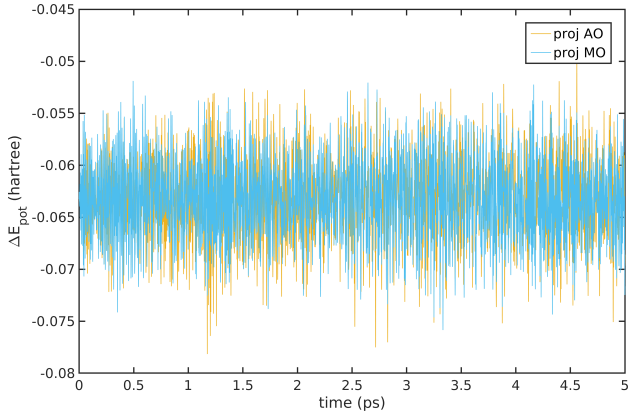
NMA B3LYP/6-311G(d,p): ADMP adiabaticity			
	Time Step (fs)		
	0.1	0.2	
default			$E_{k,R}/E_{k,P}$ $\|[\boldsymbol{F},\boldsymbol{P}]\|$ $(\cdot 10^{-2}\,\text{Ha})$ $\|d\mathcal{H}_{\text{fict}}/dt\|$ $(\cdot 10^{-5}\,\text{Ha fs}^{-1})$ $s(E_{\text{tot}})$ $(\cdot 10^{-5}\,\text{Ha})$
scalar	6 (1) 4.5 (0.5) 10 (4) (60)		
proj AO	14 (2) 3.1 (0.2) 15 (4) (10)	4 (1) 8 (2) 30 (10) (20)	
proj/energy AO	14 (2) 3.1 (0.2) 15 (4) (20)	5.2 (0.9) 7 (1) 30 (10) (30)	
proj/radius AO	14 (1) 3.1 (0.2) 15 (4) (10)	5.0 (0.9) 7 (1) 30 (10) (10)	
proj MO	5 (1) 5.1 (0.9) 13 (6) (20)		
Hessian	42 (5) 2.02 (0.08) 33 (5) (6)	9 (1) 4.3 (0.1) 24 (5) (70)	



Scalar *vs.* proj AO *vs.* Hessian.

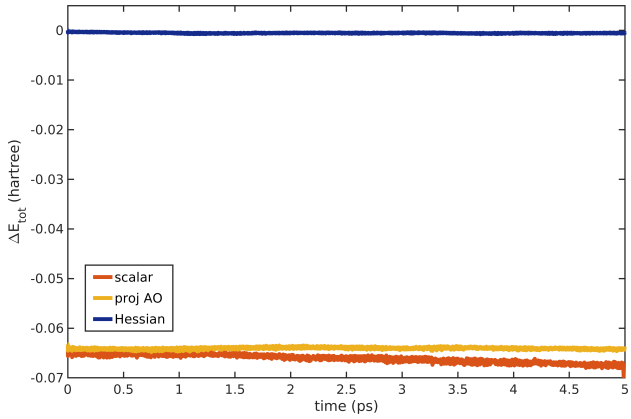


Proj *vs.* proj/energy *vs.* proj/radius AO.

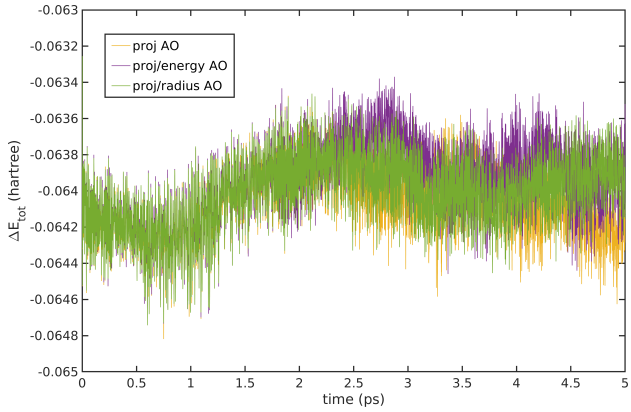


Proj AO *vs.* proj MO.

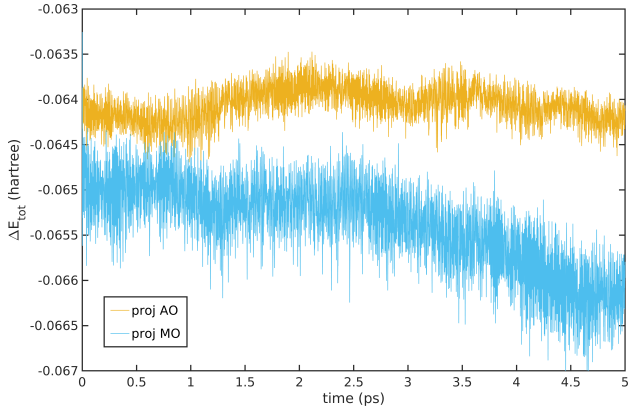
Figure 3.20: NMA B3LYP/6-311G(d,p) ADMP – BOMD E_{pot} deviations.



Scalar *vs.* proj AO *vs.* Hessian.

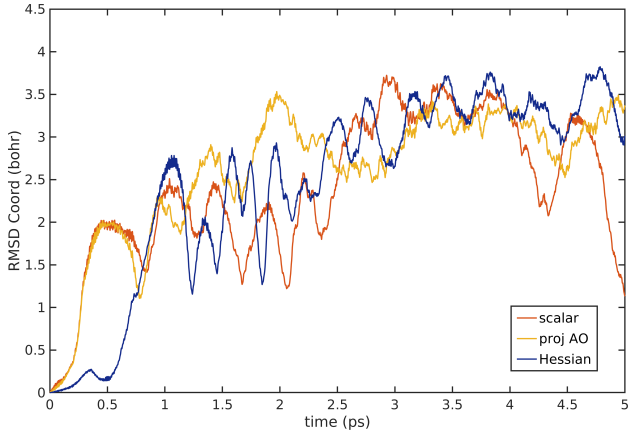


Proj *vs.* proj/energy *vs.* proj/radius AO.

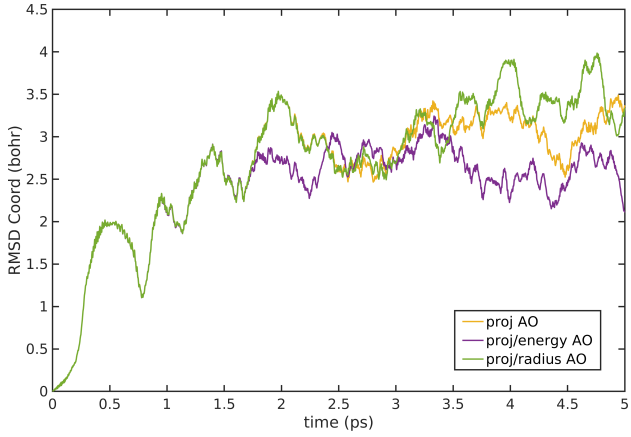


Proj AO *vs.* proj MO.

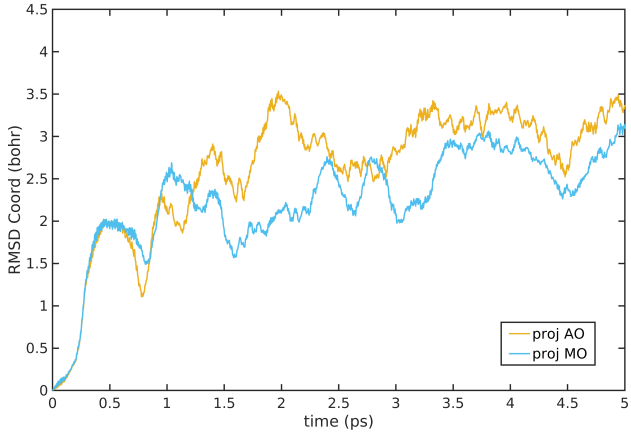
Figure 3.21: NMA B3LYP/6-311G(d,p) ADMP – BOMD $E_{\mathrm{tot,real}}$ deviations.



Scalar *vs.* proj AO *vs.* Hessian.

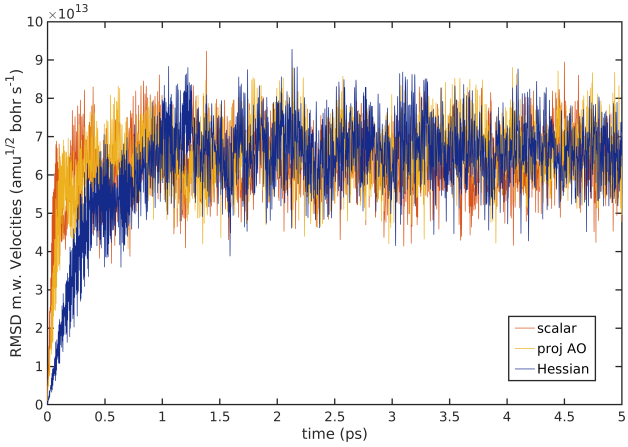


Proj *vs.* proj/energy *vs.* proj/radius AO.

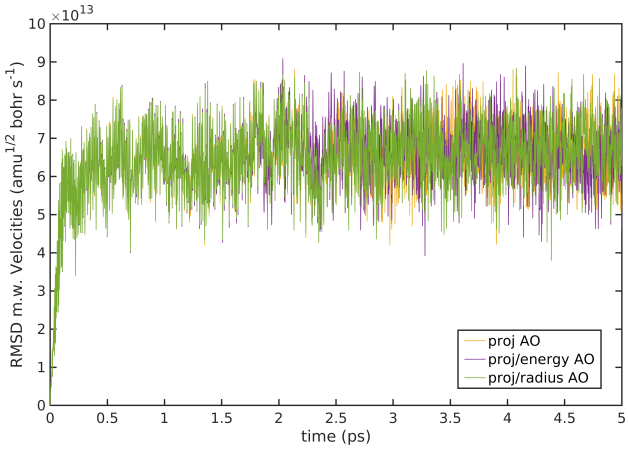


Proj AO *vs.* proj MO.

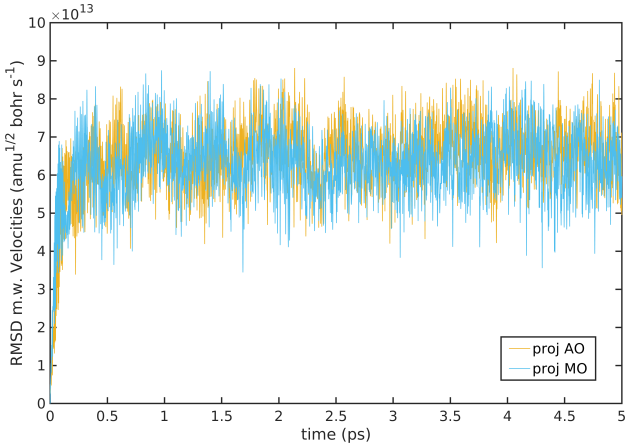
Figure 3.22: NMA B3LYP/6-311G(d,p) ADMP – BOMD RMSD of nuclear coordinates.



Scalar *vs.* proj AO *vs.* Hessian.



Proj *vs.* proj/energy *vs.* proj/radius AO.



Proj AO *vs.* proj MO.

Figure 3.23: NMA B3LYP/6-311G(d,p) ADMP – BOMD RMSD of mass-weighted nuclear velocities.

Table 3.16: ΔE_{pot}, ΔE_{tot}, RMSD Coor and RMSD m.w. Vel between NMA B3LYP/6-311G(d,p) ADMP test simulations and a BOMD reference trajectory. Data are reported as mean (st.dev.).

NMA B3LYP/6-311G(d,p): ADMP - BOMD deviations				
	ΔE_{pot} (10^{-4} hartree)	ΔE_{tot} (10^{-5} hartree)	RMSD Coor (10^{-2} bohr)	RMSD m.w. Vel (10^{13} amu$^{1/2}$ bohr s^{-1})
default				
scalar	-640 (40)	-6610 (80)	240 (80)	6.3 (0.7)
proj AO	-630 (40)	-6410 (20)	270 (70)	6.5 (0.8)
proj/energy AO	-630 (40)	-6390 (20)	240 (60)	6.6 (0.8)
proj/radius AO	-640 (40)	-6400 (20)	280 (80)	6.5 (0.8)
proj MO	-630 (40)	-6540 (50)	230 (50)	6.3 (0.8)
Hessian	0 (40)	-52 (8)	300 (100)	6 (1)

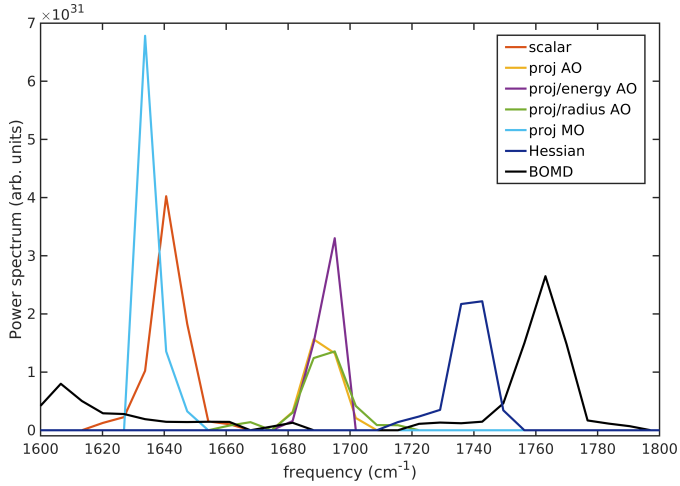
Frequency-domain analysis.

ADMP B3LYP/6-311G(d,p) (ts = 0.1 fs) estimates of NMA Amide I and Amide A are, as expected, clustered according to the different weighting schemes adiabaticities (Fig. 3.24 and Table 3.17). The most accurate results are in fact given by the Hessian-based method (-20 and $-41\,\mathrm{cm}^{-1}$deviations for Amide I and Amide A). The proj, proj/energy and proj/radius AO approaches show smaller deviations from the BOMD values (~ -70 and $-130\,\mathrm{cm}^{-1}$) than the scalar and proj MO ones, whose errors exceed instead -120 and $-240\,\mathrm{cm}^{-1}$ (as suggested by higher nuclear kinetic energy deviations, Table 3.18). The reduced adiabaticity achieved with the bigger (0.2 fs) time step significantly affects the ADMP nuclear vibrational dynamics at the B3LYP/6-311G(d,p) level, resulting in higher deviations of calculated frequencies (~ -110 and $-190\,\mathrm{cm}^{-1}$ at least) from the BOMD values.

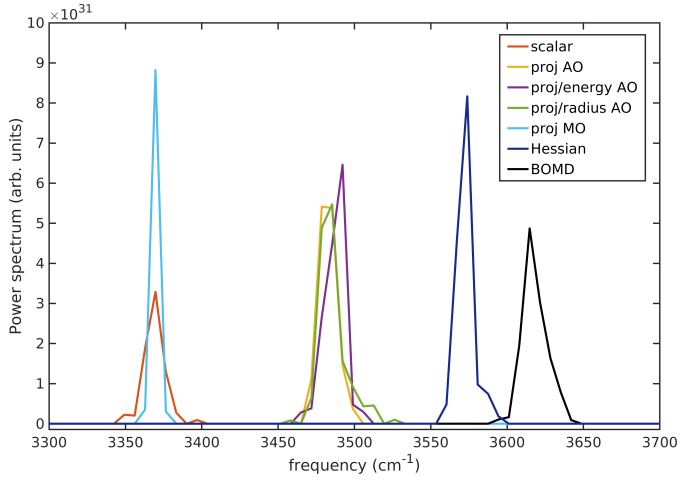
Frequency analysis of ADMP NMA B3LYP/6-311G(d,p) fictitious electronic dynamics (ts = 0.1 fs) reveals quite different spectral distributions (Fig. 3.25 and Table 3.19). The distribution from the Hessian-based approach is clearly located at higher frequencies, between $\sim 15\,000$ and $60\,000\,\mathrm{cm}^{-1}$ (around $37\,000\,\mathrm{cm}^{-1}$), allowing an over $10\,000\,\mathrm{cm}^{-1}$ separation from the highest frequency nuclear motions and so a high nuclear/electronic adiabaticity (Table 3.15). On the other hand, the spectra from the scalar and proj MO approaches are shifted towards lower frequencies and centered around $14\,000\,\mathrm{cm}^{-1}$, ensuring an only $2000\,\mathrm{cm}^{-1}$ distance from the highest fundamental vibrational frequency. No signals are found above $30\,000\,\mathrm{cm}^{-1}$. In contrast, the distributions from the projection-based AO schemes are located at higher frequencies (roughly in the $10\,000$ – $45\,000\,\mathrm{cm}^{-1}$ range), centered around $22\,000\,\mathrm{cm}^{-1}$. The first electronic frequencies are now located about $4000\,\mathrm{cm}^{-1}$ above the Amide A.

3.3.3 NMA ADMP test simulations: summary

Looking at NMA B3LYP/6-31G(d,p) trajectories, at 0.1 and 0.2 fs time steps the new projection-based schemes give only slightly lower deviations than the current default one, whose performances are themselves adequate. The



Amide I



Amide A

Figure 3.24: Amide I and Amide A vibrational bands from NMA B3LYP/6-311G(d,p) BOMD and ADMP simulations (ts = 0.1 fs).

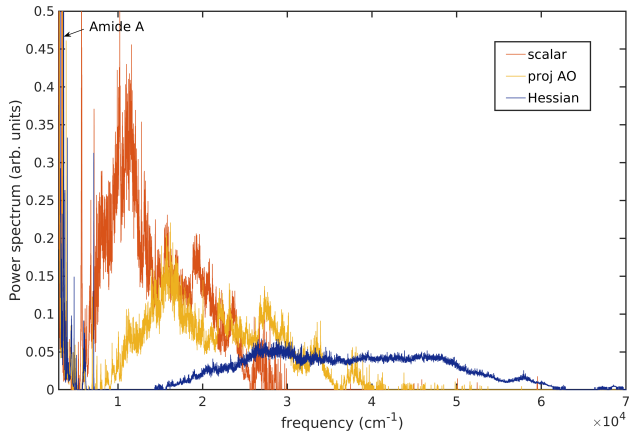
Table 3.17: Deviations $\Delta\nu$ (in cm^{-1}) of ADMP B3LYP/6-311G(d,p) NMA Amide I and Amide A stretching frequencies from the BOMD reference values. Results from harmonic and anharmonic static vibrational calculations, as well as the experimental gas-phase band positions [68], are also reported.

NMA B3LYP/6-311G(d,p): vibrational spectrum				
experimental	harmonic	anharmonic	BOMD	
1713, 1731	1766	1735	1763	Amide I (cm^{-1})
3490	3647	3478	3615	Amide A (cm^{-1})

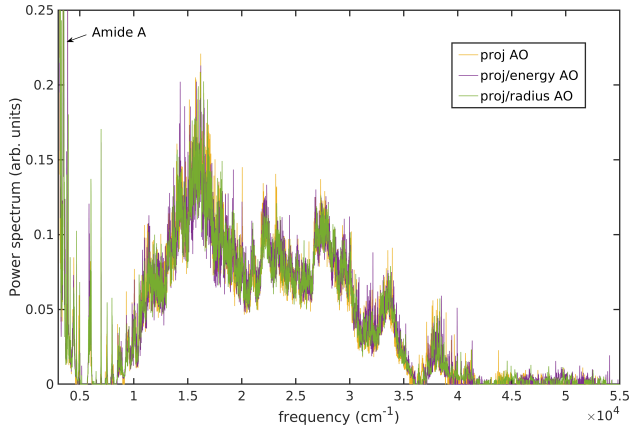
NMA B3LYP/6-311G(d,p): ADMP - BOMD $\Delta\nu$ deviations			
	Time Step (fs)		
	0.1	0.2	
default			Amide I (cm^{-1}) Amide A (cm^{-1})
scalar	-122 -245		
proj AO	-75 -136	-177 -354	
proj/energy AO	-68 -123	-170 -300	
proj/radius AO	-68 -130	-170 -327	
proj MO	-129 -245		
Hessian	-20 -41	-109 -191	

Table 3.18: Relative deviations of NMA B3LYP/6-311G(d,p) ADMP average nuclear kinetic energy from the BOMD (ts = 0.1 fs) value at the same level of theory.

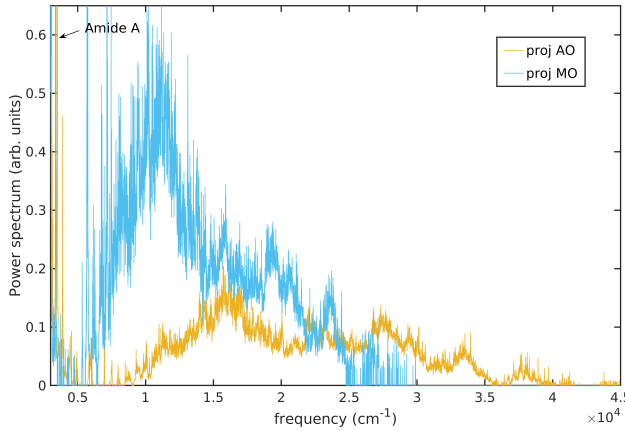
NMA B3LYP/6-311G(d,p): ADMP - BOMD $\Delta\langle E_{k,R}\rangle$		
	Time Step (fs)	
	0.1	0.2
default		
scalar	-17.1%	
proj AO	-8.4%	-22.1%
proj/energy AO	-7.3%	-15.6%
proj/radius AO	-6.0%	-17.1%
proj MO	-17.6%	
Hessian	-4.6%	-16.2%



Scalar *vs.* proj AO *vs.* Hessian.



Proj *vs.* proj/energy *vs.* proj/radius AO.



Proj AO *vs.* proj MO.

Figure 3.25: Fictitious electronic dynamics from NMA B3LYP/6-311G(d,p) ADMP simulations (ts = 0.1 fs). The label indicates the highest nuclear fundamental vibration.

Table 3.19: Distribution of the fictitious electronic frequencies in NMA B3LYP/6-311G(d,p) ADMP simulations (ts = 0.1 fs). ν_{el} is reported as: wght. average (bandwidth).

NMA B3LYP/6-311G(d,p): fictitious electronic frequencies			
	$\nu_{\mathrm{el}}\,(\mathrm{cm}^{-1})$	$\nu_{el} - \nu_N\,(\mathrm{cm}^{-1})$	τ_N/τ_{el}
default			
scalar	14631 (7483)	1947	1.58
proj AO	21453 (10833)	4044	2.16
proj/energy AO	21745 (13224)	4050	2.16
proj/radius AO	21637 (13667)	4044	2.16
proj MO	13980 (6476)	1961	1.58
Hessian	36824 (13075)	10769	4.01

Hessian-based approach, instead, proves highly accurate. A 0.3 fs time step seems to be a limit value; only the projection-based AO schemes ensure a sufficient accuracy. The 6-311G(d,p) triple-zeta basis set can be now employed, with either the proj AO or the Hessian methods, together with a 0.1 fs time step. The latter approach is again the most accurate.

3.4 Trans-dichloroethylene

Due to the difficulties by ADMP method to simulate heavy elements by full-electron calculations, trans-dichloroethylene molecule was chosen as a further simple, but effective, test-case.

Similarly to NMA simulations, a NVT ($T = 300\,\mathrm{K}$) equilibration step was carried out for 10 ps. Temperature was controlled by velocity rescaling, applied every 100 fs. ADMP and BOMD 5 ps production runs were then collected.

3.4.1 B3LYP/6-31G(d,p) level of theory.

The default mass-weighting method (based upon orbital energies) applies a substantial inertia to the Cl core orbitals, explaining the big $\|\boldsymbol{\mu}\|_F$ values (Table 3.20). At the smallest (0.1 fs) time step, all but the scalar scheme employ low mass parameters. If a 0.2 fs time step is instead chosen, the failure of the scalar approach (within the previously defined μ^{val} interval) can be observed. The non-energy or radius modified proj AO and MO schemes have to rely upon an increased ($0.2\,\mathrm{amu\,bohr^2}$) μ^{val} value. An analogous situation is found for ts = 0.3 fs: a $0.3\,\mathrm{amu\,bohr^2}$ value is required by such schemes, instead of $0.2\,\mathrm{amu\,bohr^2}$. As expected, further increasing (to 0.4 fs) the time step, only the energy and radius-corrected schemes (among the projection-based approaches) are able (together with the Hessian-based and the existing default one) to run a stable trajectory, all requiring a $0.3\,\mathrm{amu\,bohr^2}$ valence mass parameter. The Hessian-based approach allows a quite high ($85\,000\,\mathrm{cm^{-1}}$) input frequency with a 0.1 fs time step. The target frequency unavoidably decays increasing the time step, being still moderately high ($40\,000\,\mathrm{cm^{-1}}$) with ts = 0.2 fs.

Time-domain analysis.

The $E_{k,R}/E_{k,P}$ ratio temporal evolution in dichloroethylene B3LYP/6-31G(d,p) ADMP trajectories (ts = 0.1 fs) shows wide oscillations around 25 by the Hessian-based approach, which seems to ensure the highest adi-

Table 3.20: Mass parameters and norm of $\boldsymbol{\mu}$ matrix employed for dichloroethylene B3LYP/6-31G(d,p) ADMP simulations.

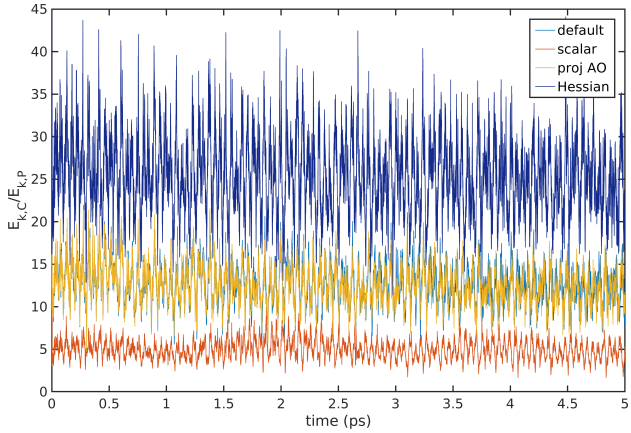
Dichloroethylene B3LYP/6-31G(d,p) (N_b: 78): ADMP mass parameters					
	Time Step (fs)				
	0.1	0.2	0.3	0.4	
default	–, 0.1 63.07	–, 0.1 63.07	–, 0.2 126.14	–, 0.3 189.21	f^{cr}, μ^{val} (amu bohr^2) / $\tilde{\nu}$ (cm^{-1}) $\|\boldsymbol{\mu}\|_F$ (amu bohr^2)
scalar	–, 0.3 2.65				
proj AO	7, 0.1 2.56	25, 0.2 17.40	53, 0.3 55.13		
proj/energy AO	2, 0.1 4.21	7, 0.1 14.48	9, 0.2 37.22	12, 0.3 74.41	
proj/radius AO	2, 0.1 1.74	21, 0.1 16.18	26, 0.2 40.05	36, 0.3 83.14	
proj MO	7, 0.1 2.56	25, 0.2 17.40	55, 0.3 57.21		
Hessian	85000 4.85	40000 21.91	25000 56.10	20000 87.65	

abaticity for this time step (Fig. 3.26 and Table 3.21). Nevertheless, the other schemes (except the scalar one) also give significantly > 10 (around 13) $E_{k,R}/E_{k,P}$ ratios.

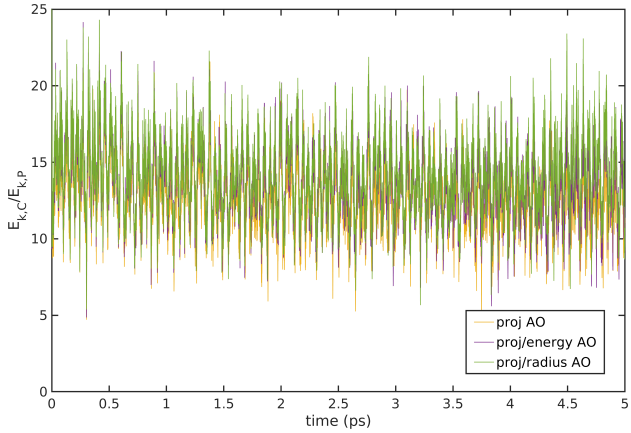
More distinct trends in $\|[\boldsymbol{F}, \boldsymbol{P}]\|$ commutator norm are instead obtained at such time step (Fig. 3.27). The lowest ($\sim$ 0.025 hartree) values are given by the Hessian-based approach and the energy and radius-modified projection-based ones, which prove slightly more accurate than the "simpler" proj AO and MO schemes (at around 0.03 hartree). Quite unexpectedly, the scalar scheme-based dynamics is closer to the converged surface (according to the lower $\|[\boldsymbol{F}, \boldsymbol{P}]\|$) than the default one, despite the lower adiabaticity.

At ts = 0.2 fs, only the default and the proj/energy AO approaches are able to give a > 10 kinetic energy ratio. A performance reduction by the Hessian (still having the best $\|[\boldsymbol{F}, \boldsymbol{P}]\|$), proj AO and MO methods from 0.1 to 0.2 fs is quite clear. Using a higher (0.3 fs) time step, no approach shows completely satisfactory results. In fact, the $E_{k,R}/E_{k,P}$ ratio does not exceed 7 (by the default scheme). Increased $\|[\boldsymbol{F}, \boldsymbol{P}]\|$ norms are consequently observed. A 0.4 fs time step, therefore, definitely appears too high for an accurate simulation, as suggested by low kinetic energy ratios.

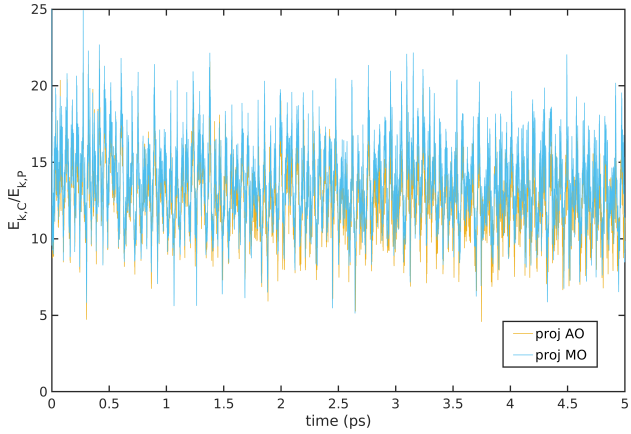
Dichloroethylene ADMP B3LYP/6-31G(d,p) simulations (ts = 0.1 fs) have been compared to a reference BOMD trajectory. The potential energy deviation is quite similar among all the tested mass-weighting approaches, showing $\sim$ 0.005 hartree oscillations around the BO potential energy (Fig. 3.28 and Table 3.22). The higher adiabaticity by the Hessian-based method leads to a lower (-2.5×10^{-4} hartree) ADMP total real energy deviation from the BOMD value (Fig. 3.29). On the other hand, an high (exceeding -0.001 hartree) deviation (with some drift) is shown by the scalar scheme, due to its low adiabaticity even with a small (0.1 fs) time step. Analogously, the higher mean RMS coordinates deviation by the scalar scheme (being instead around 0.2 bohr for the other ones) is due to a steady increase along the simulation (Fig. 3.30). The trends in RMS velocities deviations are instead more uniform (Fig. 3.31).



Default *vs.* scalar *vs.* proj AO *vs.* Hessian.

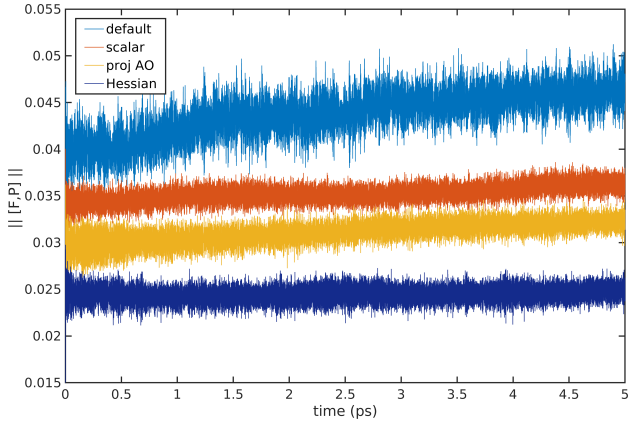


Proj *vs.* proj/energy *vs.* proj/radius AO.

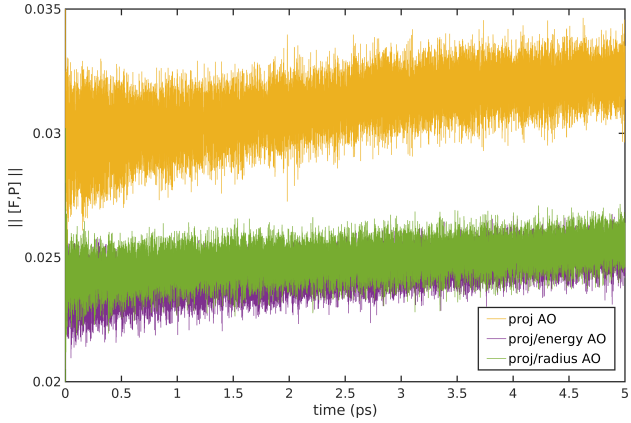


Proj AO *vs.* proj MO.

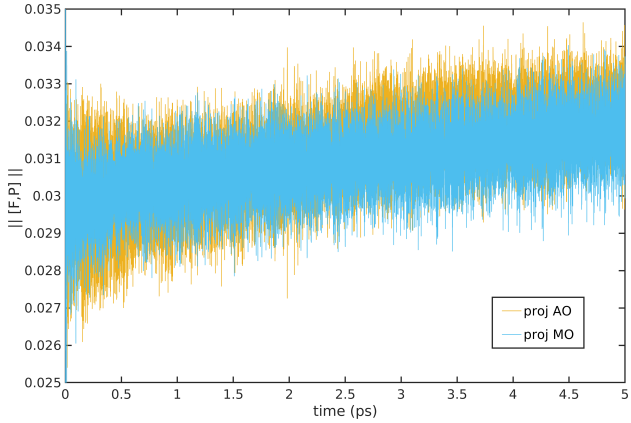
Figure 3.26: Dichloroethylene B3LYP/6-31G(d,p) ADMP (ts = 0.1 fs) simulations: $E_{k,R}/E_{k,P}$ ratio.



Default *vs.* scalar *vs.* proj AO *vs.* Hessian.



Proj *vs.* proj/energy *vs.* proj/radius AO.

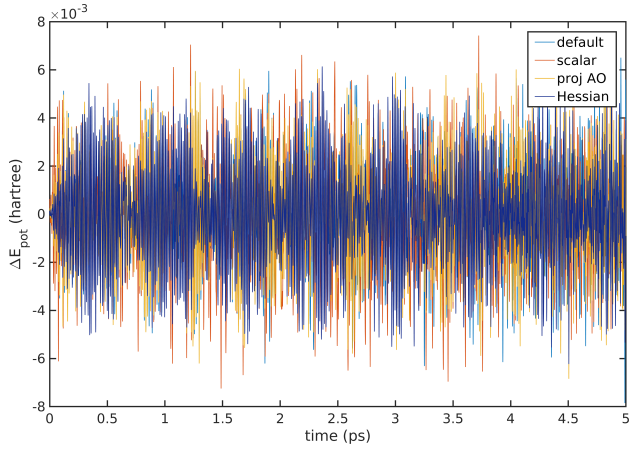


Proj AO *vs.* proj MO.

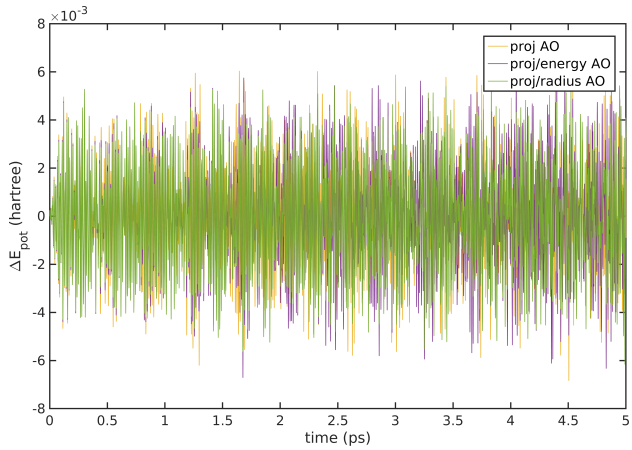
Figure 3.27: Dichloroethylene B3LYP/6-31G(d,p) ADMP (ts = 0.1 fs) simulations: $\|[\boldsymbol{F}, \boldsymbol{P}]\|$ commutator norm.

Table 3.21: Dichloroethylene B3LYP/6-31G(d,p) ADMP simulations; adiabaticity indicators. $E_{k,R}/E_{k,P}$, $\|[\boldsymbol{F},\boldsymbol{P}]\|$ and $|d\mathcal{H}_{\text{fict}}/dt|$ parameters are reported as: average (st.dev.).

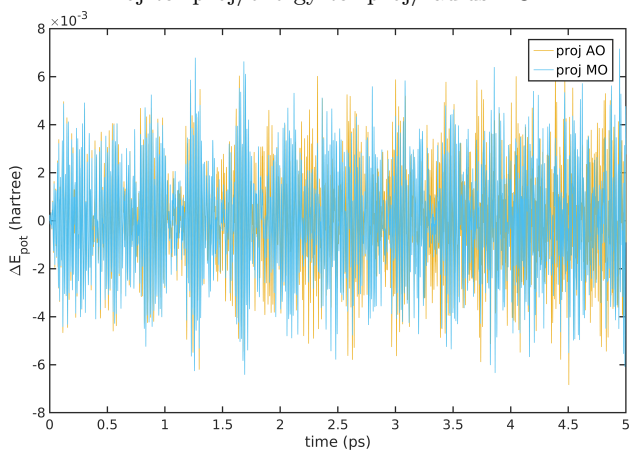
Dichloroethylene B3LYP/6-31G(d,p): ADMP adiabaticity					
	Time Step (fs)				
	0.1	0.2	0.3	0.4	
default	13 (2)	13 (2)	7 (2)	4.6 (0.9)	$E_{k,R}/E_{k,P}$
	4.4 (0.2)	5.0 (0.2)	7.9 (0.5)	10.8 (0.6)	$\|[\boldsymbol{F},\boldsymbol{P}]\|$ ($\cdot 10^{-2}$ Ha)
	5 (2)	19 (4)	22 (4)	25 (5)	$\|d\mathcal{H}_{\text{fict}}/dt\|$ ($\cdot 10^{-5}$ Ha fs^{-1})
	(2)	(2)	(3)	(10)	$s(E_{\text{tot}})$ ($\cdot 10^{-5}$ Ha)
scalar	5 (1)				
	3.53 (0.09)				
	3 (1)				
	(10)				
proj AO	12 (2)	3.9 (0.9)	0.7 (0.4)		
	3.1 (0.1)	6.3 (0.4)	26 (9)		
	6 (2)	8 (2)	50 (40)		
	(2)	(6)	(400)		
proj/energy AO	13 (2)	11 (2)	5 (1)	2.2 (0.6)	
	2.44 (0.07)	5.8 (0.3)	8.1 (0.3)	12.3 (0.7)	
	6 (2)	22 (4)	21 (4)	25 (7)	
	(2)	(2)	(7)	(20)	
proj/radius AO	14 (2)	8 (2)	2.9 (0.7)	1.4 (0.4)	
	2.49 (0.06)	5.3 (0.2)	8.3 (0.5)	11.4 (0.9)	
	7 (2)	16 (3)	17 (5)	16 (4)	
	(2)	(5)	(7)	(30)	
proj MO	13 (2)	6 (1)	3.6 (0.7)		
	3.09 (0.09)	7.7 (0.3)	20 (7)		
	6 (2)	12 (3)	30 (10)		
	(2)	(3)	(40)		
Hessian	25 (4)	6 (1)	1.7 (0.5)	1.2 (0.4)	
	2.45 (0.08)	4.5 (0.1)	7.3 (0.5)	10.0 (0.7)	
	13 (3)	10 (3)	10 (3)	10 (4)	
	(1)	(7)	(40)	(90)	



Default *vs.* scalar *vs.* proj AO *vs.* Hessian.

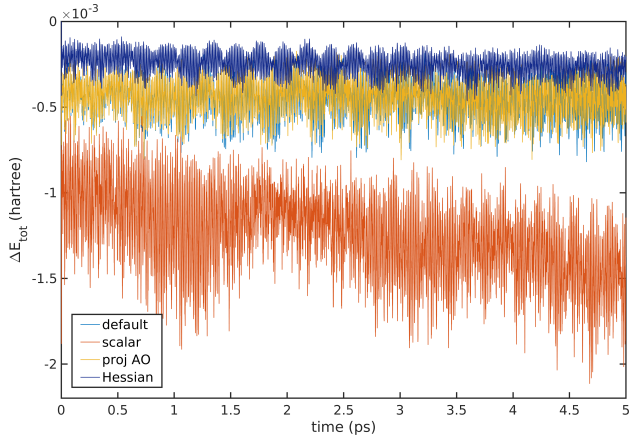


Proj *vs.* proj/energy *vs.* proj/radius AO.

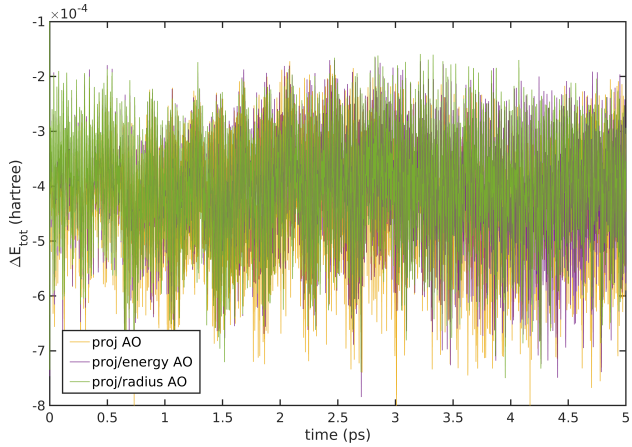


Proj AO *vs.* proj MO.

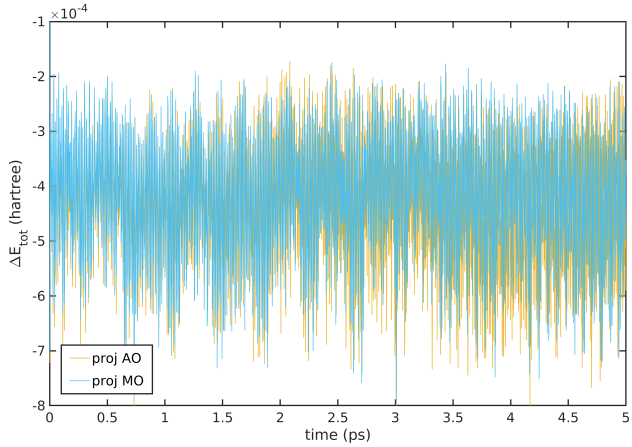
Figure 3.28: Dichloroethylene B3LYP/6-31G(d,p) ADMP – BOMD (ts = 0.1 fs) E_{pot} deviations.



Default *vs.* scalar *vs.* proj AO *vs.* Hessian.

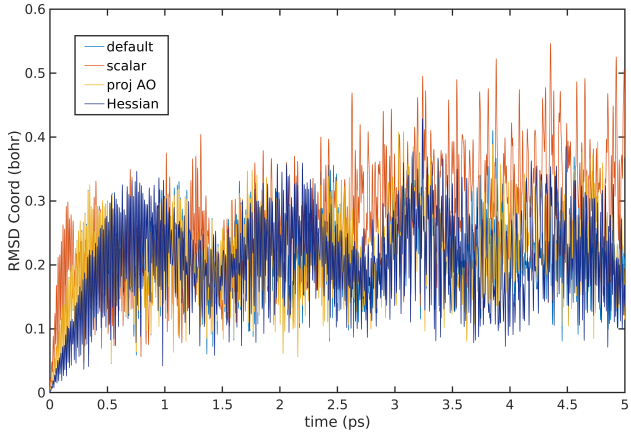


Proj *vs.* proj/energy *vs.* proj/radius AO.

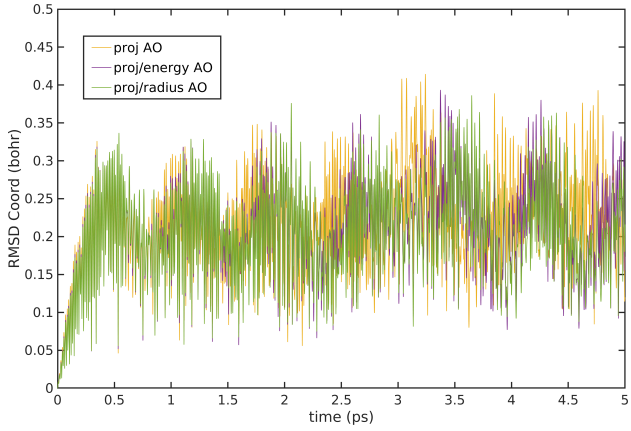


Proj AO *vs.* proj MO.

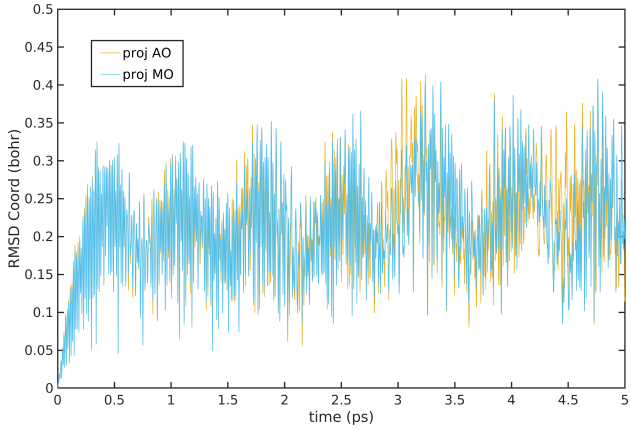
Figure 3.29: Dichloroethylene B3LYP/6-31G(d,p) ADMP – BOMD (ts = 0.1 fs) $E_{\mathrm{tot,real}}$ deviations.



Default *vs.* scalar *vs.* proj AO *vs.* Hessian.

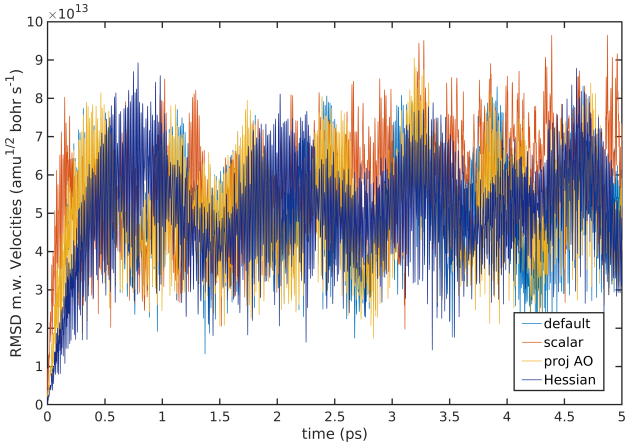


Proj *vs.* proj/energy *vs.* proj/radius AO.

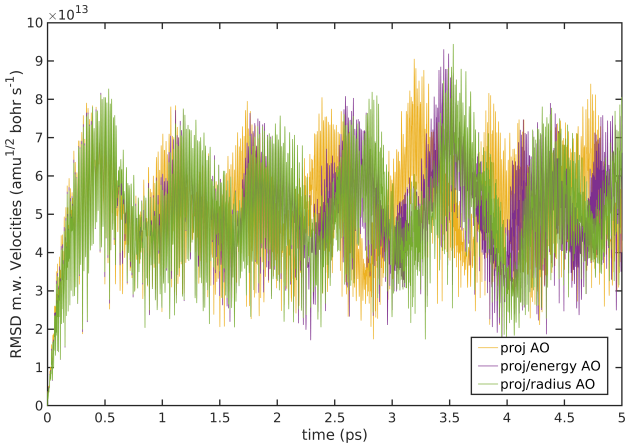


Proj AO *vs.* proj MO.

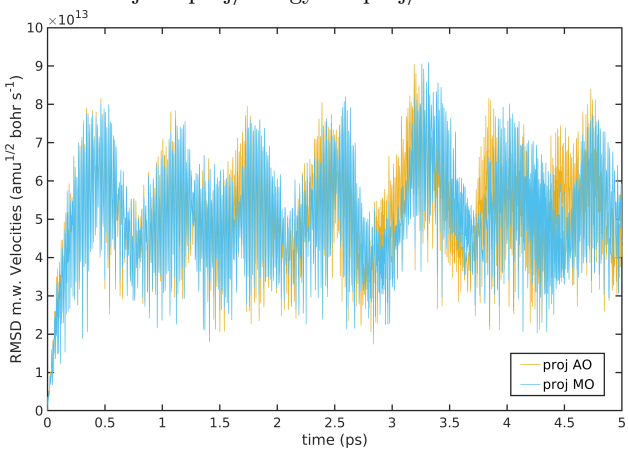
Figure 3.30: Dichloroethylene B3LYP/6-31G(d,p) ADMP – BOMD (ts = 0.1 fs) RMSD of nuclear coordinates.



Default *vs.* scalar *vs.* proj AO *vs.* Hessian.



Proj *vs.* proj/energy *vs.* proj/radius AO.



Proj AO *vs.* proj MO.

Figure 3.31: Dichloroethylene B3LYP/6-31G(d,p) ADMP – BOMD (ts = 0.1 fs) RMSD of mass-weighted nuclear velocities.

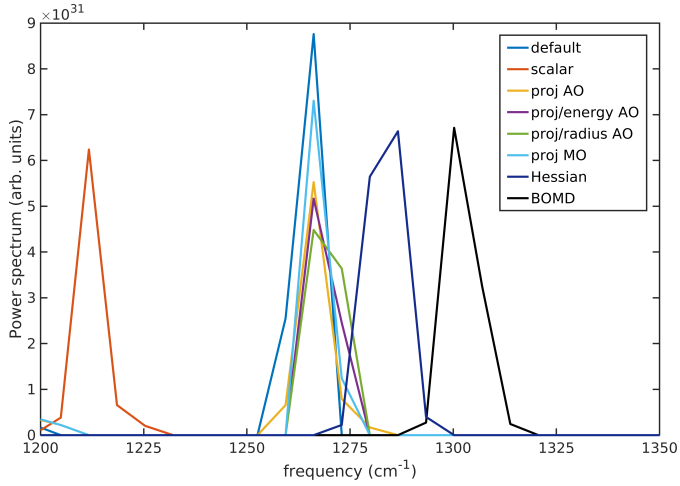
Table 3.22: ΔE_{pot}, ΔE_{tot}, RMSD Coor and RMSD m.w. Vel between dichloroethylene B3LYP/6-31G(d,p) ADMP test simulations and a BOMD reference trajectory (ts = 0.1 fs). Data are reported as mean (st.dev.).

Dichloroethylene B3LYP/6-31G(d,p): ADMP - BOMD deviations				
	ΔE_{pot} (10^{-4} hartree)	ΔE_{tot} (10^{-5} hartree)	RMSD Coor (10^{-2} bohr)	RMSD m.w. Vel (10^{13} amu$^{1/2}$ bohr s^{-1})
default	0 (20)	-50 (10)	21 (6)	5 (1)
scalar	0 (20)	-130 (20)	27 (8)	6 (1)
proj AO	0 (20)	-40 (10)	22 (6)	5 (1)
proj/energy AO	0 (20)	-40 (10)	21 (6)	5 (1)
proj/radius AO	0 (20)	-40 (10)	21 (6)	5 (1)
proj MO	0 (20)	-40 (10)	22 (6)	5 (1)
Hessian	0 (20)	-25 (6)	21 (7)	5 (1)

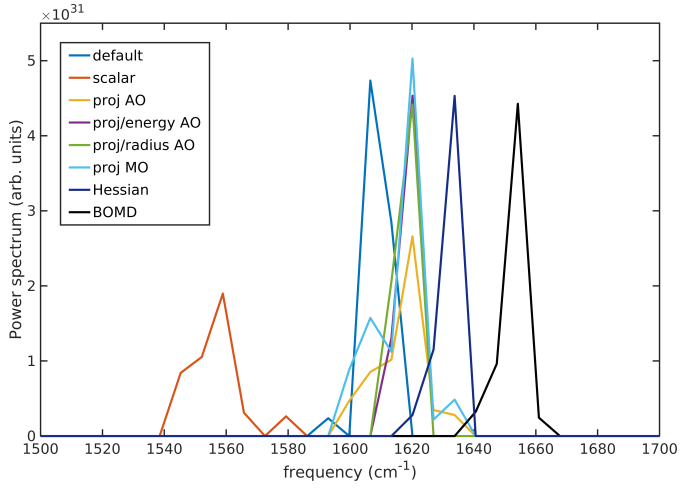
Frequency-domain analysis.

Dichloroethylene C–H rocking and the C=C stretching vibrational normal modes (located at ~ 1300 and $1650\,\mathrm{cm}^{-1}$, respectively) were considered, in order to assess the accuracy of dichloroethylene ADMP B3LYP/6-31G(d,p) vibrational dynamics. At the smallest (0.1 fs) time step (Fig. 3.32 and Table 3.23), smaller errors (-14 and $-20\,\mathrm{cm}^{-1}$) are given, as expected, by the Hessian-based scheme, being able to better control the nuclear kinetic energy deviation (Table 3.24). The results ($-34\,\mathrm{cm}^{-1}$) from the other mass-weighting approaches are quite consistent and still accurate (excluding the scalar one). At ts = 0.2 fs, as suggested by the adiabaticity results (Table 3.21), only the default and the proj/energy AO approaches manage to keep a small error ($\sim -40\,\mathrm{cm}^{-1}$) and a kinetic energy relative deviation under 10%. In particular, the error increase from 0.1 to 0.2 fs by the proj AO scheme (now exceeding $-100\,\mathrm{cm}^{-1}$) can be noticed. Due to the only partial adiabaticity achieved with a 0.3 fs time step, the default and the proj/energy AO are the only schemes able to limit the vibrational frequency error within $-100\,\mathrm{cm}^{-1}$ (~ -70 and $\sim -90\,\mathrm{cm}^{-1}$, respectively). The vibrational dynamics from the proj AO and Hessian approaches proves instead unreliable ($\Delta\nu \approx -200\,\mathrm{cm}^{-1}$). Employing a 0.4 fs time step, no scheme is able to give accurate band positions, with deviations starting from $\sim -100\,\mathrm{cm}^{-1}$ (by the default scheme).

Some differences can be observed in the fictitious electronic frequencies distribution from dichloroethylene ADMP (ts = 0.1 fs) B3LYP/6-31G(d,p) simulations (Fig. 3.33 and Table 3.25). The Hessian-based distribution is the most displaced towards higher frequencies, spanning (with some discontinuities) the 10 000 – 70 000 cm^{-1} interval and being centered around 28 000 cm^{-1}. A $\sim 7000\,\mathrm{cm}^{-1}$ gap between the nuclear (i.e., the $\sim 3100\,\mathrm{cm}^{-1}$ C–H stretch) and the electronic density motions justifies the higher adiabaticity. The projection-based approaches are located instead around $\sim 20\,000\,\mathrm{cm}^{-1}$, starting from $\sim 8000\,\mathrm{cm}^{-1}$. The energy- or radius-modified approaches show slightly higher frequencies (21 000 cm^{-1} on average, extending up to $\sim 50\,000\,\mathrm{cm}^{-1}$), than the simpler proj AO or MO ones (which



C–H rocking



C=C stretching

Figure 3.32: C–H rocking and C=C stretching vibrational bands from dichloroethylene B3LYP/6-31G(d,p) BOMD and ADMP simulations (ts = 0.1 fs).

Table 3.23: Deviations $\Delta\nu$ (in cm^{-1}) of ADMP B3LYP/6-31G(d,p) dichloroethylene C–H rocking and C=C stretching frequencies from the BOMD reference values. Results from harmonic and anharmonic static vibrational calculations, as well as the experimental band positions from liquid-phase Raman spectroscopy [69], are also reported.

Dichloroethylene B3LYP/6-31G(d,p): vibrational spectrum				
experimental	harmonic	anharmonic	BOMD	
1272	1309	1286	1300	δ(C–H) (cm^{-1})
1578	1664	1622	1654	ν(C=C) (cm^{-1})

Dichloroethylene B3LYP/6-31G(d,p): ADMP - BOMD $\Delta\nu$ deviations					
	Time Step (fs)				
	0.1	0.2	0.3	0.4	
default	-34	-34	-68	-102	δ(C–H) (cm^{-1})
	-48	-48	-75	-123	ν(C=C) (cm^{-1})
scalar	-88				
	-95				
proj AO	-34	-109	-231		
	-34	-123	-252		
proj/energy AO	-34	-41	-89	-143	
	-34	-41	-95	-150	
proj/radius AO	-34	-54	-116	-204	
	-34	-61	-136	-231	
proj MO	-34	-82	-123		
	-34	-82	-129		
Hessian	-14	-75	-177	-245	
	-20	-88	-191	-259	

Table 3.24: Relative deviations of dichloroethylene B3LYP/6-31G(d,p) ADMP average nuclear kinetic energy from the BOMD (ts = 0.1 fs) value at the same level of theory.

Dichloroethylene B3LYP/6-31G(d,p): ADMP - BOMD $\Delta\langle E_{k,R}\rangle$				
	Time Step (fs)			
	0.1	0.2	0.3	0.4
default	-7.3%	-7.3%	-12.4%	-17.1%
scalar	-18.6%			
proj AO	-7.3%	-20.0%	-43.4%	
proj/energy AO	-6.8%	-8.5%	-16.4%	-30.5%
proj/radius AO	-6.6%	-10.2%	-25.8%	-39.8%
proj MO	-6.9%	-13.9%	-21.0%	
Hessian	-4.0%	-14.9%	-33.9%	-43.5%

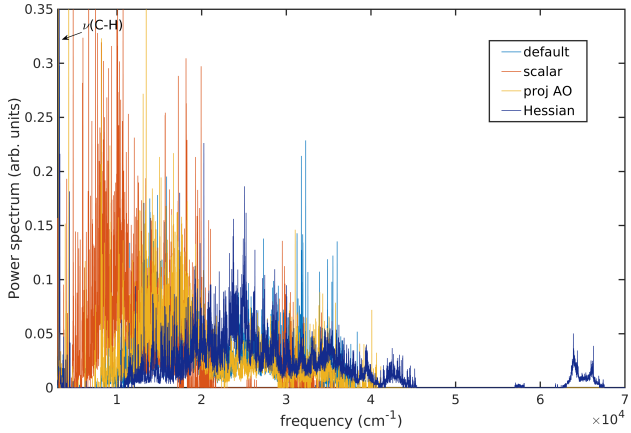
Table 3.25: Fictitious electronic frequencies distribution in dichloroethylene B3LYP/6-31G(d,p) ADMP simulations (ts = 0.1 fs). ν_{el} is reported as: wght. average (bandwidth).

Dichloroethylene B3LYP/6-31G(d,p): fictitious electronic frequencies			
	$\nu_{\mathrm{el}}\,(\mathrm{cm}^{-1})$	$\nu_{el}-\nu_N\,(\mathrm{cm}^{-1})$	τ_N/τ_{el}
default	21064 (8785)	4323	2.38
scalar	12933 (8171)	1430	1.48
proj AO	19539 (9884)	4248	2.36
proj/energy AO	21130 (10819)	4105	2.31
proj/radius AO	21233 (10995)	4125	2.31
proj MO	20268 (8624)	4411	2.41
Hessian	28127 (11932)	6950	3.19

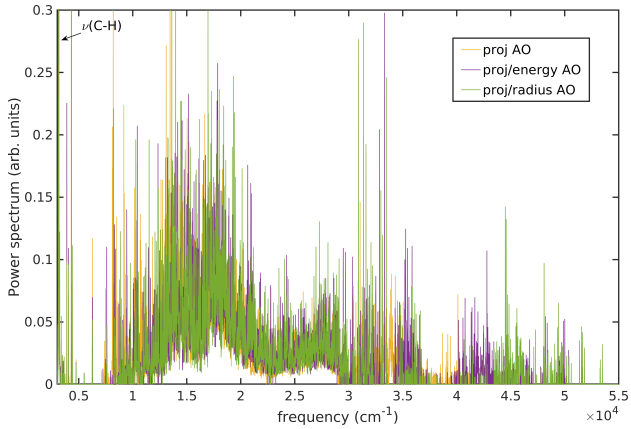
cannot be found beyond $\sim 40\,000\,\mathrm{cm}^{-1}$) Nevertheless, the nuclear-electronic frequency distances are comparable ($> 4000\,\mathrm{cm}^{-1}$) with that from the default scheme. The frequencies from the scalar approach are instead close ($\sim 1400\,\mathrm{cm}^{-1}$) to the nuclear modes (due to the requirement of a big ($0.3\,\mathrm{amu\,bohr}^2$) valence mass, Table 3.20), inducing a poor ($E_{k,R}/E_{k,P} = 5$, Table 3.21) adiabaticity.

3.4.2 B3LYP/6-311G(d,p) level of theory.

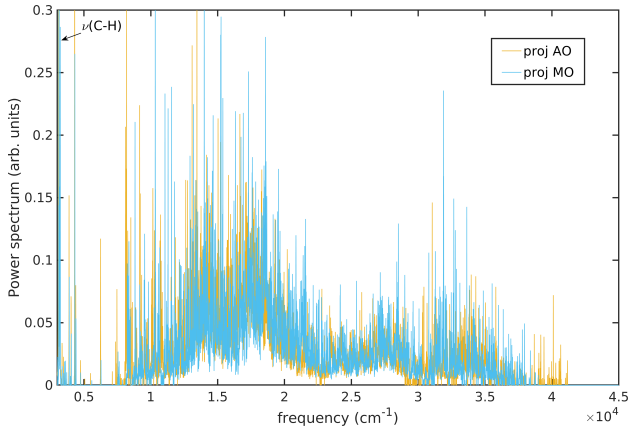
If a triple-zeta 6-311G(d,p) basis set is chosen, both currently existing schemes (default and scalar) prove unable to carry out ADMP dichloroethylene simulations within the previously chosen μ^{val} interval, even with a small (0.1 fs) time step (Table 3.26). The projection-based approaches employ instead small valence mass parameters ($0.1\,\mathrm{amu\,bohr}^2$ for the proj and proj/radius AO schemes, $0.2\,\mathrm{amu\,bohr}^2$ for the proj/energy AO one). The Hessian-based scheme allows at this time step a high ($90\,000\,\mathrm{cm}^{-1}$)



Default *vs.* scalar *vs.* proj AO *vs.* Hessian.



Proj *vs.* proj/energy *vs.* proj/radius AO.



Proj AO *vs.* proj MO.

Figure 3.33: Fictitious electronic dynamics from dichloroethylene B3LYP/6-31G(d,p) ADMP simulations (ts = 0.1 fs). The label indicates the highest nuclear fundamental vibration.

Table 3.26: Mass parameters and norm of $\boldsymbol{\mu}$ matrix employed for dichloroethylene B3LYP/6-311G(d,p) ADMP simulations.

Dichloroethylene B3LYP/6-311G(d,p) (N_b: 100): ADMP mass parameters			
	Time Step (fs)		
	0.1	0.2	
default			f^{cr}, μ^{val} (amu bohr^2) / $\tilde{\nu}$ (cm^{-1}) $\|\boldsymbol{\mu}\|_F$ (amu bohr^2)
scalar			
proj AO	41, 0.1 14.23	41, 0.4 56.94	
proj/energy AO	2, 0.2 8.47		
proj/radius AO	20, 0.1 15.00	34, 0.3 76.41	
proj MO			
Hessian	90000 12.26	45000 49.05	

target frequency. A 0.2 fs time step appears quite challenging: only some schemes (the proj AO, proj/radius AO and Hessian) are able to run a stable simulation, requiring nevertheless high mass parameters or lower input frequencies.

Time-domain analysis.

Only the Hessian-based scheme ensures a distinctly high adiabaticity ($E_{k,R}/E_{k,P} \approx 12$) at ts = 0.1 fs (Fig. 3.34 and Table 3.27). The accuracy by the three projection AO approaches is lower, ranging from $E_{k,R}/E_{k,P} \approx 3$ (by the proj

AO scheme) to ≈ 6 (by the proj/radius AO one). Confirming the results from the kinetic energy ratios, the Hessian approach keeps the $\|[\boldsymbol{F}, \boldsymbol{P}]\|$ norm constant around a low (~ 0.03 hartree) value (Fig. 3.35). Among the proj-based schemes, the lowest $\|[\boldsymbol{F}, \boldsymbol{P}]\|$ is shown by the proj/energy AO (~ 0.04 hartree), while the proj AO gives the highest (~ 0.06 hartree) value.

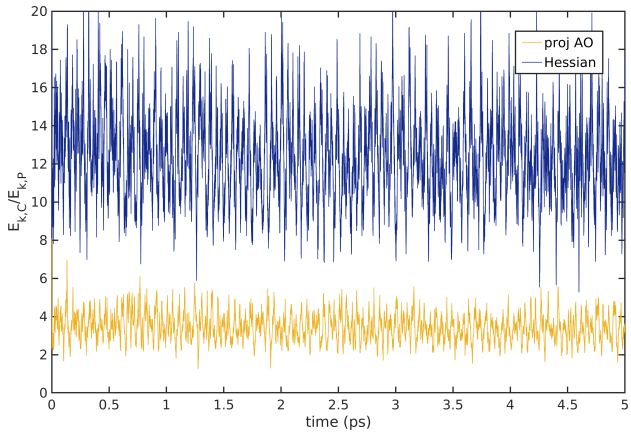
Much poorer performances are observed, as expected, with a bigger (0.2 fs) time step. The highest $E_{k,R}/E_{k,P}$ ratio is only around 3 by the Hessian method, which is the only one able to keep the $\|[\boldsymbol{F}, \boldsymbol{P}]\|$ norm below 0.1 hartree.

Dichloroethylene ADMP B3LYP/6-311G(d,p) test simulations (ts = 0.1 fs) all oscillate about 0.005 hartree around the BO potential energy (Fig. 3.36 and Table 3.28). The total energy deviation by the Hessian scheme is clearly lower (on average, -4×10^{-4} hartree) and less fluctuating than that from the projection schemes, whose deviation is not less than -9×10^{-4} hartree (by the proj/radius AO one) (Fig. 3.37). Also the RMS coordinates (Fig. 3.38) and velocities (Fig. 3.39) deviations are slightly lower for the Hessian approach (on average, ~ 0.2 bohr and $5\,\mathrm{amu}^{1/2}\,\mathrm{bohr\,s}^{-1}$, respectively), showing instead some drift along the trajectories with the proj-based ones.

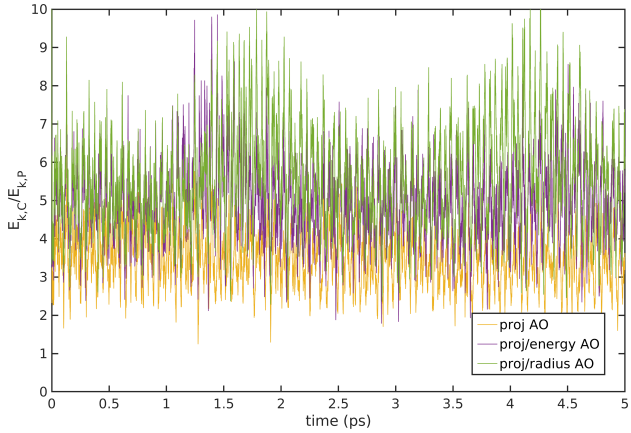
Frequency-domain analysis.

Only the Hessian-based ADMP B3LYP/6-311G(d,p) dichloroethylene simulation (ts = 0.1 fs) is able to accurately estimate the BOMD δ(C–H) and ν(C=C) vibrational frequencies (with -41 and $-20\,\mathrm{cm}^{-1}$ errors, respectively, Fig. 3.40 and Table 3.29) and limit the nuclear kinetic energy deviation (largely below 10%, Table 3.30). The δ(C–H) $\Delta\nu$ is about $-100\,\mathrm{cm}^{-1}$ for both the less accurate proj/energy and proj/radius AO schemes, while the error in ν(C=C) by proj/energy AO is reduced (~ -70, instead of $\sim -90\,\mathrm{cm}^{-1}$), probably because of the lower $\|[\boldsymbol{F}, \boldsymbol{P}]\|$ norm (Table 3.27). Bigger deviations ($\sim -130\,\mathrm{cm}^{-1}/-110\,\mathrm{cm}^{-1}$) are instead shown by the proj AO approach.

As expected by the low adiabaticity achieved with a 0.2 fs time step (Table 3.27), higher deviations are found, starting from about $-110\,\mathrm{cm}^{-1}$

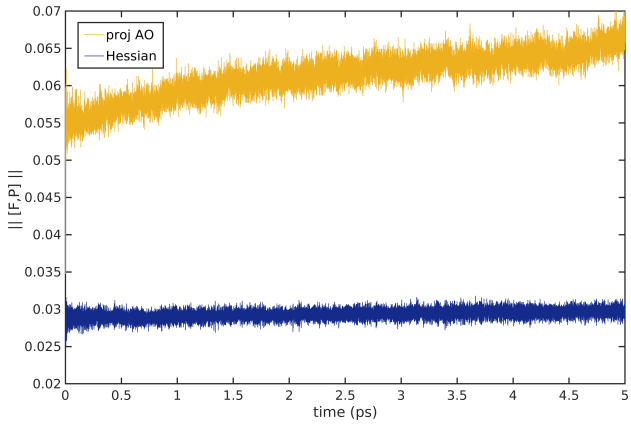


Proj AO *vs.* Hessian.

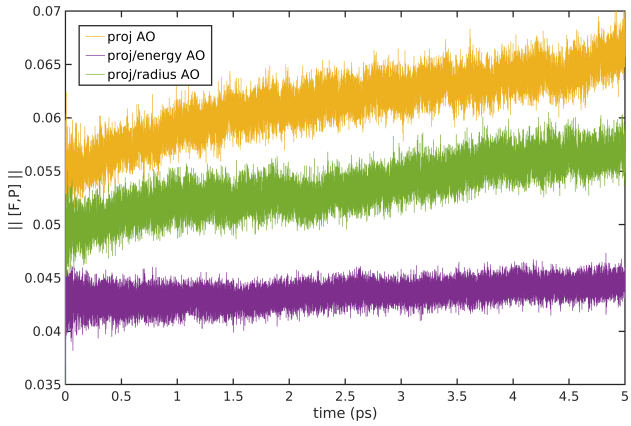


Proj *vs.* proj/energy *vs.* proj/radius AO.

Figure 3.34: Dichloroethylene B3LYP/6-311G(d,p) ADMP (ts = 0.1 fs) simulations: $E_{k,R}/E_{k,P}$ ratio.



Proj AO *vs.* Hessian.

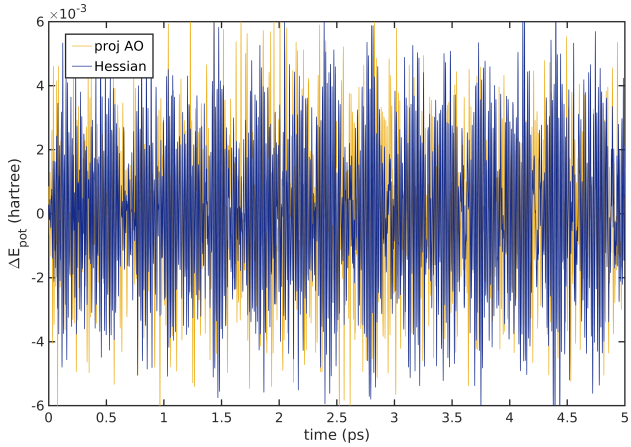


Proj *vs.* proj/energy *vs.* proj/radius AO.

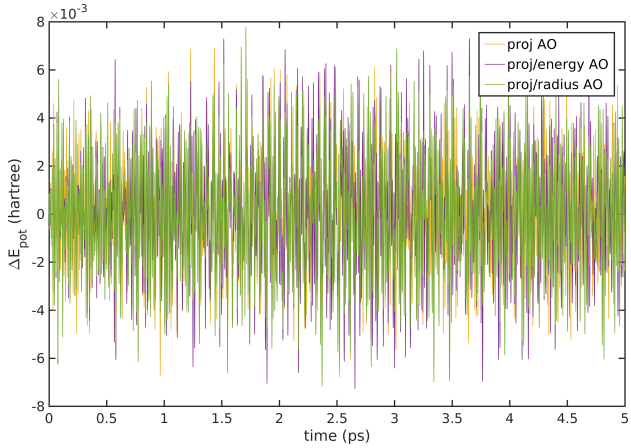
Figure 3.35: Dichloroethylene B3LYP/6-311G(d,p) ADMP (ts = 0.1 fs) simulations: $\|[\boldsymbol{F}, \boldsymbol{P}]\|$ commutator norm.

Table 3.27: Dichloroethylene B3LYP/6-311G(d,p) ADMP simulations; adiabaticity indicators. $E_{k,R}/E_{k,P}$, $\|[\boldsymbol{F},\boldsymbol{P}]\|$ and $|d\mathcal{H}_{\text{fict}}/dt|$ parameters are reported as: average (st.dev.).

Dichloroethylene B3LYP/6-311G(d,p): ADMP adiabaticity			
	Time Step (fs)		
	0.1	0.2	
default			$E_{k,R}/E_{k,P}$ $\|[\boldsymbol{F},\boldsymbol{P}]\|$ $(\cdot 10^{-2}$ Ha$)$ $\|d\mathcal{H}_{\text{fict}}/dt\|$ $(\cdot 10^{-5}$ Ha fs$^{-1})$ $s(E_{\text{tot}})$ $(\cdot 10^{-5}$ Ha$)$
scalar			
proj AO	3.4 (0.7) 6.2 (0.3) 4 (2) (5)	0.8 (0.2) 20 (20) 10 (30) (100)	
proj/energy AO	5 (1) 4.35 (0.09) 5 (2) (5)		
proj/radius AO	6 (1) 5.4 (0.2) 5 (2) (4)	1.0 (0.3) 12 (1) 5 (2) (50)	
proj MO			
Hessian	12 (2) 2.93 (0.06) 15 (3) (2)	3.1 (0.6) 6.1 (0.2) 14 (3) (20)	

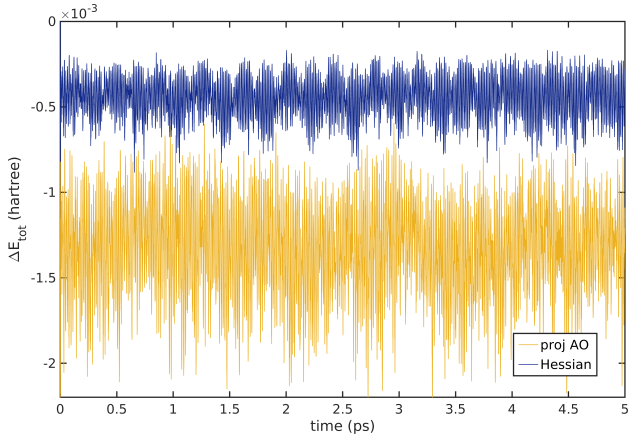


Proj AO *vs.* Hessian.

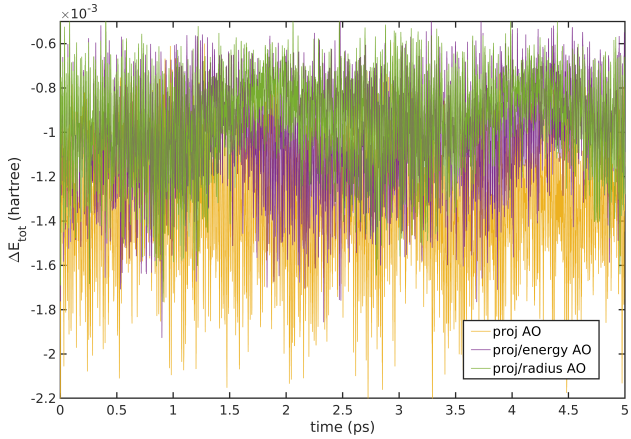


Proj *vs.* proj/energy *vs.* proj/radius AO.

Figure 3.36: Dichloroethylene B3LYP/6-311G(d,p) ADMP – BOMD E_{pot} deviations.

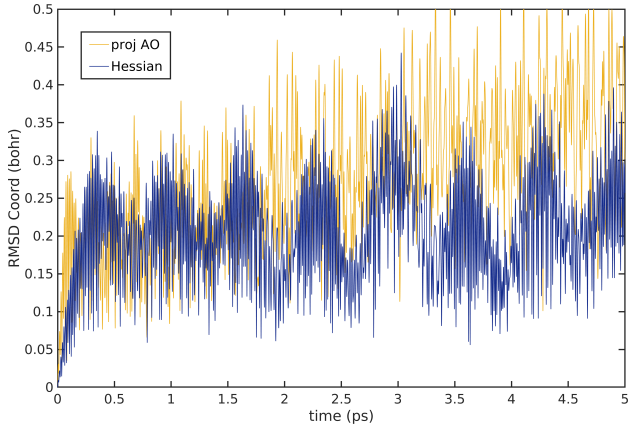


Proj AO *vs.* Hessian.

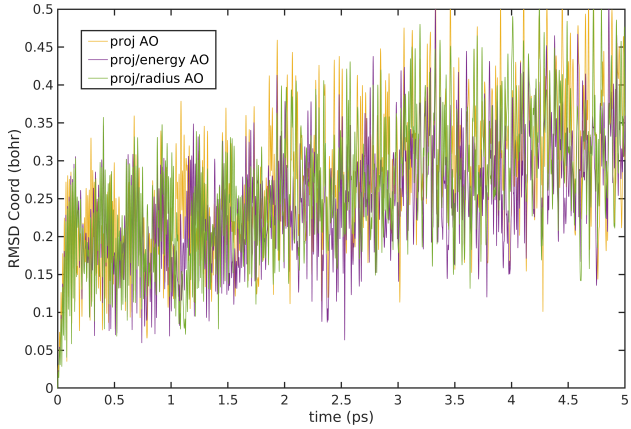


Proj *vs.* proj/energy *vs.* proj/radius AO.

Figure 3.37: Dichloroethylene B3LYP/6-311G(d,p) ADMP – BOMD $E_{\mathrm{tot,real}}$ deviations.

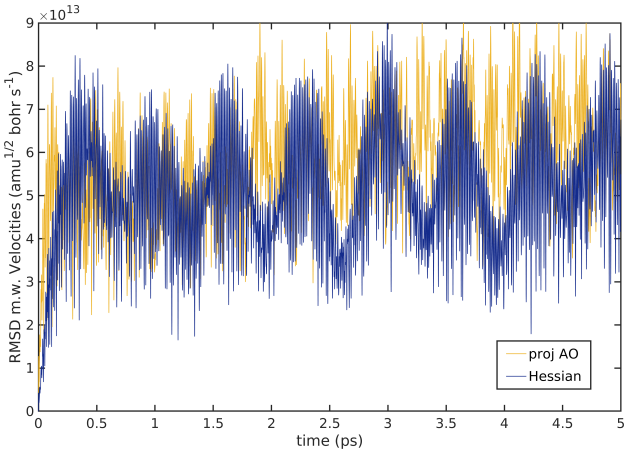


Proj AO *vs.* Hessian.

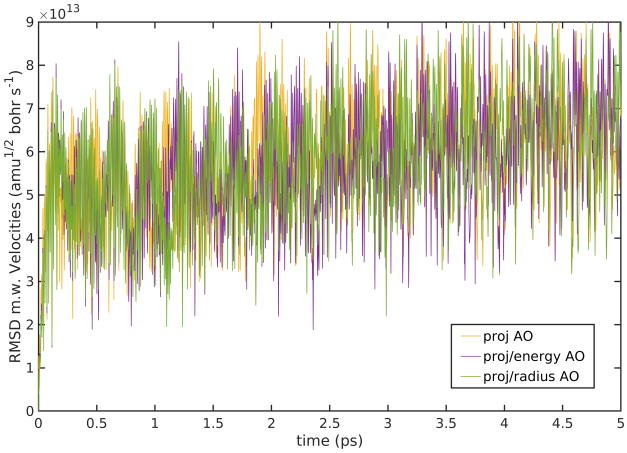


Proj *vs.* proj/energy *vs.* proj/radius AO.

Figure 3.38: Dichloroethylene B3LYP/6-311G(d,p) ADMP – BOMD RMSD of nuclear coordinates.



Proj AO *vs.* Hessian.



Proj *vs.* proj/energy *vs.* proj/radius AO.

Figure 3.39: Dichloroethylene B3LYP/6-311G(d,p) ADMP – BOMD RMSD of mass-weighted nuclear velocities.

Table 3.28: ΔE_{pot}, ΔE_{tot}, RMSD Coor and RMSD m.w. Vel between dichloroethylene B3LYP/6-311G(d,p) ADMP test simulations and a BOMD reference trajectory. Data are reported as mean (st.dev.).

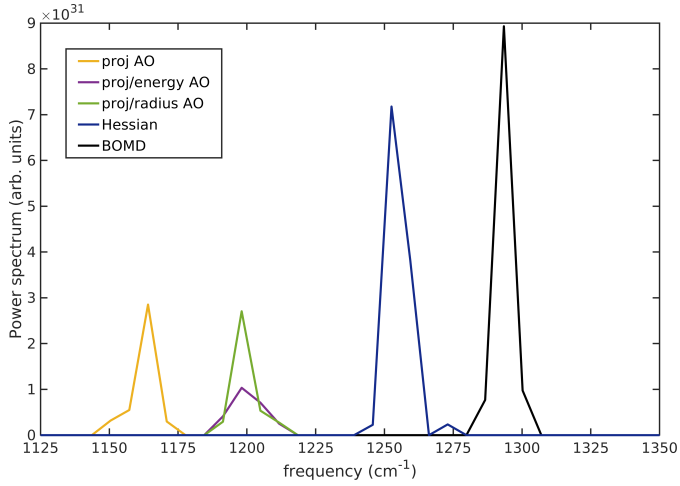
Dichloroethylene B3LYP/6-311G(d,p): ADMP - BOMD deviations				
	ΔE_{pot} (10^{-4} hartree)	ΔE_{tot} (10^{-5} hartree)	RMSD Coor (10^{-2} bohr)	RMSD m.w. Vel (10^{13} amu$^{1/2}$ bohr s^{-1})
default				
scalar				
proj AO	0 (20)	-130 (30)	28 (9)	6 (1)
proj/energy AO	0 (20)	-100 (20)	25 (7)	6 (1)
proj/radius AO	0 (20)	-90 (20)	27 (8)	6 (1)
proj MO				
Hessian	0 (20)	-40 (10)	21 (6)	5 (1)

by the Hessian approach.

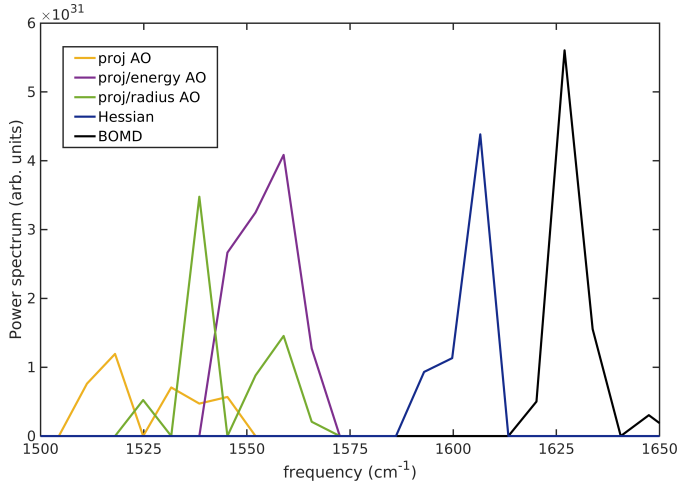
The fictitious electronic frequencies distribution in dichloroethylene ADMP B3LYP/6-311G(d,p) simulations (ts = 0.1 fs) differs among the considered mass-weighting schemes. Again, the spectrum by the Hessian approach (centered around a $\sim 25\,000\,\mathrm{cm}^{-1}$ mean value) is located at higher frequencies, up to $\sim 60\,000\,\mathrm{cm}^{-1}$ (Fig. 3.41 and Table 3.31). In particular, the $\sim 5000\,\mathrm{cm}^{-1}$ gap between the ν(C–H) stretching and the first electronic modes determines the higher observed $E_{k,R}/E_{k,P}$ ratio (Table 3.27). If the proj/energy and proj/radius AO schemes are on average both centered around $16\,000\,\mathrm{cm}^{-1}$, the former reaches higher frequencies ($35\,000\,\mathrm{cm}^{-1}$ instead of $30\,000\,\mathrm{cm}^{-1}$), but actually the latter is slightly more distant from nuclear frequencies ($\sim 2700\,\mathrm{cm}^{-1}$). The proj and proj/energy AO distributions are in fact, on the lower end of the spectrum, closer ($\sim 2200\,\mathrm{cm}^{-1}$) to the nuclear modes.

3.4.3 Dichloroethylene ADMP test simulations: summary

At ts = 0.1 fs, both the current default and the new mass-weighting schemes can be employed in full-electron dichloroethylene ADMP B3LYP/6-31G(d,p) simulations. The Hessian-based scheme, in particular, gives lower deviations from the reference BO trajectory. The default and the energy-corrected projection-AO approaches allow also to employ a 0.2 fs time step. A triple-zeta 6-311G(d,p) basis set introduces some difficulties in the propagation. Nevertheless, now it can be employed (only) with the Hessian scheme and a 0.1 fs time step.



C–H rocking



C=C stretching

Figure 3.40: C–H rocking and C=C stretching vibrational bands from dichloroethylene B3LYP/6-311G(d,p) BOMD and ADMP simulations (ts = 0.1 fs).

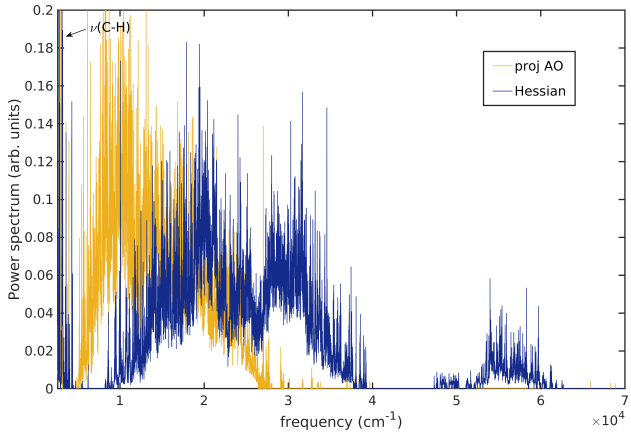
Table 3.29: Deviations $\Delta\nu$ (in cm^{-1}) of ADMP B3LYP/6-311G(d,p) dichloroethylene C–H rocking and C=C stretching frequencies from the BOMD reference values. Results from harmonic and anharmonic static vibrational calculations, as well as the experimental band positions from liquid-phase Raman spectroscopy [69], are also reported.

Dichloroethylene B3LYP/6-311G(d,p): vibrational spectrum				
experimental	harmonic	anharmonic	BOMD	
1272	1304	1281	1293	δ(C–H) (cm^{-1})
1578	1648	1602	1627	ν(C=C) (cm^{-1})

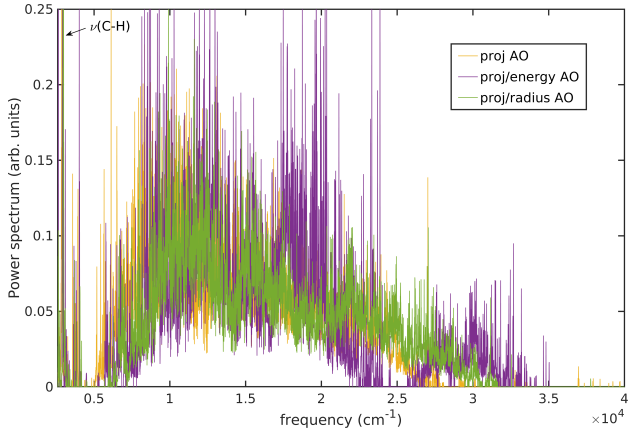
Dichloroethylene B3LYP/6-311G(d,p): ADMP - BOMD $\Delta\nu$ deviations			
	Time Step (fs)		
	0.1	0.2	
default			δ(C–H) (cm^{-1})
			ν(C=C) (cm^{-1})
scalar			
proj AO	-129	-381	
	-109	-313	
proj/energy AO	-95		
	-68		
proj/radius AO	-95	-313	
	-88	-279	
proj MO			
Hessian	-41	-143	
	-20	-109	

Table 3.30: Relative deviations of dichloroethylene B3LYP/6-311G(d,p) ADMP average nuclear kinetic energy from the BOMD (ts = 0.1 fs) value at the same level of theory.

Dichloroethylene B3LYP/6-311G(d,p): ADMP - BOMD $\Delta\langle E_{k,R}\rangle$		
	Time Step (fs)	
	0.1	0.2
default		
scalar		
proj AO	-22.3%	-52.9%
proj/energy AO	-16.9%	
proj/radius AO	-15.6%	-49.4%
proj MO		
Hessian	-7.5%	-23.4%



Proj AO *vs.* Hessian.



Proj *vs.* proj/energy *vs.* proj/radius AO.

Figure 3.41: Fictitious electronic dynamics from dichloroethylene B3LYP/6-311G(d,p) ADMP simulations (ts = 0.1 fs). The label indicates the highest nuclear fundamental vibration.

Table 3.31: Distribution of the fictitious electronic frequencies in dichloroethylene B3LYP/6-311G(d,p) ADMP simulations (ts = 0.1 fs). ν_{el} is reported as: wght. average (bandwidth).

Dichloroethylene B3LYP/6-311G(d,p): fictitious electronic frequencies			
	$\nu_{\mathrm{el}}\,(\mathrm{cm}^{-1})$	$\nu_{el} - \nu_N\,(\mathrm{cm}^{-1})$	τ_N/τ_{el}
default			
scalar			
proj AO	14422 (7880)	2219	1.77
proj/energy AO	16164 (8569)	2294	1.78
proj/radius AO	16409 (7787)	2723	1.92
proj MO			
Hessian	25503 (10908)	5112	2.64

3.5 $[Ru(dcbpy)_2(NCS)_2]^{4-}$ ('$N3^{4-}$') Ru(II) complex.

$N3^{4-}$ system was equilibrated for 2.6 ps. Temperature ($T = 300$ K) was controlled by velocity rescaling, applied every 225 fs. ADMP and BOMD 1 ps production runs were then collected.

3.5.1 B3LYP/SDD/def2-SVP level of theory.

In order to run a stable simulation, both the currently available methods require a valence mass greater than 0.1 amu bohr^2 (0.2 and 0.3 amu bohr^2 for the default and scalar schemes, respectively, Table 3.32). The projection-based AO schemes instead all employ a lower (0.1 amu bohr^2) μ^{val}, together with a small f^{cr} factor. The proj MO approach nevertheless also uses a 0.2 amu bohr^2 mass. The Hessian method proves to be stable with a 85 000 cm^{-1} maximum target frequency. In particular, due to the high dimension ($N_b = 687$) of the basis set, the 'diagonal' version of the Hessian approach was employed.

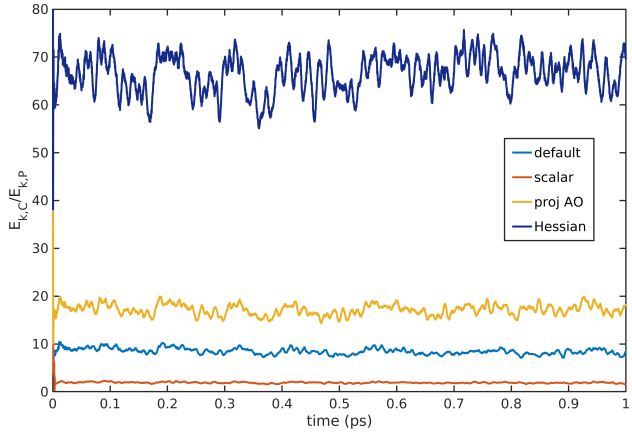
Time-domain analysis.

The scalar approach induces a low adiabaticity ($E_{k,R}/E_{k,P}$ around 2, Fig. 3.42 and Table 3.33), leading to a high deviation from the BO surface ($\|[\boldsymbol{F}, \boldsymbol{P}]\| \approx 23$, off-scale in Fig. 3.43), because of its high fictitious mass requirement (Table 3.32). The adiabaticity is higher with the default scheme, being the energy ratio nevertheless below 10. All the projection-based AO schemes allow instead better results; in particular, the 'simpler' proj AO method ($E_{k,R}/E_{k,P} \approx 17$) actually appears slightly more accurate than the more complex proj/energy and proj/radius ones. The proj MO scheme does not ensure instead the same degree of adiabaticity. Also for the $N3^{4-}$ system, the Hessian method offers the most accurate trajectory at the lower time steps, looking both at the kinetic energy ratio (~ 66) and the commutator norm (~ 0.037 hartree).

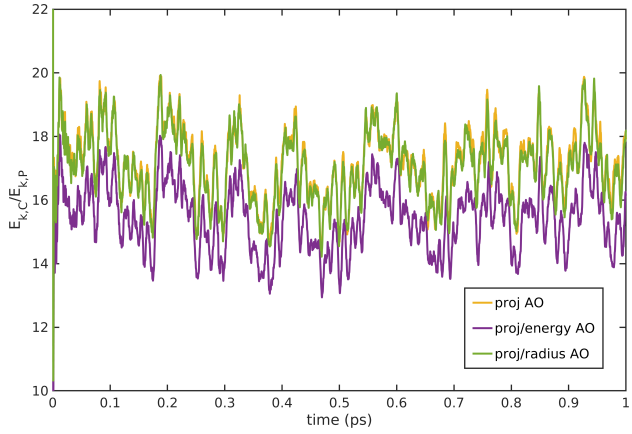
Excluding the scalar scheme, which induces high deviations from the BO surface, all the other approaches oscillate around the BO potential energy

Table 3.32: Mass parameters and norm of $\boldsymbol{\mu}$ matrix employed for $N3^{4-}$ B3LYP/SDD/def2-SVP ADMP simulations.

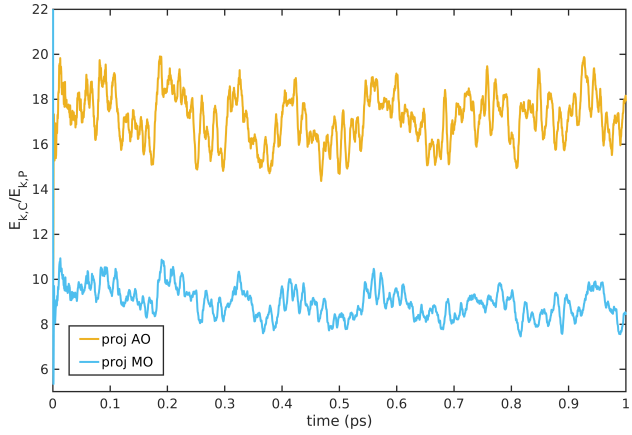
$N3^{4-}$ B3LYP/SDD/def2-SVP (N_b: 687): ADMP mass parameters		
	Time Step (fs)	
	0.1	
default	–, 0.2 130.04	f^{cr}, μ^{val} (amu bohr^2) / $\tilde{\nu}$ (cm^{-1}) $\|\boldsymbol{\mu}\|_F$ (amu bohr^2)
scalar	–, 0.3 7.86	
proj AO	6, 0.1 5.08	
proj/energy AO	2, 0.1 16.20	
proj/radius AO	2, 0.1 6.82	
proj MO	3, 0.2 6.69	
Hessian	85000 6.36	



Default *vs.* scalar *vs.* proj AO *vs.* Hessian.

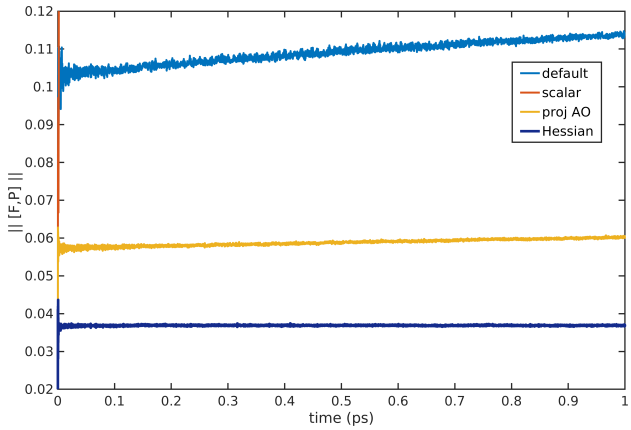


Proj *vs.* proj/energy *vs.* proj/radius AO.

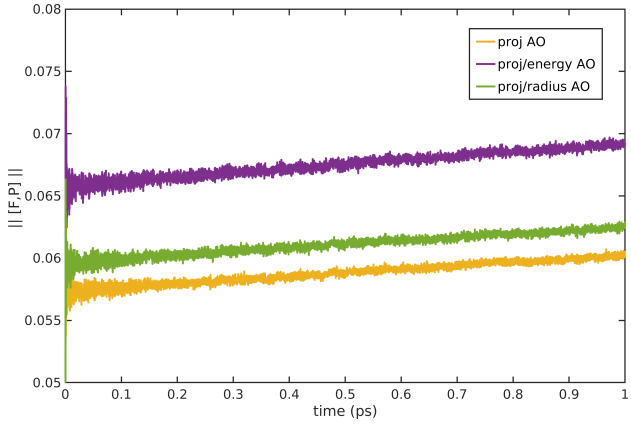


Proj AO *vs.* proj MO.

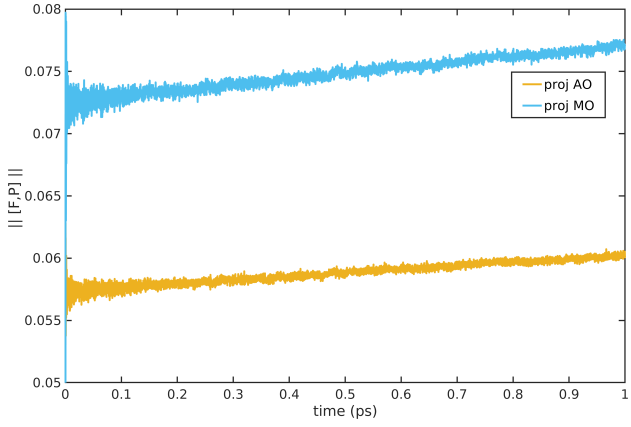
Figure 3.42: $N3^{4-}$ B3LYP/SDD/def2-SVP ADMP (ts = 0.1 fs) simulations: $E_{k,R}/E_{k,P}$ ratio.



Default *vs.* scalar *vs.* proj AO *vs.* Hessian.



Proj *vs.* proj/energy *vs.* proj/radius AO.



Proj AO *vs.* proj MO.

Figure 3.43: $N3^{4-}$ B3LYP/SDD/def2-SVP ADMP (ts = 0.1 fs) simulations: $\|[\boldsymbol{F}, \boldsymbol{P}]\|$ commutator norm.

Table 3.33: $N3^{4-}$ B3LYP/SDD/def2-SVP ADMP simulations; adiabaticity indicators. $E_{k,R}/E_{k,P}$, $\|[\boldsymbol{F},\boldsymbol{P}]\|$ and $|d\mathcal{H}_{\text{fict}}/dt|$ parameters are reported as: average (st.dev.).

$N3^{4-}$ B3LYP/SDD/def2-SVP: ADMP adiabaticity		
	Time Step (fs)	
	0.1	
default	8.5 (0.6)	$E_{k,R}/E_{k,P}$
	10.9 (0.3)	$\|[\boldsymbol{F},\boldsymbol{P}]\|$ $(\cdot 10^{-2}\,\text{Ha})$
	19 (4)	$\|d\mathcal{H}_{\text{fict}}/dt\|$ $(\cdot 10^{-5}\,\text{Ha fs}^{-1})$
	(2)	$s(E_{\text{tot}})$ $(\cdot 10^{-5}\,\text{Ha})$
scalar	1.9 (0.1)	
	2252 (2)	
	923 (1)$\cdot 10^3$	
	(600)	
proj AO	17 (1)	
	5.89 (0.08)	
	39 (4)	
	(2)	
proj/energy AO	15 (1)	
	6.8 (0.1)	
	34 (4)	
	(2)	
proj/radius AO	17 (1)	
	6.12 (0.08)	
	38 (4)	
	(2)	
proj MO	8.9 (0.7)	
	7.5 (0.1)	
	22 (4)	
	(2)	
Hessian	66 (4)	
	3.69 (0.01)	
	147 (5)	
	(3)	

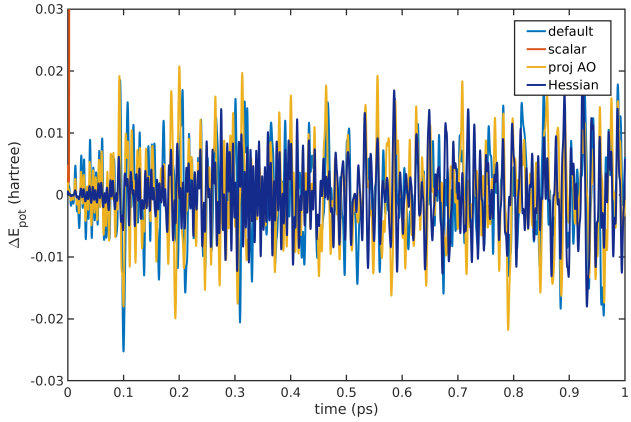
Table 3.34: ΔE_{pot}, ΔE_{tot}, RMSD Coor and RMSD m.w. Vel between $N3^{4-}$ B3LYP/SDD/def2-SVP ADMP test simulations and a BOMD reference trajectory (ts = 0.1 fs). Data are reported as mean (st.dev.).

$N3^{4-}$ B3LYP/SDD/def2-SVP: ADMP - BOMD deviations				
	ΔE_{pot} (10^{-4} hartree)	ΔE_{tot} (10^{-5} hartree)	RMSD Coor (10^{-2} bohr)	RMSD m.w. Vel (10^{13} amu$^{1/2}$ bohr s^{-1})
default	0 (70)	-840 (60)	70 (40)	6.1 (0.7)
scalar	38100 (90)	379800 (600)	70 (40)	6.1 (0.5)
proj AO	0 (70)	-430 (30)	70 (40)	6 (1)
proj/energy AO	0 (70)	-480 (40)	70 (40)	5.7 (0.9)
proj/radius AO	0 (70)	-430 (30)	70 (40)	6 (1)
proj MO	0 (70)	-790 (60)	70 (40)	6.1 (0.7)
Hessian	0 (60)	-117 (9)	70 (40)	4 (2)

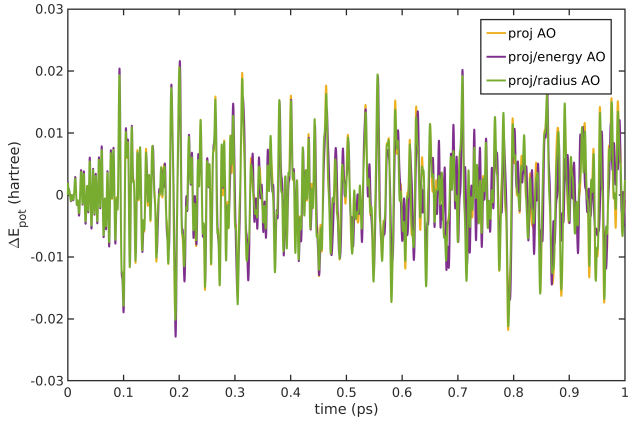
with a $\sim \pm 0.007$ hartree amplitude (Fig. 3.44 and Table 3.34). The total energy deviation from the BO trajectory (Fig. 3.45) is instead lower for the Hessian scheme ($\sim -1.2 \times 10^{-3}$ hartree), due to a lower error in the nuclear kinetic energy. In the explored simulation time (1 ps), the coordinates RMSD equally increases for all the approaches (Fig. 3.46). A similar velocities RMSD is shown by all the schemes (Fig. 3.47); the Hessian method in particular reaches this constant value more slowly than the other ones.

Frequency-domain analysis.

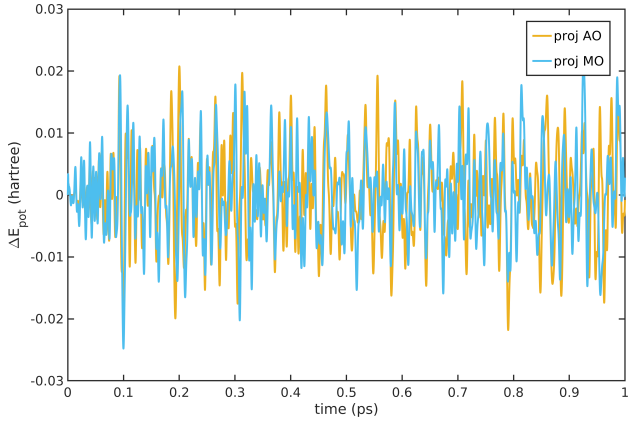
The dcbpy COO asymmetric stretching and the thiocyanate CN stretching (respectively located at $\sim$ 1600 and 2100 cm^{-1}) have been considered in order to evaluate the accuracy of the mass-weighting schemes. As expected, the Hessian method shows no error with respect to the BOMD calculated frequencies within the limited resolution allowed by the rather small (1 ps)



Default *vs.* scalar *vs.* proj AO *vs.* Hessian.

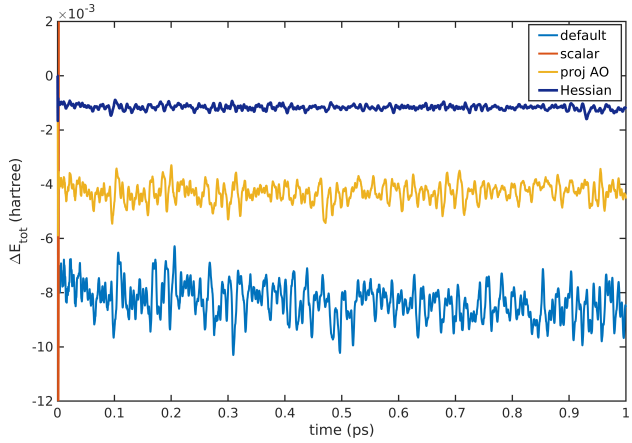


Proj *vs.* proj/energy *vs.* proj/radius AO.

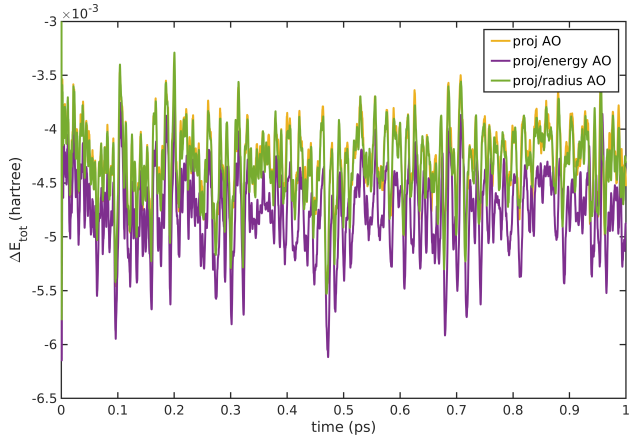


Proj AO *vs.* proj MO.

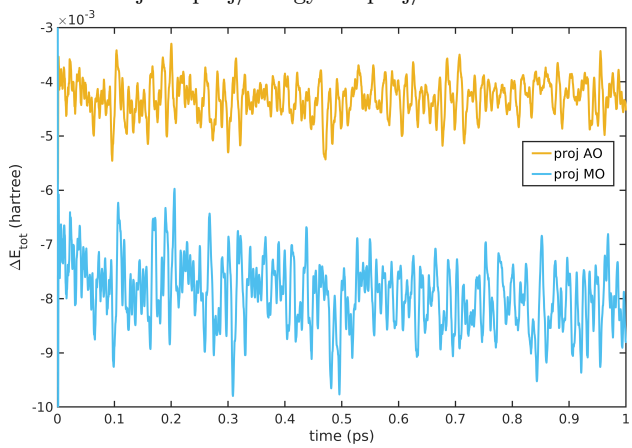
Figure 3.44: $N3^{4-}$ B3LYP/SDD/def2-SVP ADMP – BOMD (ts = 0.1 fs) E_{pot} deviations.



Default *vs.* scalar *vs.* proj AO *vs.* Hessian.

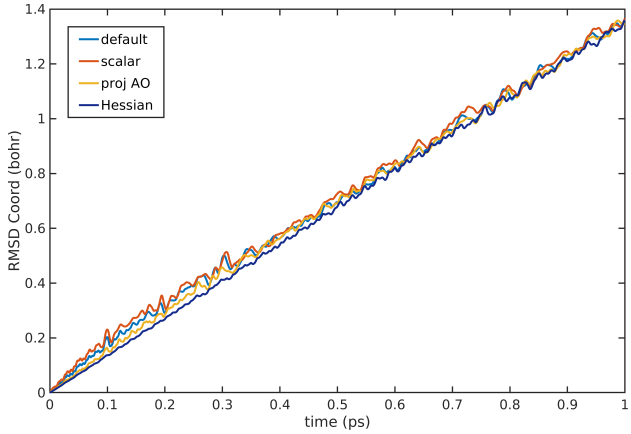


Proj *vs.* proj/energy *vs.* proj/radius AO.

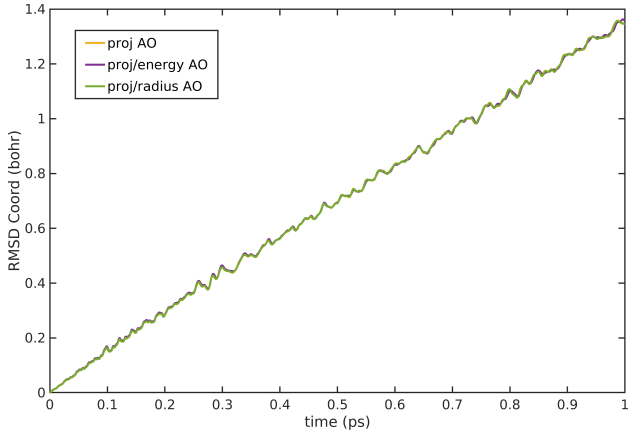


Proj AO *vs.* proj MO.

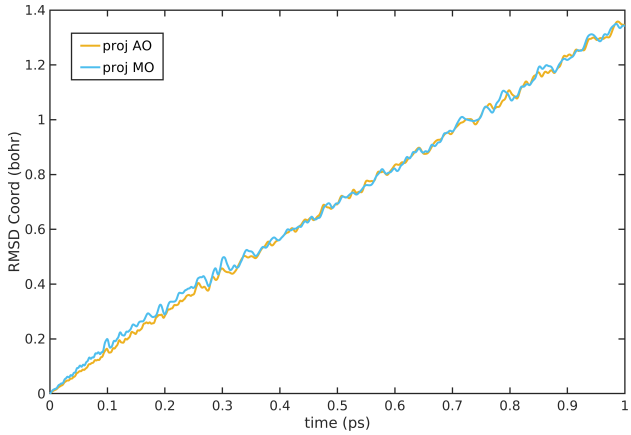
Figure 3.45: $N3^{4-}$ B3LYP/SDD/def2-SVP ADMP – BOMD (ts = 0.1 fs) $E_{\mathrm{tot,real}}$ deviations.



Default *vs.* scalar *vs.* proj AO *vs.* Hessian.

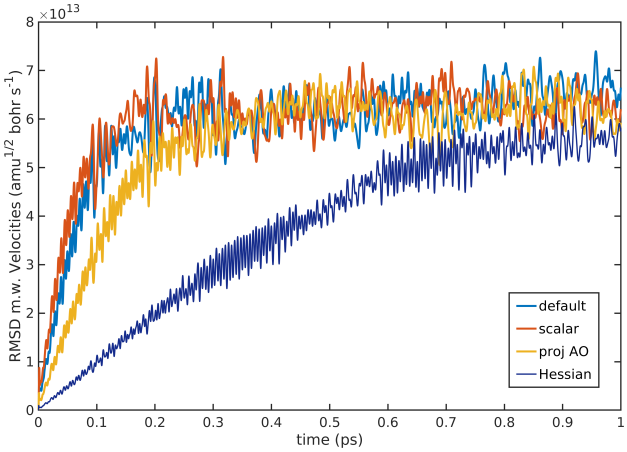


Proj *vs.* proj/energy *vs.* proj/radius AO.

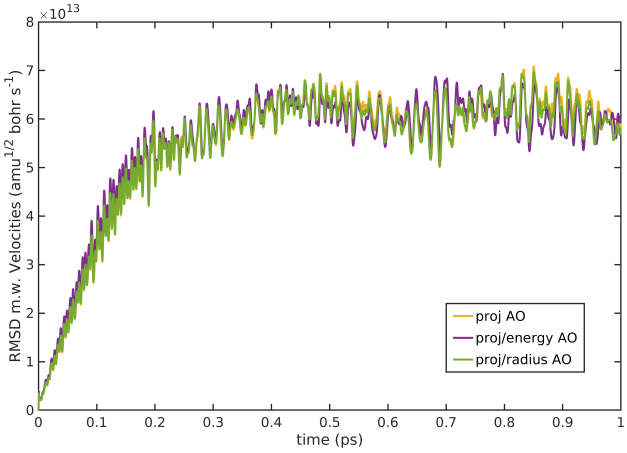


Proj AO *vs.* proj MO.

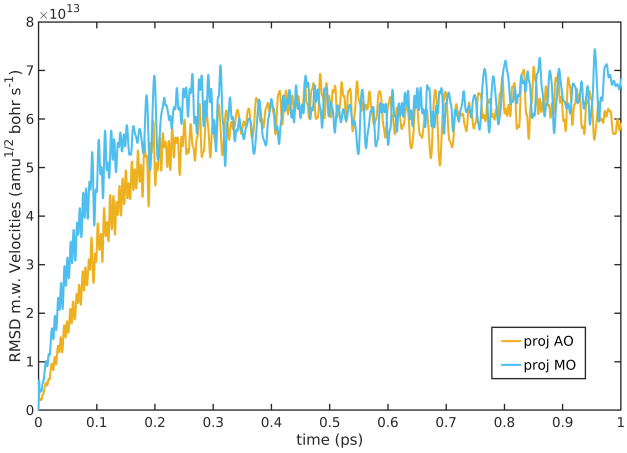
Figure 3.46: $N3^{4-}$ B3LYP/SDD/def2-SVP ADMP – BOMD (ts = 0.1 fs) RMSD of nuclear coordinates.



Default *vs.* scalar *vs.* proj AO *vs.* Hessian.



Proj *vs.* proj/energy *vs.* proj/radius AO.



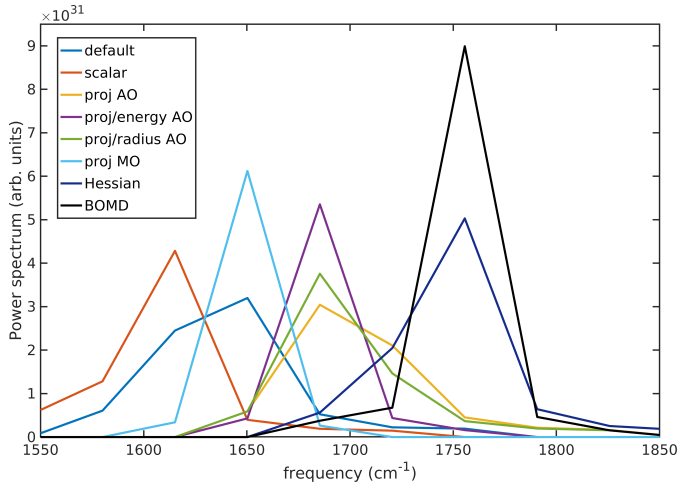
Proj AO *vs.* proj MO.

Figure 3.47: $N3^{4-}$ B3LYP/SDD/def2-SVP ADMP – BOMD (ts = 0.1 fs) RMSD of mass-weighted nuclear velocities.

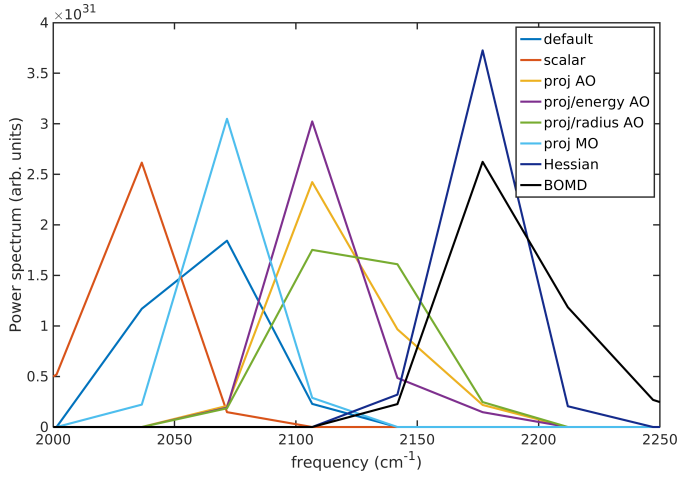
trajectory length (Fig. 3.48 and Table 3.35), as well as a reduced nuclear kinetic energy deviation (only 2%, Table 3.36). The projection-based AO schemes also induce still quite small frequency deviations ($-70\,\mathrm{cm}^{-1}$ for both bands), which instead exceed $100\,\mathrm{cm}^{-1}$ for the default and the proj MO schemes.

3.5.2 Ru-N3^{4-} ADMP test simulations: summary

N3^{4-} B3LYP/SDD/def2-SVP ADMP test trajectories reveal that only the newly developed mass-weighting schemes allow reduced deviations from the BO trajectory with a 0.1 fs time step. In particular, the Hessian-based method proves again the most accurate.



COO asymmetric stretching



CN stretching

Figure 3.48: COO asymmetric stretching and CN stretching vibrational bands from $N3^{4-}$ B3LYP/SDD/def2-SVP ADMP simulations (ts = 0.1 fs).

Table 3.35: Deviations $\Delta\nu$ (in cm^{-1}) of ADMP B3LYP/SDD/def2-SVP $N3^{4-}$ asymmetric COO and CN stretching frequencies from the BOMD reference values. Results from harmonic static vibrational calculations, as well as the experimental band positions (in water solution) [70], are also reported.

$N3^{4-}$ B3LYP/SDD/def2-SVP: vibrational spectrum			
experimental	harmonic	BOMD	
1596	1767	1756	ν_{asymm}(COO) (cm^{-1})
2120	2210	2177	ν(CN) (cm^{-1})

$N3^{4-}$ B3LYP/SDD/def2-SVP: ADMP - BOMD $\Delta\nu$ deviations		
	Time Step (fs)	
	0.1	
default	-105	ν_{asymm}(COO) (cm^{-1})
	-105	ν(CN) (cm^{-1})
scalar	-140	
	-140	
proj AO	-70	
	-70	
proj/energy AO	-70	
	-70	
proj/radius AO	-70	
	-70	
proj MO	-105	
	-105	
Hessian	0	
	0	

Table 3.36: Relative deviations of $N3^{4-}$ B3LYP/SDD/def2-SVP ADMP average nuclear kinetic energy from the BOMD (ts = 0.1 fs) value at the same level of theory.

$N3^{4-}$ B3LYP/SDD/def2-SVP: ADMP - BOMD $\Delta\langle E_{k,R}\rangle$	
	Time Step (fs)
	0.1
default	-10.6%
scalar	-14.7%
proj AO	-5.6%
proj/energy AO	-6.2%
proj/radius AO	-5.6%
proj MO	-10.1%
Hessian	-2.0%

3.6 Conclusions and future perspectives.

Strategies aimed at improving the performance and the accuracy of the extended-Lagrangian Atom-centered Density Matrix propagation (ADMP) Molecular Dynamics method have been pursued. In particular, achieving an adequate degree of adiabaticity between the nuclear degrees of freedom and the propagated electronic density, introduced as an additional fictitious degree, appears to be crucial in order to keep the electronic subsystem close to the exact Born-Oppenheimer (BO) state. This, in turn, can be obtained by a meta-stability condition characterized by well-separated nuclear and (fictitious) electronic power spectra in the frequency domain. Acting on the fictitious electronic mass (which is a tunable parameter introduced by extending the phase-space) therefore seems to be an effective way to control the fictitious electronic dynamics.

Non-homogeneous mass weighting schemes have been therefore introduced to limit the highest electronic frequencies and employ bigger time steps (reducing the computational cost), while increasing the lowest frequencies and keeping an acceptable nuclear/electronic adiabaticity (so collecting a correct trajectory). Two classes of weighting approaches have been developed. In the first one, a molecular core subspace is defined, starting from the core 'atomic MOs' belonging to each atom. Projecting each orthonormalized AO (for proj AO schemes) or MO (for proj MO schemes) onto this subspace, a decomposition into a valence and a core component is obtained. Assigning a distinct mass to the valence and each of the core unit vectors, such decomposition allows to calculate the mass attributed to each o.n. AO or MO. The same or distinct mass values can be assigned to each core vector, based upon their energy or their spatial extent. The second class assumes instead an harmonic motion of the density matrix at a fixed nuclear geometry. Electronic normal modes are thus defined from the diagonalization of the electronic mass-weighted Hessian. Then, a mass-matrix is derived, imposing a common frequency to all the modes.

The performances of the developed approaches have been evaluated by re-writing the involved subroutines in the Gaussian16 code and then collecting

several test trajectories, varying the simulated system, the basis set and the integration time step. Results show that a constant ('scalar') scheme often cannot ensure a sufficient adiabaticity even with rather small time steps (such as 0.1 fs), thus prompting for more adaptable approaches. On the other hand, the Hessian-based method always appears to be the most accurate at the lowest (0.1 and sometimes 0.2 fs) time steps, suggesting its potential employment in 'high-precision' ADMP calculations. The projection-based AO schemes, nonetheless, prove to be reliable options, also if a time step greater than 0.1 fs (such as 0.2 fs) is chosen to speed up the calculation. No substantial differences are found between the 'simple', the energy- and radius-modified projection AO methods, except with a full-electron third-period element and a >0.1 fs time step, when the energy-corrected proj AO scheme gives better results. Quite unexpectedly, assigning a mass to the MOs and then converting back to the o.n. AO basis often determines lower performances. Future investigations will be aimed to better explore this behavior. The use of a triple-zeta instead of a double-zeta split-valence basis set always increases the difficulty in correctly propagating the density matrix. In fact, a 0.1 fs time step appears to be already a limit value for this type of basis sets, moreover requiring a weighting method beyond those already available, such as the here developed projection- or Hessian-based ones.

Considering NMA B3LYP/6-31G(d,p) test trajectories, at 0.1 and 0.2 fs time steps the new projection-based schemes give only slightly lower deviations than the current default one, whose performances are themselves adequate. The Hessian-based approach, instead, proves highly accurate. With a 0.3 fs time step, only the projection-based AO schemes ensure a sufficient accuracy. The 6-311G(d,p) triple-zeta basis set can be now employed, with either the proj AO or the Hessian methods, together with a 0.1 fs time step. The latter approach is again the most accurate. At ts = 0.1 fs, both the current default and the new mass-weighting schemes can be employed in full-electron dichloroethylene ADMP B3LYP/6-31G(d,p) test simulations. The Hessian-based scheme, in particular, gives lower deviations from the reference BO trajectory. The default and the energy-corrected projection-AO approaches allow also to employ a 0.2 fs time step. A triple-zeta 6-311G(d,p)

basis set now can be employed with the Hessian scheme and a 0.1 fs time step. Only the newly developed mass-weighting schemes allow reduced errors with a 0.1 fs time step in $N3^{4-}$ B3LYP/SDD/def2-SVP simulations. In particular, the Hessian-based method proves again the most accurate.

Further studies are needed in order to understand if there is still room for improvement. Nevertheless, by expanding the useful range of levels of theory and by improving the accuracy/computational cost ratio, this work contributes to increase the capabilities of the ADMP formalism, which therefore can be considered a reliable alternative among the *ab initio* dynamical methods.

Chapter 4

Ground state characterization of $N3^{4-}$ Ru(II) complex in water solution: solvation and vibrational analysis.

4.1 Introduction

Many photocatalysis and light harvesting applications, such as dye-sensitized solar cells (DSSCs), rely onto metal-to-ligand charge transfer excited states (MLCTs) of transition metal complexes. [71–74]. A comprehension of MLCT states electronic and molecular relaxation pathways is thus fundamental in order to improve the efficiency of light harvesting devices. [75–77] In particular, the Ru(II) complex $[Ru(dcbpy)_2(NCS)_2]^{4-}$ (also called $N3^{4-}$, Fig. 4.1) has proven to be one of the most efficient solar cell dyes. [78, 79] A substantial amount of experimental evidences revealed several aspects of N3 CT and relaxation dynamics, both in solution and adsorbed on semiconductor surfaces. [80–87] The absorption in the two bands centered at 500 and 372 nm

populates a broad $Ru(NCS)_2 \rightarrow (dcbpy)_2$ ^{1}MLCT manifold. Then, an ultra-fast inter-system crossing (ISC) leads to a vibrationally excited ^{3}MLCT manifold, then relaxing on a picosecond time-scale. New insight about the fast N3 ISC have been recently offered by 2D electronic-vibrational spectroscopy in water solution. [70] The ^{1}MLCT states vibronically coupled to ^{3}MLCT vibrational modes and so likely involved in the ISC were in fact identified. Such states, called $^1MLCT_A$ and $^1MLCT_B$, respectively located at 24 400-24 700 cm^{-1} and 25 000-25 300 cm^{-1}, are characterized by a density redistribution from the $Ru(NCS)_2$ moiety towards the dcbpy rings, with a transition dipole moment on the equatorial plane.

In the first part (Chapter 4), a solvation and vibrational analysis of ground state $N3^{4-}$ in water solution is shown. In particular, a Molecular Dynamics-based generalized normal modes approach allowed to investigate how $N3^{4-}$ vibrational spectroscopic features are affected by water solvation, also contributing to the interpretation of experimental spectra.

At the same time, the electronic reorganization occurring immediately after $^1MLCT_A$ and $^1MLCT_B$ excitation and before any other electronic or structural relaxation, while contributing to the fate of this states, is instead still elusive, at least from an experimental point-of-view. Therefore, in the second part (Chapter 5), the evolution of the $^1MLCT_A$ and $^1MLCT_B$ electronic density and so the dynamics of the photoinduced hole-electron pair in the ultra-fast regime have been investigated through a computational approach, also considering the potential effects by water solvation.

4.2 Methods

4.2.1 Ground state Molecular Dynamics in explicit solvent solution.

A ground state Molecular Dynamics (MD) trajectory in explicit water solution was collected. A spherical box (of 22 Å radius) comprised the $N3^{4-}$ molecule, treated at a QM B3LYP/SDD/def2-SVP level of theory (already validated for this compound [70]) and 1462 water molecules at an MM

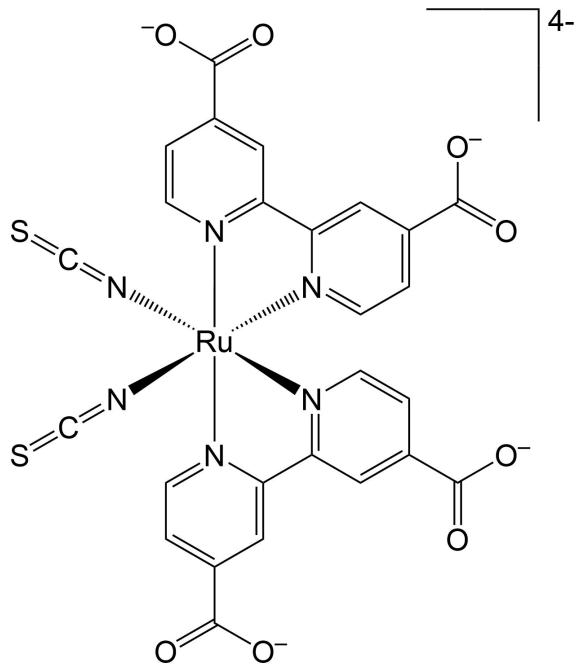


Figure 4.1: $[Ru(dcbpy)_2(NCS)_2]^{4-}$ "$N3^{4-}$" structure; dcbpy = 2,2'-bipyridyl-5,5'-dicarboxylic acid.

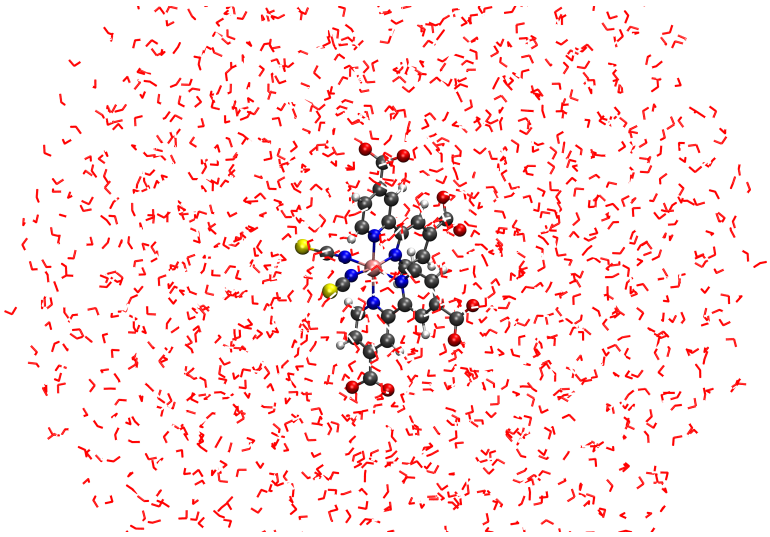


Figure 4.2: $N3^{4-}$ in a spherical water box. The solute (represented as ball-and-stick) is treated at a QM level, while the surrounding solvent (represented as lines) at a MM level.

level, described by the TIP3P force field (Fig. 4.2). [88] The electrostatic interaction between QM and MM layers was treated including the MM charges in the QM Hamiltonian (i.e., an 'electronic' embedding). General AMBER Force Field [89] atom types (and so van der Waals non-bonding parameters) were assigned to the $N3^{4-}$ system. Non-periodic boundary conditions were introduced as a confining potential to avoid solvent diffusion outside the box. [54, 90, 55, 91] After an equilibration step, a $\sim 8.6\,\mathrm{ps}$ production run was collected. A $T = 298\,\mathrm{K}$ temperature was kept through velocity rescaling every 1 ps. The Atom-centered Density Matrix Propagation extended Lagrangian approach (ADMP) was employed: [28, 29] the density matrix in an orthonormal Gaussian, atom-centered, basis is propagated along with the nuclear degrees of freedom, avoiding a convergence procedure at each step. A mass-weighting scheme which attributes a higher mass to the core functions was chosen, together with a $0.2\,\mathrm{amu\,bohr}^2$ valence mass. This allowed to employ a 0.1 fs time step.

4.2.2 Molecular Dynamics-based vibrational analysis.

Besides routine normal mode vibrational analysis through diagonalization of the Hessian matrix evaluated at an energy minimum, generalized, anharmonic, normal modes at finite temperature can be extracted from a phase-space sampling given, for example, by a Molecular Dynamics trajectory.[92–95]

The generalized normal modes Q_k are defined such that their velocities $\dot{Q}_k$ are non-correlated:

$$\langle \dot{Q}_k(t)\dot{Q}_l(t)\rangle \approx \delta_{kl} \tag{4.1}$$

Generalized normal modes (GNMs) directions are the eigenvectors of the atomic mass-weighted velocities covariance matrix $\boldsymbol{K}$:

$$K_{ij} = \frac{1}{2}(m_i m_j)^{1/2}\langle v_i(t)v_j(t)\rangle \tag{4.2}$$

The frequency associated with each generalized mode can be then obtained by a Fourier transform of the generalized mode velocity autocorrelation (i.e., $\dot{Q}_k$ power spectrum):

$$P_k(\nu) = \int \langle \dot{Q}_k(\tau)\dot{Q}_k(\tau+t)\rangle_\tau \, e^{-i\omega t}dt = \left| \int \dot{Q}_k(t)e^{-i\omega t}dt \right|^2 \tag{4.3}$$

Generalized modes velocities are calculated as the projections of atomic mass-weighted velocities along the generalized modes directions.

Table 4.1: X-O(wat) radial distributions maxima $r_{\max}$ and integrated number of solvent molecules in the first shell. Labels are defined in Fig. 4.3.

	$r_{\max}$ (Å)	n_{wat}
S39	3.10	4.49
S43	3.10	4.38
O48	2.70	2.83
O49	2.70	3.51
O50	2.70	3.03
O51	2.70	3.70
O52	2.70	3.48
O53	2.70	3.16
O54	2.70	3.66
O55	2.70	3.10

4.3 Characterization of $N3^{4-}$ solvation through Molecular Dynamics.

The $N3^{4-}$ complex has several sites (NCS^- sulfur and dcbpy oxygen atoms) able to interact with the surrounding solvent (Fig. 4.3). Because of its high negative charge, a strong solvation by polar solvents (such as water) is expected. Solute-solvent $g(r)$ radial distribution functions reveal that the S(NCS^-)-O(wat) and O(dcbpy)-O(wat) most probable distances are 3.10 and 2.70 Å, respectively (Table 4.1). The solvent molecules are therefore closer to the oxygen sites, likely because of the dcbpy oxygens higher negative charge. While, on average, ~ 4 water molecules are around NCS^- sulfur atoms, $\sim$ 3-4 water molecules are in the O(dcbpy) first solvation shells.

Looking in detail to selected S-O(wat) and O-O(wat) radial distribution functions (Fig. 4.4), actually the sulfur solvation peak is located at a slightly higher distance than the oxygen peaks, but it does not appear less structured. Moreover, a second solvation shell around the oxygen sites can be detected at a 4.5-5 Å distance.

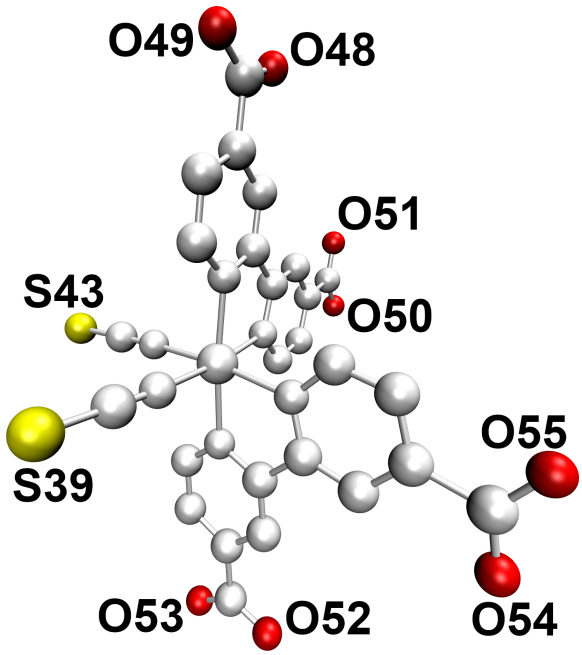


Figure 4.3: $N3^{4-}$ solvation sites. Dcbpy oxygen and NCS^{-} sulfur atoms are highlighted in red and yellow, respectively.

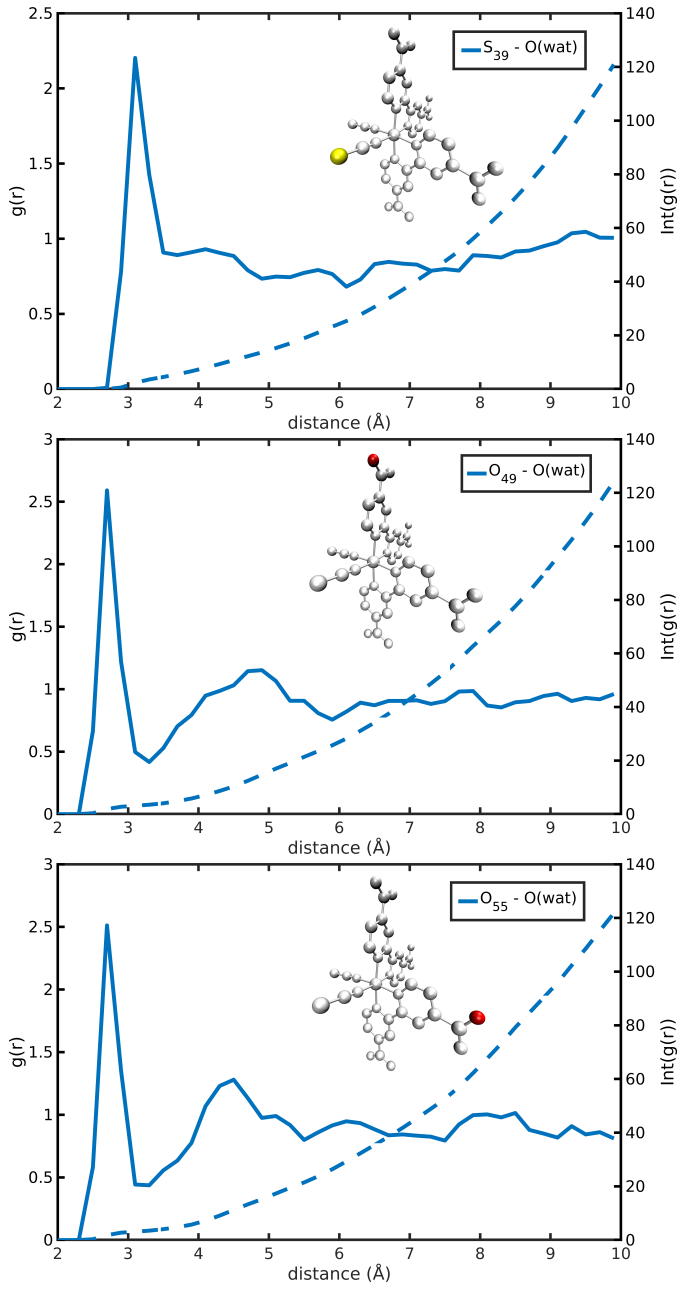


Figure 4.4: X-O(wat) radial distribution functions and integrated number of solvent molecules for selected S(NCS^-) and O(dcbpy) $N3^{4-}$ solvation sites.

4.4 N3^{4-} vibrational analysis in water solution through Molecular Dynamics.

A vibrational analysis of the sampled N3^{4-} MD trajectory in water solution necessarily includes both anharmonicity and solvent effects, which cannot be completely captured instead by 'static' vibrational calculations (i.e., evaluating the Hessian matrix on a minimum energy structure). In particular, dcbpy carboxy groups symmetric and asymmetric stretching and thiocyanates C=N and C=S stretching modes have been characterized through both approaches (Table 4.2 and Fig. 4.6). Two static vibrational calculations have been performed, one on a gas-phase optimized N3^{4-} structure and another on an optimized N3^{4-} • 10wat cluster (Fig. 4.5, one water molecule for each solvation site, Fig. 4.3) surrounded by implicit water, modeled through the Conductor-like Polarizable Continuum Model (C-PCM, [96, 97]). Several works have experimentally characterized the N3^{4-} IR absorption, in solution [70, 98], in the solid state and adsorbed onto TiO_2 films [78, 99]. Experimental frequencies from Ref. [70] are here provided for comparison, since they were measured in water solution as the calculated ones.

Considering first the symmetric COO^- stretching (experimentally found at 1375 cm^{-1}), the inclusion of solvent effects through the two distinct approaches (explicitly adding some QM water molecules and introducing an implicit bulk solvent, or a dynamics in explicit MM water) leads to opposite deviations from the harmonic gas-phase value (41 and -14 cm^{-1}, respectively), being the 'dynamical' approach more accurate (by -21 cm^{-1}), if compared to the experiment. Both solvent methods predict instead a red-shift of the asymmetric COO^- stretching (experimentally at 1596 cm^{-1}) from the gas-phase harmonic value (-67 and -146 cm^{-1}); the higher red-shift by the MD vibrational approach allows again a lower (25 cm^{-1}) error from the experimental value. While the inclusion of one explicit QM water molecule near each NCS^- ligand does not significantly alter the gas-phase C=N and C=S stretchings, the MD vibrational analysis reveals instead -130 and -34 cm^{-1} red-shifts, achieving a better accuracy in particular for the C=N stretching (a -40 cm^{-1} error from the 2120 cm^{-1} experimental value).

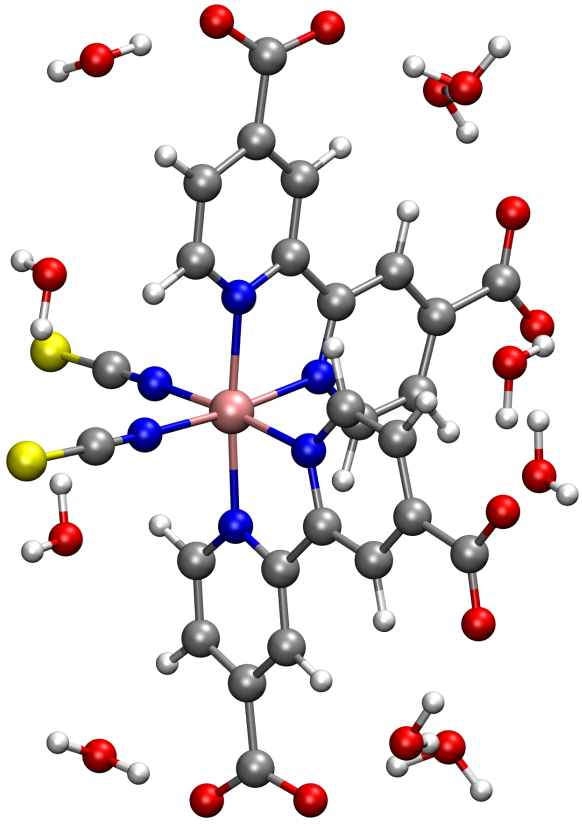
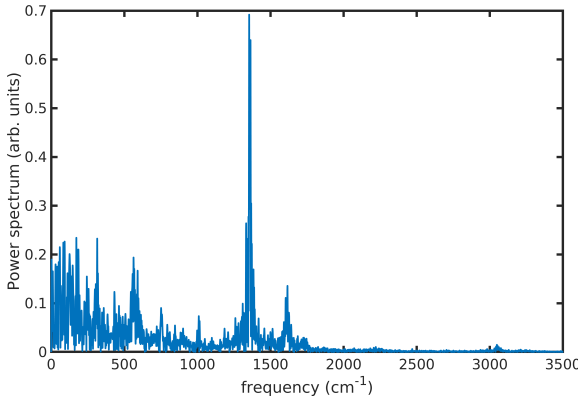


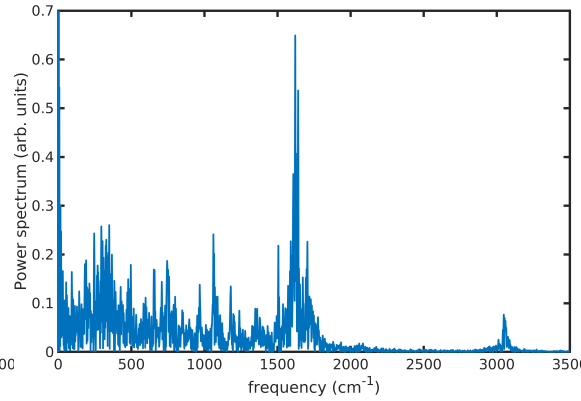
Figure 4.5: $N3^{4-} \bullet 10$wat cluster employed in static vibrational calculations. One water molecule is placed near each N3 solvation site.

Table 4.2: Selected $N3^{4-}$ vibrational frequencies obtained through static harmonic and dynamical vibrational analysis. If available, also experimental, water solution, values [70] are reported for comparison.

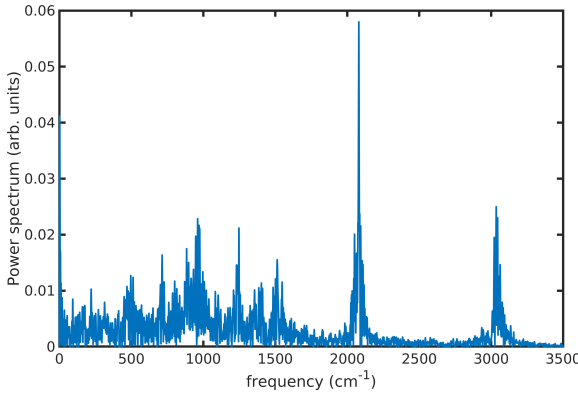
	experimental	static, harmonic		water MD
		gas-phase $N3^{4-}$	PCM/$N3^{4-} \bullet 10$wat	
ν_{symm}(COO) (cm^{-1})	1375	1368	1409	1354
ν_{asymm}(COO)	1596	1767	1700	1621
ν(CN)	2120	2210	2209	2080
ν(CS)		820	814	786



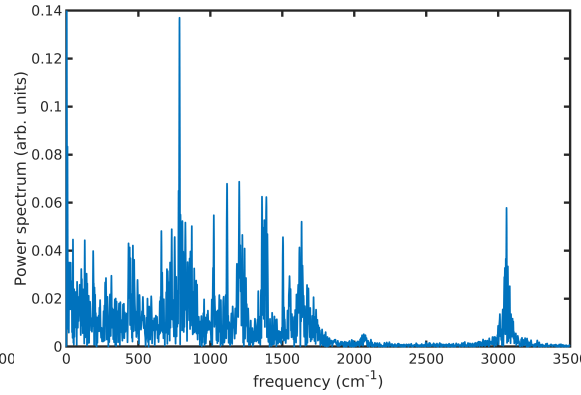
(a) $\nu_{\mathrm{symm}}(\mathrm{COO})$



(b) $\nu_{\mathrm{asymm}}(\mathrm{COO})$



(c) $\nu(\mathrm{CN})$



(d) $\nu(\mathrm{CS})$

Figure 4.6: Power spectra of selected generalized normal modes from $N3^{4-}$ dynamical vibrational analysis.

Chapter 5

Exploring the ultra-fast excited state electronic dynamics of Ru(II) $N3^{4-}$ complex.

5.1 Methods

5.1.1 The Real-Time Time-Dependent Density Functional Theory approach.

The recently developed real-time formulation of time-dependent Density Functional Theory (RT-TDDFT) [100–103] has been successfully applied to the study of the molecular response to electromagnetic fields, the prediction of spectroscopic properties and CT dynamics. [104–109]

Real-time methods explicitly propagate quantum systems in time by seeking solutions to the time-dependent Schrödinger equation (TDSE). In particular, a mean-field approximation leads to the TDDFT equation (in an orthonormal basis):

$$i\frac{d\boldsymbol{P}(t)}{dt} = [\boldsymbol{F}(t), \boldsymbol{P}(t)] \tag{5.1}$$

where $\boldsymbol{P}(t)$ is the density matrix and $\boldsymbol{F}(t)$ is the Kohn-Sham matrix. Eq. (5.1) now is not used to calculate the (linear) density response in the frequency domain, but to propagate the time-dependent density, observing how it responds to some perturbation in the time domain. $\boldsymbol{F}(t)$ time dependency arises not only from the time-dependent perturbation (if present), but from the time-dependent density $n(\boldsymbol{r}, t)$ through the Coulomb and exchange-correlation potentials. In particular, the v_{xc} potential is formally a functional of the density n at all the previous instants, the initial many-body state and the initial Kohn-Sham state. Actually, the common implementation of TDDFT employs just the instantaneous electron density (ignoring any "memory"), with a ground state DFT v_{xc} (the TDDFT adiabatic approximation). For excited state dynamics, the initial electronic structure can be prepared promoting an electron from an occupied to an unoccupied ground state MO without relaxation (a Koopman excitation). This is of course not a stationary state, but a superposition of the ground and the excited state of interest.

Eq. (5.1) is numerically integrated with the so-called modified midpoint unitary transformation (MMUT) algorithm:

$$\boldsymbol{P}(t_{k+1}) = \boldsymbol{U}(t_k)\boldsymbol{P}(t_{k-1})\boldsymbol{U}^{\dagger}(t_k) \tag{5.2}$$

$$\boldsymbol{U}(t_k) = \exp[-i2\Delta t\boldsymbol{F}(t_k)] = \boldsymbol{C}(t_k)\exp[-i2\Delta t\boldsymbol{\varepsilon}(t_k)]\boldsymbol{C}^{\dagger}(t_k) \tag{5.3}$$

where $\boldsymbol{U}(t_k)$ is the unitary transformation propagating the density $\boldsymbol{P}$, obtained from $\boldsymbol{F}(t_k)$ eigenvectors $\boldsymbol{C}(t_k)$ and eigenvalues $\boldsymbol{\varepsilon}(t_k)$.

5.1.2 Analysis of RT-TDDFT trajectories.

In order to disentangle the most relevant features underlying $N3^{4-}$ ^{1}MLCT electronic dynamics, several parameters were evaluated along the RT-TDDFT trajectories and analysed both in time and frequency domains. The time-evolving electronic density matrix propagated in a (Löwdin) orthonormal basis ($\boldsymbol{P}(t)$) is transformed back into the atomic orbitals (AO) basis ($\boldsymbol{P}'(t)$) and then projected onto the ground state MO basis (represented in the AO

basis by $\boldsymbol{C}'(0)$) as:

$$n_i(t) = \boldsymbol{C}_i'^{\dagger}(0)\boldsymbol{P}'(t)\boldsymbol{C}_i'(0) \tag{5.4}$$

where $n_i(t)$ is the occupation number of the $|\psi_i(0)\rangle$ ground state MO. In particular, the occupation of several $N3^{4-}$ frontier orbitals (from HOMO-20 to LUMO+20) was tracked.

The time-dependent electric dipole moment $\boldsymbol{\mu}(t)$ is a useful quantity to characterize the evolution of charge transfer states. It can be calculated as:

$$\mu_q(t) = \mathrm{Tr}\left[\boldsymbol{d}'^{(q)}\boldsymbol{P}'(t)\right] \tag{5.5}$$

where $\boldsymbol{d}'^{(q)}$ $(q = x, y, z)$ is the q-component of the one-electron electric dipole moment operator in the AO basis, $d'^{(q)}_{\mu\nu} = -\left\langle \phi'_\mu \middle| q \middle| \phi'_\nu \right\rangle$.

$N3^{4-}$ structure has been partitioned into seven fragments, comprising the distinct aromatic rings of each dcbpy ligand, the two NCS^- ligands and the Ru(II) metal ion (Fig. 5.1). Actually, for $N3^{4-}$ optimized structures NCS1 and NCS2, dcbpy1a and dcbpy2a, dcbpy1b and dcbpy2b fragments are equivalent because of the C_2 symmetry axis bisecting the NCS–Ru–NCS angle.

Time-evolving group charges were then obtained by atomic charges summation over each molecular fragment.

A cross-correlation analysis both in time and frequency domains can offer a deeper understanding of charge density transfer and redistribution mechanisms occurring in $N3^{4-}$ following the initial photo-excitation.

Considering $x(t)$ and $y(t)$ as two distinct (average-subtracted) time-series (such as time-dependent group charges), their normalized cross-correlation at time-lag τ was evaluated as:

$$r_{xy}(\tau) = \left(\langle x^2(t)\rangle\langle y^2(t)\rangle\right)^{-1/2}\langle x(t+\tau)\, y(t)\rangle \tag{5.6}$$

where the average was taken over the length of the trajectory:

$$\langle x(t+\tau)\, y(t)\rangle = \frac{1}{T}\int_0^T x(t+\tau)\, y(t)\, dt \approx \frac{1}{N}\sum_{i=1}^{N} x(t_i+\tau)\, y(t_i) \tag{5.7}$$

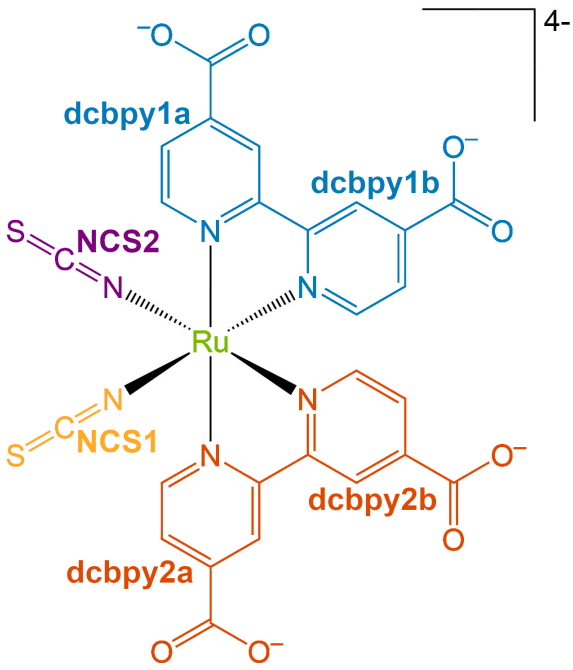


Figure 5.1: Partition of $N3^{4-}$ structure into molecular fragments.

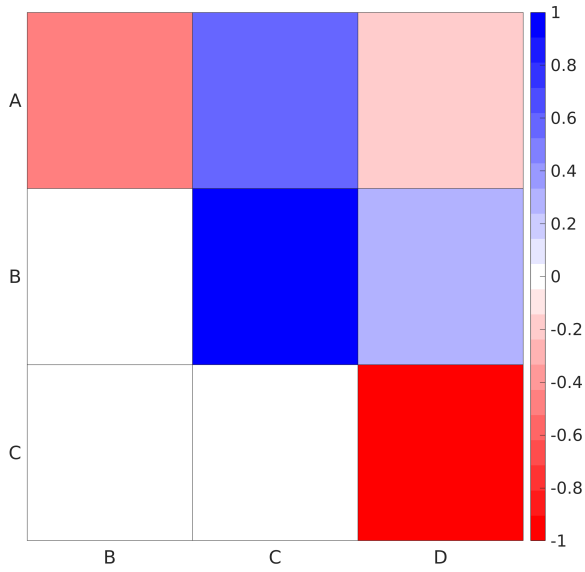


Figure 5.2: Example of a charge cross-correlation map. The molecular fragments are called A, B, C and D. r_{xy} is reported for each unique x/y pair (A/B, A/C, A/D, B/C, B/D, C/D) through a red/blue color scale. So, the B/C and C/D pairs show a high positive or negative correlation, respectively.

The $\left(\langle x^2(t)\rangle\langle y^2(t)\rangle\right)^{-1/2}$ normalization factor (i.e., the inverse square root of the product of the two auto-correlations at $\tau = 0$) allows $r_{xy}(\tau)$ to assume values in the $[-1, 1]$ interval. A high positive (negative) correlation $r_{xy}(\tau)$ at time-lag τ suggests a high correlation between $y(t)$ and $x(t)$ ($-x(t)$), the latter shifted by $-\tau$ along the time-axis.

A systematic evaluation of the cross-correlation for each unique pair of time-dependent group charges can be collected into a cross-correlation 'map' such as that shown in Fig. 5.2.

The cross power spectrum $|S_{xy}(\nu)|$ (i.e., the Fourier transform of the cross-correlation function) allows to detect common frequencies shared by $x(t)$ and $y(t)$. If calculated from time-dependent group charges, the charge-transfer frequency between two distinct $N3^{4-}$ molecular fragments (and so the charge carriers mobility) can be estimated. The Wiener-Khinchin

theorem allows to calculate $S_{xy}(\nu)$ directly from $x(t)$ and $y(t)$:

$$S_{xy}(\nu) = X^*(\nu)\, Y(\nu) \tag{5.8}$$

where $X(\nu)$ and $Y(\nu)$ are the Fourier transforms of $x(t)$ and $y(t)$, respectively.

Charge-transfer dynamics can be described through hole/electron pairs. Their barycenters can be calculated from the atomic charges:

$$\vec{r}_{h^+}(t) = \Big(\sum_{A^+} \Delta q_{A^+}(t)\Big)^{-1} \sum_{A^+} \Delta q_{A^+}(t)\, \vec{r}_{A^+} \tag{5.9}$$

$$\vec{r}_{e^-}(t) = \Big(\sum_{A^-} \Delta q_{A^-}(t)\Big)^{-1} \sum_{A^-} \Delta q_{A^-}(t)\, \vec{r}_{A^-} \tag{5.10}$$

where A^+ and A^- are positively or negatively charged atoms and $\Delta q_A(t)$ are atomic charges differences with respect to the ground state: $\Delta q_A(t) = q_A(t) - q_{A,S_0}$. Charge carriers velocities $\vec{v}_c(t)$ are then obtained by numerical differentiation of $\vec{r}_c(t)$, $c = h^+, e^-$ with a central finite difference approximation. RMS hole/electron distance

$$\langle d_{h^+/e^-} \rangle = \Big(T^{-1} \int_0^T \|\vec{r}_{h^+}(t) - \vec{r}_{e^-}(t)\|^2 dt\Big)^{1/2} \tag{5.11}$$

and velocities

$$\langle \vec{v}_c \rangle = \Big(T^{-1} \int_0^T \|\vec{v}_c(t)\|^2 dt\Big)^{1/2} \tag{5.12}$$

where $c = h^+, e^-$, can respectively account for the mean charge carriers separation and mobilities.

5.1.3 RT-TDDFT $N3^{4-}$ dynamics: initial conditions and computational details.

RT-TDDFT trajectories were propagated on fixed $N3^{4-}$ nuclear configurations, since it is reasonable to expect that the electronic reorganization immediately following the CT excitation (< 20 fs), which is the subject of this study, cannot be affected by nuclear motion.

In order to investigate the effect of solvation on the ultra-fast $N3^{4-}$

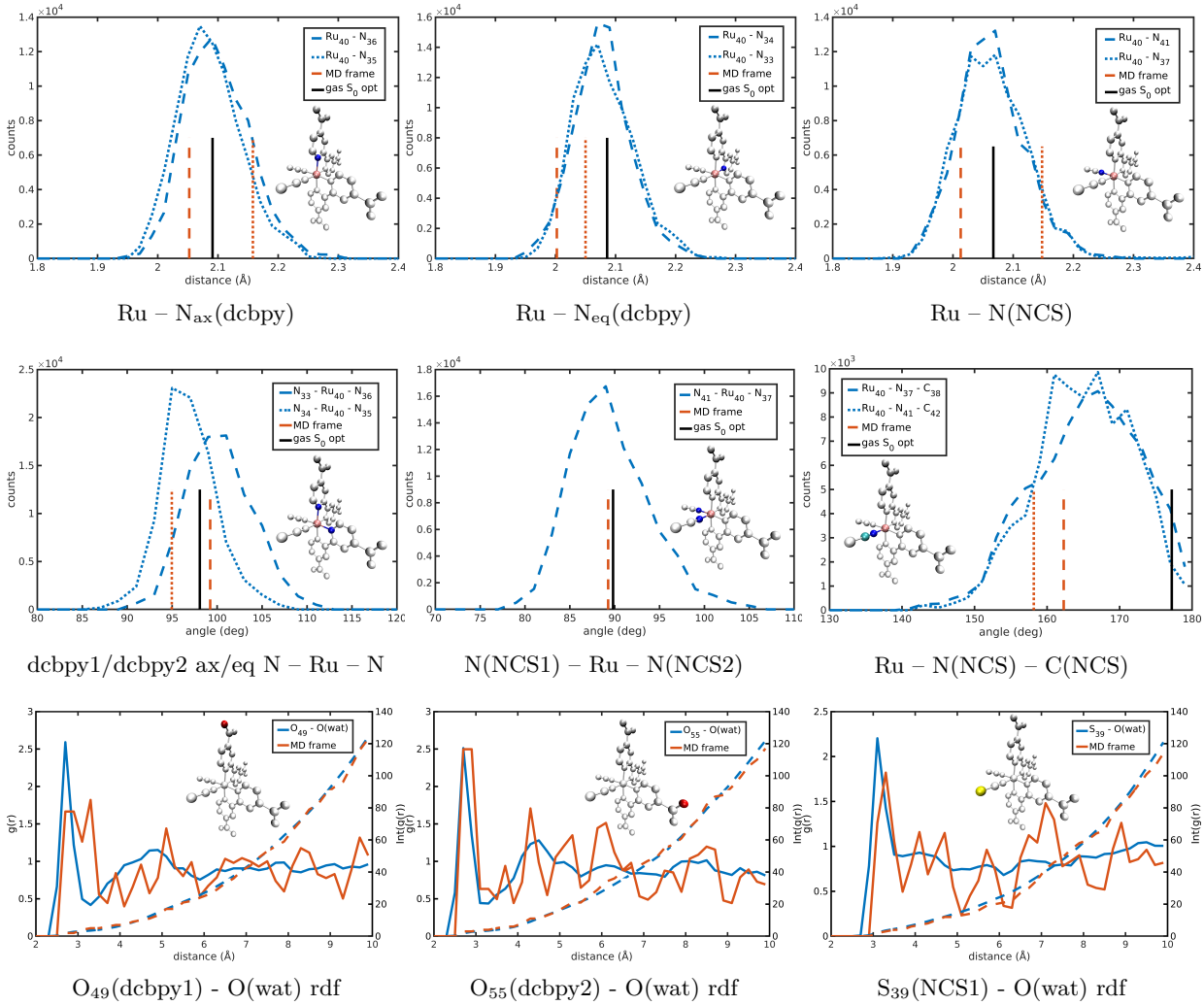
CT dynamics, distinct nuclear configurations were employed. Gas-phase reference simulations were performed on a C_2 symmetric $N3^{4-}$ structure (called M-G, Fig. 5.4), optimized at the ground state in gas-phase at the B3LYP/SDD/def2-SVP level of theory.

Comparing this gas-phase optimized structure to the structural distributions from the MD in water solution (Chapter 4), some differences in Ru(II) coordination geometry can be observed (Fig. 5.3). In particular, the isothiocyanate coordination appears much more bent ($\sim 167°$ Ru-N(NCS)-C(NCS) angle) in solution than in the gas-phase optimized structure, showing instead an almost linear ($\sim 177°$) arrangement. A solvent-induced desymmetrization seems moreover to affect the two axial-equatorial N(dcbpy1)-Ru-N(dcbpy2) angles, both slightly deviating from the gas-phase value.

A frame from the $N3^{4-}$ MD trajectory in explicit water solution was then randomly selected, in order to obtain a reliable configuration of both the $N3^{4-}$ solute and the surrounding water solvent molecules. Ru(II) coordination structural parameters, as well as the solvation around dcbpy carboxy O atoms and isothiocyanate S atoms, sampled by such MD frame are quite close to MD distributions maxima (Fig. 5.3). The number of solvent molecules close to solvation sites (on average, 3-4) is moreover comparable to that obtained from MD solute-solvent radial distribution functions.

A first structure, named D1-G (Fig. 5.4), was extracted from the selected MD frame retaining only the $N3^{4-}$ solute. This configuration is therefore (partially) representative of the average solvent-induced distortions, accounting only for an indirect solvent effect on the electronic dynamics. Then, the MD frame water molecules were included (D1-W structure). The first-shell solvent molecules were treated at a QM level and the other ones as point charges. The D1-W structure should therefore give an accurate prediction of solvent effects on $N3^{4-}$ CT dynamics, avoiding the potential over-polarization by close point charges.

For each structure, a linear response TD-B3LYP/SDD/def2-SVP excited state calculation was performed. The excited states characterized by transition dipole moments, Natural Transition Orbitals (NTOs, [110], see Section 5.2) and energy separations most similar to the $^1\mathrm{MLCT}_A$ and



Ru – N_{ax}(dcbpy) Ru – N_{eq}(dcbpy) Ru – N(NCS)

dcbpy1/dcbpy2 ax/eq N – Ru – N N(NCS1) – Ru – N(NCS2) Ru – N(NCS) – C(NCS)

O_{49}(dcbpy1) - O(wat) rdf O_{55}(dcbpy2) - O(wat) rdf S_{39}(NCS1) - O(wat) rdf

Figure 5.3: Distributions of selected $N3^{4-}$ structural parameters and solute-solvent radial distribution functions (rdf) from *ab initio* Molecular Dynamics simulation in explicit water solution. Values observed in the gas-phase optimized structure and in the MD frame employed for RT-TDDFT electronic dynamics are also shown.

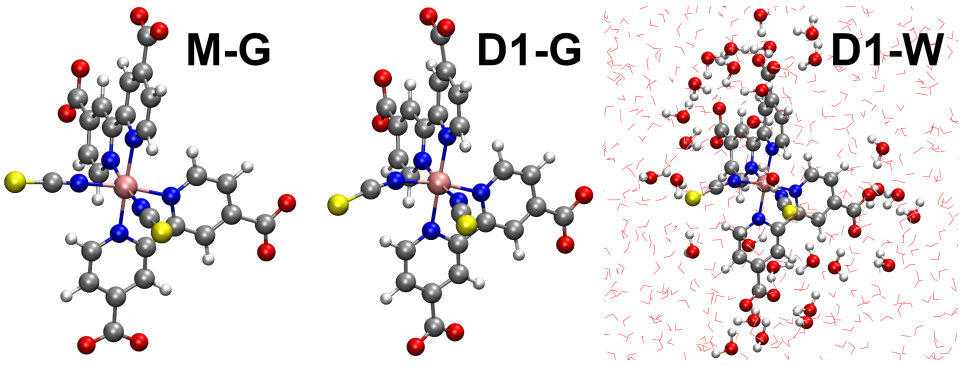


Figure 5.4: $N3^{4-}$ structures employed in $^1MLCT_A$ and $^1MLCT_B$ excited states propagation. M-G: Gas-phase S_0 minimum; D1-G: MD snapshot, only $N3^{4-}$; D1-W: MD snapshot, $N3^{4-}$ + first-shell QM water + water charges.

$^1MLCT_B$ states described in Ref. [70] were selected. Then, the initial states for RT-TDDFT simulations were prepared promoting an electron from an occupied to an unoccupied ground state MO (Section 5.1.1), according to the one-particle transition amplitudes shown by LR-TDDFT calculations.

RT-TDDFT $^1MLCT_A$ and $^1MLCT_B$ excited states simulations were performed for each structure at the TD-B3LYP/SDD/def2-SVP level with a development version of the Gaussian16 program. 25 fs trajectories were collected, employing a 0.001 fs (M-G, D1-G) or 0.002 fs (D1-W) time-step. Mulliken population analysis was performed every 50 steps.

Table 5.1: $N3^{4-}$ $^1MLCT_A$ and $^1MLCT_B$ excited states.

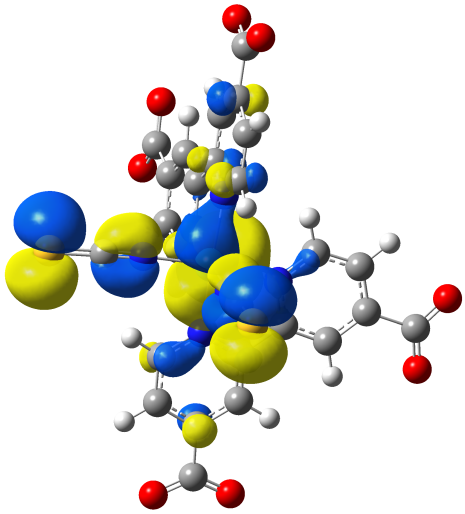
	Energy (cm^{-1})	osc. strength	character	structure
$^1MLCT_A$	24665	0.0012	HOMO-1 → LUMO+2 (S_{19})	M-G
	25565	0.0487	HOMO-1 → LUMO+3 (S_{33})	D1-G
	25421	0.0220	HOMO-1 → LUMO+3 (S_{11})	D1-W
$^1MLCT_B$	25424	0.0446	HOMO → LUMO+5 (S_{24})	
	25946	0.0384	HOMO → LUMO+5 (S_{36})	
	26441	0.0369	HOMO → LUMO+5 (S_{14})	

5.2 $N3^{4-}$ excited states.

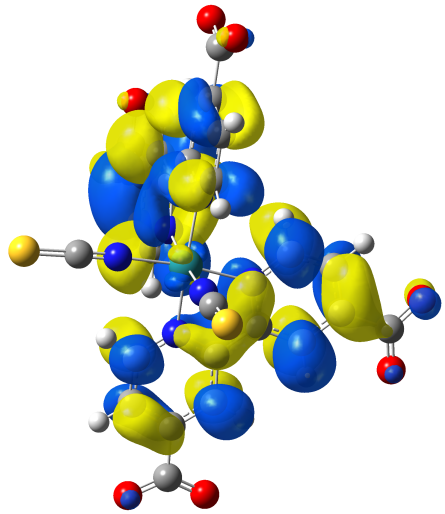
$^1MLCT_A$ and $^1MLCT_B$ $N3^{4-}$ excitations respectively involve the $N3^{4-}$ HOMO-1 or HOMO, populating distinct orbitals above the LUMO (Table 5.1). $^1MLCT_A$ state is quite dark in symmetric C_2 M-G structure, but brighter in the more distorted, MD derived, ones. The $^1MLCT_B$ - $^1MLCT_A$ calculated energy gap (M-G: 759 cm^{-1}, D1-G: 381 cm^{-1}, D1-W: 1020 cm^{-1}) is comparable to the experimental value from 2D electronic-vibrational spectroscopy ($\sim$ 450 - 650 cm^{-1}, [70])

As suggested by hole/electron NTOs spatial distributions (Fig. 5.5), the $^1MLCT_A$ excitation in the symmetric M-G structure moves electron density from $(NCS^-)_2$ π^* + Ru d orbitals towards π^* orbitals comprising the whole dcbpy ligands. In the distorted MD structures (Figs. 5.6 and 5.7), a remarkable asymmetry between the two NCS^- ligands characterizes the hole distribution, increasing with the introduction of surrounding water molecules (D1-W).

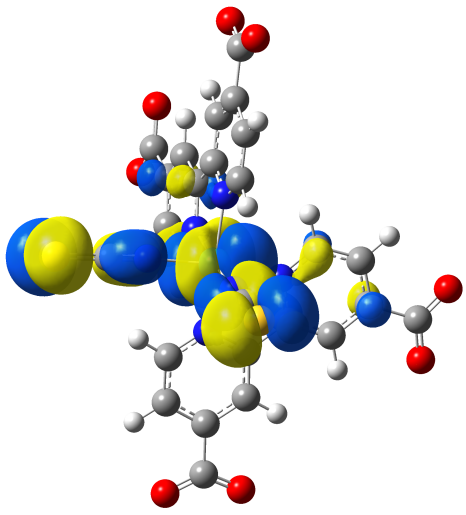
The $^1MLCT_B$ hole orbitals on the electron-donating $(NCS)_2Ru$ moiety are orthogonal to those contributing to $^1MLCT_A$ hole (Fig. 5.5). Moreover, in the symmetric M-G structure the electron density is transferred only on the dcbpy aromatic rings *trans* to the NCS^- ligands and so on the equatorial plane. Now the hole asymmetry on the two NCS^- groups in the solvent-distorted structures is not as high as in $^1MLCT_A$. (Figs. 5.6 and 5.7) However, the 'electron' distribution appears delocalized not only on the equatorial, but also on the axial dcbpy rings.



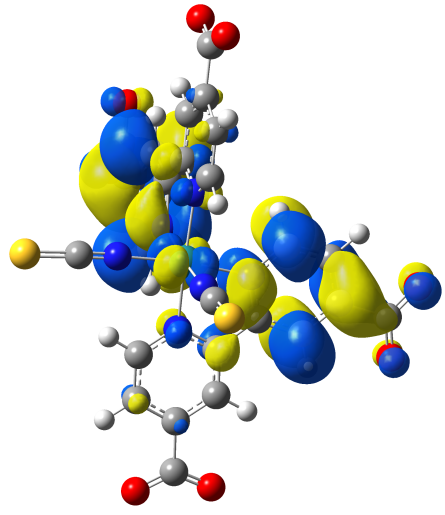
$^1\text{MLCT}_A$ "hole"



$^1\text{MLCT}_A$ "electron"

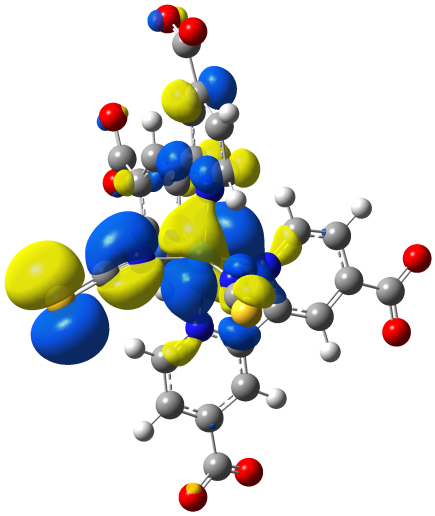


$^1\text{MLCT}_B$ "hole"

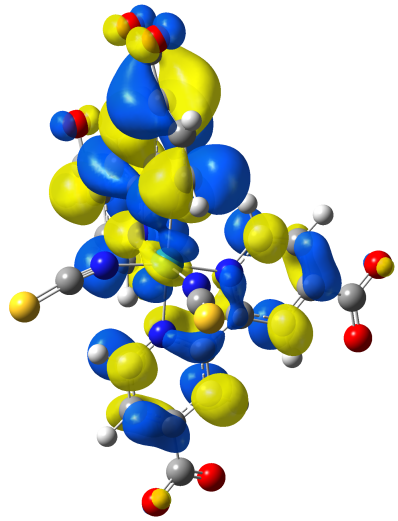


$^1\text{MLCT}_B$ "electron"

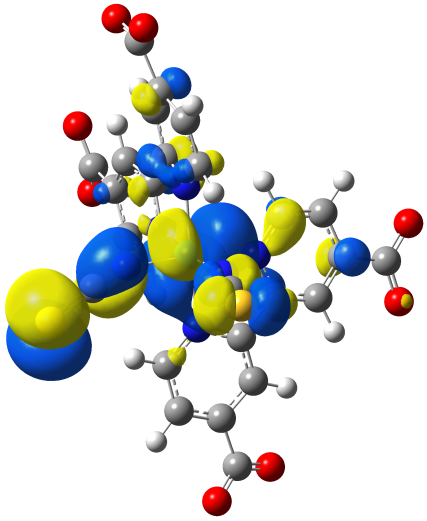
Figure 5.5: $^1\text{MLCT}_A$ and $^1\text{MLCT}_B$ excited states NTOs (M-G structure).



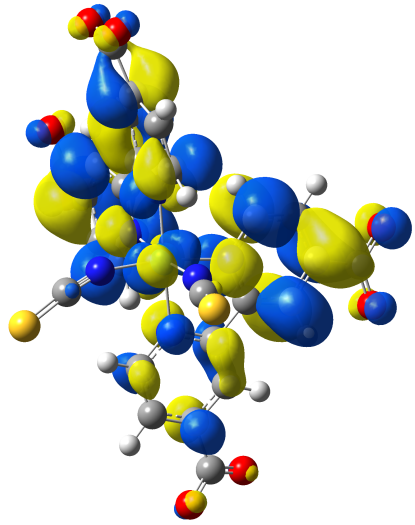
$^1\text{MLCT}_A$ "hole"



$^1\text{MLCT}_A$ "electron"

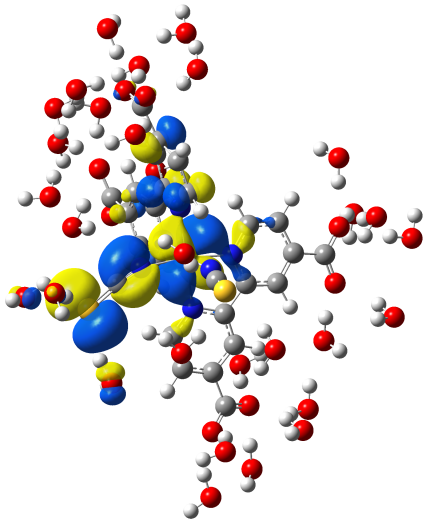


$^1\text{MLCT}_B$ "hole"

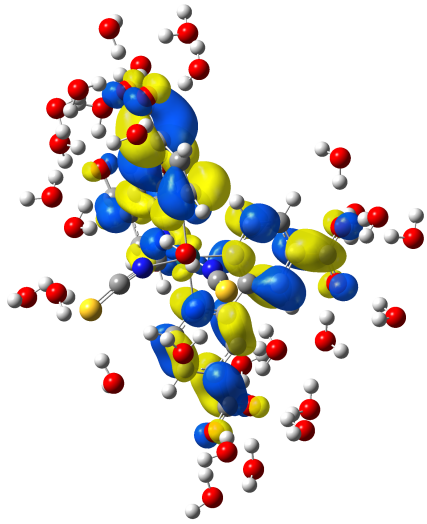


$^1\text{MLCT}_B$ "electron"

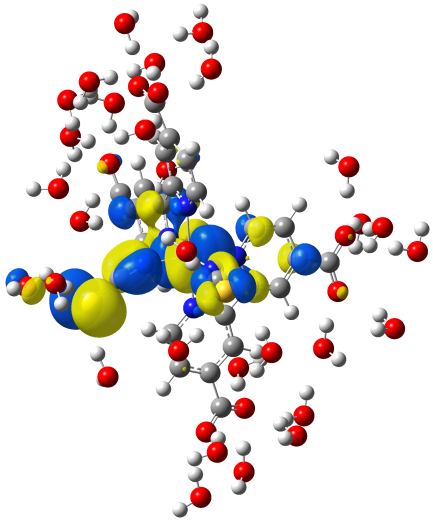
Figure 5.6: $^1\text{MLCT}_A$ and $^1\text{MLCT}_B$ excited states NTOs (D1-G structure).



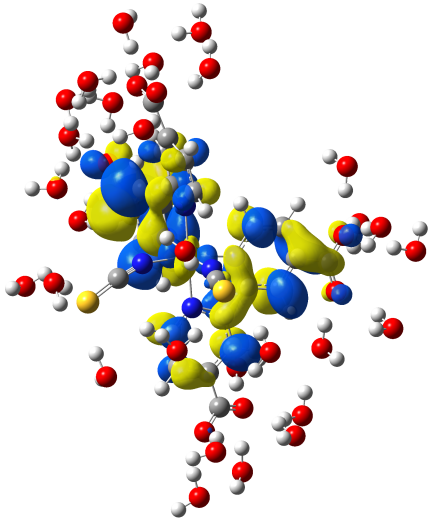
$^1\text{MLCT}_A$ "hole"



$^1\text{MLCT}_A$ "electron"



$^1\text{MLCT}_B$ "hole"



$^1\text{MLCT}_B$ "electron"

Figure 5.7: $^1\text{MLCT}_A$ and $^1\text{MLCT}_B$ excited states NTOs (D1-W structure).

5.3 ^{1}MLCT$_A$ and ^{1}MLCT$_B$ electronic dynamics: optimized gas-phase structure (M-G).

5.3.1 Charges and hole/electron distribution.

A dynamical picture of the hole-electron distribution can be obtained by time-dependent $\Delta q_F(t) = q_F(t) - q_{F,S_0}$ fragment charge differences with respect to S_0 state, with positive and negative values corresponding to the hole and electron, respectively.

The starting ($t = 0$) HOMO-1 $\rightarrow$ LUMO+2 (Figs. 5.39 and 5.40) ^{1}MLCT$_A$ excitation moves electron density from NCS^- ligands towards both the axial and equatorial dcbpy rings (Fig. 5.8). Charge density appears equally distributed on same-kind ligands (i.e., NCS1 and NCS2, dcbpy1 and dcbpy2) along all the simulation. Visual inspection of Fig. 5.8 and fragment charges cross-correlation analysis suggests a charge transfer between Ru+dcbpy1+dcbpy2 and NCS1+NCS2 (for instance, $r_{\mathrm{dcbpy1/NCS1}} = -0.89$, $r_{\mathrm{dcbpy1/Ru}} = 0.66$, $r_{\mathrm{NCS1/Ru}} = -0.83$, Figs. 5.9 and 5.10), acting at a $13\,343\,\mathrm{cm}^{-1}$ frequency (Fig. 5.10). The 'hole' thus oscillates between the Ru center and the two NCS^- ligands. A closer inspection of dcbpy ligands (sharing the 'electron') reveals also a small charge oscillation between the axial and equatorial aromatic rings ($r_{\mathrm{dcbpy1a/dcbpy1b}} = -0.77$), characterized by both slow and fast frequency components (2669, 13343 and $34\,691\,\mathrm{cm}^{-1}$, Fig. 5.10).

Hole and electron barycenters distributions are therefore respectively located on the $(NCS)_2$ and $(dcbpy)_2$ sides, exactly on the C_2 symmetry axis (Fig. 5.14), keeping a mean 2.179 Å distance (Table 5.2). Hole mobility ($1.223\,\mathrm{Å\,fs}^{-1}$) is clearly higher than the electron one ($0.6837\,\mathrm{Å\,fs}^{-1}$).

In contrast to the ^{1}MLCT$_A$ state, the starting ^{1}MLCT$_B$ HOMO $\rightarrow$ LUMO+5 excitation relocates NCS1 and NCS2 charge density only onto the dcbpy equatorial rings (Fig. 5.11). A fast ($17\,345\,\mathrm{cm}^{-1}$, Fig. 5.13) NCS1+NCS2/Ru charge oscillation ($r_{\mathrm{NCS1/Ru}} = -0.72$, Fig. 5.12) also characterizes ^{1}MLCT$_B$ time-evolution, leading to an 'hole' redistribution between the $(NCS)_2$ and Ru moieties. Dcbpy ligands, whose equatorial rings share the

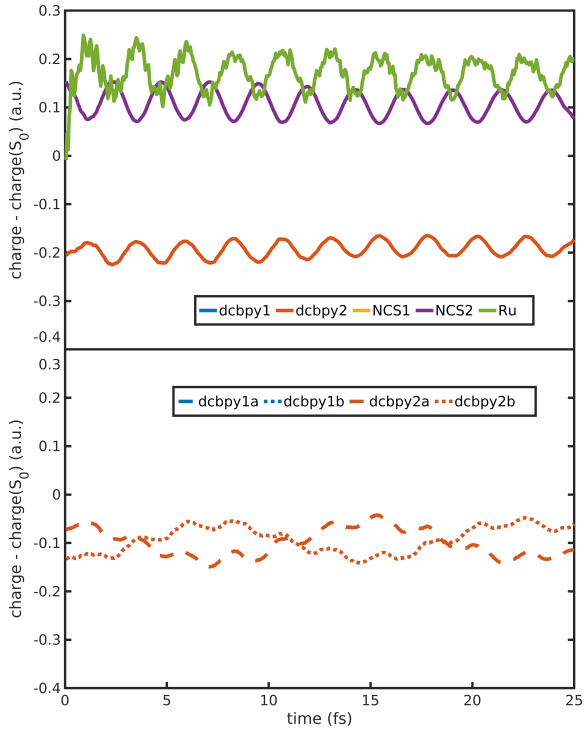


Figure 5.8: Fragments charges (with respect to the S_0 state) along $^1MLCT_A$ RT-TDDFT electronic dynamics (M-G structure). Dcbpy1 and NCS1 charges are actually equal to dcbpy2 and NCS2 ones, respectively.

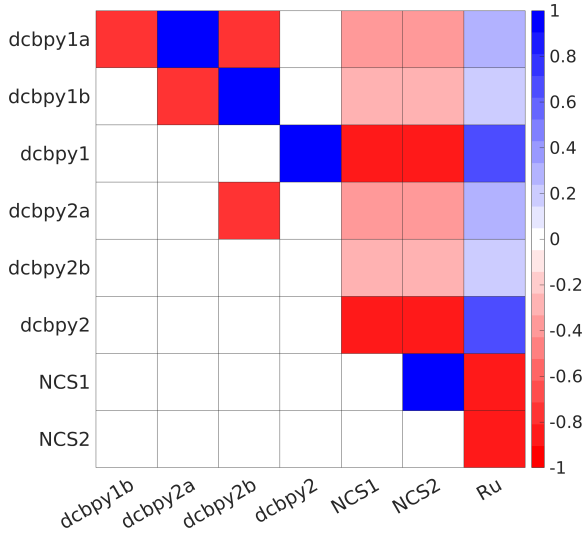


Figure 5.9: Normalized r_{xy} cross-correlations map between fragment charges time series from ^{1}MLCT$_A$ RT-TDDFT electronic dynamics (M-G structure).

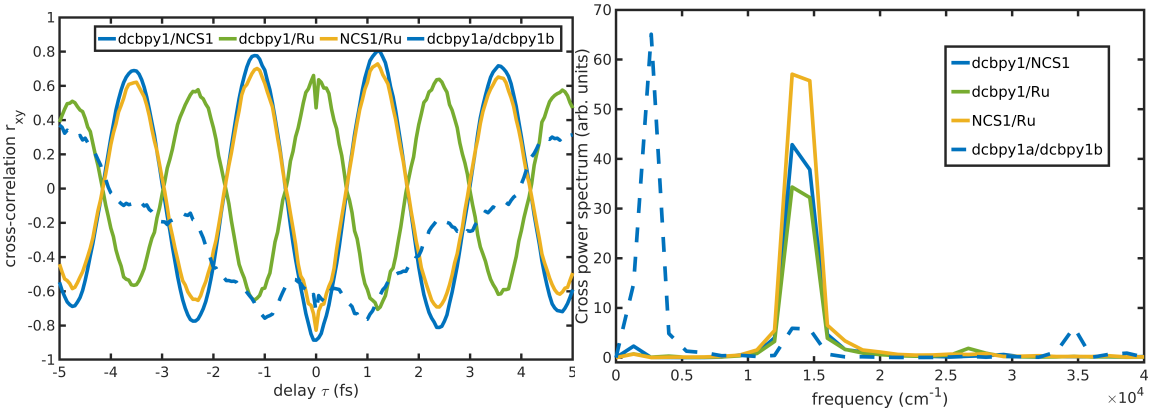


Figure 5.10: Cross-correlations and cross power spectra between selected pairs of fragment charges time-series collected in the ^{1}MLCT$_A$ RT-TDDFT dynamics (M-G structure).

Table 5.2: Hole - electron RMS distance and RMS velocities from $^1\mathrm{MLCT}_A$ and $^1\mathrm{MLCT}_B$ RT-TDDFT dynamics (M-G structure).

	d_{h^+/e^-} (Å)	v_{h^+} (Å fs^{-1})	v_{e^-} (Å fs^{-1})
$^1\mathrm{MLCT}_A$	2.179	1.223	0.6837
$^1\mathrm{MLCT}_B$	2.891	1.190	0.9390

'electron', seem instead to be unaffected by charge transfer processes, up until ~ 15 fs, when a substantial dcbpy1/dcbpy2 transfer takes place. Such slow ($<1334\,\mathrm{cm}^{-1}$, i.e. the actual FT resolution, Fig. 5.13) process mostly involves dcbpy equatorial rings ($r_{\mathrm{dcbpy1b/dcbpy2b}} = -0.90$), but also the axial ones ($r_{\mathrm{dcbpy1a/dcbpy2a}} = -0.70$). The electron thus becomes more concentrated onto the dcbpy2b equatorial ring. The $^1\mathrm{MLCT}_B$ excitation seems therefore to induce an unstable charge arrangement, evolving through a substantial (maybe transient) dcbpy1/dcbpy2 charge transfer and de-symmetrization, even in a symmetric $N3^{4-}$ structure.

The hole and electron barycenters are in fact non as symmetrically arranged as in $^1\mathrm{MLCT}_A$ dynamics (Fig. 5.14). Some sampled hole positions are in fact closer to the dcbpy1 ligand (corresponding to the ED snapshots with $\Delta q_{\mathrm{dcbpy1a}} > 0$ in the second half of the trajectory, Fig. 5.11), while the electron becomes displaced towards the dcbpy2b equatorial ring. The hole and the electron are moreover on average more distant (2.891 Å) than in $^1\mathrm{MLCT}_A$. While the hole mobility is similar to that in $^1\mathrm{MLCT}_A$ (1.190 Å fs^{-1}), a higher electron mobility (and more similar to the hole one, 0.9390 Å fs^{-1}) is instead found.

5.3.2 Electric dipole moment.

The electric dipole moment from $N3^{4-}$ excited states electronic dynamics has been projected onto three orthogonal directions defined by the Ru-NCS1, Ru-NCS2 and Ru-N(dcbpy1a) bonds.

In $^1\mathrm{MLCT}_A$ gas-phase propagation, the electric dipole moment is mainly parallel to the equatorial $N3^{4-}$ plane, along the NCS1-Ru-NCS2 bisector

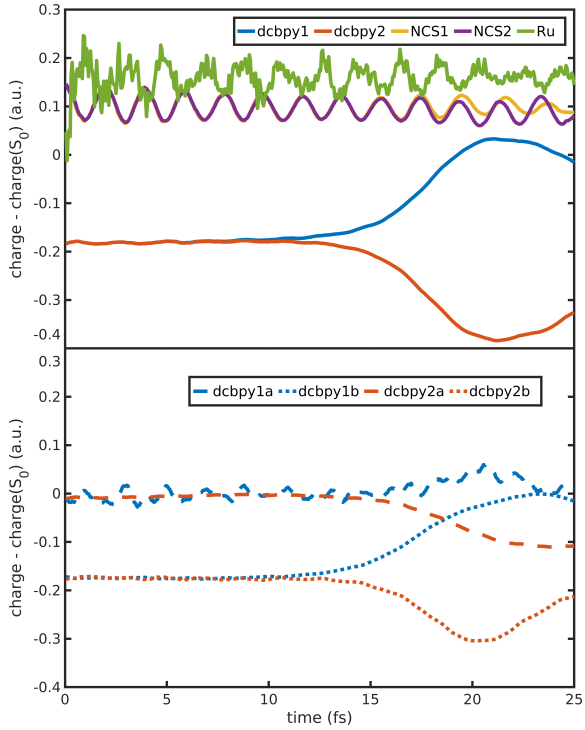


Figure 5.11: Fragments charges (with respect to the S_0 state) along $^1MLCT_B$ RT-TDDFT electronic dynamics (M-G structure).

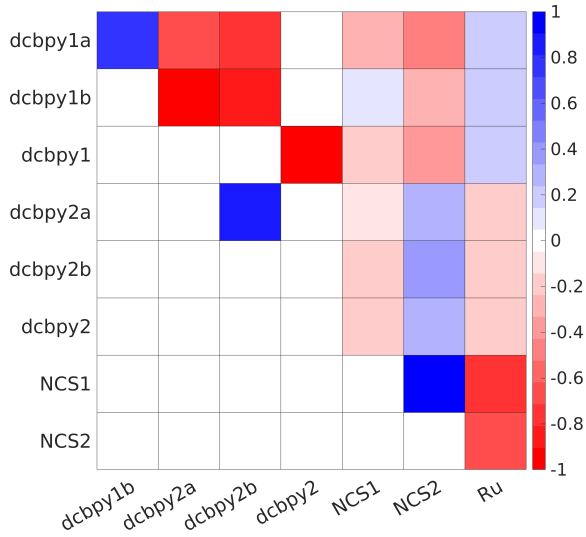


Figure 5.12: Normalized r_{xy} cross-correlations map between fragment charges time series from ^{1}MLCT$_B$ RT-TDDFT electronic dynamics (M-G structure).

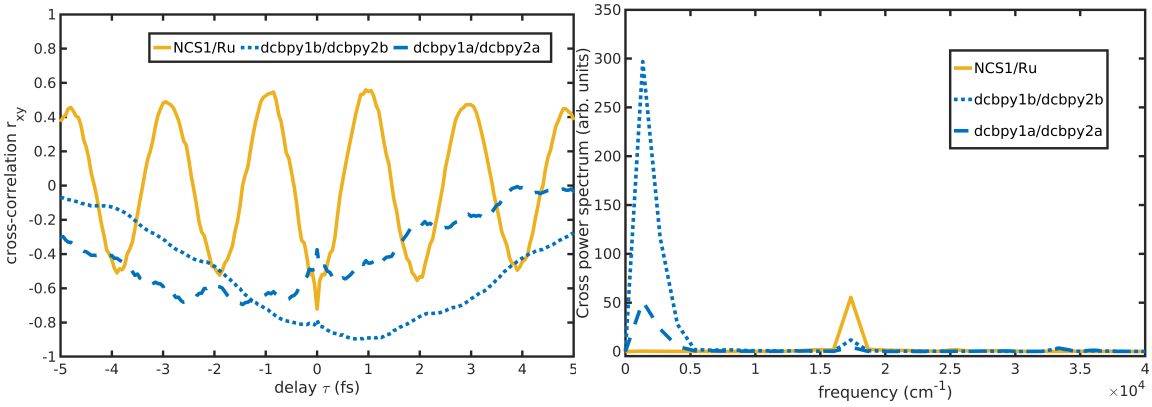


Figure 5.13: Cross-correlations and cross power spectra between selected pairs of fragment charges time-series collected in the ^{1}MLCT$_B$ RT-TDDFT dynamics (M-G structure).

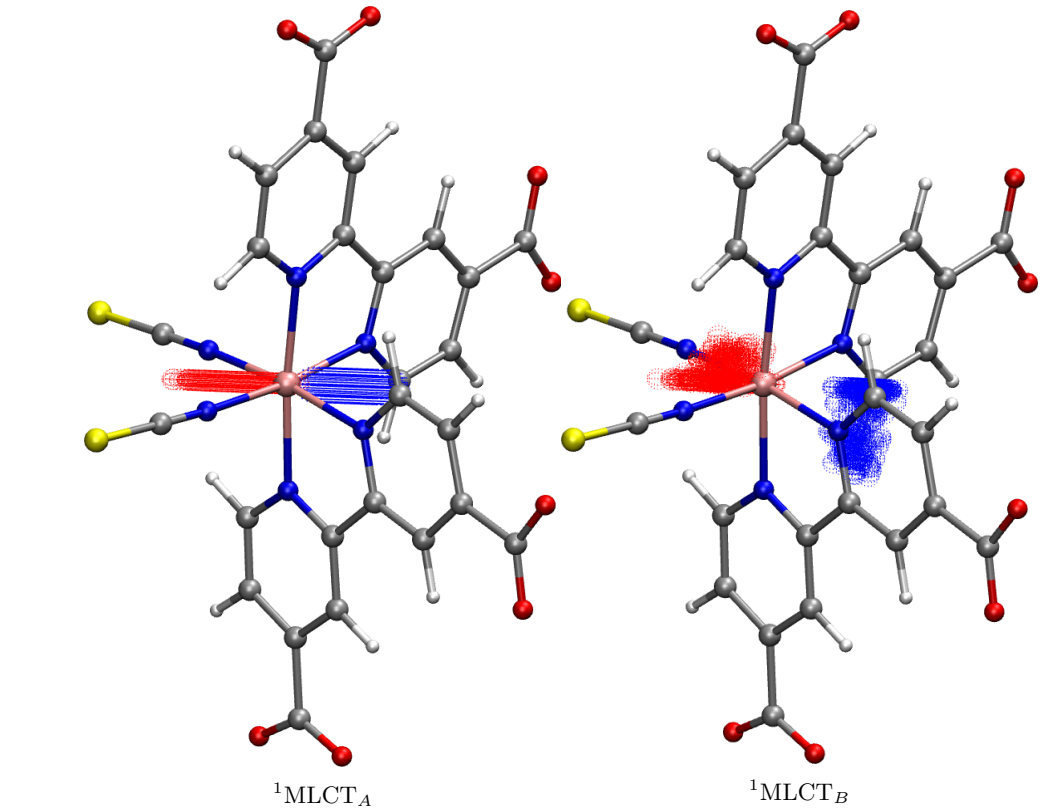


Figure 5.14: Hole and electron distributions from ^{1}MLCT$_A$ and ^{1}MLCT$_B$ RT-TDDFT dynamics (M-G structure).

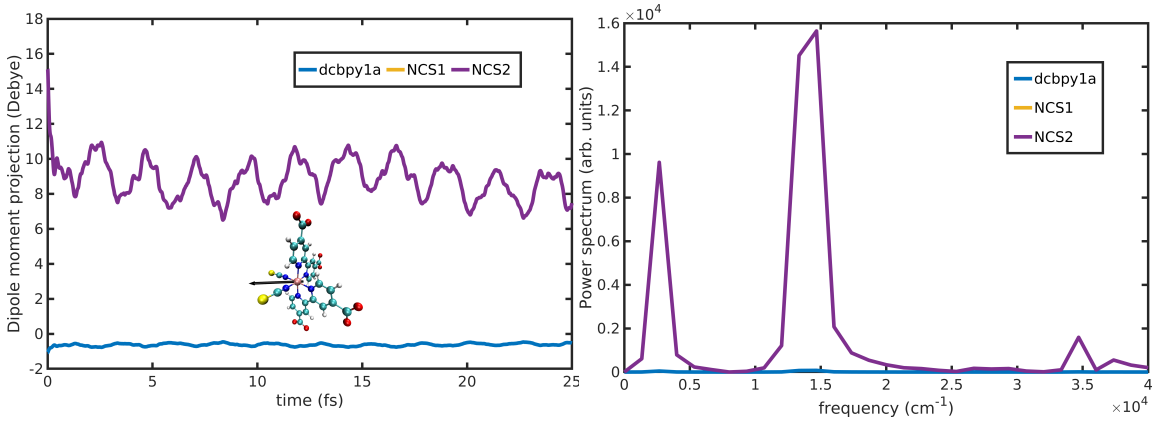


Figure 5.15: Time-dependent electric dipole moment projections along Ru-N(dcbpy1a), Ru-NCS1 and Ru-NCS2 bonds from ^{1}MLCT$_A$ electronic dynamics (M-G structure). Ru-NCS1 and Ru-NCS2 projections are actually equal along all the simulation.

(i.e., the C_2 symmetry axis), as shown by a low Ru-N(dcbpy1a) component and equal Ru-NCS1 and Ru-NCS2 ones (Fig. 5.15). The previously unveiled dcbpy1+dcbpy2+Ru/NCS1+NCS2 and the dcbpy axial/equatorial charge transfer mechanisms (Fig. 5.8) respectively contribute to in-phase 14 677 cm^{-1} and 2669 + 34 691 cm^{-1} charge displacements along the Ru-NCS1 and Ru-NCS2 axes (Figs. 5.10 and 5.15).

In ^{1}MLCT$_B$ gas-phase electronic dynamics, the time-dependent electric dipole moment is almost parallel to the C_2 symmetry axis until $\sim$ 15 fs (Fig. 5.16), due to the symmetric charge distribution shown in the first half of the trajectory (Fig. 5.11). The high-frequency 17 345 cm^{-1} in-phase dipole oscillations along the Ru-NCS1 and Ru-NCS2 axes can be related to the fast Ru/NCS1+NCS2 charge transfer (Fig. 5.13). The slow dcbpy1b/dcbpy2b equatorial and dcbpy1a/dcbpy2a axial charge flows occuring after $\sim$ 15 fs induce respectively, instead, low-frequency, $<$1334 cm^{-1}, out-of-phase changes of the two Ru-NCS1 and Ru-NCS2 dipole projections and a perturbation of the Ru-N(dcbpy1a) one. In the second half of the trajectory the electric dipole moment therefore departs from the NCS-Ru-NCS equatorial plane.

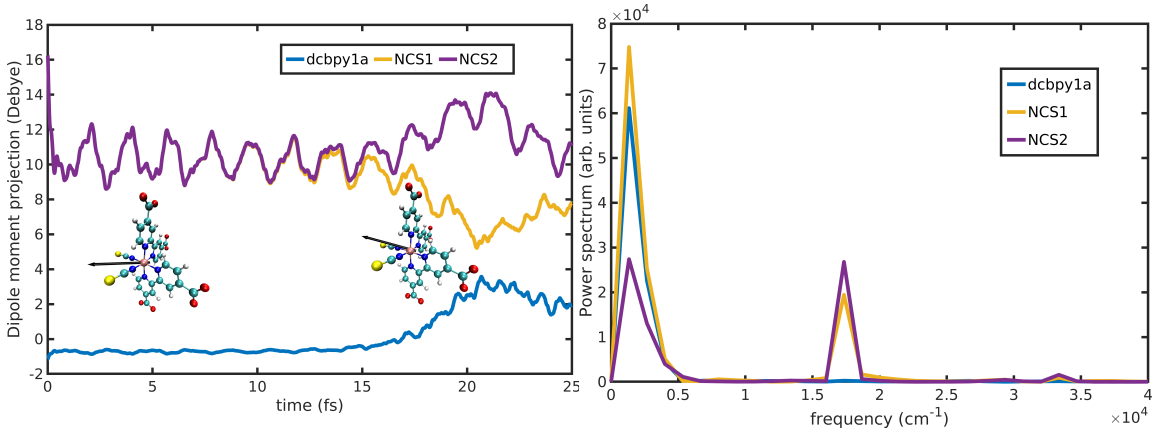


Figure 5.16: Time-dependent electric dipole moment projections along Ru-N(dcbpy1a), Ru-NCS1 and Ru-NCS2 bonds from ^{1}MLCT$_B$ electronic dynamics (M-G structure).

5.3.3 Molecular orbitals occupation numbers.

Ground state MOs occupation number dynamics has been partitioned into two distinct time scales (5 and 25 fs), in order to simplify the discussion.

Following the initial HOMO-1 → LUMO+2 ^{1}MLCT$_A$ excitation (Fig. 5.17), a $\sim 0.3e^-$ fast density oscillation between similar MOs sharing the hole (the NCS^- and Ru(II)-centered HOMO-17 and the initially depleted HOMO-1, Fig. 5.39) occurs. This process is clearly linked to the NCS1+NCS2/Ru charge oscillation. The small ($\sim 0.1e^-$) and slow exchange between LUMO+2 and LUMO+4 (both localized on the whole dcbpy ligands, Fig. 5.40) is instead representative of the electron redistribution between the axial and equatorial dcbpy rings.

After HOMO → LUMO+5 ^{1}MLCT$_B$ excitation (Fig. 5.18), the 'hole' (this time, in the HOMO) is shared with the similar NCS^- and Ru(II)-centered HOMO-18 orbital (Fig. 5.39) by high-frequency, medium-amplitude ($\sim 0.3e^-$), oscillations, describing in the MO basis the previously shown NCS1+NCS2/Ru exchange. The 'electron' is instead kept by LUMO+5 (localized on the dcbpy1b and 2b equatorial rings, Fig. 5.40) until $\sim$ 15 fs. The substantial (but maybe transient) density transfer towards LUMO+2 and LUMO+4 (distributed on the whole dcbpy ligands) can be linked to the

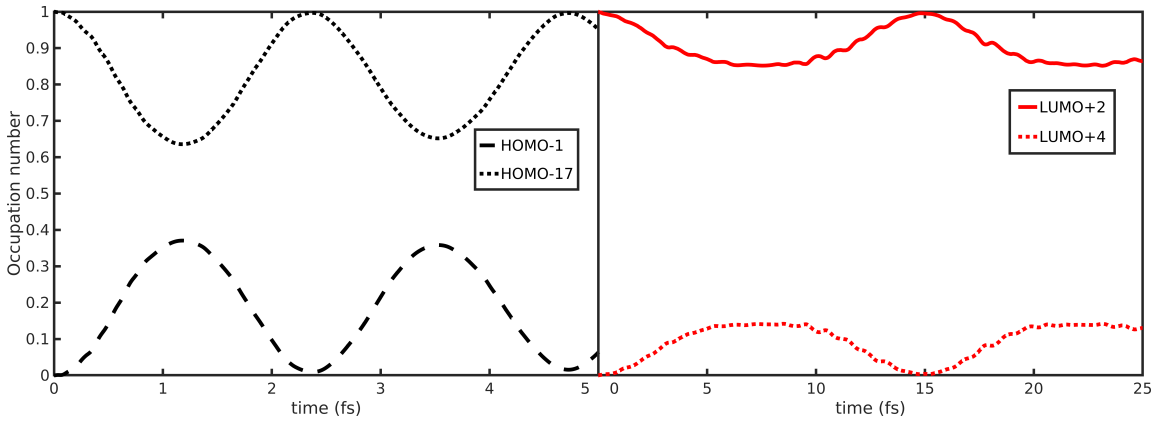


Figure 5.17: Occupation numbers of selected MOs from ^{1}MLCT$_A$ RT-TDDFT dynamics (M-G structure). Only MOs whose occupation significantly changes along the simulation are reported. Different (5 and 25 fs) time domains are employed to show fast (left panel) and slow (right panel) oscillations, respectively.

'electron' concentration onto the dcbpy2b equatorial ring.

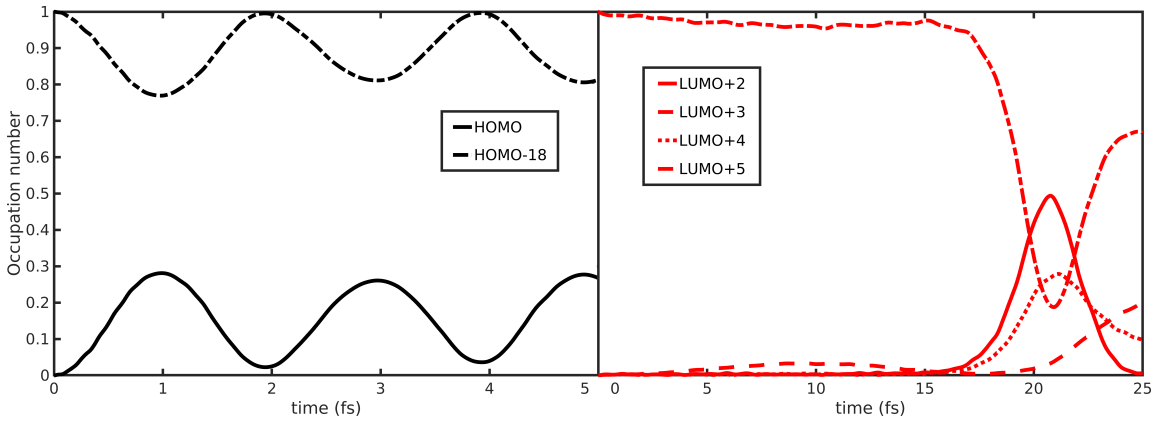


Figure 5.18: Occupation numbers of selected MOs from ^{1}MLCT$_B$ RT-TDDFT dynamics (M-G structure).

5.4 ^{1}MLCT$_A$ and ^{1}MLCT$_B$ electronic dynamics: solvent effects (D1-G and D1-W).

5.4.1 Charges and hole/electron distribution.

The electronic dynamics on D1-G structure should be affected only by (indirect) solvent structural distortion effects.

The starting ($t = 0$) HOMO-1 $\rightarrow$ LUMO+3 (Figs. 5.41 and 5.42) ^{1}MLCT$_A$ excitation induces a charge transfer from NCS2 ligand towards the axial dcbpy1a ring (Fig. 5.19, left panel). The dcbpy1 ligand (and in particular the dcbpy1a ring) appears to be able to keep the 'electron' until ~ 10 fs, when a substantial, slow ($<1334\,\mathrm{cm}^{-1}$, Fig. 5.21, left panel) exchange with the other dcbpy ligand takes place ($r_{\mathrm{dcbpy1/dcbpy2}} = -0.94$, Figs. 5.20 and 5.21, left panels), spreading the electron over all the four rings. Similarly to the M-G symmetric structure, a fast $16\,011\,\mathrm{cm}^{-1}$ charge oscillation between the 'hole'-sharing NCS2 ligand and the Ru center occurs ($r_{\mathrm{NCS2/Ru}} = -0.77$). Due to the D1-G structure asymmetry, the hole is instead almost absent on the other NCS^- ligand.

The hole barycenter is therefore mostly along the Ru-NCS2 axis, sometimes coming closer to the dcbpy2b ring (Fig. 5.22, left panel). The electron position explores regions close to the dcbpy1a axial ring (in the first part of the trajectory), then moving also near dcbpy1b and between dcbpy2a and dcbpy2b. The RMS hole-electron distance (2.254 Å, Table 5.3) is only slightly higher than that of the corresponding state in the M-G structure (Table 5.2). Both carriers RMS velocities (in particular the electron one) appear increased ($v_{h^+} = 1.329\,\text{Å}\,\mathrm{fs}^{-1}$, $v_{e^-} = 1.165\,\text{Å}\,\mathrm{fs}^{-1}$).

The initial D1-W ^{1}MLCT$_A$ HOMO-1 $\rightarrow$ LUMO+3 excitation moves electron density from the NCS2 and dcbpy1 ligand onto both dcbpy2 rings (Fig. 5.19, right panel). While NCS1 density is almost constant along the simulation (like in D1-G), the 'hole' is shared between NCS2 and Ru center ($r_{\mathrm{NCS2/Ru}} = -0.57$, Fig. 5.20, right panel) through a $16\,012\,\mathrm{cm}^{-1}$ fast exchange (Fig. 5.21, right panel). Such frequency is comparable to that in D1-G and so higher than in M-G, suggesting that the solvent distortion effect

Table 5.3: Hole - electron RMS distance and RMS velocities from ^{1}MLCT$_A$ RT-TDDFT dynamics (D1-G and D1-W structures).

	d_{h^+/e^-} (Å)	v_{h^+} (Å fs^{-1})	v_{e^-} (Å fs^{-1})
D1-G	2.254	1.329	1.165
D1-W	3.100	0.777	0.766

can induce a slight increase in NCS/Ru exchange frequency. Nevertheless, the hole now appears more localized on the Ru center (like in M-G) and not equally shared as in D1-G. A modest charge exchange between NCS1 and NCS2 ($r_{\mathrm{NCS1/NCS2}} = -0.47$) is instead barely detectable.

After the photo-excitation, the 'electron' appears to be quite stable on the dcbpy2 ligand. Although only one dcbpy acquires a substantial negative charge, no major charge transfer between distinct dcbpy ligands occurs, like M-G ^{1}MLCT$_A$ dynamics and in contrast to the D1-G one. In fact, the electron is mostly shared within dcbpy2 ($r_{\mathrm{dcbpy2a/dcbpy2b}} = -0.67$, $\omega = 2669$ and $6672\,\mathrm{cm}^{-1}$) and only a small charge is transferred between dcbpy2b and dcbpy1b rings ($r_{\mathrm{dcbpy1b/dcbpy2b}} = -0.52$, $\omega = 2669$ and $5337\,\mathrm{cm}^{-1}$).

The hole barycenter is therefore located between NCS2 and Ru, while the electron one is found nearly between dcbpy2 rings (Fig. 5.22, right panel). The average hole-electron distance (3.100 Å, Table 5.3) is ~ 1 Å higher than in M-G and D1-G ^{1}MLCT$_A$ states. While the hole RMS velocity (0.777 Å fs^{-1}) appears very reduced with respect to both gas-phase structures, the electron velocity (0.766 Å fs^{-1}) is lower than the D1-G value, but approximately recovers that found for M-G. The (correct) solute-solvent polarization therefore induces an increased charge carriers separation, as well as reduced hole and electron velocities.

D1-G ^{1}MLCT$_B$ HOMO $\rightarrow$ LUMO+5 (Figs. 5.41 and 5.42) starting excitation asymmetrically moves electron density from NCS$^-$ ligands towards both dcbpy2 rings and, to a lesser extent, the equatorial dcbpy1 one (Fig. 5.23, left panel). Similarly to ^{1}MLCT$_A$, the acquired 'electron' is located on one dcbpy ligand (now the dcbpy2) for no more than

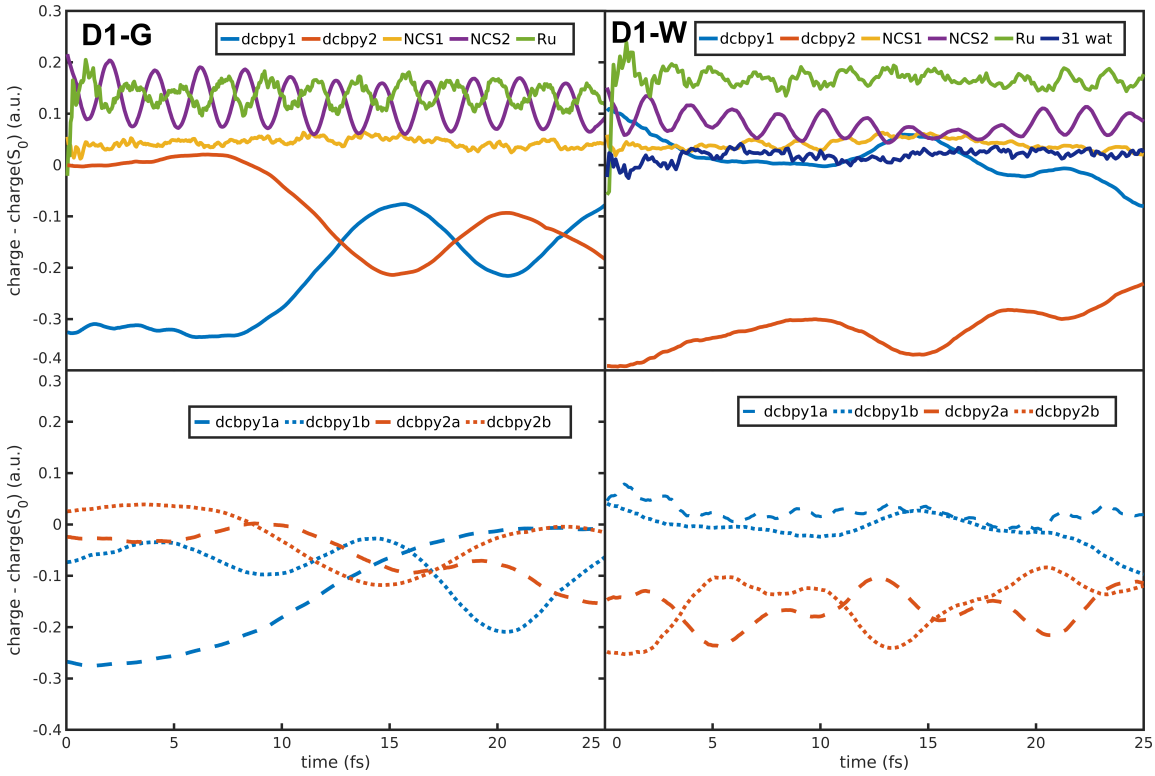


Figure 5.19: Fragments charges (with respect to the S_0 state) along $^1MLCT_A$ RT-TDDFT electronic dynamics (D1-G: left panels, D1-W: right panels).

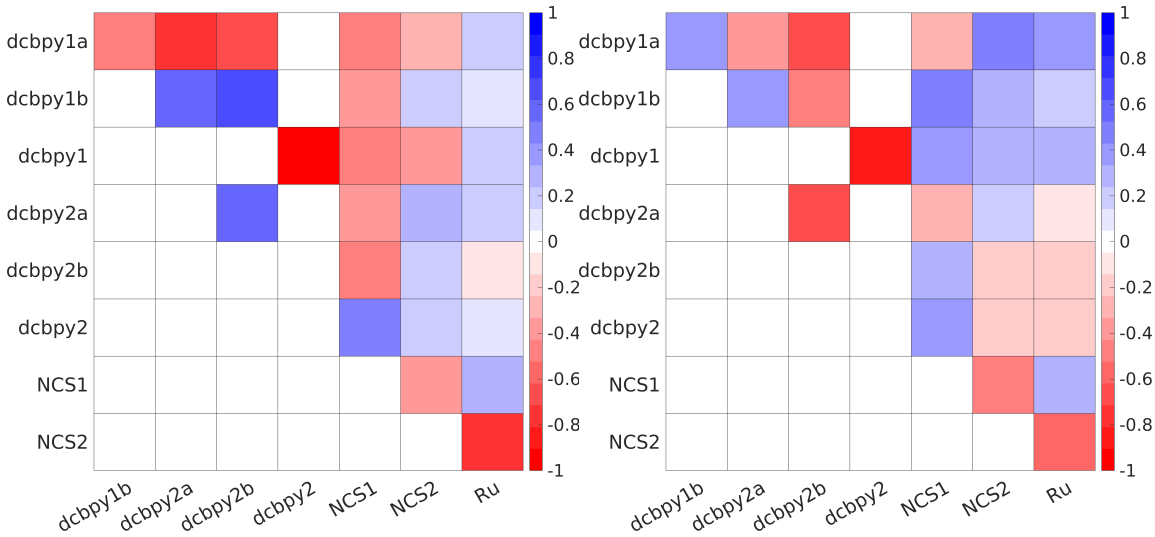


Figure 5.20: Normalized r_{xy} cross-correlations map between fragment charges time series from $^1\text{MLCT}_A$ RT-TDDFT electronic dynamics (D1-G: left panel, D1-W: right panel).

10 fs and then given to the other one ($<$1334 cm^{-1}, $r_{\text{dcbpy1/dcbpy2}} = -0.98$, Figs. 5.24 and 5.25, left panels). The $^1\text{MLCT}_B$ 'electron' distribution in D1-G dcbpy ligands therefore appears even more unstable than in the M-G structure. Both rings of each dcbpy ligand exchange charge density, probably through axial/axial ($r_{\text{dcbpy1a/dcbpy2a}} = -0.82$) and equatorial/equatorial ($r_{\text{dcbpy1b/dcbpy2b}} = -0.96$) concurrent processes, leading to an electron accumulation mainly on the dcbpy1b ring. At the same time, the 'hole' swiftly (17 345 cm^{-1}) bounces between NCS2 (and secondarily NCS1) and Ru ($r_{\text{NCS1/NCS2}} = 0.66$, $r_{\text{NCS2/Ru}} = -0.58$).

Also in D1-G $^1\text{MLCT}_B$ dynamics, the hole barycenter moves between the two NCS^- ligands and the Ru center, more displaced towards NCS2 (Fig. 5.26, left panels). The electron barycenter is initially located instead quite near dcbpy2a and dcbpy2b rings, then moving towards dcbpy1b. The average carriers separation is quite similar to that in $^1\text{MLCT}_A$ (2.553 Å, Table 5.4), but smaller than in the corresponding M-G state (Table 5.2). While the electron velocity is totally comparable to that from $^1\text{MLCT}_A$ (1.173 Å fs^{-1}), a smaller hole velocity is observed (1.266 Å fs^{-1}), even though

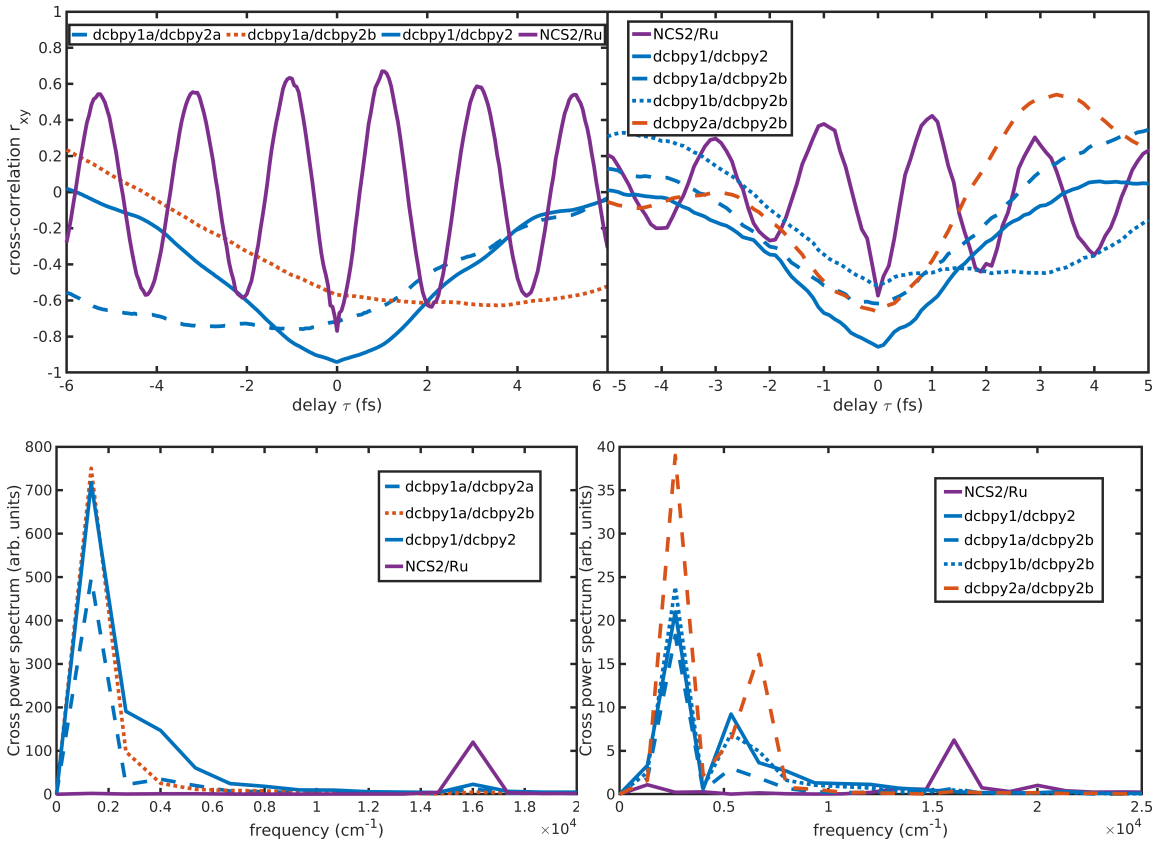


Figure 5.21: Cross-correlations and cross power spectra between selected pairs of fragment charges time-series collected in the ^{1}MLCT$_A$ RT-TDDFT dynamics (D1-G: left panels, D1-W: right panels).

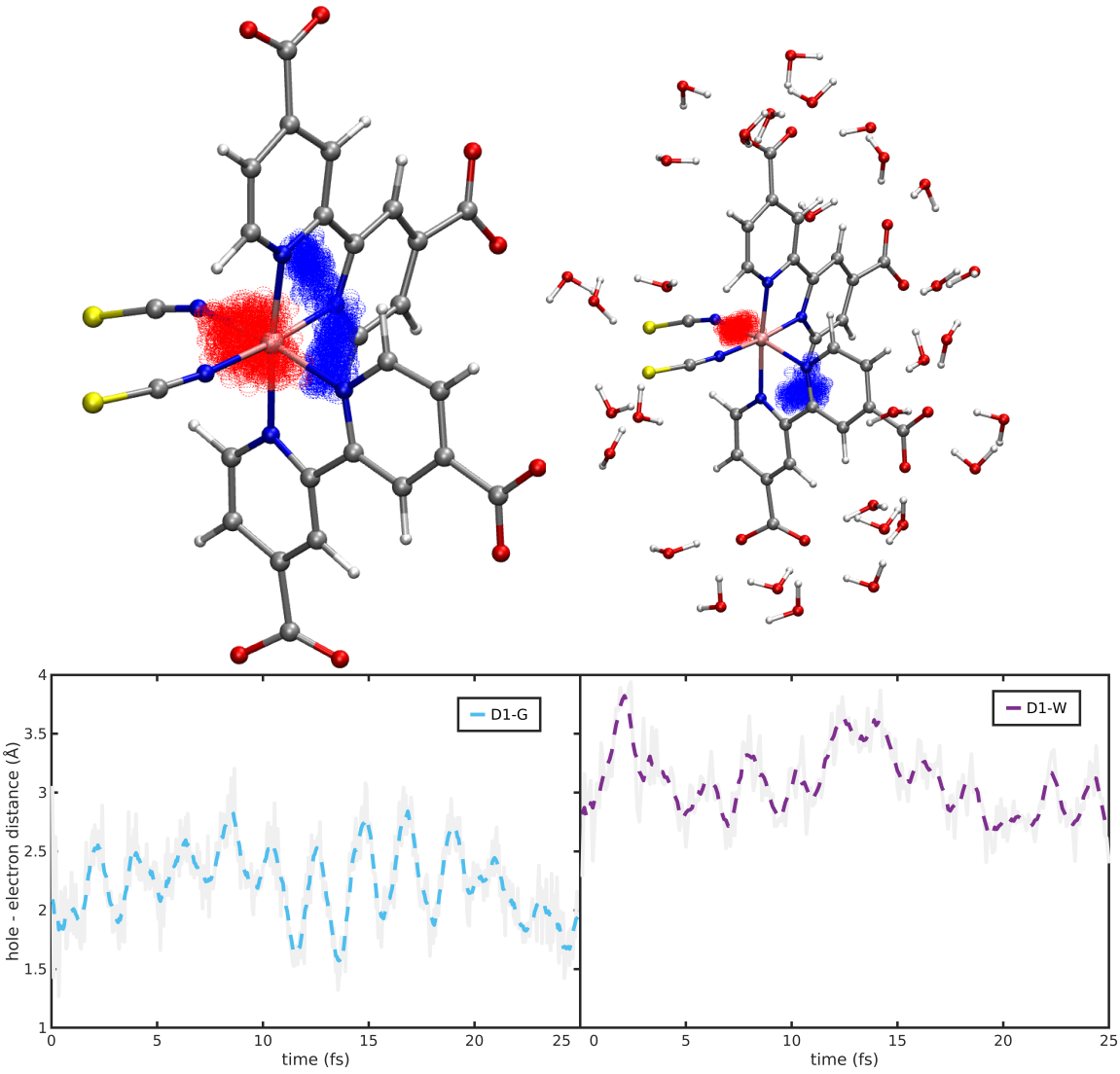


Figure 5.22: Hole and electron distributions from $^1\mathrm{MLCT}_A$ RT-TDDFT dynamics (D1-G: left panel, D1-W: right panel).

both values are higher than the corresponding ones in the symmetric M-G structure.

D1-W ^{1}MLCT$_B$ HOMO $\rightarrow$ LUMO+5 excitation transfers the NCS2 and NCS1 density to the dcbpy2 ligand (Fig. 5.23, right panel). A fast (16 012 and 20 015 cm^{-1}, Fig. 5.25, right panel) charge flow allows the hole sharing between NCS2 and Ru(II) (less clearly than in ^{1}MLCT$_A$: $r_{\mathrm{NCS2/Ru}} = -0.49$, Fig. 5.24, right panel). The oscillation frequency is reduced by $\sim 1000\,\mathrm{cm}^{-1}$ with respect to the gas-phase structures. The hole is more concentrated on the Ru center, more like M-G than D1-G ^{1}MLCT$_B$ state. NCS1 charge density is somewhat correlated to the NCS2 one, but in a delayed fashion ($r_{\mathrm{NCS1/NCS2}} = 0.53$, $\tau = 3.20\,\mathrm{fs}$).

The photo-induced 'electron' is hosted by dcbpy2 for $\sim 15\,\mathrm{fs}$ and then transferred to dcbpy1 ($r_{\mathrm{dcbpy1/dcbpy2}} = -0.99$), unlike D1-W ^{1}MLCT$_A$. This time-scale is more similar to that observed in M-G than in D1-G (which is about $\sim 10\,\mathrm{fs}$). All dcbpy rings show some charge exchange, in particular the equatorial dcbpy1b and the axial dcbpy2a ones ($r_{\mathrm{dcbpy1b/dcbpy2a}} = -0.97$, $<1334\,\mathrm{cm}^{-1}$), leading to an electron repositioning onto the dcbpy1b ring.

The hole barycenter is near the $(\mathrm{NCS})_2\mathrm{Ru}$ moiety also in ^{1}MLCT$_B$, more symmetrically placed between the two NCS^- ligands than in ^{1}MLCT$_A$ (Fig. 5.26, right panel). The electron barycenter explores a wider region. In the first part of the trajectory, it is more located near the dcbpy2 ligand (in particular near the dcbpy2a axial ring), then moving towards the dcbpy1b equatorial ring. The average hole-electron distance (2.759 Å, Table 5.4), is ~ 0.1 Å lower than the distance found in M-G, but ~ 0.2 Å higher than that in D1-G. Hole ($0.838\,\mathrm{Å\,fs}^{-1}$) and electron ($0.760\,\mathrm{Å\,fs}^{-1}$) RMS velocities appear reduced with respect to both M-G and D1-G values. Therefore, also in ^{1}MLCT$_B$ solute-solvent polarization slows down both charge carriers.

No significant dynamic N3^{4-}-H_2O charge transfer involving D1-W first-shell QM water molecules can be observed in ^{1}MLCT$_A$ and ^{1}MLCT$_B$ states.

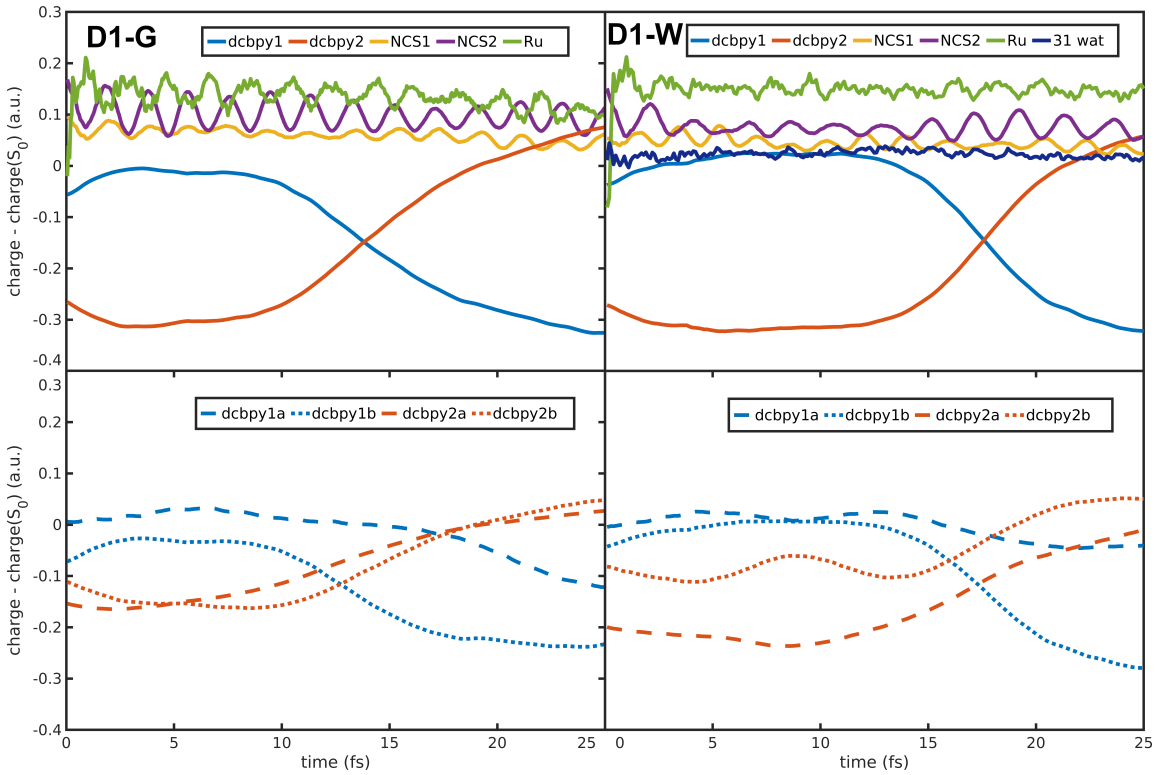


Figure 5.23: Fragments charges (with respect to the S_0 state) along $^1MLCT_B$ RT-TDDFT electronic dynamics (D1-G: left panels, D1-W: right panels).

Table 5.4: Hole - electron RMS distance and RMS velocities from $^1MLCT_B$ RT-TDDFT dynamics (D1-G and D1-W structures).

	d_{h^+/e^-} (Å)	v_{h^+} (Å fs^{-1})	v_{e^-} (Å fs^{-1})
D1-G	2.553	1.266	1.173
D1-W	2.759	0.838	0.760

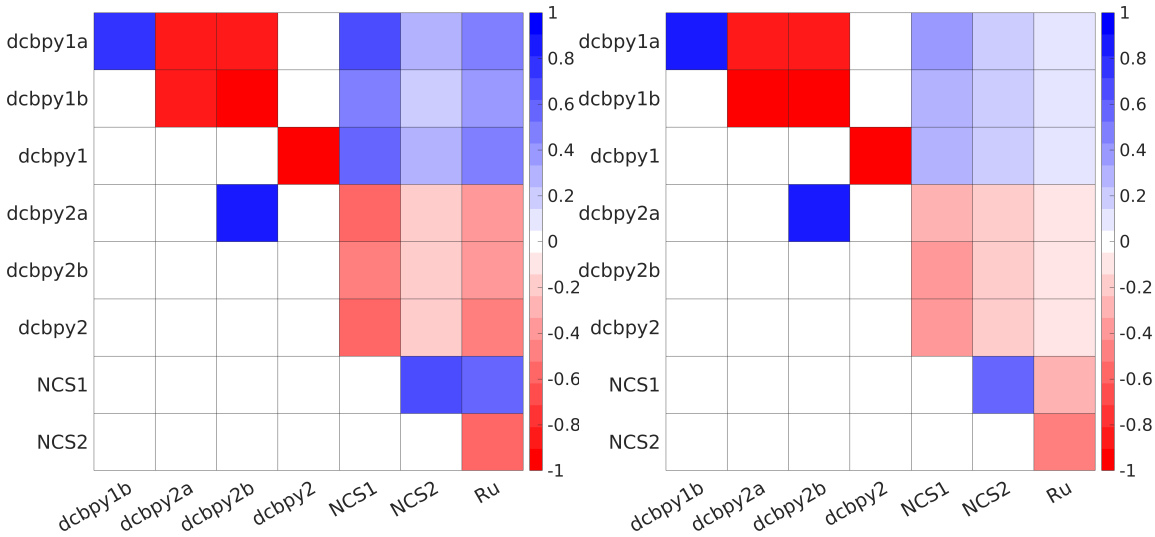


Figure 5.24: Normalized r_{xy} cross-correlations map between fragment charges time series from $^1\text{MLCT}_B$ RT-TDDFT electronic dynamics (D1-G: left panel, D1-W: right panel).

5.4.2 Electric dipole moment.

Two distinct frequency contributions (<1334 and 16 011 cm^{-1}) characterize the time-dependent D1-G $^1\text{MLCT}_A$ dipole moment component along the Ru-NCS2 bond (Fig. 5.27, left panels), respectively related to the charge flow involving the dcbpy2b ring and the NCS2/Ru transfer (Fig. 5.19, left panels). On the other hand, the steady increase of the Ru-N(dcbpy1a) projection mirrors the slow loss of electron density by the dcbpy1a ring. Since the NCS1 charge is almost constant along the simulation, dcbpy1b charge oscillations (which become wider after $\sim$ 15 fs) induce only minor perturbations in the Ru-NCS1 dipole component.

The D1-W $^1\text{MLCT}_A$ time-dependent electric dipole moment (Fig. 5.27, right panels) shows a quite static picture, as a consequence of reduced charge density exchanges (Fig. 5.19, right panels), being confined between the Ru-NCS2 and Ru-N(dcbpy1a) axes along all the simulation. The Ru-NCS1 component is almost constant, since both NCS1 and dcbpy1b charges do not show significant perturbations along the trajectory. The dcbpy2a/dcbpy2b

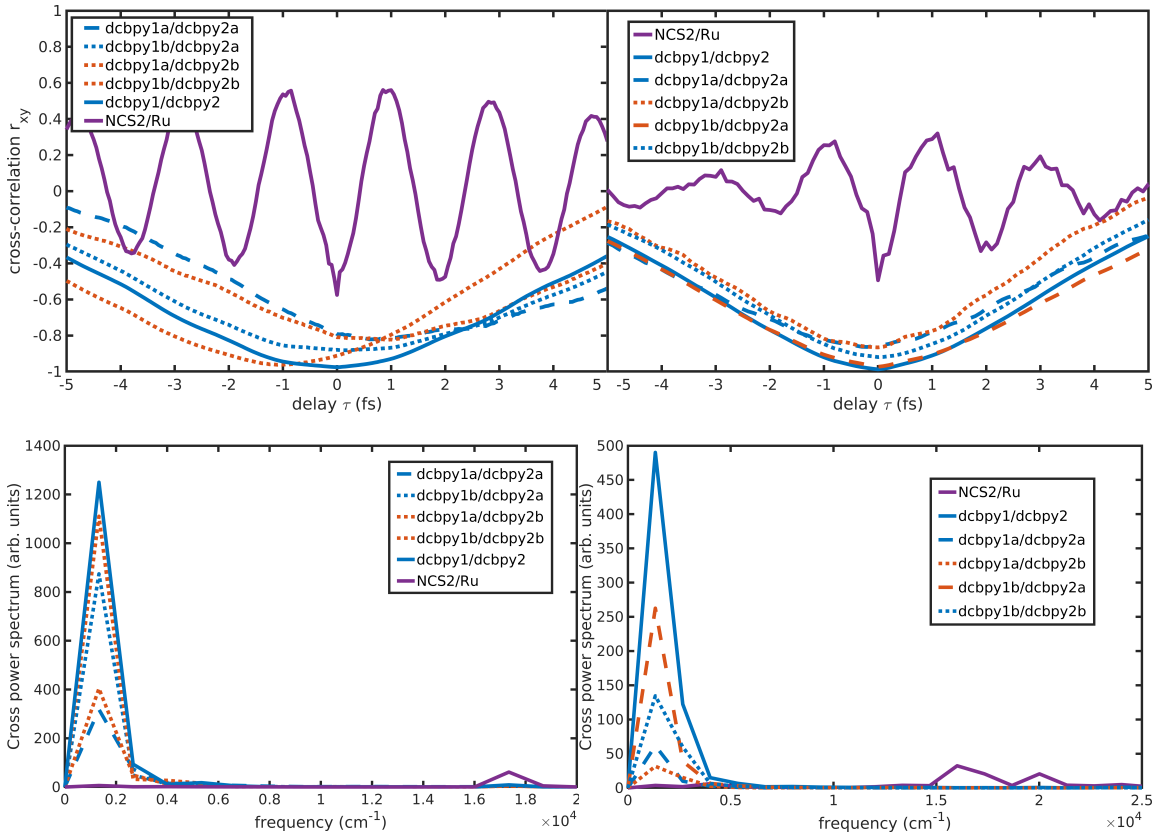


Figure 5.25: Cross-correlations and cross power spectra between selected pairs of fragment charges time-series collected in the ^{1}MLCT$_B$ RT-TDDFT dynamics (D1-G: left panels, D1-W: right panels).

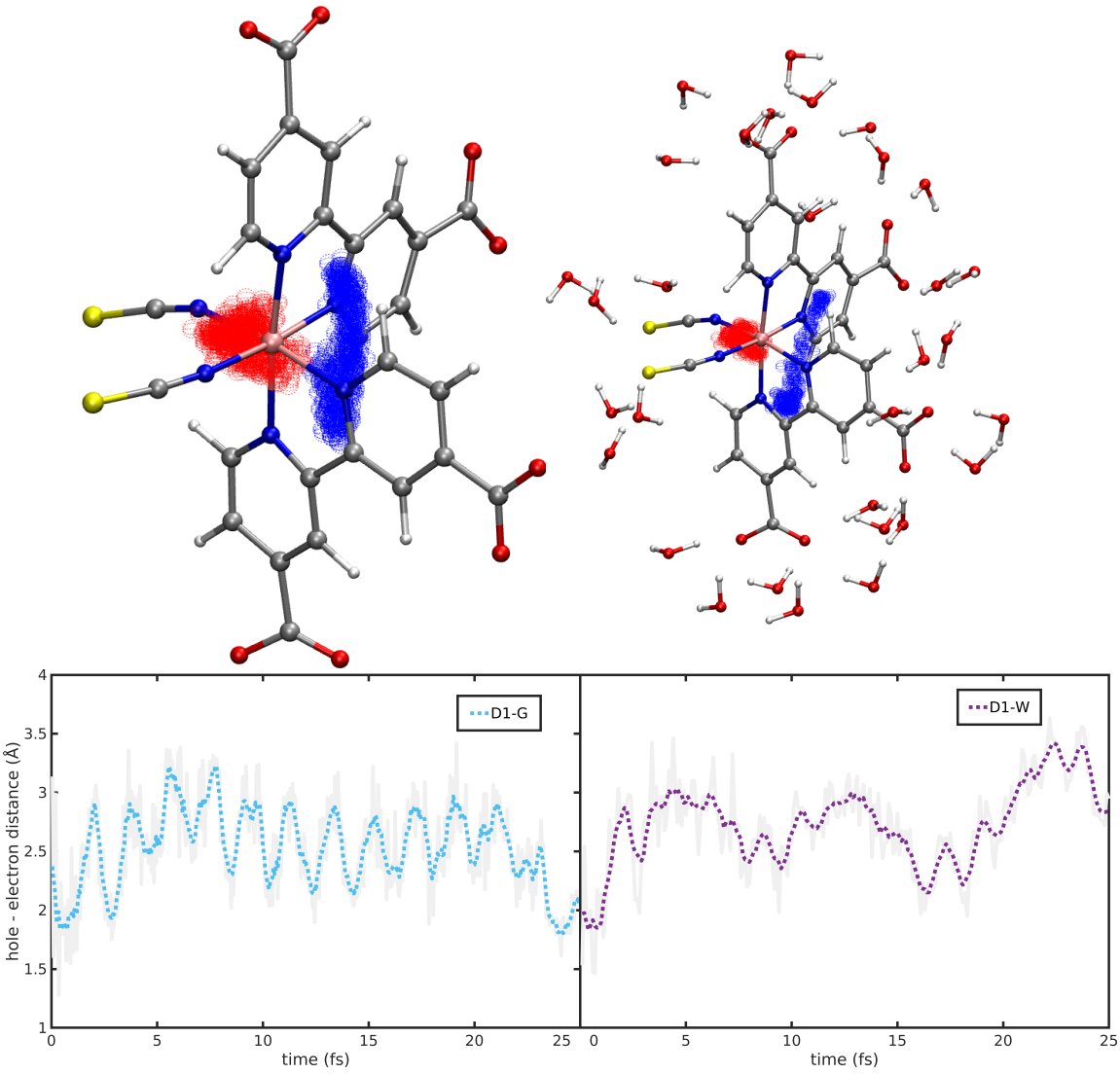


Figure 5.26: Hole and electron distributions from $^1\mathrm{MLCT}_B$ RT-TDDFT dynamics (D1-G: left panel, D1-W: right panel).

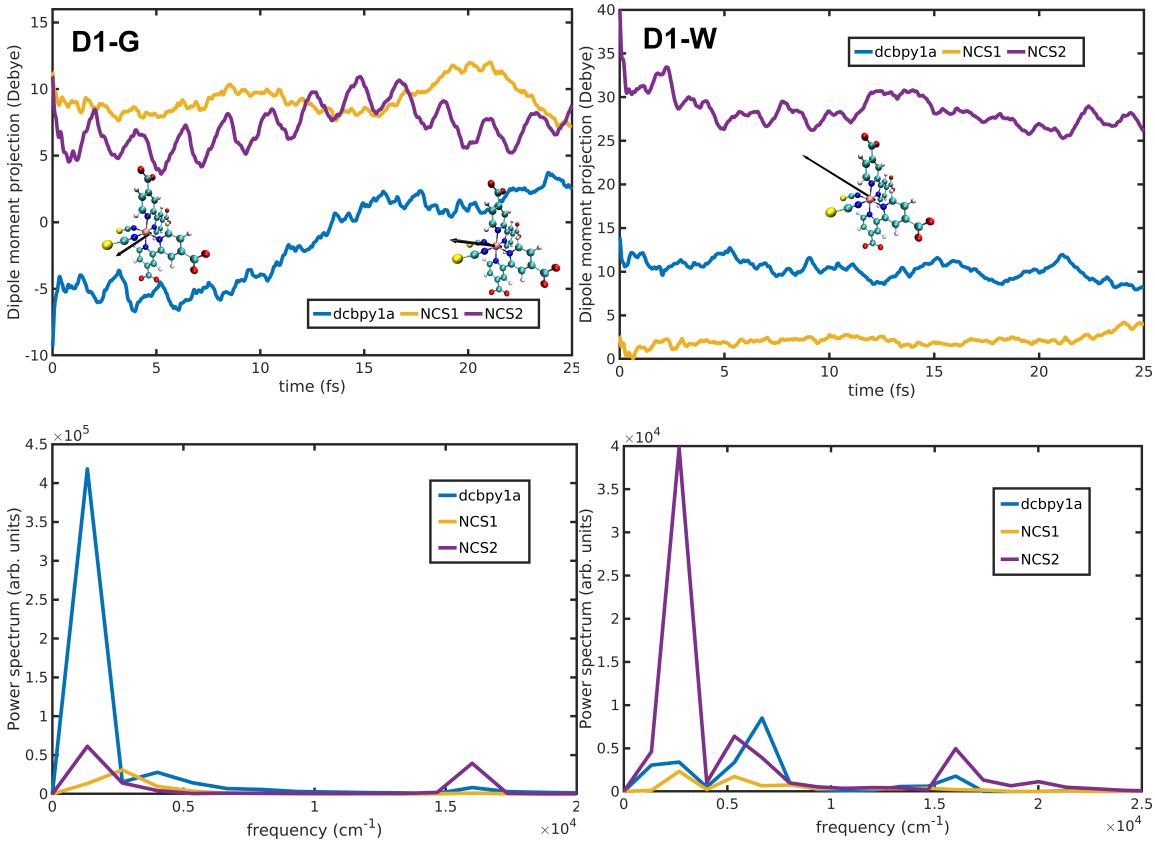


Figure 5.27: Time-dependent electric dipole moment projections along Ru-N(dcbpy1a), Ru-NCS1 and Ru-NCS2 bonds from $^1\mathrm{MLCT}_A$ electronic dynamics (D1-G: left panels, D1-W: right panels).

charge transfer induces a small out-of-phase 2669 + 6672 cm^{-1} oscillation of the Ru-N(dcbpy1a) and Ru-NCS2 projections. Moreover, the 16 012 cm^{-1} NCS2/Ru charge transfer is observed as an additional fast oscillation in the Ru-NCS2 projection.

In D1-G $^1\mathrm{MLCT}_B$ propagation, the dipole moment projections along Ru-N(dcbpy1a) and Ru-NCS2 bonds are out-of-phase with respect to the Ru-NCS1 projection (Fig. 5.28, left panels). For instance, the anti-correlated dcbpy1a and dcbpy2b time-dependent charges (Fig. 5.23, left panels) justify the in-phase trends of the Ru-N(dcbpy1a) and Ru-NCS2 components, while the positive correlation of dcbpy1b charge to the dcbpy1a one gives the Ru-

NCS1 projection an opposite behavior. The in-phase 17 345 cm^{-1} oscillations superimposed on Ru-NCS1 and Ru-NCS2 dipole projections are instead related to the NCS2+NCS1/Ru fast charge exchange.

The out-of-phase, low frequency (<1334 cm^{-1}) trends of the Ru-N(dcbpy1a) and Ru-NCS1 projections in D1-W $^1MLCT_B$ dynamics (Fig. 5.28, right panels) can be attributed to the anti-correlated dcbpy1b and dcbpy2a charges (Fig. 5.23, right panels). The Ru-NCS2 projection is instead in-phase with respect to the Ru-N(dcbpy1a) one, because of the correlated evolution of dcbpy2a and dcbpy2b charges. The 16 012 cm^{-1} additional frequency in the Ru-NCS2 component is instead due to the fast hole sharing between NCS2 and Ru(II).

5.4.3 Molecular orbitals occupation numbers.

After D1-G $^1MLCT_A$ excitation, the 'hole' initially in the HOMO-1 is readily shared with the HOMO-18 and HOMO-17 (also centered on Ru and NCS^- ligands, Fig. 5.41) by a fast $\sim$ 0.3 e^- occupation exchange (Fig. 5.29, left panels), analogously to M-G $^1MLCT_A$ state (Fig. 5.17), related to the NCS2/Ru transfer. A wider ($\sim$ 0.5 e^-) exchange at bigger time-scales enable instead an 'electron' oscillation between LUMO+3 and LUMO+2 (both asymmetrically distributed over the whole dcbpy ligands, Fig. 5.42), also involving the LUMO+4 and LUMO+5 MOs.

In the shorter time-scale, the D1-W $^1MLCT_A$ depleted HOMO-1 (Fig. 5.43) shares the 'hole' with the lower HOMO-6 (both centered on NCS2 and Ru(II)) through a $\sim$ 0.2e^- fast occupation transfer (Fig. 5.29, right panels), mirroring the NCS2/Ru charge transfer. On longer time-scales, about half hole is transferred instead between the HOMO-1 and the HOMO-2 (more centered on NCS1). This solvation-induced mechanism is not found in gas-phase systems. The LUMO+3/LUMO+4 (Fig. 5.44) electron sharing process is instead comparable to that shown by gas-phase D1-G structure and it is probably linked to the small dcbpy1/dcbpy2 charge transfer.

D1-G $^1MLCT_B$ electronic dynamics in the MO basis is again similar in the shorter time-scale to that in the symmetric M-G structure, showing

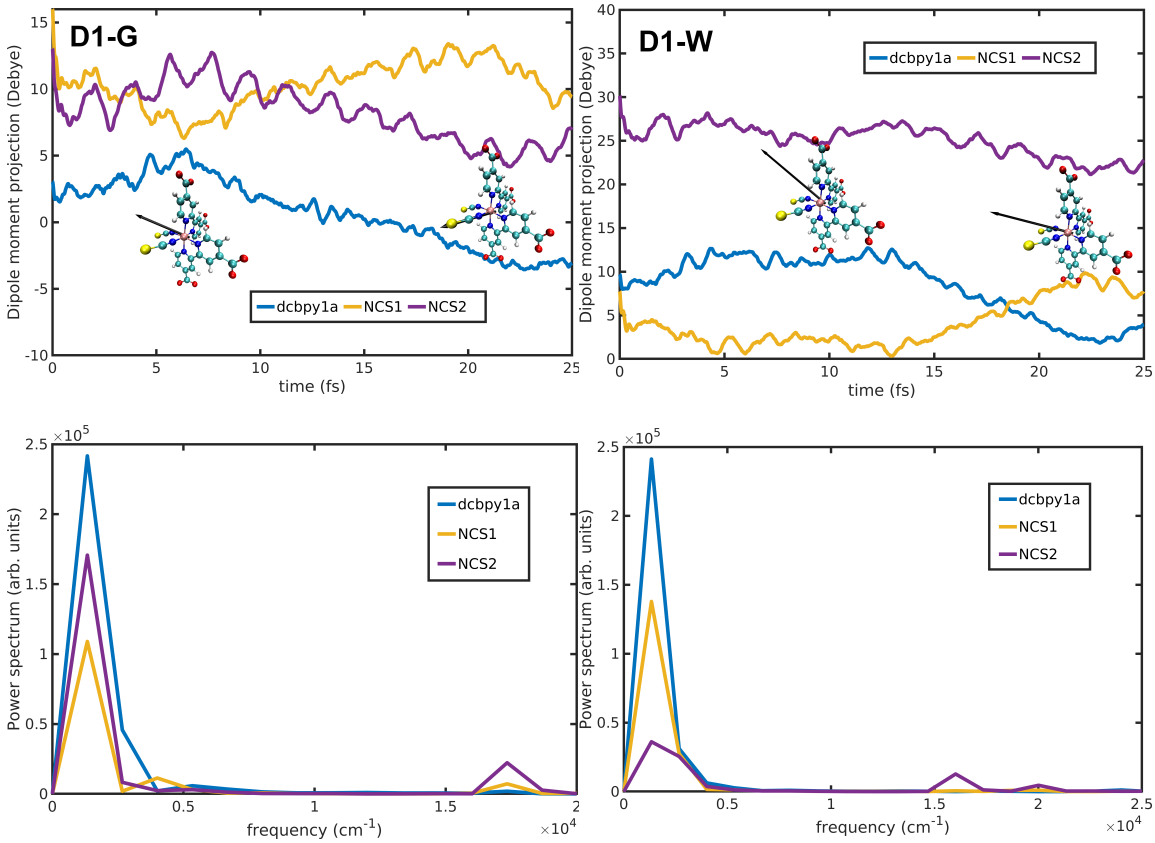


Figure 5.28: Time-dependent electric dipole moment projections along Ru-N(dcbpy1a), Ru-NCS1 and Ru-NCS2 bonds from ^{1}MLCT$_B$ electronic dynamics (D1-G: left panels, D1-W: right panels).

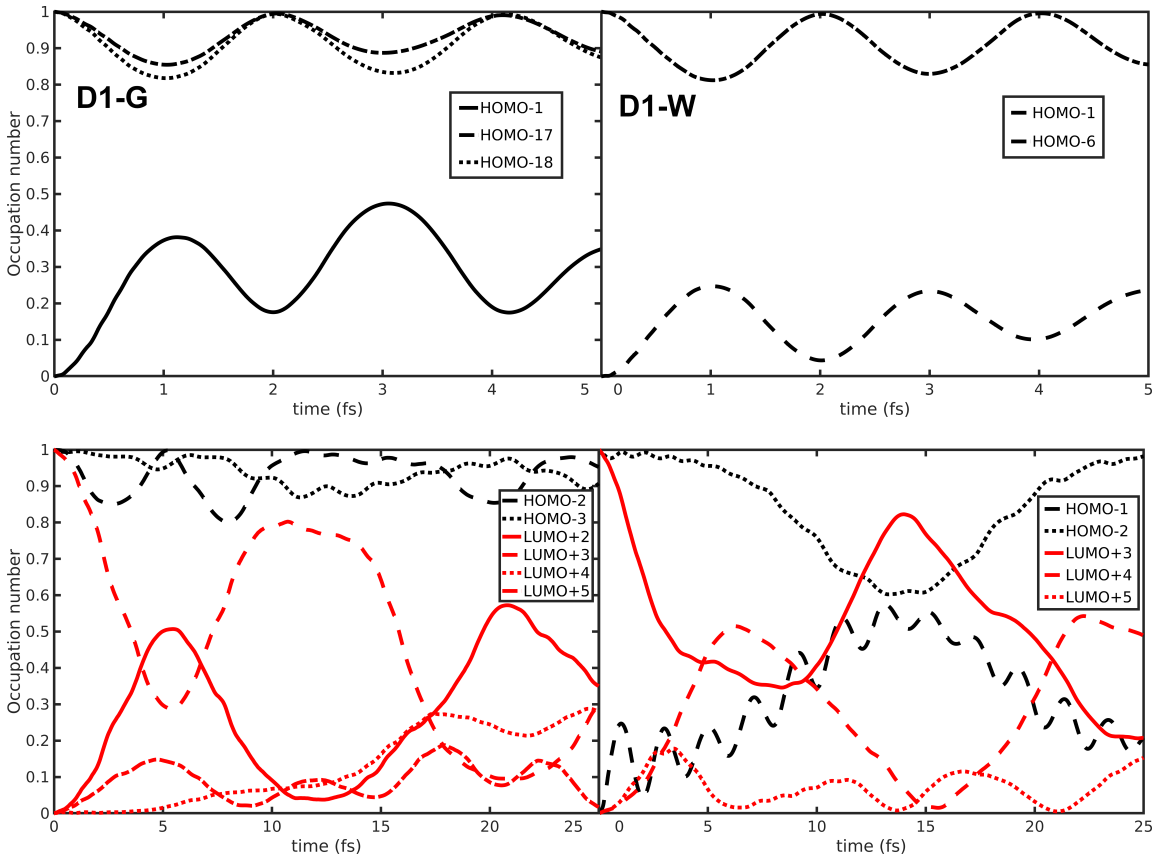


Figure 5.29: Occupation numbers of selected MOs from ^{1}MLCT$_A$ RT-TDDFT dynamics (D1-G: left panels, D1-W: right panels). Fast and slow oscillations are reported in the upper and lower panels, respectively.

a ~ 0.2 e$^-$ 'hole' exchange between the HOMO and HOMO-17, HOMO-18 (Fig. 5.30, left panels), describing the NCS1+NCS2/Ru charge transfer process. The structural distortion seems instead to accelerate the 'electron' transfer from the initially populated LUMO+5 (now localized also on an axial dcbpy ring, Fig. 5.42) towards the more widespread LUMO+3 and LUMO+2. $\sim 70\%$ of the starting occupation is in fact now lost in the first 5 fs (as in ^{1}MLCT$_A$), even though it is almost completely recovered through slow, wide oscillations.

A rapid HOMO/HOMO-3 hole exchange, involving similar NCS$^-$ π^* + Ru(II) d orbitals, but with different bonding/antibonding features, characterizes also D1-W ^{1}MLCT$_B$ evolution (Fig. 5.30, right panels). A slower hole exchange (now with the HOMO-1) is again found only after the inclusion of QM water molecules. The photo-excited electron is exchanged by the LUMO+5 (with the LUMO+4 and LUMO+3) through wide-amplitude oscillations as in the D1-G system, but with a higher frequency.

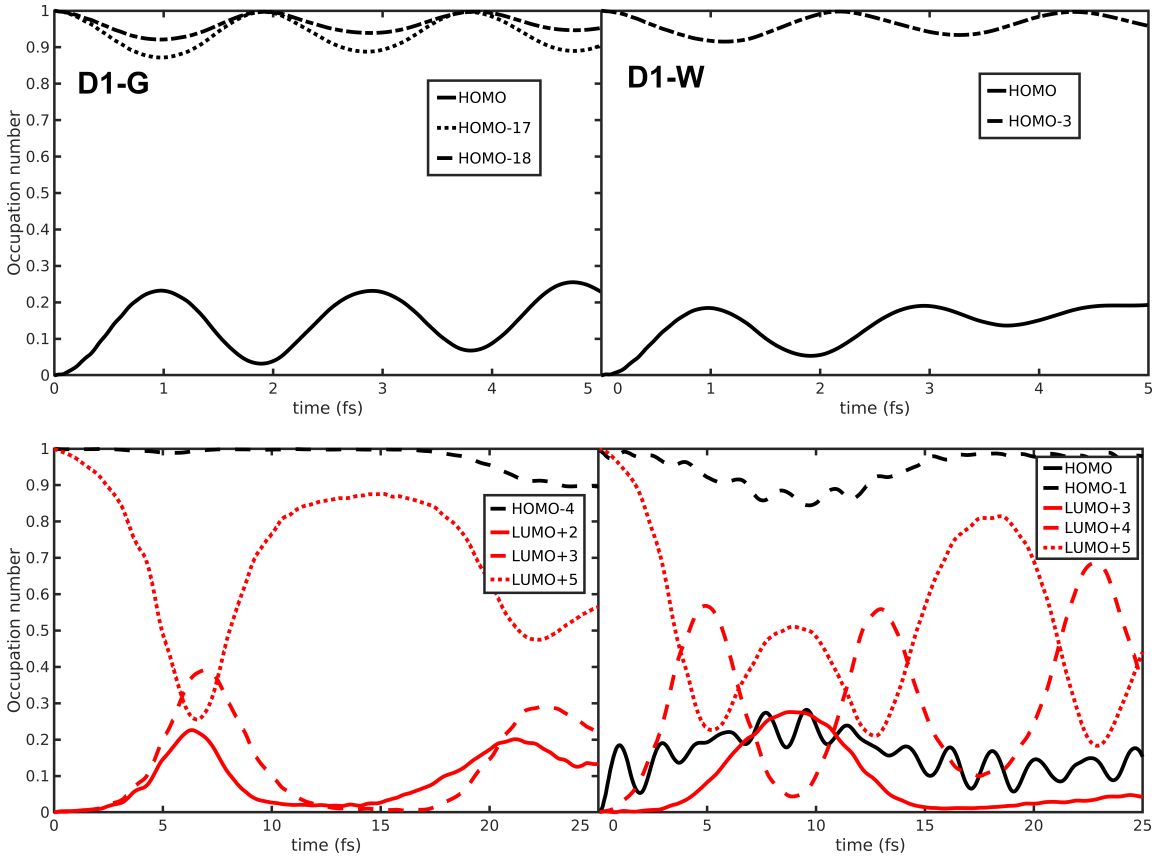


Figure 5.30: Occupation numbers of selected MOs from ^{1}MLCT$_B$ RT-TDDFT dynamics (D1-G: left panels, D1-W: right panels). Fast and slow oscillations are reported in the upper and lower panels, respectively.

5.5 Inter-Ligand Electron Transfer in $N3^{4-}$: insights from theory.

A first question about the dynamics of the photo-generated electron in Ru-based complexes is its localized or delocalized nature. Considering the extensively studied $[Ru(bpy)_3]^{2+}$, it is accepted that the excited MLCT states are localized, with the electron excited into the π^* MO of a single bipyridine. The excited electron is localized probably already in the Franck-Condon or the ^{1}MLCT excited state (i.e., before the inter-system crossing towards the ^{3}MLCT state and the following vibrational relaxation), because of the instantaneous solvation- and vibration-induced breaking of the average D_3 symmetry. [111, 77, 112–117] Experimental evidence seems to suggest localized MLCT excited states with a dcbpy ligand formally reduced and the other one neutral also for the structurally similar $[Ru(dcbpy)_2(NCS)_2]$ (N3) and its deprotonated forms. [98, 80, 118]

A natural consequence of the localization of the photo-excitation is the possibility that the electron could "hop" among the bpy-type ligands. This process, known as Inter-Ligand Electron Transfer (ILET), is both of fundamental and practical interest. In fact, among the $N3^{4-}$ possible binding modes to a TiO_2 surface, anchoring through a single dcbpy ligand is also predicted. [83, 119–121] In this case, if the excitation is localized on the non-surface-bound ligand, then the electron must first hop to the bridging one in order to be then injected into the semiconductor. Thus, the overall electron-transfer rate *could* be limited by a slow, activated, ILET process potentially trapping the excited electron. Excited state deactivation processes may become therefore competitive, lowering the solar cell efficiency.

ILET kinetics in Ru-polypyridine complexes has been usually studied through transient absorption anisotropy. Two limit situations are defined, characterized in fact by different anisotropies: a non-randomized, fully localized, MLCT state, where the formally reduced bipyridine is the one that was initially photo-selected, and a randomized state, where the excited electron is randomly (i.e., with equal probability) located on the bpy ligands, losing memory about the localization of the inital photo-excitation. The

non-randomized/randomized transition is clearly obtained through ILET among bpy ligands.

No definitive consensus exists so far about the time scale of ILET process. In particular, earlier works about ILET in N3 dye suggested high time-constants (1.5 ns [80] or 20 ps [118]). However, Rimgard and coworkers recently questioned such measurements, finding that a randomized MLCT distribution is present already after a few ps, suggesting therefore a sub-ps, ultra-fast, ILET in the non-relaxed ^{3}MLCT or even already in the ^{1}MLCT state. [98] Similar ultra-fast time-scales have been proposed before also for the analogous $[Ru(bpy)_3]^{2+}$ complex [122, 123].

Insights about ultra-fast ILET processes in N3^{4-} are offered by the here reported ^{1}MLCT excited states electronic dynamics. First, the localized nature of the excited electron in water solution and room temperature is confirmed by our excited states calculations. In fact, considering the fully C_2 symmetric N3^{4-} structure (the gas-phase optimized M-G structure), the photo-excited electron appears equally shared between the two dcbpy ligands, as can be seen from the ^{1}MLCT$_A$ and ^{1}MLCT$_B$ NTO spatial distributions (Fig. 5.5), the equal starting ($t = 0$) dcbpy negative fragment charges (Figs. 5.8 and 5.11) and the symmetric (i.e., along the C_2 axis) initial dipole moment orientation (Figs. 5.15 and 5.16). Nevertheless, while a symmetric electron delocalization is shown by M-G ^{1}MLCT$_A$ along all the trajectory, the electron localization on a single dcbpy ligand after ~ 15 fs in ^{1}MLCT$_B$ dynamics (Fig. 5.11), occurring despite an initial symmetric distribution, appears in this context indeed interesting, suggesting an inherent tendency by some MLCT states to localize the excited electron, even in a symmetric structure. On the other hand, calculations on a N3^{4-} structure randomly extracted from an *ab inito* MD trajectory in water solution at room temperature (D1-G, the only N3^{4-} structure, and D1-W, with surrounding water molecules), reveal, as expected by the lower symmetry, a localization of the photo-excited electron mainly on only one dcbpy. The ^{1}MLCT NTO 'electron' orbitals are in fact asymmetrically distributed on the dcbpy ligands (Figs. 5.6 and 5.7) and the population analysis at $t = 0$ further confirms the preferential localization of the excited electron on a single

dcbpy (Figs. 5.19 and 5.23). Such initial asymmetric density distribution opens up the possibility of an electron exchange between the acceptor ligands. ^{1}MLCT$_A$ electronic dynamics on the gas-phase, MD-extracted, low-symmetry structure (D1-G, Fig. 5.19, left panel) reveals an electron displacement from dcbpy1 after ~ 10 fs. An intermediate distribution with the electron shared by both dcbpys seems to evolve (maybe after the simulated 25 fs time) towards a localization onto dcbpy2. In contrast, solvent polarization effects (D1-W, Fig. 5.19, right panel) contribute to localize the electron on a single dcbpy, slowing down the electron-transfer process (actually not seen within the simulated time). A clearer ILET can be instead seen in ^{1}MLCT$_B$ simulated electronic dynamics. Both in D1-G and D1-W a complete dcbpy/dcbpy electron transfer is observed within 25 fs (Fig. 5.23). Now solvation effects induce only a slight delay with respect to the corresponding *in vacuo* system (~ 20 fs instead of ~ 15 fs).

An accurate kinetics of the ILET process cannot be of course obtained with only a single MD-extracted structure, due to an insufficient sampling. Nevertheless, results from RT-TDDFT electronic dynamics on a vibration-distorted N3^{4-} structure in polar solvent actually suggest dcbpy/dcbpy ILET mechanisms potentially occurring on an ultra-fast time-scale in some ^{1}MLCT localized excited states (such as the ^{1}MLCT$_B$ state), so before inter-system crossing and vibrational relaxation. Confirming the most recent experimental observations, [98] the theoretically predicted ILET time-scale, as already pointed out, likely cannot limit the electron injection ultra-fast component (< 100 fs). [124–130]

5.6 ^{1}MLCT$_A$ and ^{1}MLCT$_B$ electronic dynamics: modelling first-shell solvent molecules (D1-C and D1-W).

A further structure (called D1-C) has been considered for $N3^{4-}$ electronic dynamics, characterized by first-shell water molecules treated not at a QM level, but as embedded point charges. Comparison with D1-W results should point out if this lower level approach can model solute-solvent interactions with a sufficient accuracy for electronic dynamics simulations.

D1-C ^{1}MLCT$_A$ HOMO-1 $\rightarrow$ LUMO+4 starting photoexcitation moves electron density from NCS2 ligand towards dcbpy2, as in D1-W, but now mainly onto the axial dcbpy2a ring (Fig. 5.31, left panel). NCS2/Ru hole exchange ($r_{\mathrm{NCS2/Ru}} = -0.50$, Figs. 5.32 and 5.33, left panels) is $\sim 3000\,\mathrm{cm}^{-1}$ faster ($18\,680\,\mathrm{cm}^{-1}$) than in D1-W. NCS1 is again only marginally involved in charge transfer processes.

The most remarkable difference with respect to D1-W is the dcbpy1/dcbpy2 electron sharing ($r_{\mathrm{dcbpy1/dcbpy2}} = -0.96$), which appears artificially induced (at a $2669\,\mathrm{cm}^{-1}$ frequency) by the close water molecules point charges, being in fact absent with QM water molecules. In particular, a dcbpy1b/dcbpy2a equatorial/axial mechanism ($r_{\mathrm{dcbpy1b/dcbpy2a}} = -0.93$) seems to prevail.

Therefore, while the hole barycenter spatial distribution is quite similar to D1-W ^{1}MLCT$_A$, the electron barycenter is not confined anymore around dcbpy2, but oscillates between dcbpy2a and dcbpy1b rings (Fig. 5.34, left panels). The mean hole/electron distance (2.168 Å, Table 5.5) is ~ 1 Å lower than in D1-W, while RMS hole ($1.389\,\mathrm{Å\,fs}^{-1}$) and electron velocities ($1.326\,\mathrm{Å\,fs}^{-1}$) are nearly doubled with respect to D1-W ^{1}MLCT$_A$ propagation.

While in D1-W ^{1}MLCT$_B$ a weak negative correlation between Ru and NCS2 charges still exists, in D1-C they appear decoupled (Fig. 5.35, left panels). A moderate positive, but delayed, correlation between the two NCS^- ligands is instead still found ($r_{\mathrm{NCS1/NCS2}} = 0.52$ at $\tau = 1.15$ fs, Fig. 5.36, left panel).

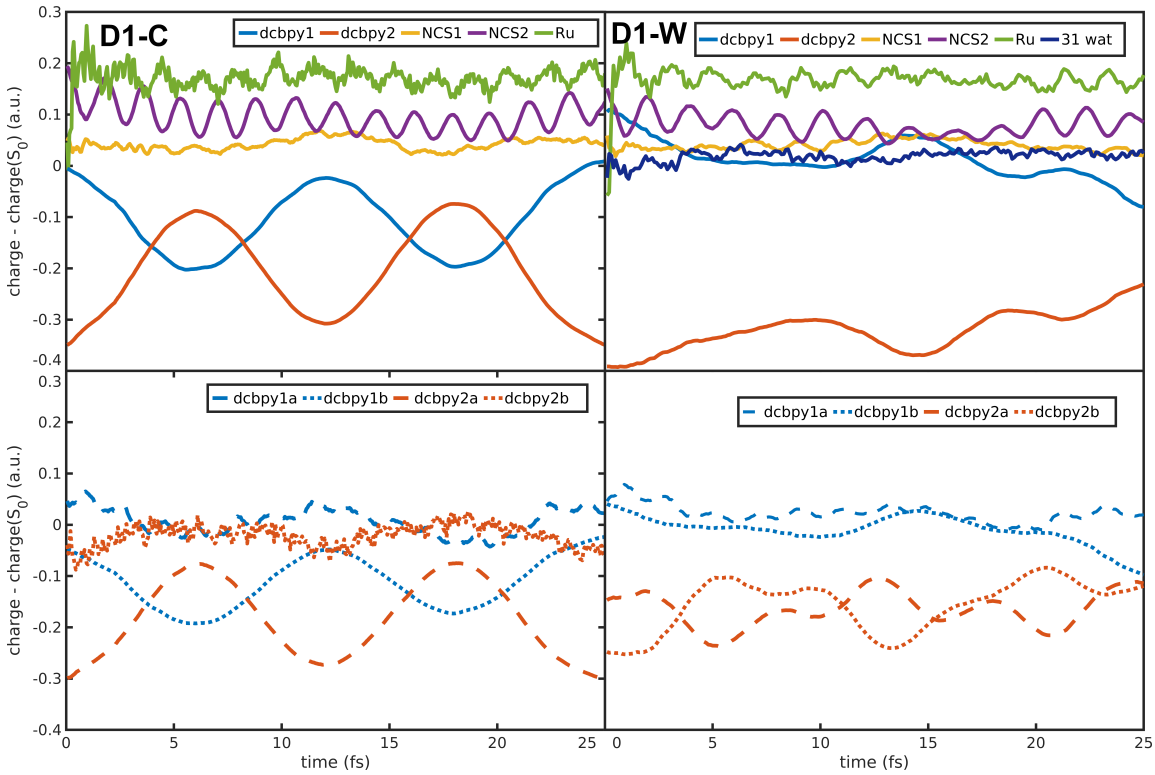


Figure 5.31: Fragments charges (with respect to the S_0 state) along $^1MLCT_A$ RT-TDDFT electronic dynamics (D1-C: left panels, D1-W: right panels).

Table 5.5: Hole - electron RMS distance and RMS velocities from $^1MLCT_A$ RT-TDDFT dynamics (D1-C and D1-W structures).

	d_{h^+/e^-} (Å)	v_{h^+} (Å fs^{-1})	v_{e^-} (Å fs^{-1})
D1-C	2.168	1.389	1.326
D1-W	3.100	0.777	0.766

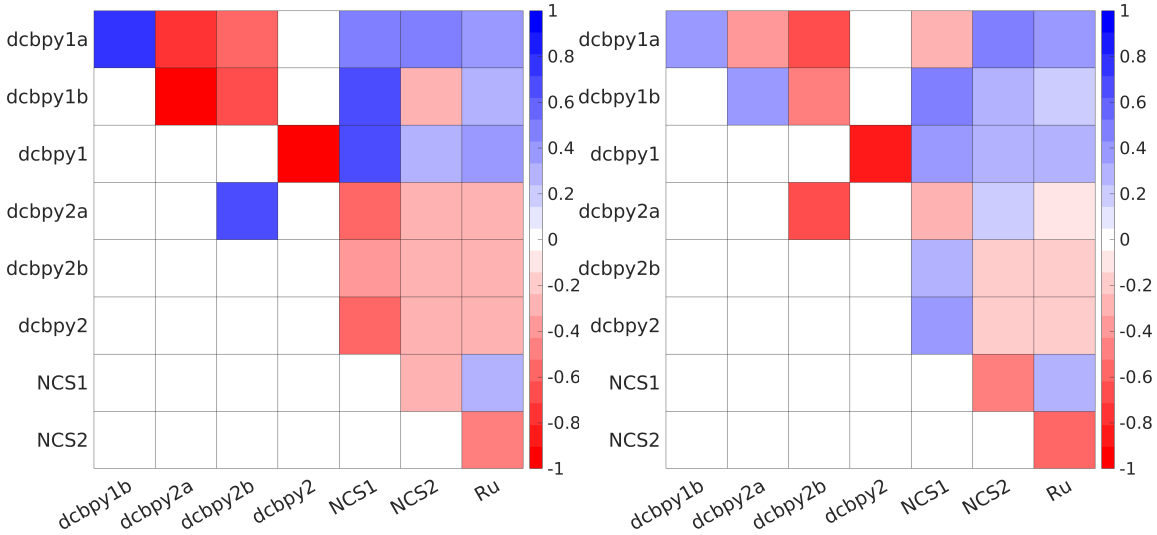


Figure 5.32: Normalized r_{xy} cross-correlations map between fragment charges time series from $^1\text{MLCT}_A$ RT-TDDFT electronic dynamics (D1-C: left panel, D1-W: right panel).

Now the electron is initially located on the dcbpy1 ligand (in particular on dcbpy1b ring), and not on dcbpy2, as in D1-W. Moreover, the water molecules point charges seem to accelerate the dcbpy1/dcbpy2 exchange ($r_{\text{dcbpy1/dcbpy2}} = -0.97$). Again a predominant dcbpy1b/dcbpy2a ($r_{\text{dcbpy1b/dcbpy2a}} = -0.94$) transfer is observed.

The hole barycenter distribution is on the $(\text{NCS})_2\text{Ru}$ side, near the Ru center (Fig. 5.38, left panels). The electron barycenter position explores the region from dcbpy1b to dcbpy2a, as in D1-W $^1\text{MLCT}_B$. The charge carriers are on average ~ 0.6 Å closer (2.196 Å, Table 5.6) than in D1-W. Also in $^1\text{MLCT}_B$, the water point charges close to $N3^{4-}$ induce high mobilities to the hole ($1.514\,\text{Å}\,\text{fs}^{-1}$) and the electron ($1.470\,\text{Å}\,\text{fs}^{-1}$), which, compared to the lower D1-W values, appear therefore unphysical.

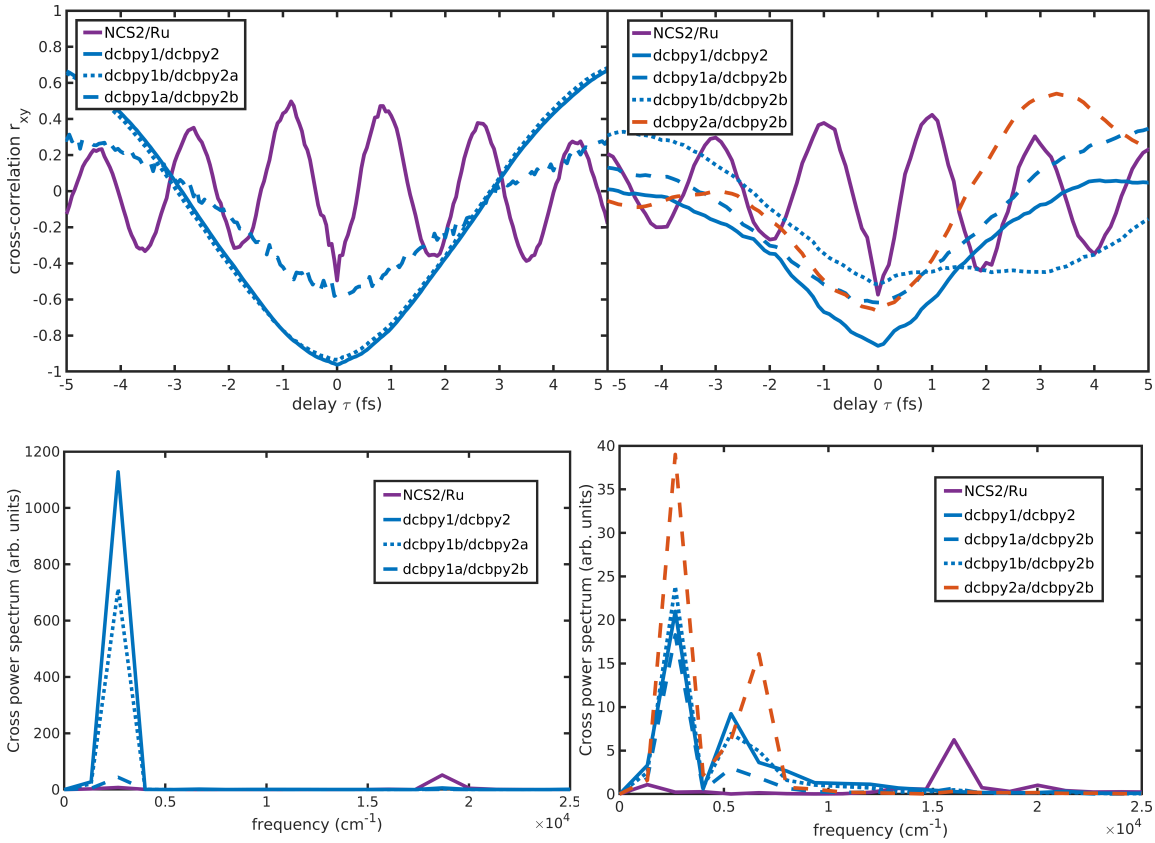


Figure 5.33: Cross-correlations and cross power spectra between selected pairs of fragment charges time-series collected in the ^{1}MLCT$_A$ RT-TDDFT dynamics (D1-C: left panels, D1-W: right panels).

Table 5.6: Hole - electron RMS distance and RMS velocities from ^{1}MLCT$_B$ RT-TDDFT dynamics (D1-C and D1-W structures).

	d_{h^+/e^-} (Å)	v_{h^+} (Å fs^{-1})	v_{e^-} (Å fs^{-1})
D1-C	2.196	1.514	1.470
D1-W	2.759	0.838	0.760

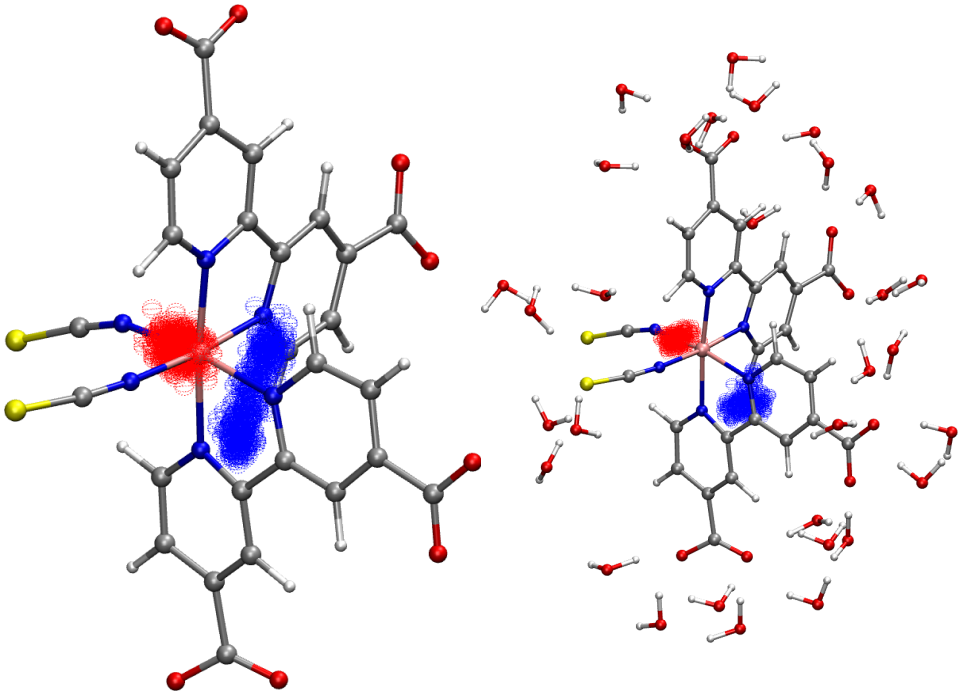


Figure 5.34: Hole and electron distributions from $^{1}\mathrm{MLCT}_{A}$ RT-TDDFT dynamics (D1-C: left panel, D1-W: right panel).

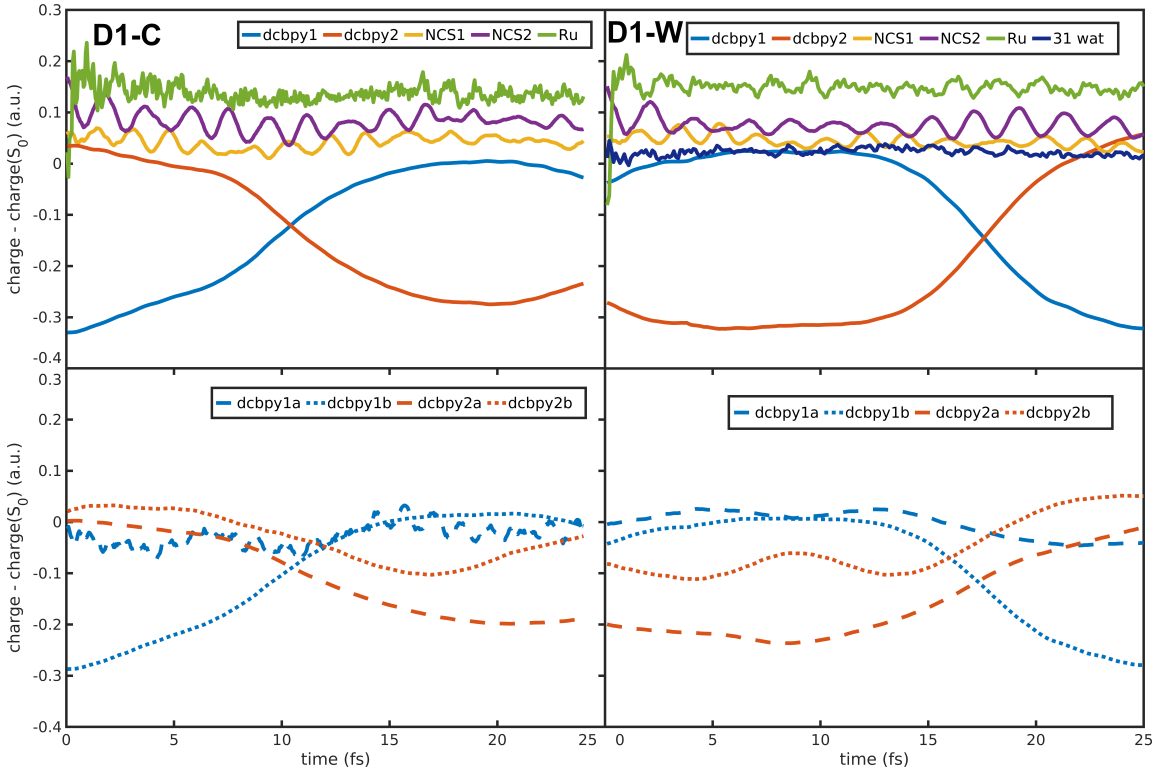


Figure 5.35: Fragments charges (with respect to the S_0 state) along $^1MLCT_B$ RT-TDDFT electronic dynamics (D1-C: left panels, D1-W: right panels).

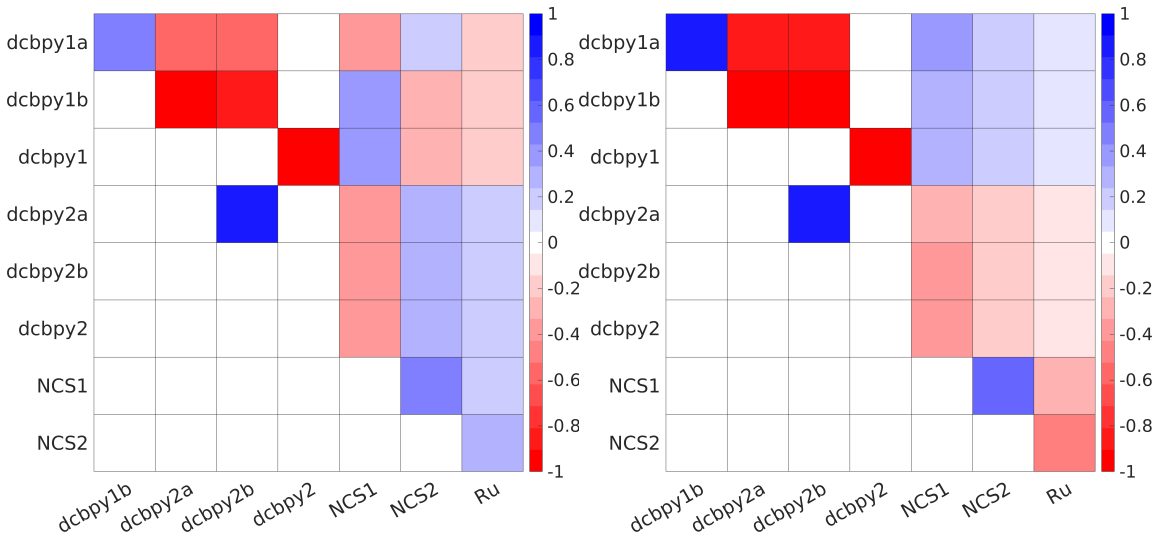


Figure 5.36: Normalized r_{xy} cross-correlations map between fragment charges time series from ^{1}MLCT$_B$ RT-TDDFT electronic dynamics (D1-C: left panel, D1-W: right panel).

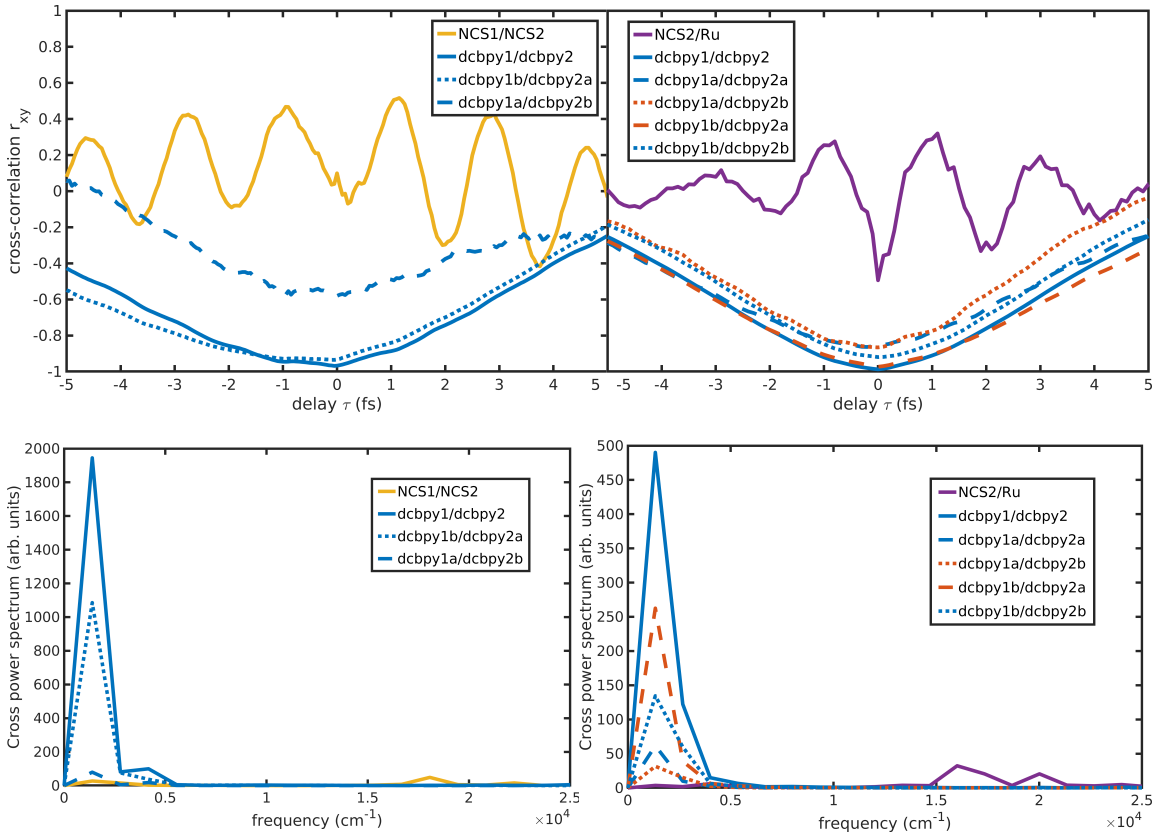


Figure 5.37: Cross-correlations and cross power spectra between selected pairs of fragment charges time-series collected in the ^{1}MLCT$_B$ RT-TDDFT dynamics (D1-C: left panels, D1-W: right panels).

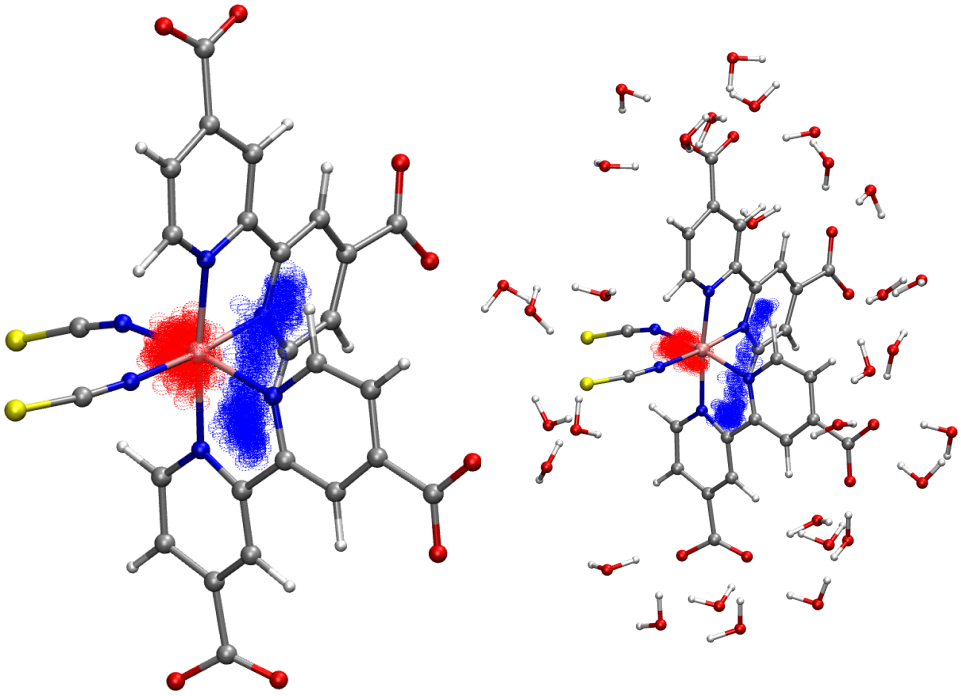


Figure 5.38: Hole and electron distributions from $^1\text{MLCT}_B$ RT-TDDFT dynamics (D1-C: left panel, D1-W: right panel).

5.7 Conclusions

The solvation, vibrational and excited state electronic properties of the popular dye sensitizer $[Ru(dcbpy)_2(NCS)_2]^{4-}$ ('$N3^{4-}$') have been investigated through molecular and electronic dynamics computational approaches.

A ground state sampling in explicit water solution reveals a clear solvation around thiocyanate sulfur (4 solvent molecules in the first shell) and dcbpy oxygen atoms (3-4 water molecules) solvation sites.

The dcbpy asymmetric carboxylate stretching and the thiocyanate C=S and C=N stretchings appear to be affected by a solvent shift in water solution (in particular, $> 100\,\mathrm{cm}^{-1}$ for $\nu_{\mathrm{asymm}}(\mathrm{COO})$ and $\nu(\mathrm{CN})$), as shown by a generalized normal modes vibrational analysis.

Two excited states (called $^1\mathrm{MLCT}_A$ and $^1\mathrm{MLCT}_B$) implied in the relaxation process following the photo-excitation have been investigated from a dynamical perspective in different environments. Both charge transfer states induce a 'hole' in the $(NCS)_2$/Ru moiety, placing the 'electron' respectively onto all the dcbpy rings, or only onto those *trans* to the NCS^- ligands. $^1\mathrm{MLCT}_A$ and $^1\mathrm{MLCT}_B$ RT-TDDFT propagation shows that the photo-generated hole and electron do not appear to recombine in the simulated (25 fs) time, oscillating instead within their respective domains. Very different frequencies seem to characterize the hole (13 000-17 000 cm^{-1}) and the electron ($< 1000\,\mathrm{cm}^{-1}$) oscillations among distinct groups. Simulations carried out on an optimized gas-phase $N3^{4-}$ symmetric structure reveal a substantial stability of the electron on the dcbpy ligands, although a high electron desymmetrization after ~ 15 fs is observed in $^1\mathrm{MLCT}_B$ evolution.

The possible effects of a polar solvent onto $N3^{4-}$ excited states electronic dynamics have been then investigated. $N3^{4-}$ ground state molecular dynamics simulation in explicit water solution reveals some distortions in Ru coordination geometry with respect to the gas-phase minimum. A snapshot has been then selected for $^1\mathrm{MLCT}_A$ and $^1\mathrm{MLCT}_B$ electronic dynamics in water solution. A single structure, not being able of course to resume the whole structural and solvation sampling given by the full MD trajectory, includes, nevertheless, some distortion and solute-solvent interaction effects.

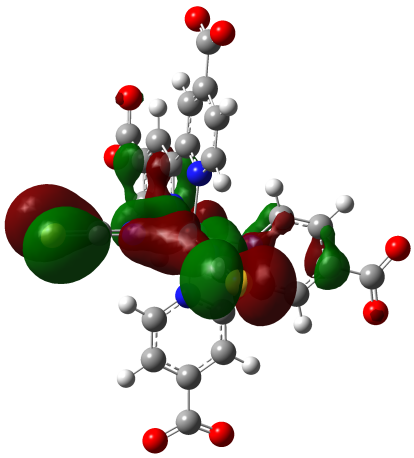
The MD-derived N3^{4-} structure without any solvent molecule therefore represents an 'intermediate step', showing how the deviations from the symmetric gas-phase structure affect the electronic dynamics. A first consequence is a charge distribution asymmetry. The hole is shared between the Ru metal center and only one of the two NCS^- ligands, while the electron, initially localized on one of the two dcbpy ligands, is shared with ($^1MLCT_A$) or completely transferred to ($^1MLCT_B$) the other one. The distortion seems moreover to substantially increase the electron barycenter velocity in the $^1MLCT_A$ state.

In order to achieve an accurate modelling of mutual solute-solvent polarization in N3^{4-} excited states electronic dynamics, first-shell water solvent molecules have been then included at a quantum mechanical level and the other ones as embedded atomic point charges. Hole and electron asymmetries still characterize both $^1MLCT_A$ and $^1MLCT_B$ states. Now the hole sharing between the Ru(II) and one of the two NCS^- ligand is less clear. Quite unexpectedly, in the $^1MLCT_A$ evolution the polarization effect by the surrounding water molecules contributes to keep the electron mainly on only one dcbpy ligand along all the trajectory. In $^1MLCT_B$, an electron exchange between the two dcbpy ligands is nevertheless observed, but ~ 20 fs after the excitation (so for a longer time than in the MD-derived gas-phase structure). Average charge carriers velocities are globally reduced with respect to both the optimized and the MD-extracted gas-phase structures. Moreover, in $^1MLCT_A$ the hole and the electron are on average closer. The prediction of an ultra-fast dcbpy/dcbpy inter-ligand electron transfer in N3^{4-} ^{1}MLCT excited states is potentially relevant for electron injection on semiconductor surfaces and agrees with the most recent experimental findings about the time-scale of this process.

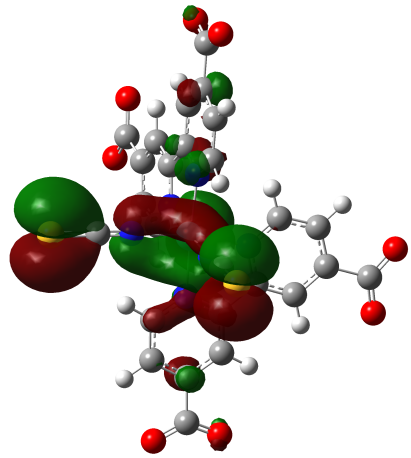
From a more methodological point of view, the opportunity to model the first-shell water molecules not as QM centers, but as simpler embedded point charges, has been explored. The electron dynamics appears enhanced by the close charges, in particular for the $^1MLCT_A$ state. This approach induces moreover a reduced hole-electron distance and higher mean velocities, probably due to an artificially increased polarization effect.

5.8 Appendix: N3^{4-} MOs.

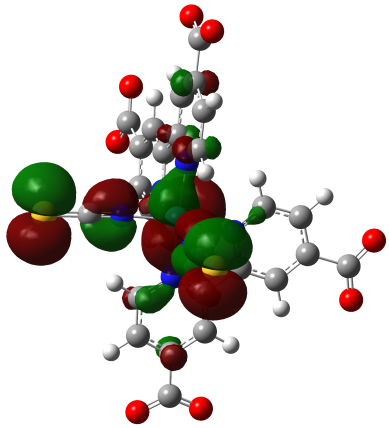
N3^{4-} molecular orbitals mostly involved in the electronic dynamics are reported in Figs. 5.39 and 5.40 (M-G structure), Figs. 5.41 and 5.42 (D1-G structure) and Figs. 5.43 and 5.44 (D1-W structure).



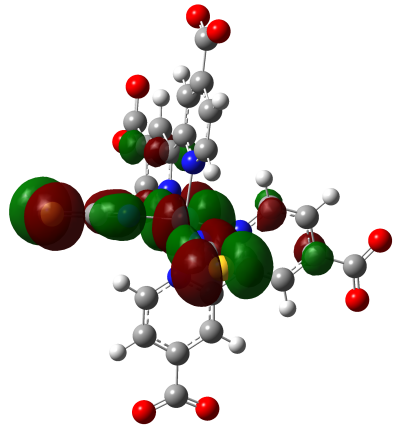
HOMO-18 (MO 145)



HOMO-17 (MO 146)

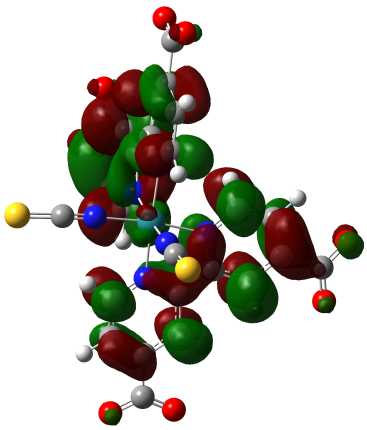


HOMO-1 (MO 162)

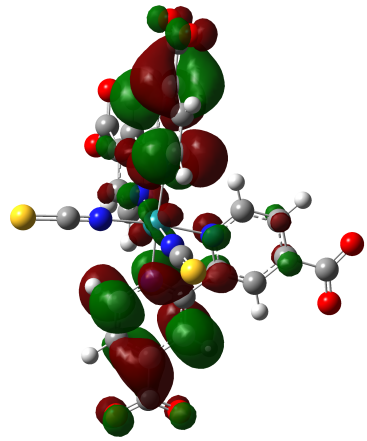


HOMO (MO 163)

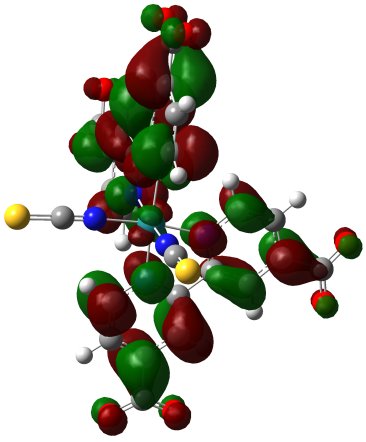
Figure 5.39: Occupied MOs (M-G structure).



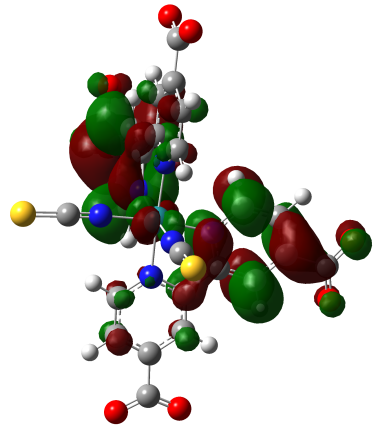
LUMO+2 (MO 166)



LUMO+3 (MO 167)

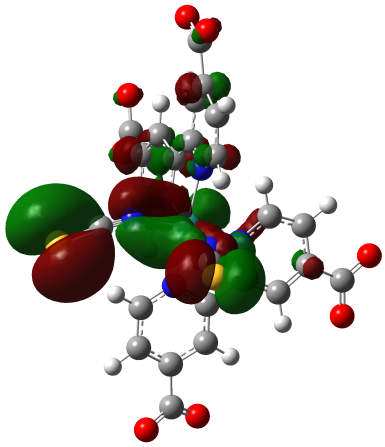


LUMO+4 (MO 168)

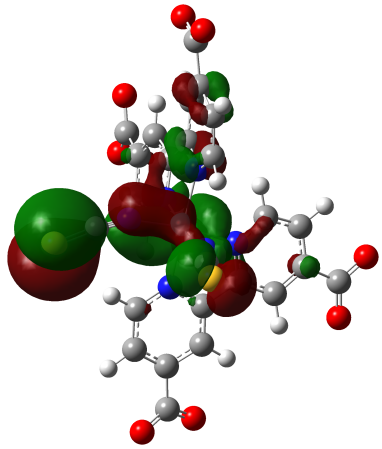


LUMO+5 (MO 169)

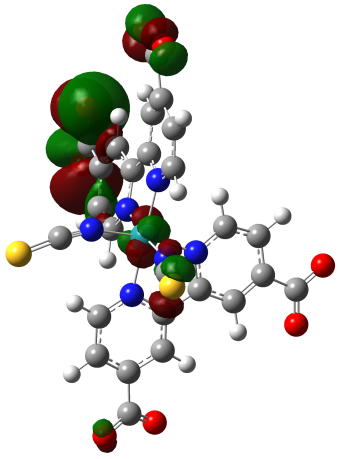
Figure 5.40: Unoccupied MOs (M-G structure).



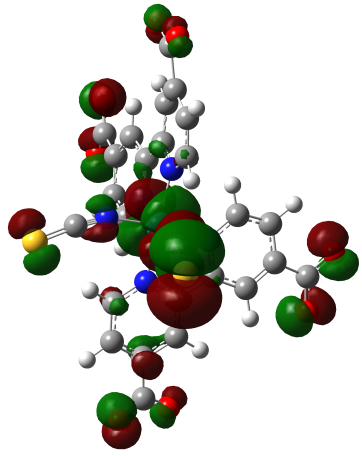
HOMO-18 (MO 145)



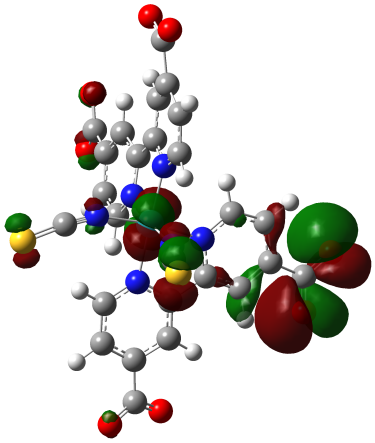
HOMO-17 (MO 146)



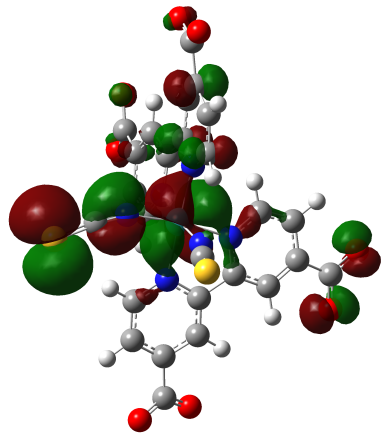
HOMO-4 (MO 159)



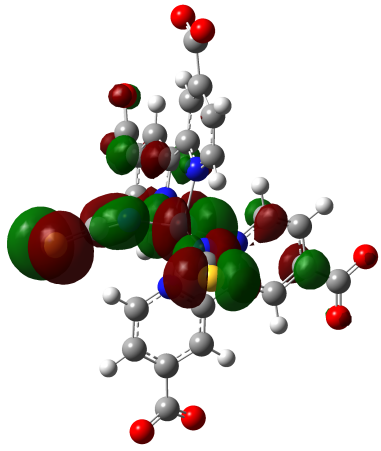
HOMO-3 (MO 160)



HOMO-2 (MO 161)

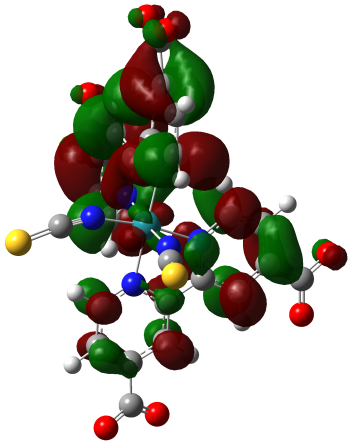


HOMO-1 (MO 162)

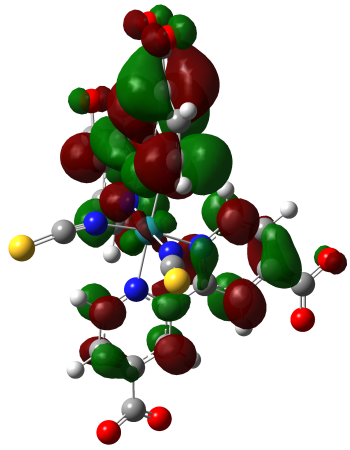


HOMO (MO 163)

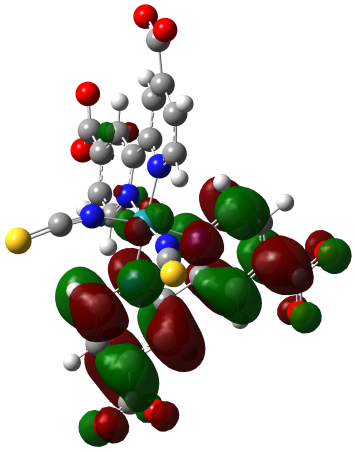
Figure 5.41: Occupied MOs (D1-G structure).



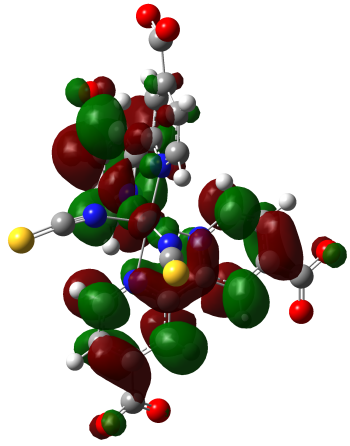
LUMO+2 (MO 166)



LUMO+3 (MO 167)

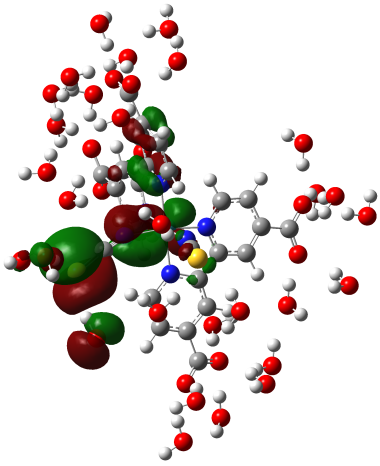


LUMO+4 (MO 168)

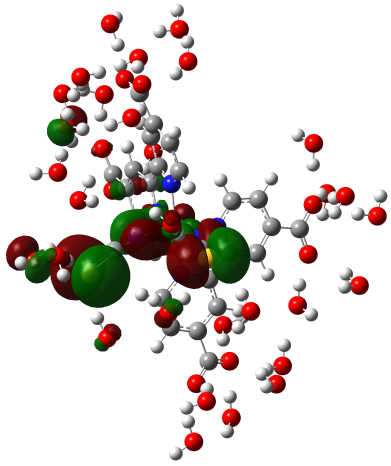


LUMO+5 (MO 169)

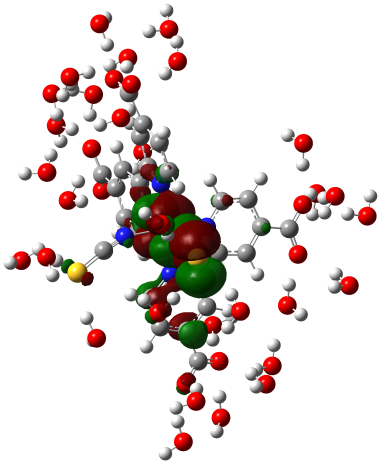
Figure 5.42: Unoccupied MOs (D1-G structure).



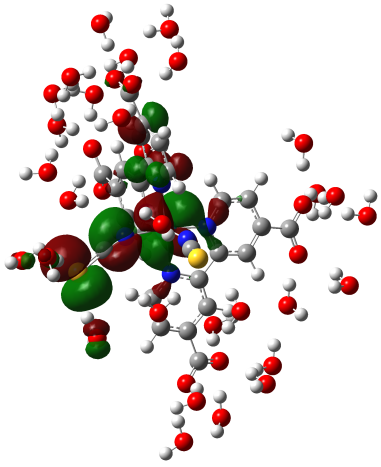
HOMO-6 (MO 312)



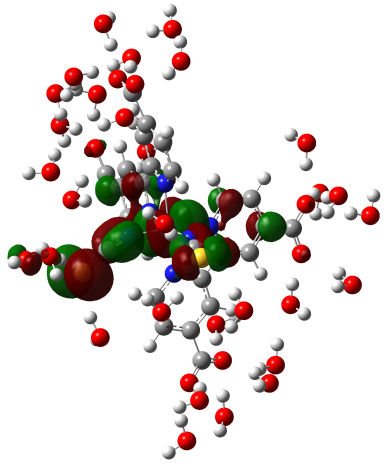
HOMO-3 (MO 315)



HOMO-2 (MO 316)

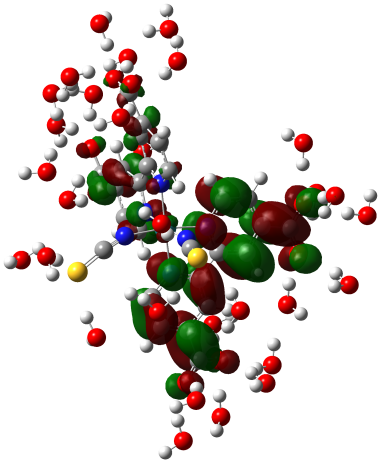


HOMO-1 (MO 317)

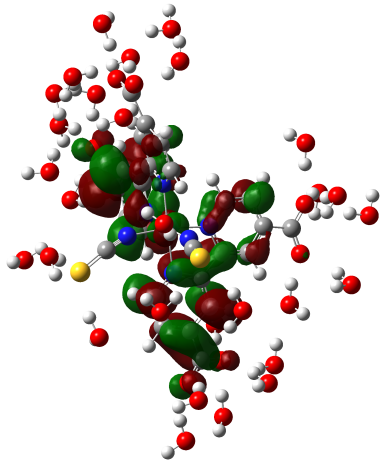


HOMO (MO 318)

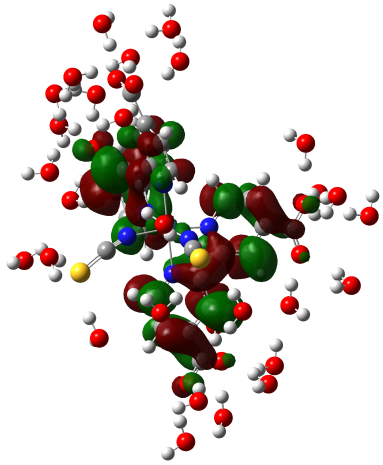
Figure 5.43: Occupied MOs (D1-W structure).



LUMO+3 (MO 322)



LUMO+4 (MO 323)



LUMO+5 (MO 324)

Figure 5.44: Unoccupied MOs (D1-W structure).

Bibliography

[1] Hansson, T.; Oostenbrink, C.; van Gunsteren, W. *Curr. Opin. Struc. Biol.* **2002**, *12*, 190–196.

[2] Karplus, M.; McCammon, J. A. *Nat. Struct. Biol.* **2002**, *9*, 646–652.

[3] Binder, K. *Monte Carlo and molecular dynamics simulations in polymer science*; Oxford University Press, 1995.

[4] Durrant, J. D.; McCammon, J. A. *BMC Biol.* **2011**, *9*, 1–9.

[5] Rapaport, D. C. *The art of molecular dynamics simulation*; Cambridge university press, 2004.

[6] Rahman, A.; Stillinger, F. H. *J. Chem. Phys.* **1971**, *55*, 3336–3359.

[7] Kresse, G.; Hafner, J. *Phys. Rev. B* **1993**, *47*, 558.

[8] Kresse, G.; Hafner, J. *Phys. Rev. B* **1993**, *48*, 13115.

[9] Van Gunsteren, W. F.; Berendsen, H. J. *Angew. Chem. Int. Ed.* **1990**, *29*, 992–1023.

[10] Marx, D.; Hutter, J. *Ab initio molecular dynamics: basic theory and advanced methods*; Cambridge University Press, 2009.

[11] Kohn, W.; Becke, A. D.; Parr, R. G. *J. Phys. Chem.* **1996**, *100*, 12974–12980.

[12] Parr, R. G.; Yang, W. *Annu. Rev. Phys. Chem.* **1995**, *46*, 701–728.

[13] Cramer, C. J.; Truhlar, D. G. *Phys. Chem. Chem. Phys.* **2009**, *11*, 10757–10816.

[14] Koch, W.; Holthausen, M. C. *A chemist's guide to density functional theory*; John Wiley & Sons, 2015.

[15] Parr, R. G. In *Horizons of quantum chemistry*; Springer, 1980; pp 5–15.

[16] Hohenberg, P.; Kohn, W. *Phys. Rev.* **1964**, *136*, B864.

[17] Kohn, W.; Sham, L. J. *Phys. Rev.* **1965**, *140*, A1133.

[18] Car, R.; Parrinello, M. *Phys. Rev. Lett.* **1985**, *55*, 2471.

[19] Hutter, J. *WIRES Comput. Mol. Sci.* **2012**, *2*, 604–612.

[20] Iannuzzi, M.; Laio, A.; Parrinello, M. *Phys. Rev. Lett.* **2003**, *90*, 238302.

[21] Tuckerman, M. E.; Parrinello, M. *J. Chem. Phys.* **1994**, *101*, 1302–1315.

[22] Pastore, G.; Smargiassi, E.; Buda, F. *Phys. Rev. A* **1991**, *44*, 6334.

[23] Remler, D. K.; Madden, P. A. *Mol. Phys.* **1990**, *70*, 921–966.

[24] Tangney, P.; Scandolo, S. *J. Chem. Phys.* **2002**, *116*, 14–24.

[25] Tangney, P. *J. Chem. Phys.* **2006**, *124*, 044111.

[26] Bornemann, F. A.; Schütte, C. *Numer. Math.* **1998**, *78*, 359–376.

[27] Ong, S. W.; Tok, E. S.; Kang, H. C. *Phys. Chem. Chem. Phys.* **2010**, *12*, 14960–14966.

[28] Schlegel, H. B.; Millam, J. M.; Iyengar, S. S.; Voth, G. A.; Daniels, A. D.; Scuseria, G. E.; Frisch, M. J. *J. Chem. Phys.* **2001**, *114*, 9758–9763.

[29] Iyengar, S. S.; Schlegel, H. B.; Millam, J. M.; A. Voth, G.; Scuseria, G. E.; Frisch, M. J. *J. Chem. Phys.* **2001**, *115*, 10291–10302.

[30] Schlegel, H. B.; Iyengar, S. S.; Li, X.; Millam, J. M.; Voth, G. A.; Scuseria, G. E.; Frisch, M. J. *J. Chem. Phys.* **2002**, *117*, 8694–8704.

[31] Iyengar, S. S.; Schlegel, H. B.; Voth, G. A.; Millam, J. M.; Scuseria, G. E.; Frisch, M. J. *Israel J. Chem.* **2002**, *42*, 191–202.

[32] Rega, N.; Iyengar, S. S.; Voth, G. A.; Schlegel, H. B.; Vreven, T.; Frisch, M. J. *J. Phys. Chem. B* **2004**, *108*, 4210–4220.

[33] McWeeny, R. *Rev. Mod. Phys.* **1960**, *32*, 335.

[34] Dunning, T. H.; Hay, P. J. In *Methods of electronic structure theory*; Springer, 1977; pp 1–27.

[35] Laasonen, K.; Pasquarello, A.; Car, R.; Lee, C.; Vanderbilt, D. *Phys. Rev. B* **1993**, *47*, 10142.

[36] Sousa, S. F.; Fernandes, P. A.; Ramos, M. J. *J. Phys. Chem. A* **2007**, *111*, 10439–10452.

[37] Todorova, T.; Seitsonen, A. P.; Hutter, J.; Kuo, I.-F. W.; Mundy, C. J. *J. Phys. Chem. B* **2006**, *110*, 3685–3691.

[38] Dahlke, E. E.; Truhlar, D. G. *J. Phys. Chem. B* **2005**, *109*, 15677–15683.

[39] Sprik, M.; Hutter, J.; Parrinello, M. *J. Chem. Phys.* **1996**, *105*, 1142–1152.

[40] Zhang, C.; Donadio, D.; Gygi, F.; Galli, G. *J. Chem. Theory Comput.* **2011**, *7*, 1443–1449.

[41] Yoo, S.; Zeng, X. C.; Xantheas, S. S. *J. Chem. Phys.* **2009**, *130*, 221102.

[42] VandeVondele, J.; Mohamed, F.; Krack, M.; Hutter, J.; Sprik, M.; Parrinello, M. *J. Chem. Phys.* **2005**, *122*, 014515.

[43] Guidon, M.; Schiffmann, F.; Hutter, J.; VandeVondele, J. *J. Chem. Phys.* **2008**, *128*, 214104.

[44] Li, X.-P.; Nunes, R. W.; Vanderbilt, D. *Phys. Rev. B* **1993**, *47*, 10891.

[45] Li, X.; Millam, J. M.; Scuseria, G. E.; Frisch, M. J.; Schlegel, H. B. *J. Chem. Phys.* **2003**, *119*, 7651–7658.

[46] Li, X.; Moss, C. L.; Liang, W.; Feng, Y. *J. Chem. Phys.* **2009**, *130*, 234115.

[47] Pulay, P.; Fogarasi, G.; Pang, F.; Boggs, J. E. *J. Am. Chem. Soc.* **1979**, *101*, 2550–2560.

[48] Raucci, U.; Perrella, F.; Donati, G.; Zoppi, M.; Petrone, A.; Rega, N. *J. Comput. Chem.* **2020**, *41*, 2228–2239.

[49] Coppola, F.; Perrella, F.; Petrone, A.; Donati, G.; Rega, N. *Front. Mol. Biosci.* **2020**, *7*.

[50] Donati, G.; Petrone, A.; Rega, N. *Phys. Chem. Chem. Phys.* **2020**, *22*, 22645–22661.

[51] Chiariello, M. G.; Rega, N. *J. Phys. Chem. A* **2018**, *122*, 2884–2893.

[52] Caruso, P.; Causa, M.; Cimino, P.; Crescenzi, O.; D'Amore, M.; Improta, R.; Pavone, M.; Rega, N. *Theor. Chem. Acc.* **2012**, *131*, 1211.

[53] Raucci, U.; Chiariello, M. G.; Rega, N. *J. Chem. Theory Comput.* **2020**, *16*, 7033–7043.

[54] Brancato, G.; Rega, N.; Barone, V. *Chem. Phys. Lett.* **2009**, *483*, 177–181.

[55] Rega, N.; Brancato, G.; Barone, V. *Chem. Phys. Lett.* **2006**, *422*, 367–371.

[56] Harris, J. *Phys. Rev. B* **1985**, *31*, 1770.

[57] Austin, A. J.; Frisch, M. J.; Montgomery, J. A.; Petersson, G. A. *Theor. Chem. Acc.* **2002**, *107*, 180–186.

[58] Van Loan, C. F. *J. Comput. Appl. Math.* **2000**, *123*, 85–100.

[59] Bennett, C. H. *J. Comput. Phys.* **1975**, *19*, 267–279.

[60] Van Loan, C. F.; Pitsianis, N. In *Linear algebra for large scale and real-time applications*; Springer, 1993; pp 293–314.

[61] Golub, G.; Van Loan, C.; Van Loan, C.; Van Loan, P. *Matrix Computations*; Johns Hopkins Studies in the Mathematical Sciences; Johns Hopkins University Press, 1996.

[62] Thomas, M.; Brehm, M.; Fligg, R.; Vöhringer, P.; Kirchner, B. *Phys. Chem. Chem. Phys.* **2013**, *15*, 6608–6622.

[63] Chatfield, C. *The analysis of time series: an introduction*; Chapman and Hall/CRC, 2003.

[64] Grossman, J. C.; Schwegler, E.; Draeger, E. W.; Gygi, F.; Galli, G. *J. Chem. Phys.* **2004**, *120*, 300–311.

[65] Herbert, J. M.; Head-Gordon, M. *J. Chem. Phys.* **2004**, *121*, 11542–11556.

[66] Vidale, G. L. *J. Phys. Chem.* **1960**, *64*, 314–318.

[67] Bandekar, J. *Biochim. Biophys. Acta* **1992**, *1120*, 123–143.

[68] Venkatachalapathi, Y. V.; Mierke, D. F.; Taulane, J. P.; Goodman, M. *Biopolymers* **1987**, *26*, 763–773.

[69] Craig, N. C.; Lacuesta, N. N. *J. Chem. Educ.* **2004**, *81*, 1199.

[70] Gaynor, J. D.; Petrone, A.; Li, X.; Khalil, M. *J. Phys. Chem. Lett.* **2018**, *9*, 6289–6295.

[71] Grätzel, M. *Inorg. Chem.* **2005**, *44*, 6841–6851.

[72] Hagfeldt, A.; Boschloo, G.; Sun, L.; Kloo, L.; Pettersson, H. *Chem. Rev.* **2010**, *110*, 6595–6663.

[73] Lee, B.; He, J.; Chang, R. P.; Kanatzidis, M. G. *Nature* **2012**, *485*, 486–489.

[74] Grätzel, M. *J. Photoch. Photobio. C* **2003**, *4*, 145–153.

[75] Chergui, M. *Acc. Chem. Res.* **2015**, *48*, 801–808.

[76] Juban, E. A.; Smeigh, A. L.; Monat, J. E.; McCusker, J. K. *Coordin. Chem. Rev.* **2006**, *250*, 1783–1791.

[77] McCusker, J. K. *Acc. Chem. Res.* **2003**, *36*, 876–887.

[78] Nazeeruddin, M. K.; Humphry-Baker, R.; Liska, P.; Grätzel, M. *J. Phys. Chem. B* **2003**, *107*, 8981–8987.

[79] Meng, Q.-B.; Takahashi, K.; Zhang, X.-T.; Sutanto, I.; Rao, T.; Sato, O.; Fujishima, A.; Watanabe, H.; Nakamori, T.; Uragami, M. *Langmuir* **2003**, *19*, 3572–3574.

[80] Waterland, M.; Kelley, D. *J. Phys. Chem. A* **2001**, *105*, 4019–4028.

[81] Asbury, J. B.; Ellingson, R. J.; Ghosh, H. N.; Ferrere, S.; Nozik, A. J.; Lian, T. *J. Phys. Chem. B* **1999**, *103*, 3110–3119.

[82] Horvath, R.; Fraser, M. G.; Clark, C. A.; Sun, X.-Z.; George, M. W.; Gordon, K. C. *Inorg. Chem.* **2015**, *54*, 11697–11708.

[83] Shoute, L. C.; Loppnow, G. R. *J. Am. Chem. Soc.* **2003**, *125*, 15636–15646.

[84] Zhang, X.; Smolentsev, G.; Guo, J.; Attenkofer, K.; Kurtz, C.; Jennings, G.; Lockard, J. V.; Stickrath, A. B.; Chen, L. X. *J. Phys. Chem. Lett.* **2011**, *2*, 628–632.

[85] Kallioinen, J.; Benkö, G.; Sundström, V.; Korppi-Tommola, J. E.; Yartsev, A. P. *J. Phys. Chem. B* **2002**, *106*, 4396–4404.

[86] Durrant, J.; Tachibana, Y.; Mercer, I.; Moser, J.; Grätzel, M.; Klug, D. *Z. Phys. Chem.* **1999**, *212*, 93–98.

[87] Pellnor, M.; Myllyperkiö, P.; Korppi-Tommola, J.; Yartsev, A.; Sundström, V. *Chem. Phys. Lett.* **2008**, *462*, 205–208.

[88] Mark, P.; Nilsson, L. *J. Phys. Chem. A* **2001**, *105*, 9954–9960.

[89] Wang, J.; Wolf, R. M.; Caldwell, J. W.; Kollman, P. A.; Case, D. A. *J. Comput. Chem.* **2004**, *25*, 1157–1174.

[90] Brancato, G.; Rega, N.; Barone, V. *J. Chem. Phys.* **2008**, *128*, 04B607.

[91] Brancato, G.; Barone, V.; Rega, N. *Theor. Chem. Acc.* **2007**, *117*, 1001–1015.

[92] Strachan, A. *J. Chem. Phys.* **2004**, *120*, 1–4.

[93] Thicoipe, S.; Carbonniere, P.; Pouchan, C. *Chem. Phys. Lett.* **2014**, *591*, 243–247.

[94] Carbonniere, P.; Dargelos, A.; Ciofini, I.; Adamo, C.; Pouchan, C. *Phys. Chem. Chem. Phys.* **2009**, *11*, 4375–4384.

[95] Rega, N. *Theor. Chem. Acc.* **2006**, *116*, 347–354.

[96] Barone, V.; Cossi, M. *J. Phys. Chem. A* **1998**, *102*, 1995–2001.

[97] Cossi, M.; Rega, N.; Scalmani, G.; Barone, V. *J. Comput. Chem.* **2003**, *24*, 669–681.

[98] Rimgard, B. P.; Föhlinger, J.; Petersson, J.; Lundberg, M.; Zietz, B.; Woys, A. M.; Miller, S. A.; Wasielewski, M. R.; Hammarström, L. *Chem. Sci.* **2018**, *9*, 7958–7967.

[99] Finnie, K. S.; Bartlett, J. R.; Woolfrey, J. L. *Langmuir* **1998**, *14*, 2744–2749.

[100] Marques, M. A.; Gross, E. K. *Annu. Rev. Phys. Chem.* **2004**, *55*, 427–455.

[101] Marques, M.; Rubio, A.; Gross, E. K.; Burke, K.; Nogueira, F.; Ullrich, C. A. *Time-dependent density functional theory*; Springer Science & Business Media, 2006; Vol. 706.

[102] Li, X.; Govind, N.; Isborn, C.; DePrince III, A. E.; Lopata, K. *Chem. Rev.* **2020**, *120*, 9951–9993.

[103] Goings, J. J.; Lestrange, P. J.; Li, X. *WIREs Comput. Mol. Sci.* **2018**, *8*, e1341.

[104] Takimoto, Y.; Vila, F.; Rehr, J. *J. Chem. Phys.* **2007**, *127*, 154114.

[105] Lopata, K.; Govind, N. *J. Chem. Theory Comput.* **2011**, *7*, 1344–1355.

[106] Meng, S.; Kaxiras, E. *J. Chem. Phys.* **2008**, *129*, 054110.

[107] Provorse, M. R.; Isborn, C. M. *Int. J. Quant. Chem.* **2016**, *116*, 739–749.

[108] Goings, J. J.; Li, X. *J. Chem. Phys.* **2016**, *144*, 234102.

[109] Petrone, A.; Lingerfelt, D. B.; Rega, N.; Li, X. *Phys. Chem. Chem. Phys.* **2014**, *16*, 24457–24465.

[110] Martin, R. L. *J. Chem. Phys.* **2003**, *118*, 4775–4777.

[111] Damrauer, N. H.; Cerullo, G.; Yeh, A.; Boussie, T. R.; Shank, C. V.; McCusker, J. K. *Science* **1997**, *275*, 54–57.

[112] Kalyanasundaram, K. *Coordin. Chem. Rev.* **1982**, *46*, 159–244.

[113] Juris, A.; Balzani, V.; Barigelletti, F.; Campagna, S.; Belser, P. l.; von Zelewsky, A. v. *Coordin. Chem. Rev.* **1988**, *84*, 85–277.

[114] Kober, E. M.; Sullivan, B. P.; Meyer, T. J. *Inorg. Chem.* **1984**, *23*, 2098–2104.

[115] Dallinger, R. F.; Woodruff, W. H. *J. Am. Chem. Soc.* **1979**, *101*, 4391–4393.

[116] Oh, D. H.; Boxer, S. G. *J. Am. Chem. Soc.* **1989**, *111*, 1130–1131.

[117] Myrick, M.; Blakley, R.; DeArmond, M. *J. Am. Chem. Soc.* **1987**, *109*, 2841–2842.

[118] Benkö, G.; Kallioinen, J.; Myllyperkiö, P.; Trif, F.; Korppi-Tommola, J. E.; Yartsev, A. P.; Sundström, V. *J. Phys. Chem. B* **2004**, *108*, 2862–2867.

[119] Cole, J. M.; Gong, Y.; McCree-Grey, J.; Evans, P. J.; Holt, S. A. *ACS Appl. Energy Mater.* **2018**, *1*, 2821–2831.

[120] Mukaddem, K. T.; Chater, P. A.; Devereux, L. R.; Al Bahri, O. K.; Jain, A.; Cole, J. M. *J. Phys. Chem. C* **2020**, *124*, 11935–11945.

[121] Kley, C. S.; Dette, C.; Rinke, G.; Patrick, C. E.; Čechal, J.; Jung, S. J.; Baur, M.; Dürr, M.; Rauschenbach, S.; Giustino, F.; et al. *Nano Lett.* **2014**, *14*, 563–569.

[122] Wallin, S.; Davidsson, J.; Modin, J.; Hammarström, L. *J. Phys. Chem. A* **2005**, *109*, 4697–4704.

[123] Stark, C. W.; Schreier, W. J.; Lucon, J.; Edwards, E.; Douglas, T.; Kohler, B. *J. Phys. Chem. A* **2015**, *119*, 4813–4824.

[124] Asbury, J. B.; Anderson, N. A.; Hao, E.; Ai, X.; Lian, T. *J. Phys. Chem. B* **2003**, *107*, 7376–7386.

[125] Wenger, B.; Grätzel, M.; Moser, J.-E. *J. Am. Chem. Soc.* **2005**, *127*, 12150–12151.

[126] Ellingson, R. J.; Asbury, J. B.; Ferrere, S.; Ghosh, H. N.; Sprague, J. R.; Lian, T.; Nozik, A. J. *J. Phys. Chem. B* **1998**, *102*, 6455–6458.

[127] Tachibana, Y.; Moser, J. E.; Grätzel, M.; Klug, D. R.; Durrant, J. R. *J. Phys. Chem.* **1996**, *100*, 20056–20062.

[128] Benkö, G.; Kallioinen, J.; Korppi-Tommola, J. E.; Yartsev, A. P.; Sundström, V. *J. Am. Chem. Soc.* **2002**, *124*, 489–493.

[129] Benkö, G.; Myllyperkiö, P.; Pan, J.; Yartsev, A. P.; Sundström, V. *J. Am. Chem. Soc.* **2003**, *125*, 1118–1119.

[130] Teuscher, J.; Décoppet, J.-D.; Punzi, A.; Zakeeruddin, S. M.; Moser, J.-E.; Grätzel, M. *J. Phys. Chem. Lett.* **2012**, *3*, 3786–3790.